Design and characterization of metal-thiocyanate coordination polymers

by

Didier Savard

M.Sc., University of Ottawa, 2010

Thesis Submitted in Partial Fulfillment of the
Requirements for the Degree of
Doctor of Philosophy

in the
Department of Chemistry
Faculty of Science

SIMON FRASER UNIVERSITY

Spring 2018

Approval

Name: **Didier Savard**

Degree: **Doctor of Philosophy**

Title: ***Design and characterization of metal-thiocyanate coordination polymers***

Examining Committee: **Chair:** Hua-Zhong Yu
Professor

Daniel B. Leznoff
Senior Supervisor
Professor

Tim Storr
Supervisor
Associate Professor

Zuo-Guang Ye
Supervisor
Professor

Jeffrey J. Warren
Internal Examiner
Assistant Professor

Prof. Mark M. Turnbull
External Examiner
Professor
Carlson School of Chemistry
Clark University

Date Defended/Approved: January 12, 2018

Abstract

This thesis focuses on exploring the synthesis and chemical reactivity of thiocyanate-based building blocks of the type $[M(SCN)_x]^{y-}$ for the synthesis of coordination polymers. A series of potassium, ammonium, and tetraalkylammonium metal isothiocyanate salts of the type $Q_y[M(SCN)_x]$ were synthesized and structurally characterized. Most of the salts were revealed to be isostructural and classic Werner complexes, but for $(Et_4N)_3[Fe(NCS)_6]$ and $(n\text{-}Bu_4N)_3[Fe(NCS)_6]$, a solid-state size-dependent change in colour from red to green was observed. This phenomenon was attributed to a Brillouin light scattering effect by analyzing the UV-Visible spectra of various samples with different sized crystals.

Coordination polymers of the type $[M(L)_x][Pt(SCN)_4]$ were prepared and structurally characterized using a variety of bi- or tri-dentate capping ligands (ethylenediamine, 2,2'-bipyridine, 2,2';6',2"-terpyridine, *N*,*N*,*N*′,*N*′-Tetramethylethane-1,2-diamine). Overall, structural correlations between the ligand, the metal centre, the coordinating mode of the $[Pt(SCN)_4]^{2-}$ building block and the topologies of the coordination polymers were established. Similar systems were synthesized using the ligands N,N'-bis(methylpyridine)ethane-1,2-diamine (bmpeda) and N,N'-bis(methylpyridine)cyclohexane-1,2-diamine (bmpchda) and were revealed to be multidimensional coordination polymers by structural analysis.

Five complexes of the type $[Cu_2(\mu\text{-}OH)_2(L)_2][A]_x \cdot yH_2O$ (where L = 1,10-Phenanthroline, tmeda and 2,2'-bipyridine) were prepared and have been characterized by spectroscopic and crystallographic structural analyzes and by SQUID magnetometry. Two complexes were revealed to be dinuclear molecular units capped with the SCN^- ligand. The complexes involving the $[Au(CN)_4]^-$ anion were structurally characterized as double salts involving the dinuclear Cu(II) unit with a varying degree of hydration. The complex $[Cu_2(\mu\text{-}OH)_2(tmeda)_2Pt(SCN)_4]$ was revealed to be a 1D coordination polymer with trans-bridging $[Pt(SCN)_4]^{2-}$ units. The magnetic susceptibility versus temperature was measured and fitted for each system to obtain J-coupling values that were qualitatively compared to the previously published magnetostructural correlation for dinuclear hydroxide-bridged units. The birefringence and luminescent properties for four new complexes of the type $[Pb(4'\text{-}R\text{-}terpy)(SCN)_2]$ were measured. The complexes presented unique luminescence based on the presence of the SCN^- unit, whereas the birefringence of the complexes was compared to $[Au(CN)_2]^-$ analogues and was correlated to the structural properties of the system.

For my grandfather, Gilles

Acknowledgements

I would first like to thank my supervisor, Prof. Daniel B. Leznoff for his teachings, his understanding and insights, his enthusiasm about this work and his support throughout the years.

I would like to thank the members of my supervisory committee, Prof. Zuo-Guang Ye and Prof. Tim Storr for guiding me through my research, for encouraging me to persevere through the hardships and for providing wisdom over the years. I would like to specifically thank Prof. Tim Storr for teaching me about DFT calculations.

I would like to thank Dr. Jeffrey J. Warren and Prof. Mark M. Turnbull for taking to the time carefully read my thesis and for their comments and corrections.

I would also like to thank Prof. Ken Sakai from Kyushu University and Mr. Masayuki Kobayashi for their previous work on $[Pt(SCN)_4]^{2-}$ complexes, Prof. Vance E. Williams for his insight on Brillouin Light Scattering, Prof. Christian Réber for his advice and analysis on FTIR and Raman spectroscopic data, Dr. Michael J. Katz for his teachings on solving X-ray structures and for his work on birefringence, Mr. Frank Haftbaradaran and Mr. Paul Mulyk for their help with elemental analyses, Dr. Jeffrey S. Ovens for his insights on X-ray crystallography and birefringence, Dr. John K. Thompson for his teachings for birefringence measurements, Dr. Ryan J. Roberts for his help on luminescence and uv-visible spectroscopy, Dr. Cassandra Hayes for her insights on air-sensitive chemistry and for being a good friend and Mr. Ian Johnston for his hard work and a great summer work term.

I would also like to thank the Natural Science and Engineering Council, the government of British Columbia, Simon Fraser University and Natural Resources of Canada (ARG) for research funding. I also thank Westgrid and Compute Canada.

Table of Contents

List of Tables

List of Figures

List of Abbreviations

0D	Zero dimensional
1D	One dimensional
2,2'-bipy	2,2'-bipyridine
2D	Two dimensional
3D	Three dimensional
Anal.	Analysis
Bmpchda	N,N'-bis(methylpyridine)cyclohexane-1,2-diamine
Bmpeda	N,N'-bis(methylpyridine)ethane-1,2-diamine
br	Broad
Calc.	calculated
CP	Coordination Polymer
Δn	Birefrigence
EA	Elemental analysis
En	Ethylenediamine
FTIR	Fourier-Transform Infrared
HOIF	Hybrid Organic-Inorganic Framework
IR	Infrared
J	Magnetic J-coupling
k_B	Boltzman's constant
m	Medium
Me	Methyl group, CH_3^-
Me_2phen	2,9-dimethyl-1,10-phenanthroline
Me_4phen	3,4,7,8-Tetramethyl-1,10-phenanthroline
mL	Millilitre
MOF	Metal-Organic Framework
N	Avogrado's number
n	Refractive index
νCN	C≡N stretch
NLO	Non-linear optics

NMR	Nuclear magnetic resonance
NTE	Negative thermal expansion
Ph	Phenyl group, $C_6H_5^-$
Phen	1,10-Phenanthroline
PXRD	Powder X-ray Diffraction
RT	Room temperature
s	Small
SC-XRD	Single-Crystal X-ray Diffraction
SEM	Scanning electron microscope
SFU	Simon Fraser University
sh	sharp
T	Temperature
t	Thickness
Terpy	2,2';6',2"-terpyridine
Tmeda	N,N,N′,N′-Tetramethylethane-1,2-diamine
UV	Ultraviolet
UV-vis	UV-visible

Chapter 1. **Introduction**

1.1. **Coordination polymers**

Since the early 1990s, coordination polymers (CPs) have been of great interest to the research community due to the ability to control their properties depending on the choice of building blocks during their synthesis.[1-6] Since their discovery, CPs have been known to show physical properties of interest such as magnetism, porosity, luminescence, vapochromism, and birefringence.[7-29] For example, CPs showing magnetic properties can be used in electronic devices[30] and porous complexes can have applications as gas storage devices.[31-33] CPs can also be multifunctional materials; they can possess two or more of the properties mentioned above, enabling a wide variety of industrial applications. These materials are the target of an ever growing interest as more properties are discovered.

CPs consist of extended networks of solid-state materials and are made of repeating arrays of optionally ligand-capped metal centres (nodes) connected by bridging units (linkers) via dative bonds (Figure 1.1). They form through self-assembly of molecular components, also known as building blocks, and can result in a wide variety of complexes for which the structure (including their dimensionality, i.e., a 1D, 2D or 3D polymers) and properties are strictly dependent on the choice of building blocks.[1-33] When the building blocks are mixed in solution (e.g., $FeCl_3$ and $K_4[Fe(CN)_6]$), a metathesis reaction is usually targeted to exchange ions, thus forming the desired CP (e.g., $Fe_4[Fe(CN)_6]_3$) and a secondary material (e.g., KCl) which is usually eliminated via precipitation or solution in the mother liquor (Equation 1.1).[34] Depending on the solvent, the secondary material can have a low solubility and can be separated from the reaction easily by filtration, or have a high solubility, in which case the formation and crystallization of the CP is usually the preferred outcome. In this specific case, when the building blocks are mixed together, the materials self-assemble into a pseudo-cubic 3D

array called Prussian Blue where the Fe(III) and Fe(II) metal centres are alternating and bridged by CN^- units. Prussian Blue is insoluble in water, so when the two solutions are mixed together, the material is immediately obtained as pure blue powder and the secondary material, KCl, remains in solution. Initially, Prussian Blue was used exclusively as a dye for commercial applications, but subsequent usages were later discovered, such as being a cure for Thalium(I) poisoning.[36] In the early 1900s, the discovery of the magnetic properties of Prussian Blue, where the material shows ferromagnetic coupling below 5.6 K, led to a growing interest in synthesizing similar materials and other types of CPs.[37]

$$[M(L)_n][An]_y + [Cat]_x[B] \xrightarrow[\text{Solvents}]{} [M(L)_n][B] + [Cat]_x[An]_y$$

M = Metal centre; L = Ancillary ligand (optional); B = Bridging building block
Cat = Countercation; An = Counteranion

Equation 1.1 General synthetic approach for the synthesis of CPs involving metal-containing precursors and a metathesis reaction.

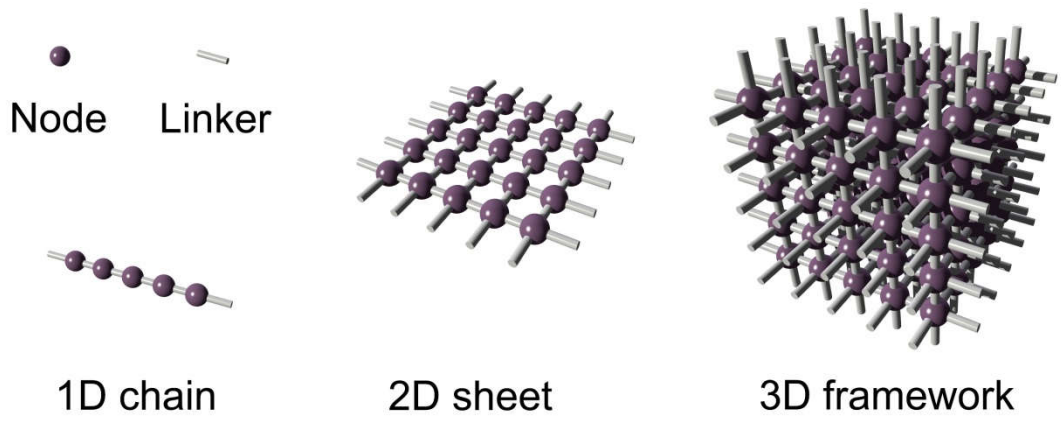

Figure 1.1 General structures of CPs formed by the self-assembly of nodes (purple) and linkers (grey) connected via dative bonds.

CPs are not the only type of polymeric materials; organic polymers, such as polyethylene, are also made of repeating units and can present similar properties to CPs depending on their structure. What differentiates CPs from these other materials is the fact that CPs are composed of units linked by metal-ligand coordination bonds, as opposed to covalent bonds in the case of organic polymers.[38-39] Because of that, CPs are exclusively solid-state materials; when in solution, the coordination bond presents

lability that enables reversibility of the assembly of the CPs. More specifically, when using an appropriate solvent, a CP can be dissolved and reassembled anew by forced precipitation or crystallization. In the case of organic polymers, the stronger covalent bonding between the units prevents disassembly and reassembly of the material without resorting to more complex reactions. Another type of polymeric material are Solid-State Materials (SSMs), which are usually prepared via solid-state reactions that require harsh reaction conditions, such as high temperatures or high pressures.[40] One example of such a material are the Perovskite-type complexes, which are often prepared by ball milling the metallic precursors followed by calcination at 750-800 °C for a few hours. Both CPs and SSMs exist in the solid-state, but in the case of CPs, organic ligands, which would not survive the reaction conditions for the synthesis of SSMs, can be added as capping ligands on either the bridging unit or nodal unit, enabling further customization of the structure and its properties. In general, for CPs, when the bridging unit is exclusively organic, such as 4,4'-bipyridine, the complex is more commonly referred to as a Metal-Organic Framework (MOF) or a Hybrid Organic-Inorganic Framework (HOIF).[41-44] When the bridging unit is entirely inorganic or contains a metal centre coordinated to a ligand, such as $[Fe(CN)_6]^{4-}$, the material is usually referred to as a CP.

The difficulty of synthesis and crystallization of CPs depends on the choice of building blocks used for their preparation.[1-30] In order for a material to be viable for commercial applications, one must design it so that it can be synthesized easily on a large scale, using either traditional synthetic methods or process chemistry, and as pure as possible.

The structure and properties of a CP are guided by the building blocks chosen. Traditionally, the nodal unit in the system consists of a metal centre that may or may not be capped by an organic ligand. The organic ligand can either be ancillary or functional, depending on the properties sought in the targeted CP. Examples of traditionally used capping ligands include pyridine, imidazole and carboxylate derivatives, and are shown in Figure 1.2.[1-30]

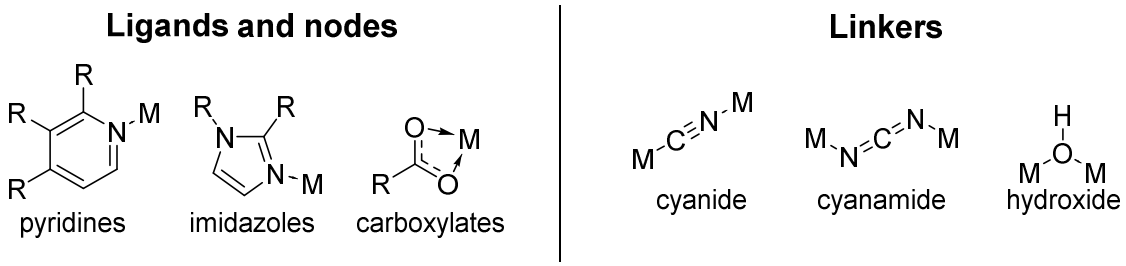

Figure 1.2 Example of ligands and linkers (bridging units) traditionally used in the synthesis of CPs.

For the bridging units, a wide variety of building blocks have been used for the synthesis of CPs, ranging from simple pseudohalides (an anion that is similar in size to halides and has similar a coordination behaviour), such as CN^-, NCN^- and OH^-, to more elaborate inorganic units such as bidentate oxalate-based complexes, $[M(C_2O_4)_3]^{3-}$. Since the 1930s, first-row cyanometallate building blocks, such as $[Co(CN)_4]^{2-}$ and $[Fe(CN)_6]^{4-}$, have also been used for the synthesis of CPs, mostly due to their ease of synthesis, high stability and low lability in solution, but also due to the strong interest developed for Prussian Blue analogues.[34-37]

As mentioned above, the structural and physical properties of the materials are dependent on the choice of nodes and linkers for the targeted CP. More specifically, nodes and linkers each present a specific number of coordination sites available for the formation of the CP.[1-30] By changing the number of coordination sites either with capping ligands on the node (e.g., by varying the ligand from 2,2'-bipy to terpy) or with more or less ligands on the linkers (e.g., $[Au(CN)_4]^-$ vs. $[Au(CN)_2]^-$), one can design a CP targeting a specific topology and dimensionality, and thus control the structural properties of the system. Physically, the properties of the individual nodes and linkers are often induced in the resulting CP, and thus a careful choice in the composition of either can result in functional materials. For example, if a node system that generally presents fluorescence in the solid-state is chosen (such as $[M(terpy)]^{2+}$), the same physical property is often observed in the prepared CP with alterations depending on the supramolecular structure or interactions with the bridging units.[1-30] Similarly, if a bridging system is known to present a specific property of interest, such as metal-metal bonding (e.g., for $[Au(CN)_2]^-$), it is probable that these properties could be present in the resulting CP.

In the Leznoff group, previous CP work has extensively used $K[Au(CN)_2]$ or $K[Au(CN)_4]$ as the bridging building block in combination with a wide variety of metal cations capped with ancillary ligands.[47-53] In general, the choice of ancillary ligands and metal centre combinations for the nodal unit has been focused on mono- or multidentate nitrogen-based ligands coordinated to a first-row metal centre. Examples of nodal complexes used previously include ligands such as 2,2'-bipy, en, terpy, tmeda, and phen (Figure 1.3) coordinated to first-row transition metal centres including Cr(III), Mn(II), Fe(II), Fe(III), Co(II), Ni(II), Cu(II), Zn(II), and/or heavier metals such as Pb(II). For example, structures of the type $[M(L)_2(Au(CN)_2)_2]$ were obtained and presented unique physical properties such as Au-Au based emission, magnetic properties, and negative thermal expansion (when L was removed), which sparked interest in developing analogous structures using alternative bridging units and ligands.

More recently, the selection of both the bridging units and nodal units was expanded to other complexes in order to widen the achievable range of properties using the synthetic techniques described in Section 1.5.[47-53] These new systems included new gold-based building blocks, such as $K[Au(CN)_2X_2]$ where X = Cl, Br, I and analogous building blocks based on other late-transition metals such as $K_2[Pt(CN)_4]$. However, the possibility of using thiocyanate-based building blocks remained unexplored.

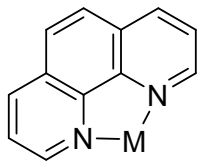

1,10-phenanthroline (phen)

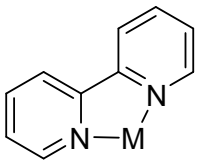

2,2'-bipyridine (bipy)

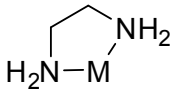

ethylenediamine (en)

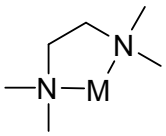

N,N,N',N'-tetramethylethylenediamine (tmeda)

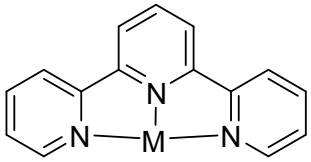

2,2';6',2"-terpyridine (terpy)

Figure 1.3 Typical nodal complexes used in the synthesis of CPs in the Leznoff group where M is a range of first-row transition metals and Pb(II).

1.2. **The chemistry of the (iso)thiocyanate (SCN^-) ligand**

The thiocyanate ion, which is part of the chalcogenocyanate family XCN^- (where X = S (thiocyanate), Se (selenocyanate) and Te (tellurocyanate)), is a triatomic ambidentate ligand.[55-56] By itself, thiocyanates have been known since the early 1600s, but, to our knowledge, the oldest publication regarding this species consists of the establishment of the classic Fe detection method using KSCN in biology in 1934 by Theodore G. Klumpp.[57] In the early 1930s, the thiocyanate species was mostly used for this application until the early 1940s, where more work was done with respect to its applications in organic chemistry, as a substituent, and in inorganic chemistry, as a ligand. It was not until the late 1940s that the properties of thiocyanate precursors, such as KSCN, NaSCN, LiSCN, etc., were reported, prompting the investigation of the first-row transition metal classic Werner complexes of the type $Q_x[M(SCN)_y]$ (see Section 2.1).

As an inorganic ligand, the SCN^- ion can coordinate through two atoms, either the sulfur or the nitrogen, or through both, giving rise to a versatile variety of coordination modes.[58-66] When coordinated through the sulfur atom, it is commonly referred to as thiocyanate and when coordinated through the nitrogen atom, isothiocyanate. Based on the hard/soft acid/base theory,[67-68] each end of SCN^- possess different chemical properties; the sulfur end is softer and tends to coordinate to soft metals such as late-

transition metals, whereas the nitrogen end is harder and coordinates to harder transition metals. Comparatively, the sulfur end of the ligand is harder than sulfide and halogen ions, and the nitrogen end is softer than cyanide and other comparable ions. Overall, this makes the thiocyanate an ideal candidate for the synthesis of heterobimetallic CPs, which, compared to homometallic CPs, can lead to a wider variety of properties and an easier access to multifunctionality in the resulting CP due to the significant difference in chemical reactivity and properties between early and late-transition metals. By carefully choosing the metal cation precursors for the synthesis of a targeted polymer, one can take advantage of this difference between the two ends of the ligand.

Structurally, the thiocyanate ion presents unique properties. Despite being defined classically as linear, when coordinated to metal centres, the ligand shows a coordination angle (M-S-C or M-N-C) that varies depending on the metal and whether or not it is coordinated to a single metal, or to two metals.[69-84] Typically, the sulfur end of the ligand shows a coordination angle that varies between 50 and 90° whereas the nitrogen end shows a coordination angle between 12 and 18°. In terms of CPs, this means that the ligand generates one or two additional degrees of freedom in the overall structure, which then can lead to unique topologies compared to, for example, the linear CN^- ion.

In a CP, the thiocyanate ion can either be terminal or bridging. When terminal, i.e., coordinated to a single metal centre, the thiocyanate ligand can form hydrogen bonding to adjacent species which is usually observed through the nitrogen end of the ligand.[85] It is also a pseudohalide, and its size can lead to steric interactions with other species.[58-66, 69-85] When bridging, the thiocyanate ligand (Figure 1.4) can coordinate either in a 1,3 template, where the ligand is coordinated to one metal centre at either end, a 1,1 template, where the ligand is coordinated to two metal centres at one end and the other end is dangling as if the ligand was terminal, or as a 1,1,3 template, where the ligand is bridging both in a 1,1 and 1,3 fashion at the same time.[85] Just like for the unusual coordination angles, this variety in coordination modes encourages unique structural topologies, which is an aspect often sought when using simple pseudohalides for the synthesis of CPs.

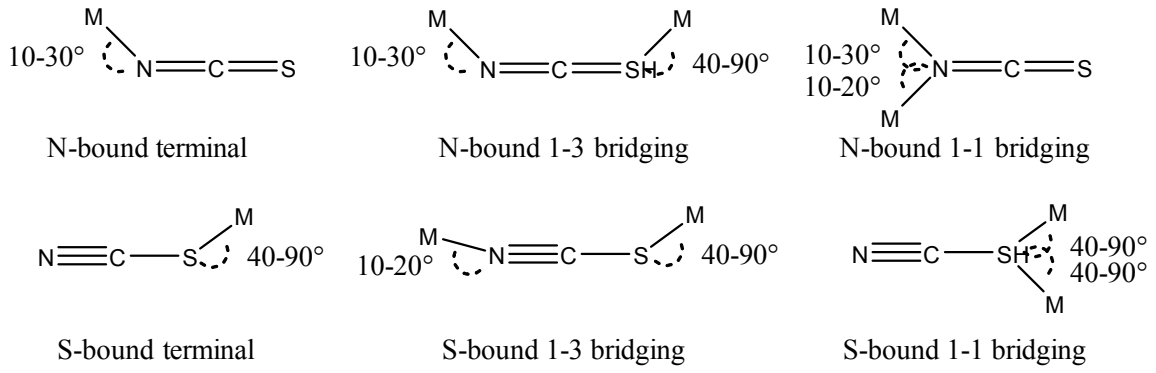

Figure 1.4 Structure, coordination modes and angles of the thiocyanate ligand.

1.3. **Thiocyanates and their usage in CPs**

To our knowledge, the earliest report of a CP involving SCN^- consisted of the work by Jeffery *et al.* in 1948 where the structure of $CoHg(SCN)_4$ was examined.[86] In this work, it was revealed that the complex consists of a 1D CP involving the 1,3 coordination of SCN^- units between Co(II) and Hg(II) metal centres. In 1950, the structure of $[Cu(en)_2][Hg(SCN)_4]$ was reported in *Nature* by Scouloudi *et al.*.[87] At the time, it was believed that the structure consisted of a double salt involving rings of $[Cu(en)_2]^{2+}$ and $[Hg(SCN)_4]^{2-}$ showing disorder, but was later revealed to be a 1D CP with a 1,3 coordination of the SCN^- ligand between the Cu(II) and Hg(II) metal centres. This material became a standard for the calibration of Gouy balances due to its stability, ease of synthesis, and reliable magnetic properties. Details of the synthesis were not reported, and thus one cannot assume that a strategic approach was used for the synthesis of this material. Later, the structure of AgSCN was reported by Dr. Lindqvist in 1954. In this case, the structure consists of a 1D zig-zag CP for which the SCN^- unit coordinates in a 1,3 fashion.[88]

Between the 1960s and 1980s, there was a rise in the number of publications involving thiocyanate ligands in CPs. Generally, the structures consisted of simple homometallic CPs where the bridging unit was SCN^- acting as a pseudohalide ion and the metal centre was capped with a mono- or bidentate ancillary ligand (see Figure 1.4). In most cases, the SCN^- followed a 1,3 coordination template, and overall, the bridges consisted of two inverted SCN^- ligands, resulting in a 1D linear (for monodentate ligands) or zig-

zag structure (for bidentates ligands). Examples of such CPs are depicted in Table 1.1 and the general structure of these complexes in Figure 1.4. In these works, most presented physical properties of interest depending on the ligand chosen and the metal centre, such as antiferromagnetic interactions between the metal centres or fluorescence, but these properties were often depicted as secondary to the structural analyses of the complexes.

Table 1.1 Example of homometallic 1D CPs synthesized between 1960 and 1980.

Complexes	Reference(s)
$Cd(SCN)_2(L)_2$ where L = 1,3-ethylene-2-thiourea and derivatives	89
$M(L)_2(SCN)_2$ where L = thioacetamine and derivatives, and M = Ni(II), Co(II)	90
$M(2,2'\text{-bipy})(SCN)_2$ where M = Fe(II), Mn(II), Co(II), Ni(II), Cu(II)	91, 92
$Cu(L)(SCN)_2$ where L = pyridine, 2,2'-bipy, en and pyrazine, and derivatives	93

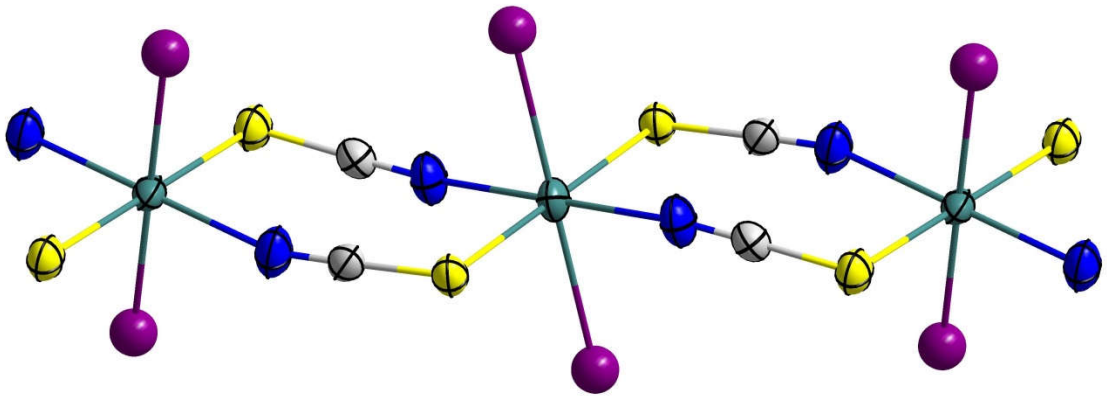

Figure 1.5 General structure of the 1D chain in homometallic complexes of the type $[M(L)_2(SCN)_2]$ where M is a first-row transition metal and L is a monodentate ligand. Colour code: Green (M), Yellow (S), Grey (C), Blue (N), Purple (Ligand).

It was not until the late 1990s that interest in SCN^- CPs shifted, after the publication of the work by Jiang *et al.,*[94] which consisted of the synthesis and structures of $ZnAg_2SCN_4$, $ZnCdSCN_4$ and other similar analogues, and of the work by Tuck *et al.* which reported the formation constants for a wide variety of classic SCN^- Werner complexes.[95] At the

same time, interest in CN^- based CPs was also quickly rising, and consequently, the synthesis of other pseudohalide-based CPs also rose, including SCN^-.

In the early 2000s, there were many complexes reported where SCN^- was used as an alternative pseudohalide to CN^- in the synthesis of homometallic CPs. In most cases, the synthesis involved the *in situ* preparation of the complexes where the ligands, the metal centres, and KSCN were simply mixed without a definitive strategic approach or building block methodology. Examples of the resulting complexes are shown in Table 1.2. This type of structure and uncontrolled synthetic approach persisted throughout the 2000s up until the beginning of this work.

Table 1.2 Example of homometallic and heterometallic complexes where the bridging SCN^--based complex was prepared *in situ*.

Complexes	Reference(s)
$[(CuSCN)_2(pyrimidine)]$	96, 97
[CuSCN(2-Rpyz)] where Rpyz = pyrazine, and its CN and CH_4 substitutes	98-100
$Cu(en)_2[Ni(SCN)_3(en)]_2$	101

The first report of a SCN^- CP where a building block approach was used during its synthesis was authored by Wrzeszcz *et al.* in 2002.[102] In this work, the complex of $[Ni(en)_3]_n[Ni(en)_2Cr(NCS)_6]_{2n}$ was synthesized by mixing $Ni(en)_2Cl_2$, which was prepared as a separate reaction, with $K_3[Cr(SCN)_6]$ in methanol. After the reaction was slightly heated and stirred, the KCl precipitate was removed by filtration and the mother liquor was left undisturbed for 2 days which resulted in dark purple crystals of the title complex. The complex consisted of a 1D coordination polymer of $[Ni(en)_2Cr(SCN)_6]$ with $[Ni(en)_3]^{2+}$ countercations. In this case, the thiocyanate ligands are bridging the Ni(II) and Cr(III) metal centres in a 1,3 *trans*- fashion. To our knowledge, this was the first and only publication that involved such a building block approach, and as such, sparked our interest towards the goals of this research, along with similar work done in the Leznoff group using cyanide-based building blocks.

1.4. **Research Objectives**

As demonstrated above, the thiocyanate ligand has been used as a ligand in the synthesis of CPs very sparingly during the last few decades. Compared to other pseudohalide analogues such as CN^- and NCN^-, the thiocyanate ligand remains relatively underexplored when it comes to its chemistry for the synthesis of CPs, and to its structural properties. In most cases, the synthesis of SCN^- CPs did not involve a strategic approach during the synthesis.

As mentioned above, the possibility of using SCN^- and SCN^--based building blocks in the Leznoff group remained unexplored at the beginning of this work. As such, the general goal of this research consists of synthesizing CPs using SCN^--based building blocks (or SCN^- itself) and to assess the viability of these building blocks for the synthesis of CPs and for targeting specific physical properties compared to that of the traditionally used CN^--based units.

In order to achieve this goal, a methodic approach was used where a reaction matrix was determined for a chosen SCN^- building block, such as $[Fe(SCN)_6]^{3-}$ (Chapter 2), $[Co(SCN)_4]^{2-}$ (Chapter 2) and $[Pt(SCN)_4]^{2-}$ (Chapter 3) and then mixed with a selection of metal centres optionally capped with ancillary ligands in an appropriate solvent. By systematically covering a wide range of combinations, assessing the chemical reactivity and structural chemistry of the building blocks was accomplished.

At the same time, depending on the ligand and metal centre chosen, specific physical properties were targeted. In this thesis, systems involving the ligand terpy and its derivatives were targeted in order to produce CPs with a possibility for fluorescence and birefringence (Chapter 5), and systems involving dimeric Cu(II)-based building blocks were targeted for the purpose of assessing their magnetic properties (Chapter 4). Furthermore, by crystallizing the complexes and measuring their crystal structures using SC-XRD, trends in the topologies were determined in relation to the choice of ligand and metal centres, and a correlation between the structure and the physical properties of thiocyanate-based CPs was established.

1.5. Synthesis, characterization methods and optical properties

1.5.1. General synthetic approach to synthesis of CPs.

Previous research in the Leznoff group focused on cyanide-based species such as $[Au(CN)_2]^-$ and $[Au(CN)_4]^-$ for the synthesis of CPs. In order to prepare and crystallize a CP using these species, we used a standard metathesis method[47-53] which was proven to work well for the synthesis of CPs: combining a potassium or sodium-based anion with a pseudohalide or halide-based cation results in a simple salt and the targeted CP. In order to facilitate elimination of the simple salt by precipitation, when alcoholic solvents were involved, the potassium salts of the bridging species were chosen over their sodium or lithium analogues due to their lower solubility.

As detailed in Equation 1.1 in Section 1.1, the standard method consists of first preparing *in situ* the metal precursor capped with an ancillary ligand by mixing the ligand and the metal halide or metal pseudohalide of choice in a polar solvent, usually water or methanol. Afterwards, the potassium salt of the bridging ligand is added to the mixture as a solution in methanol, ethanol, or water and then the reaction mixture is stirred for a few minutes. At this point, if alcohols are chosen, a precipitate of the metathesis product is obtained, usually potassium chloride or potassium bromide, and filtered out, leaving the targeted precursors in solution in the mother liquor. If water is used, the mother liquor is simply filtered to remove any impurities (such as small insoluble particles) that could interfere with the crystallization process. For crystallizing the products, the mother liquor is set aside for slow evaporation by covering it with Parafilm™ and leaving it undisturbed for a few days. Other crystallization methods include the H-tube method, crystallization at low temperature, slow mixing of the solutions, and a solvothermal reaction followed by slow cooling. The latter method is unsuitable for thiocyanate species because they tend to decompose at temperatures higher than 60 °C when accompanied by a metal centre, leaving a cyanide product and a variety of unidentified sulfur compounds.

1.5.2. X-ray crystallography

One main goal of this research is to correlate the structure of the material synthesized with its physical properties and to improve these properties by making targeted structural changes. As such, in order to establish the structure of the materials synthesized, Single-Crystal X-Ray Diffraction (SC-XRD) is central.[103] By using this method, a visual representation of the structural arrangement of the atoms for the material synthesized is obtained. Once single crystals of the complex are obtained (as opposed to polycrystalline aggregates), the X-ray Diffraction data are collected and refined to give the visual representation of the structure.

If one cannot obtain single crystals of the complex, then one must defer to other methods of characterization for establishing the structure of the complex, or at least its general chemical formulae. One such method consists of Powder X-Ray Diffraction (PXRD),[104-106] from which the structure of the complex can either be refined from the data obtained, usually at a lower quality when compared to SC-XRD, or can be compared to an existing structure (usually obtained by SC-XRD) at a good level of accuracy and precision to note the structural differences. To collect the PXRD data, a powder sample of the complex is required and the spectrum of the X-ray diffraction intensity vs. 2θ ° for which the peaks are the angles at which the X-ray interference satisfies the Bragg condition is measured. In combination with other methods, this technique can lead to a fairly accurate definition of the complex and its structural properties, but also involves a longer timeframe and generally more challenging work when compared to SC-XRD.

1.5.3. Vibrational spectroscopy

Since both the cyanide and the thiocyanate species present strong vibrational spectroscopy signals, methods involving vibrational spectra are a major focus in this research.[108-109] In most cases, in combination with SC-XRD, EA, FT-IR, and Raman spectra were collected for the complexes herein in order to assess a) whether or not the sample is pure and b) to determine the relationship between the structure and the vibrational spectroscopy data. In the case of SCN^- and CN^- species, the main signal observed and assessed using vibrational spectroscopy is located between 2000 and

2200 cm^{-1}, which is assigned to the stretching of the CN bond (denoted as ν_{CN}).[109] As an example, if two unique terminal thiocyanate species are present in the structure, but one of them forms a hydrogen bond, a different vibrational signal will be obtained for each species due to the shifting of the electron distribution in the ligand, and thus the presence of hydrogen bonding is further confirmed using these data. Most of the characterization of thiocyanate-based complexes prior to the 1970s was performed exclusively using vibrational spectra data, and thus a considerable amount of data is available for comparison purposes.[109]

1.5.4. **Luminescence**

Besides unique topologies in the structure of the CPs, one of the targeted properties of this research is luminescence. As such, ligands that present emissive properties independently and when coordinated to a metal centre, such as 2,2'-bipy and terpy, were chosen in order to infuse these properties in the targeted CP.[16-22] Classically, luminescence is measured in solution, but since the complexes herein are solid-state materials, measures have to be taken to obtain the spectra in the solid-state using spectrometers generally designed for measuring solutions. As such, we use sample holders that can accommodate a small rectangular piece of quartz to which the fluorescent material is then attached using grease or wax that does not show any signal in the spectral range measured. Herein, eicosane ($C_{20}H_{42}$) was the main wax used for measuring the luminescent data. To obtain the data, the source beam was targeted at the piece of quartz which was held in place at an angle of 30°, and the resulting emission can be measured without interference of the scattering of the source beam. Another method used consists of using a quartz NMR tube filled with a powder of the material, which is then held in place using a quartz dewar flask holder. This method is mostly meant for measurement at low temperature, as the holder can be filled with liquid nitrogen. The disadvantage of using this method, however, is that scattering of the source beam can be observed in the emission spectra at fairly high intensities, which varies depending on the temperature of the dewar flask, and thus might obscure any signal for the sample itself unless the sample presents a high emission intensity. In all cases, background data are measured and subtracted from the collected data, but no further corrections are performed.

1.5.5. **Birefringence**

Another property for which a growing interest in the research community has been shown is birefringence, which is defined as the difference in the refractive indexes of two (Δn) orthogonal axes of an anisotropic crystal.[110] When a ray of light passes through a birefringent crystal along its optical axis, it is split into two different rays, known as the ordinary ray and the extraordinary ray, and emerges at the other end of the medium as mutually perpendicularly polarized rays. To the naked eye, this results in the observation of two different images when an object is observed through the crystal along its optical axis. The difference in the optical paths of the rays is dependent on the refractive indices (n), and on the thickness of the crystal. The greater this n value is, the greater the angular difference between the two rays emerging from the crystal. A more detailed definition, technicalities and measurement methods regarding the concept of birefringence are available in Appendix A. For an anisotropic crystal, the refractive indexes are dependent on the polarizability and on the density of the material along the measured axis, which is of course dependent on the choice of nodal and bridging systems in the case of CPs. By carefully choosing the building blocks of a CP, one can hope to increase the birefringence value of a material by either increasing the density of the material along the axis, or by increasing bond polarization along the axis. The Leznoff group has recently shown that systems involving terpy or bis(benzimidazole) ligands and their derivatives, and the $[Au(CN)_2]^-$ building block, formed amongst the most highly birefringent materials ever recorded, and as such, investigation of this property is an area of focus when choosing the building blocks for the synthesis of CPs. In the case of thiocyanate-based building blocks, it is easily conceivable that the density of the material could be increased due to the presence of the high coordination angle in the relevant bridging units, and that the soft, polarizable S atom along the axis of SCN^- could also contribute to an increased birefringence due to the presence of the extra bond when compared to CN^-. As such, an investigation of the birefringent properties of analogous systems to those previously synthesized in our group but using SCN^- as a building block instead of $[Au(CN)_2]^-$ was performed and is described in Chapter 5.

Chapter 2. **Synthesis, structure and light scattering properties of metal isothiocyanate salts**[1]

2.1. **Introduction**

As mentioned in Chapter 1, the thiocyanate ligand possesses useful characteristics for the synthesis of heterobimetallic coordination polymers (CPs), namely the duality in the softness/hardness of the coordination sites and the inherent coordination angle that varies between 4 and 60 ° on average.[69-85] This thesis postulates that the combination of both of these characteristics could lead to CPs with unique topologies. As shown in Chapter 1, homometallic CPs have been well studied but there are far fewer heterobimetallic CPs based on thiocyanate building blocks.[69-85]

In order to synthesize heterometallic CPs using the building blocks approach, it was initially decided to use first-row transition metal building blocks of the type $[M(NCS)_x]^{y-}$, mostly because of their ease of preparation and the wide range of topologies that could be accessed from using those building blocks (e.g., using the octahedral, tetrahedral and square planar geometries for Fe(III), Co(II) and Ni(II), respectively). In general, when a transition metal salt is mixed with an excess of isothiocyanate anion in solution, the result is usually a classic Werner complex of the form $Q_x[M(NCS)_y]$ or $Q_x[M(SCN)_y]$ (where Q is a cation and M is a metal). The optical properties of these classic complexes have been very well studied over the past century due to the strong absorption arising from the thiocyanate ion when coordinated to a metal centre.

[1] Part of the work in this chapter is reproduced with permission from D. Savard, and D. B. Leznoff, "Synthesis, structure and light scattering properties of tetraalkylammonium metal isothiocyanate salts", *Dalton Transactions*, vol. 42, pp. 14982-14991, 2013, Copyright 2013 The Royal Society of Chemistry

Despite those extensive works, information regarding the synthesis, purification and structural properties of these classic Werner complexes remains surprisingly sparse in the literature. To our knowledge, only a few solid-state structures determined by SC-XRD and/or EXAFS and XANES have been reported (Table 2.1). Outside of this list, only the crystal structures of potassium or tetraalkylammonium thiocyanometallate salts of Zn(II), which are tetrahedral $Q_2[M(SCN)_4]$ complexes, have been reported. Only a handful of early transition metal complexes, such as the octahedral $Q_3[Mo(NCS)_6]$, have been reported in early literature.[111] In regards to the lanthanide series, the structures of several isothiocyanometallates with various degrees of hydration have yielded a good understanding of their structural behaviour.[112-114] Overall, however, there is only a scattering of structural reports (Table 2.1) for potassium and tetraalkylammonium salts of homoleptic first-row transition metal isothiocyanates (often without any synthetic details or purification procedures), which made it clear that a thorough investigation of these aspects of simple isothiocyanometallate chemistry was necessary in advance of using the anionic complexes as CP building blocks.

Table 2.1 Structurally characterized homoleptic isothiocyanate complexes of first-row transition metal complexes.

Compound	Reference
$(n\text{-}Bu_4N)_3[Sc(NCS)_6]$	115
$Na_3[Cr(NCS)_5]\cdot 9H_2O$	116
$(n\text{-}Bu_4N)_2[Cr(NCS)_4]$	117
$Na_4[Mn(NCS)_6]\cdot 13H_2O$	118
$(Me_4N)_3[Fe(NCS)_6]$	119
$(Et_4N)_3[Fe(NCS)_6]$	120
$K_2[Co(NCS)_4]\cdot H_2O\cdot 2CH_3NO_2$	121
$K_2Co(NCS)_4\cdot 3H_2O$	122
$(NH_4)_2[Co(NCS)_4]\cdot 3H_2O$	123
$(Me_4N)_2[Co(NCS)_4]$	124
$(Me_4N)_4[Ni(NCS)_6]$	125
$(Et_4N)_4[Ni(NCS)_6]$	126
$(n\text{-}Bu_4N)_3[Ni(NCS)_5]$	126
$(Ph_4As)_2[Ni(NCS)_4]$	127
$(Et_4N)_2[Cu(NCS)_4]$	128
$(Ph_4P)_2[Cu(NCS)_4]$	129

The optical properties of $[Ni(NCS)_4]^{2-}$ and some dinuclear analogues have been thoroughly characterized.[125-126] In $(n\text{-}Bu_4N)_3[Ni(NCS)_5]$,[126] the NCS^- ligand has been shown to promote a thermal phase transition and in $(Me_4N)_3[Fe(NCS)_6]$,[119] an unusual coordination geometry of the NCS^- ligand was reported. From the very limited amount of reports, it was clear unusual solid-state properties of isothiocyanometallates and intrinsic characteristics of the NCS^- ligand are still waiting to be uncovered and that a more complete study of the structural and physical properties of the simple $Q_x[M(NCS)_y]$ class of materials is worthwhile.

With these goals in mind, in this chapter, the detailed synthetic procedures of a series of simple salts of the type $Q_x[M(NCS)_y]$ (where Q = K^+, NH_4^+, Me_4N^+, Et_4N^+ or $n\text{-}Bu_4N^+$ and M = Cr(III), Mn(II), Fe(III), Co(II), Ni(II), Eu(III), Gd(III) or Dy(III)) and the characterization of their structural and optical properties is presented. The potassium and tetraalkylammonium salts are of particular interest due to their tunable solubility (*via* the

ammonium R-group and the potassium ion) in a wide range of solvents, therefore facilitating their use in further reactivity.

2.2. **Syntheses**

In general, the synthesis of isothiocyanometallate building blocks consisted of one-pot reactions where the potassium salt was first synthesized by mixing KSCN with metal chlorides in an appropriate solvent, such as H_2O or acetone, followed by a cation exchange performed by adding stoichiometric amounts of the respective tetraalkylammonium salt (Equation 2.1 and Table 2.2). The reactions were then driven to completion if necessary by refluxing the mixture and by extraction of the complex using CH_2Cl_2 or $CHCl_3$. Of course, this general synthetic strategy was tuned to suit the subtleties of the products to facilitate the purification, to maximize the yield and purity, and to ease their crystallization by slow evaporation (Figure 2.1, see Section 2.8).

$$MCl_y + Y[Cat][SCN] \xrightarrow[\text{Solvents}]{} M(SCN)_y + Y[Cat][Cl]$$

M = Metal precursor; Cat = K, NH_4^+, Me_4N^+, Et_4N^+ or Bu_4N^+

Equation 2.1 General metathesis reaction used for the synthesis for isothiocyanate building blocks depicted in this chapter.

Table 2.2 List of all complexes described herein and their composition.

$K_3[Cr(NCS)_6]\cdot H_2O$ (**2.1**)	$(Me_4N)_3[Fe(NCS)_6]$ (**2.11**)
$(NH_4)_3[Cr(NCS)_6]\cdot 3(H_2O)$ (**2.2**)	$(Et_4N)_3[Fe(NCS)_6]$ (**2.12**)
$(NH_4)_3[Cr(NCS)_6]\bullet[(CH_3)_2CO]$ (**2.3**)	$(n\text{-}Bu_4N)_3[Fe(NCS)_6]$ (**2.13**)
$(Me_4N)_3[Cr(NCS)_6]$ (**2.4**)	$(n\text{-}Bu_4N)_2[Co(NCS)_4]$ (**2.14**)
$(Et_4N)_3[Cr(NCS)_6]$ (**2.5** and **2.6**)	$(Me_4N)_4[Ni(NCS)_6]\bullet(H_2O)$ (**2.15**)
$(n\text{-}Bu_4N)_3[Cr(NCS)_6]$ (**2.7**)	$(Me_4N)_4[Ni(NCS)_6]$ (**2.16**)
$K_4[Mn(NCS)_6]$ (**2.8**)	$(n\text{-}Bu_4N)_3[Eu(NCS)_6]$ (**2.17**)
$(Me_4N)_4[Mn(NCS)_6]$ (**2.9**)	$(n\text{-}Bu_4N)_3[Gd(NCS)_6]$ (**2.18**)
$(Et_4N)_3[Mn(NCS)_5]$ (**2.10**)	$(n\text{-}Bu_4N)_3[Dy(NCS)_6]$ (**2.19**)

In the case of the potassium salts of Cr(III) and Mn(II), the methodology consisted of mixing the metal precursor, either $CrCl_3$ or $MnCl_2 \cdot 4H_2O$, with a stoichiometric amount of KSCN in H_2O. The solvent was then removed and the crude residue was then extracted using acetone, which led to the precipitation of KCl, thus driving the metathesis reaction to completion and simplifying the purification process greatly. The products were then crystallized by slowly evaporating the solutions over a few days, which led to either dark purple crystals of $K_3[Cr(NCS)_6] \cdot H_2O$ (**2.1**) or colorless crystals of $K_4[Mn(NCS)_6]$ (**2.8**).

To prepare $(NH_4)_3[Cr(NCS)_6] \cdot 3(H_2O)$ (**2.2**), stoichiometric amounts of NH_4NCS and $CrCl_3 \cdot 6H2O$ were mixed in acetone. The precipitate of NH_4Cl was filtered off and the solvent removed *in vacuo*. Afterwards, the crude reside was washed with Et_2O to remove the impurities which resulted in a polycrystalline sample of **2.2**. To obtain crystals of $(NH_4)_3[Cr(NCS)_6] \cdot [(CH_3)_2CO]$ (**2.3**), the sample of **2.2** was recrystallized from an acetone solution over a period of 24 hours. The simpler "one-pot" procedure, i.e., mixing NH_4Cl, KSCN and $CrCl_3 \cdot 6H_2O$ in ethanol, resulted in a far worse yield and a more difficult purification procedure.

All of the Me_4N^+ and Et_4N^+ salts of Cr(III), Mn(II) and Fe(III) were prepared using similar methods. Stoichiometric amounts of the precursor ammonium salts (Me_4NCl and Et_4NBr) were mixed with the metal chlorides and KSCN in the appropriate solvent. In the case of acetone or ethanol solutions, the mixtures were refluxed for 2 hours, which yielded a precipitate of KCl or KBr. The solid was filtered off before crystallization of the complexes was performed by slow evaporation of the mother liquor. When water was used, the complexes were crystallized from the mother liquor directly. In this case, the chloride-based metallic precursors (e.g., $FeCl_3$) were chosen over the nitrate analogues (e.g., $Fe(NO_3)_3 \cdot 6H_2O$) due to the lower solubility in acetone of the synthesized salts (e.g., Me_4NCl vs. Me_4NNO_3), thus simplifying the purification process by allowing the removal of more impurities during the reaction. In this fashion, $(Me_4N)_3[Cr(NCS)_6]$ (**2.4**), $(Et_4N)_3[Cr(NCS)_6]$ (**2.5**), $(Me_4N)_4[Mn(NCS)_6]$ (**2.9**), $(Et_4N)_3[Mn(NCS)_5]$ (**2.10**), $(Me_4N)_3[Fe(NCS)_6]$ (**2.11**), $(Et_4N)_3[Fe(NCS)_6]$ (**2.12**) and $(Me_4N)_4[Ni(NCS)_6] \cdot x(H_2O)$ (**2.15**, x = 1; **2.16**, x = 0) were prepared.

Synthesis of the *n*-Bu_4N^+ salts of Cr(III), Fe(III) and Co(II) ((*n*-$Bu_4N)_3[Cr(NCS)_6]$ (**2.7**), (*n*-$Bu_4N)_3[Fe(NCS)_6]$ (**2.13**) and (*n*-$Bu_4N)_2[Co(NCS)_4]$ (**2.14**), respectively) was performed by first mixing the metal chloride precursors and KSCN in water or acetone to make the potassium salts. Then, the complexes were extracted into a *n*-Bu_4NBr solution of CH_2Cl_2 or $CHCl_3$ or mixed directly with *n*-Bu_4NBr in acetone. In the latter case, the mixture was extracted with $CHCl_3$ yielding a pure solution of the complexes in $CHCl_3$. The solvent was then removed *in vacuo* and the complexes were recrystallized from methanol or ethanol by slow evaporation over the course of a few days.

The NH_4^+ and *n*-Bu_4N^+ salts of Mn(II) could not be recrystallized using simple methods. By conducting a one-pot procedure (i.e., NH_4NCS and $MnCl_2 \cdot 4H_2O$) in acetone, an oily residue was obtained from which NH_4NCS recrystallized over a period of two weeks, suggesting a weaker formation constant for $(NH_4)_4[Mn(NCS)_6]$ compared to NH_4NCS. When using the methodology described below for synthesizing the *n*-Bu_4N^+ salt, *n*-Bu_4NNCS recrystallized directly from the mixture. Other methods of synthesis and separation of the products were attempted, such as slow diffusion in an H-tube, slow diffusion through a membrane, layering, and slow mixing. All cases resulted in the preferential crystallization of NH_4NCS or *n*-Bu_4NNCS. In the end, pure samples of the NH_4^+ and *n*-Bu_4N^+ salts could not be obtained, although the K^+ and Me_4N^+ salts of the $[Mn(NCS)_6]^{4-}$ anion could be prepared.

However, using the above synthetic strategies for the synthesis of the lanthanide salts resulted in impure mixtures of salts with varying degree of thiocyanate substitution. In order to synthesize the pure lanthanide-based *n*-Bu_4N^+ salts, a modified synthetic method was used:[130-136] First, *n*-Bu_4NNCS was prepared by simple metathesis between KSCN and *n*-Bu_4NBr in acetone. Then, three equivalents of *n*-Bu_4NNCS were mixed with one equivalent of the metal chloride precursor and three equivalents of KSCN in acetone. The resulting mixture was heated for a few minutes, leaving a precipitate of KCl that was removed by filtration. Crystallization of these complexes was performed directly from the mother liquor at room temperature. Significantly larger crystals were obtained if the solution was additionally cooled in at -35 °C for a period of 24 hours.

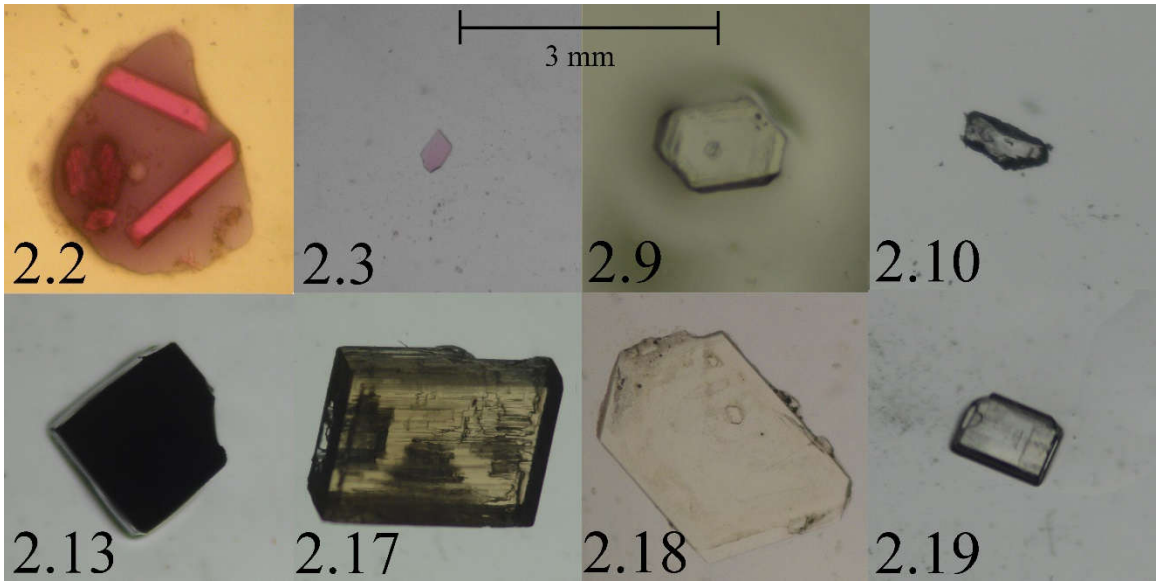

Figure 2.1 Pictures of the crystals of **2.2**, **2.3**, **2.9**, **2.10**, **2.13** and **2.17**-**2.19**.

2.3. **Vibrational Spectroscopy**

For all complexes, the infrared and Raman spectra are consistent with the values expected for classic Werner complexes of the type $Q_x[M(NCS)_y]$ with the ν_{CN} signal appearing between 2030 and 2130 cm^{-1}. Table 2.3 shows a comparison of the infrared data for complexes prepared herein to the previously reported values, if applicable. In the case of **2.11** and **2.18**, the values are close to those published previously. However, in the case of **2.12** and **2.17**, there is the presence of an additional peak in the ν_{CN} region. This may be attributed to the fact that more recent instruments present a higher resolution and increased beam intensity, since in these publications (published in 1977 and 1990, respectively), the peaks were described as being broad, whereas in the case of the measured spectra of **2.12** and **2.17**, the peaks appeared sharp, but slightly overlapping. Overall, the frequency of the signals decreases as the mass of the ion increases, which is a trend usually observed in cyanide-based species. For the latter complexes, this effect is due to the presence of metal-to-cyanide π back-bonding.[137-139] Since the coordination of the thiocyanate species when N-bound is very similar to that of cyanide due to the nature of the molecular orbitals, one may expect to observe a similar trend in the ν_{CN} signals of N-bound thiocyanate-based classic Werner complexes. In the cases where more ν_{CN} peaks than expected appear in either the FT-IR or Raman data, it

can be attributed to either the lower symmetry of the anionic core (for **2.11** and **2.12**)[119-120] or to the presence of SCN^- impurities in the samples. For the thiocyanate species, there are other FT-IR active vibrational modes of interest, but these are seldom discussed in publications in favor of the ν_{CN} signal. The modes are ν_{CS} which is the stretching of the C-S bond located at around 755 cm^{-1}, and δ_{SCN} which is the bending of the SCN^- species at approximately 460 cm^{-1}. When coordinated to a metal centre, the stretching frequencies of the metal coordination (ν_{MS} or ν_{MN}) are located around 285 cm^{-1}.[55] The IR spectra of **2.1**, **2.13** and **2.17** with assigned SCN^- frequencies are available in Appendix B.

In the literature, to our knowledge, the Raman spectroscopy data have never been reported for the Werner complexes reported in this chapter. Table 2.4 presents a compilation of the ν_{CN} signals for the Raman data.

Table 2.3 The ν_{CN} infrared data for all Chapter 2 complexes and, if applicable, a comparison with their published counterparts.

Complex	Observed (cm^{-1})	Published	Reference
2.1	2087		
2.2	2089		
2.3	2084		
2.4	2081		
2.5	2080		
2.7	2137, 2085		
2.8	2074		
2.9	2073		
2.10	2067, 2050		
2.11	2073, 2058, 2023	2075, 2057, 2026	119
2.12	2101, 2070, 2054	2098, 2052	120
2.13	2064, 2057		
2.14	2070		
2.15	2069		
2.16	2062		
2.17	2047, 2037	2040	55
2.18	2043	2045	55
2.19	2054	2052	55

Table 2.4 The ν_{CN} Raman data for all Chapter 2 complexes.

Complex	Observed (cm^{-1})	Complex	Observed (cm^{-1})
2.1	2085	**2.12**	2114, 2101, 2055, 2026
2.2	2131, 2091	**2.13**	2086, 2058
2.4	2134, 2085, 2054	**2.14**	2095, 2072
2.5	2134, 2093	**2.15**	2081, 2068
2.7	2128, 2079	**2.16**	2084, 2071
2.8	2096, 2071	**2.17**	2083, 2054, 2042
2.9	2095, 2073	**2.18**	2088, 2046
2.10	2070, 2059	**2.19**	2088, 2046
2.11	2115, 2101, 2073, 2055		

2.4. **Structural Analyses**

2.4.1. **Chromium(III) salts**

Crystals of $K_3[Cr(NCS)_6]\cdot H_2O$ (**2.1**) crystallized as dark purple plates and/or blocks in H_2O or acetone. The structure of **2.1** consists of two unique Cr(III) metal centres coordinated to six N-bound NCS^- ligands, each in an octahedral geometry (Figure 2.2) with Cr-N distances close to 2.00(1) Å and coordination angles varying between 168.7(1) and 172.5(2)° (Table 2.3), which are comparable to other Cr(III)-NCS distances (on average between 1.99 and 2.01 Å)[140] and angles found in the literature for non-bridging NCS^- ligands in classic Werner complexes. The two unique $[Cr(NCS)_6]^{3-}$ anions are well separated by the K^+ countercations. One water molecule is located between the sulfur atoms and forms hydrogen bonds with the metallocyanate units (O-S = 3.91 Å). Due to the poor quality of the crystals and of the collected data, the structure could not be refined to an appropriate value but atom assignment was successfully completed.

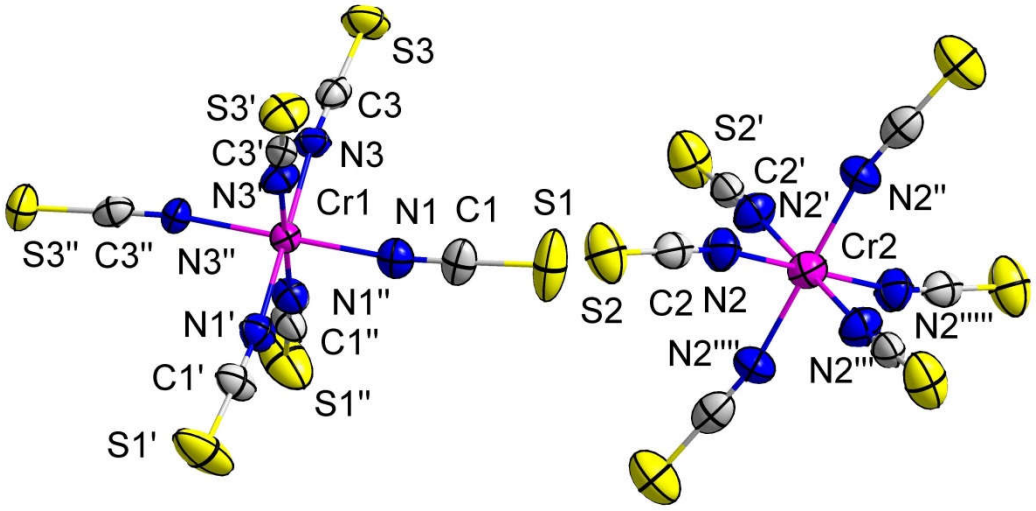

Figure 2.2 The structure of the anions of $K_3[Cr(NCS)_6]\cdot H_2O$ (**2.1**). The water molecule and K^+ ions were removed for clarity. Colour code: Purple (Cr), Blue (N), Yellow (S), Gray (C).

Complex **2.3** crystallizes as purple plates from acetone; the aqua adduct **2.2** formed very poor quality and/or multiply twinned crystals from water or ethanol (Figure 2.3). The structure of **2.3** is very similar to that of **2.1** with coordination distances (Cr-N) varying between 1.992(4) and 2.005(5) Å (Table 2.5) and coordination angles (Cr-N-C) varying between 165.8(4) and 177.2(5)°. Again, these are comparable to other Cr(III)-NCS distances and angles found in the literature for non-bridging NCS^- ligands.[140] In this case, the $[Cr(NCS)_6]^{3-}$ anions are well separated by the three NH_4^+ countercations and the acetone and water solvates. Two of the crystallographically unique sulfur atoms hydrogen bond with the ammonium cations (S3-N6 = 3.313(7) Å and S1-N5 = 3.521(5) Å).

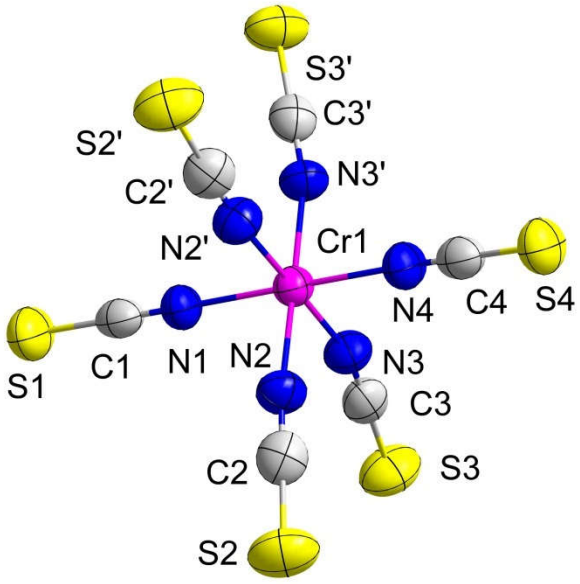

Figure 2.3 The structure of the anion of $(NH_4)_3[Cr(NCS)_6]\cdot[(CH_3)_2CO]$ (**2.3**). The solvent molecule and NH_4^+ ions were removed for clarity. Colour code: Purple (Cr), Blue (N), Yellow (S), Gray (C).

Table 2.5 Selected bond lengths (Å) and angles (°) for $K_3[Cr(NCS)_6]\cdot H_2O$ (**2.1**), $(NH_4)_3[Cr(NCS)_6]\cdot[(CH_3)_2CO]$ (**2.3**), (n-$Bu_4N)_3[Cr(NCS)_6]$ (**2.7**), $K_4[Mn(NCS)_6]$ **(2.8),** $(Me_4N)_4[Mn(NCS)_6]$ (**2.9**) and (n-$Bu_4N)_3[Fe(NCS)_6]$ (**2.13**).

Compounds	2.1		2.3	2.7	2.8	2.9	2.13
M-N1	1.99(1)	-	2.005(5)	2.057(1)	2.21(1)	2.202(9)	2.061(3)
M-N2	-	1.99(1)	1.997(4)	2.026(1)	2.18(1)	2.214(9)	2.032(3)
M-N3	2.00(4)	-	1.992(4)	--	2.21(1)	2.223(8)	--
M-N4	-	-	2.000(5)	--	2.23(2)	--	--
M-N1-C	172.5(2)	-	177.2(5)	168.23(1)	168.0(1)	176.7(9)	168.8(3)
M-N2-C	-	168.7(1)	170.1(4)	173.95(1)	161.5(2)	176.9(9)	173.6(3)
M-N3-C	171.9(1)	-	165.8(4)	--	171.6(2)	169.5(9)	--
M-N4-C	-	-	168.1(5)	--	179(2)	--	--

$(Me_4N)_3[Cr(NCS)_6]$ (**2.4**) (Figure 2.4) consists of two crystallographically unique octahedral Cr(III) centres each coordinated to six isothiocyanate ligands, with Cr-NCS distances varying between 1.985(5) and 1.999(5) Å (Table 2.6), similar to **2.1** and **2.3**. Four of the NCS^- ligands have a typical Cr-NCS angle between 171.8(4) and 177.4(4)°. However, as observed for the analogous Fe(III) species (Complexes **2.11** and **2.12**, see below), two *cis*- NCS^- ligands have a Cr-NCS angle of 150.9(4)°, which is significantly lower than for typical metal-bound NCS^- groups. This phenomenon was previously attributed either to the mechanical softness of the lattice or to a weak interaction between the countercations and the SCN^- ligands.[119]

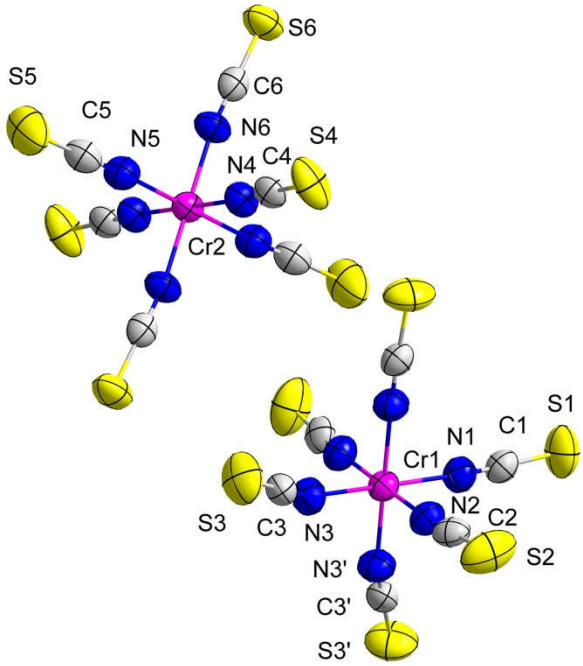

Figure 2.4 The structures of the anions of $(Me_4N)_3[Cr(NCS)_6]$ (**2.4**). The Me_4N^+ ions were removed for clarity. Colour code: Purple (Cr), Blue (N), Yellow (S), Gray (C).

By PXRD measurements, $(Et_4N)_3[Cr(NCS)_6]$ was revealed to crystallize as two polymorphs in an approximate 50:50 ratio. The two compounds (**2.5** and **2.6**) co-crystallize as plates, preventing their characterization using SC-XRD. The polymorph **2.5** was isolated from the mixture as a handful of multiply twinned crystals by first dissolving the crude mixture in a 50:50 acetone:Et_2O solution and then recrystallizing by slow evaporation. Pawley refinement revealed that **2.5** crystallized in the cubic space group I a -3 with a lattice parameter of 26.9232(1) Å (Figure 2.5). The second polymorph,

complex **2.6**, could not be isolated from the mixture in significant amounts using standard separation and recrystallization methods. No further structural analyses were attempted.

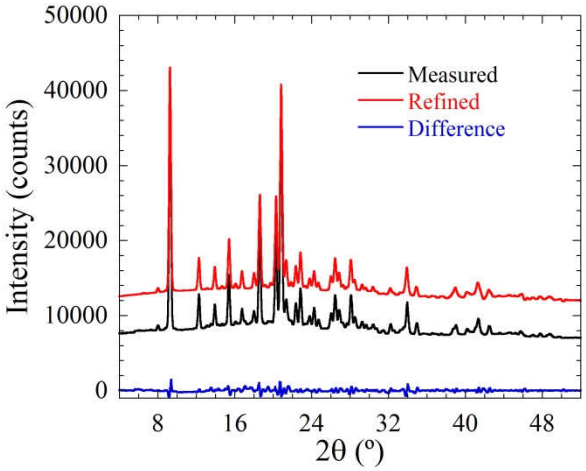

Figure 2.5 Measured PXRD pattern (black), Pawley refinement (red) and difference pattern (blue) of $(Et_4N)_3[Cr(NCS)_6]$ (**2.5**).

For $(n\text{-}Bu_4N)_3[Cr(NCS)_6]$ (**2.7**), PXRD studies revealed that the complex is isostructural to $(n\text{-}Bu_4N)_3[Fe(NCS)_6]$ (**2.13**). Rietveld refinement of the structure of **2.7** (Figures 2.6 and 2.7) was performed using the atomic coordinates of **2.13** as a starting structure. The Cr-NCS coordination distances 2.026(1) and 2.057(1) Å and the Cr-N-C angles are 168.23(1) and 173.95(1)° (Table 2.5), and are close to the expected values for Cr(III). Compounds **2.1**, **2.3** and **2.4** represent the first single-crystal structures of homoleptic Cr(III) isothiocyanates.

Table 2.6 Selected bond lengths (Å) and angles (°) for $(Me_4N)_3[Cr(NCS)_6]$ (**2.4**).

Identity	Length (Å) / Angle (°)
Cr1-N1	1.999(5)
Cr1-N2	1.993(5)
Cr1-N3	1.992(5)
Cr2-N4	1.999(4)
Cr2-N5	1.993(5)
Cr2-N6	1.985(5)
Cr1-N1-C1	177.4(4)
Cr1-N2-C2	173.8(4)
Cr1-N3-C3	150.9(4)
Cr2-N4-C4	175.9(4)
Cr2-N5-C5	176.8(4)
Cr2-N6-C6	171.8(4)

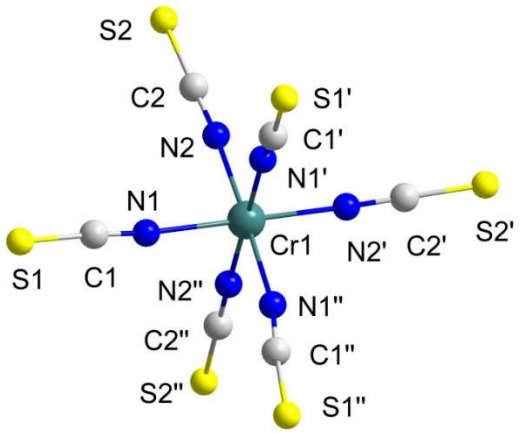

Figure 2.6 The generated crystal structure of anionic core of $(Bu_4N)_3[Cr(NCS)_6]$ (**2.7**) from Rietveld refinement. The Bu_4N^+ ions were removed for clarity. Color code: Green (Cr), Blue (N), Yellow (S), Gray (C).

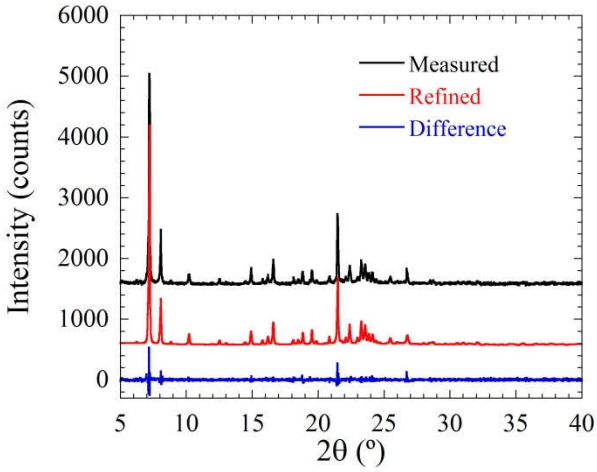

Figure 2.7 Measured PXRD pattern (black), calculated Rietveld refinement (red) and difference pattern (blue) of $(n\text{-}Bu_4N)_3[Cr(NCS)_6]$ (**2.7**).

2.4.2. **Manganese(II) salts**

Structural analyses of the crystals of $K_4[Mn(NCS)_6]$ (**2.8**) revealed that the complex crystallizes in the orthorhombic space group Pmna (Figure 2.8). The structure of the $[Mn(NCS)_6]^{4-}$ consists of a typical octahedral geometry with Mn-N distances varying between 2.17(1) and 2.23(1) Å and N-Mn-N angles between 178.6(6) and 178.7(8) °; all are within range of the expected values for Mn(II). The coordination angles of the NCS^- ligand to the metal centre vary between 168.0(1) and 179.0(1) °, which also indicates

very little variation from a regular octahedral arrangement. In the packing arrangement, the anions are separated by four K^+ countercations, and there is no evidence of strong interactions between the ions.

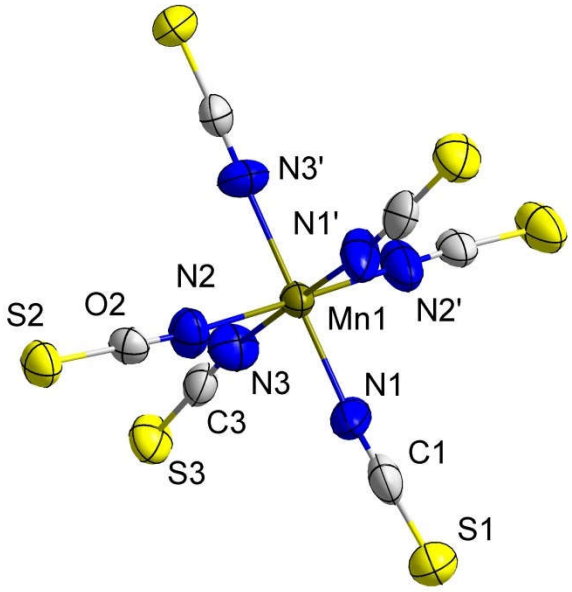

Figure 2.8 The structure of the anion of $K_4[Mn(NCS)_6]$ (**2.8**). The K^+ ions were removed for clarity. Colour code: Dark Yellow (Mn), Blue (N), Yellow (S), Gray (C).

The Me_4N^+ salt, $(Me_4N)_4[Mn(NCS)_6]$ (**2.9**), presents an octahedral geometry with six NCS^- ligands (Figure 2.9) that is very similar to the classic Werner core. The coordination distances of the NCS^- ligand vary between 2.201(9) and 2.223(8) Å (Table 2.5) and reflect the 0.22 Å difference in ionic radii between Cr(III) and Mn(II).[141-143] These distances are comparable to other Mn(II)-NCS distances of non-bridging NCS^- ligands found in the literature (which range between 2.06 and 2.26 Å).[144-145] The coordination angles vary between 169.3(9) and 177.0(9)°. To determine the spin-state of **2.9**, magnetic susceptibility measurements ($\chi_M T$) were performed at 300 K. The value of 4.37 cm^3 K / mol matches the expected value of 4.375 cm^3 K / mol (g ~ 2.00, S = 5/2) for a high spin d^5 Mn(II) complex.[146] In order to lessen concerns that the material contained different polymorphs, as was observed for complexes **2.5** and **2.6**, PXRD measurements were performed on the bulk of the material (Figure 2.10). As shown in Figure 2.9, nearly all of the material was indeed pure **2.9** with very little variation in the crystalline structure. When compared to Cr(III) and Fe(III), the Mn(II) Me_4N^+ analogues present higher

coordination lengths which is as expected due to the lower charge of the metal centre, but otherwise present a similar geometry around the metal centre with very little variation in the coordination angles.

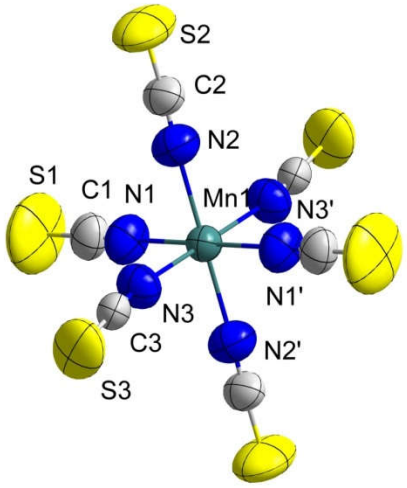

Figure 2.9 The structure of the anion of $(Me_4N)_4[Mn(NCS)_6]$ (**2.9**). The Me_4N^+ ions were removed for clarity. Colour code: Green (Mn), Blue (N), Yellow (S), Gray (C).

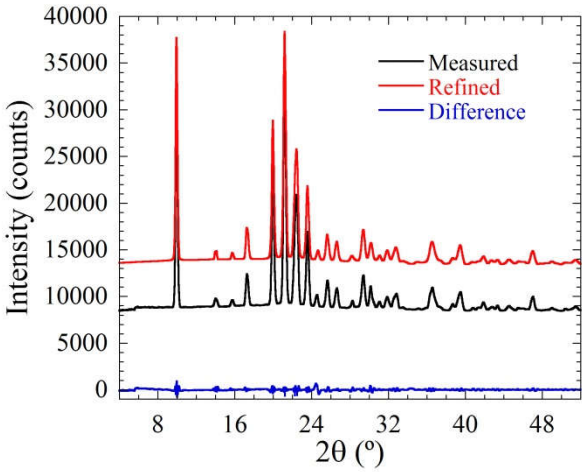

Figure 2.10 Measured PXRD pattern (black), Pawley refinement (red) and difference pattern (blue) of $(Me_4N)_4[Mn(NCS)_6]$ (**2.9**).

For $(Et_4N)_3[Mn(NCS)_5]$ (**2.10**), crystallographic analyses indicated that this complex consists of a 5-coordinate metallic core, as opposed to the common 6-coordinate core of NCS^- complexes (Figure 2.12). In this case, the NCS^- coordination distances varied between 2.110(5) and 2.226(4) Å (Table 2.7) and the coordination angles between 166.1(4) and 175.7(4)°. These distances are shorter than those observed for **2.9** and

usual Mn-N coordination distances, but they are also consistent with a lower coordination number and five-coordinate geometries for Mn(II).[144-145] The calculated τ (tau) value for five-coordinate complexes indicates the level of structural distortion compared to an ideal square-based pyramid (τ=0) or a perfect trigonal bipyramid (τ=1).[147] Using the N1-Mn1-N4 and N3-Mn1-N5 angles (170.3(2) ° and 133.2(2) °, respectively), the τ value of **2.10** was calculated to be 0.61, which corresponds to a distorted trigonal bipyramidal geometry. Just like for **2.9**, the high spin state of the complex was confirmed by SQUID magnetometry. The $\chi_M T$ value of 4.08 cm^3 K / mol is slightly lower than the expected value for a high spin d^5 complex.[146] In a similar fashion as for **2.9**, SC-XRD assessment for **2.10** was made difficult due to the scarcity of viable single crystals in the bulk material. PXRD was used to confirm the purity and the absence of polymorphs in the material (Figure 2.12).

In the packing arrangement of **2.10**, 2D sheets of the metallic cores are separated by sheets of the Et_4N^+ countercations. The shortest distance between two Mn(II) metal centres is 10.92(1) Å, indicating that minimal interactions exist between the anionic units. The lower Mn(II) coordination number of five is likely stabilized due to electrostatic interactions between the NCS^- ligands and the Et_4N^+ cations, as was observed and postulated for the previously published Ni(II) complex $(Bu_4N)_3[Ni(NCS)_5]$, which is, to our knowledge, the only other five coordinate tetraalkylammonium isothiocyanometallate complex.[126] As a comparison, the τ value of this Ni(II) complex was calculated to be 0.08, which suggests that it has an only slightly distorted square-based pyramidal geometry. The difference in distortion of these five coordinate complexes may be due to a difference in their electronic configuration (d^5 versus d^8) or due to the difference in the nature of the countercation and the strength of the electrostatic interactions between the anionic core and the countercations. To our knowledge, complexes **2.9** and **2.10** represent the second and third structurally characterized homoleptic Mn(II) isothiocyanates to date, the first being the Na^+ salt as mentioned in section 2.1.

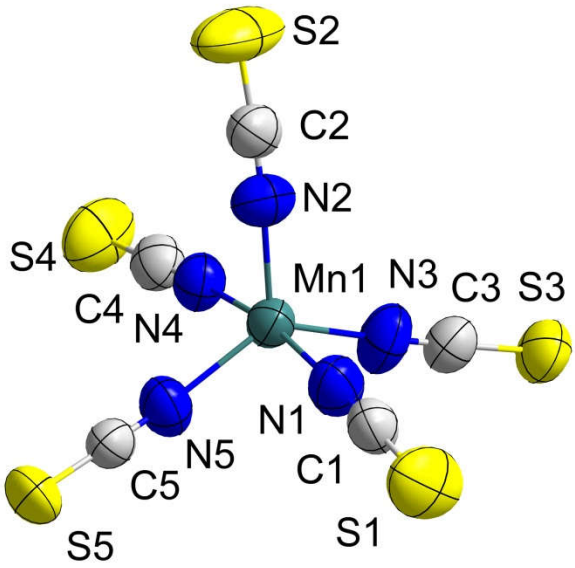

Figure 2.11 The structure of the anion of $(Et_4N)_3[Mn(NCS)_5]$ (**2.10**). The Et_4N^+ ions were removed for clarity. Colour code: Green (Mn), Blue (N), Yellow (S), Gray (C).

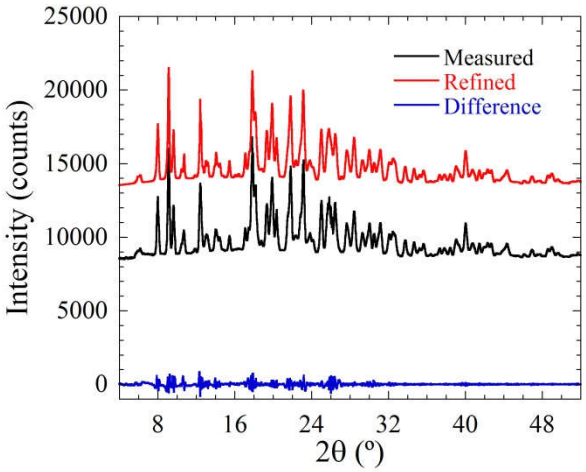

Figure 2.12 Measured PXRD pattern (black), Pawley refinement (red) and difference pattern (blue) of $(Et_4N)_3[Mn(NCS)_5]$ (**2.10**).

Table 2.7 Selected bond lengths (Å) and angles (°) for $(Et_4N)_3[Mn(NCS)_5]$ (**2.10**).

Identity	Length (Å) / Angle (°)	Identity	Length (Å) / Angle (°)
Mn1-N1	2.216(5)	Mn1-N1-C1	171.6(4)
Mn1-N2	2.110(5)	Mn1-N2-C2	171.9(4)
Mn1-N3	2.143(4)	Mn1-N3-C3	172.7(4)
Mn1-N4	2.226(4)	Mn1-N4-C4	175.7(4)
Mn1-N5	2.173(4)	Mn1-N5-C5	166.1(4)
N1-Mn1-N2	98.3(2)	N2-Mn1-N3	110.8(2)
N1-Mn1-N3	87.8(2)	N2-Mn1-N4	91.0(2)
N1-Mn1-N4	170.3(2)	N2-Mn1-N5	116.0(2)
N1-Mn1-N5	85.9(2)	N4-Mn1-N5	87.4(2)
N3-Mn1-N4	91.5(2)	N3-Mn1-N5	133.2(2)

2.4.3. **Iron(III) salts**

As mentioned in Section 2.1, isothiocyanoferrate(III) systems are well-studied systems in relation to the other first-row transition metals, due to their varied utility in many areas of science.[119-120] Modified syntheses to obtain purer material and larger crystals are reported herein for $(Me_4N)_3[Fe(NCS)_6]$ (**2.11**) and $(Et_4N)_3[Fe(NCS)_6]$ (**2.12**). Among other parameters, such as their formation constants and IR and Raman spectra, the crystal structures of these complexes were previously reported. Crystallographic assessment of the products from the modified syntheses indicated that the crystals consisted of the same complexes when compared to published data. For $(n\text{-}Bu_4N)_3[Fe(NCS)_6]$ (**2.13**), structural analyses revealed that the complex is very similar to **2.12**, with differences only in the countercations spatial distribution surrounding the anions. The Fe-N distances varied between 2.032(3) and 2.061(3) Å and the coordination angles between 168.8(3) and 173.6(3) ° (Figure 2.13 and Table 2.3). The complex does not present the distorted coordination of one of the NCS^- ligands that was observed in **2.11**.[119]

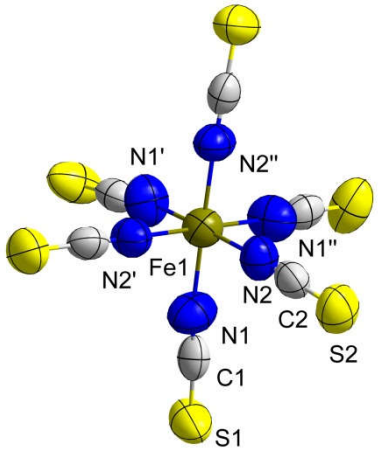

Figure 2.13 The structure of the anion of $(n\text{-}Bu_4N)_3[Fe(NCS)_6]$ (**2.13**). The Bu_4N^+ ions were removed for clarity. Colour code: Dark Yellow (Fe), Blue (N), Yellow (S), Gray (C).

2.4.4. **Cobalt(II) salts**

In the case of the Co(II) series, the K^+, NH_4^+, Me_4N^+ and Et_4N^+ crystal structures were all previously reported as tetrahedral salts of the type $Q_2[Co(NCS)_4]$.[121-124] For the Bu_4N^+ salt, namely $(n\text{-}Bu_4N)_2[Co(NCS)_4]$ (**2.14**), despite numerous efforts, only highly twinned poorly diffracting crystals could be isolated. The resulting poor quality X-ray diffraction dataset yielded sufficient resolution to confirm that the metallic core is unambiguously a tetrahedral $[Co(NCS)_4]^{2-}$ anion. Nevertheless, this structural information is consistent with the tetrahedral $[Co(NCS)_4]^{2-}$ anions identified in the analogous NH_4^+, Me_4N^+ and Et_4N^+ salts.[121-122]

2.4.5. **Nickel(II) salts**

$(Me_4N)_4[Ni(NCS)_6]\bullet x(H_2O)$ (**2.15**, x = 1; **2.16**, x = 0) crystallizes as green and yellow plates from acetone, respectively. The structure of the dehydrated complex, **2.16**, was previously published.[125] Structural investigations revealed that the complexes are isostructural. Both complexes crystallize in the triclinic space group P-1, and the only difference between the two complexes is the presence of an interstitial water molecule in the case of **2.15**. The presence of this water molecule does not affect the structure, but the crystals tend to convert over 2 to 3 days between the hydrated complex **2.15** and the dry complex **2.16** when left at room temperature in a dry environment. In both cases, the

cif files could not be refined to an acceptable R value due to the poor quality of the crystals, but assignment of the atoms was performed to a reasonable level. The structures both corresponded to the published structure, with the exception of the absence of the interstitial molecule in the case of **2.16**.

2.4.6. **Lanthanide salts**

For the lanthanide series, it has been shown that all lanthanides have analogous structures, but that the level of hydration in the species causes major changes in the packing arrangement and coordination core of the $[Ln(NCS)_x(H_2O)_y]^{z-}$ system.[130-136] To remain constant in this thesis, assessment of six-coordinate species and for the approach towards the synthesis of CPs, focus was placed on the non-hydrated type of complexes. Structural analyses of $(n\text{-}Bu_4N)_3[Ln(NCS)_6]$ (with Ln = Eu(III) (**2.17**), Gd(III) (**2.18**) and Dy(III) (**2.19**) indicated that all three complexes are isostructural (Table 2.8 and Figure 2.14), with an octahedral geometry around the Ln(III) metal centres, which are coordinated by six N-bound NCS^- ligands. All three complexes are isostructural to the published structure of $(n\text{-}Bu_4N)_3[Er(NCS)_6]$.[112] The Ln-N distances vary between 2.332(4) and 2.404(3) Å (Table 2.8), which are similar to the aforementioned Er(III) species with a Ln-N distances of approximately 2.33 Å. The decrease in the coordination distances between **2.17**, **2.18**, **2.19** and the Er(III) species reflect the systematic decrease in the ionic radii of the lanthanide centres.[112-114]

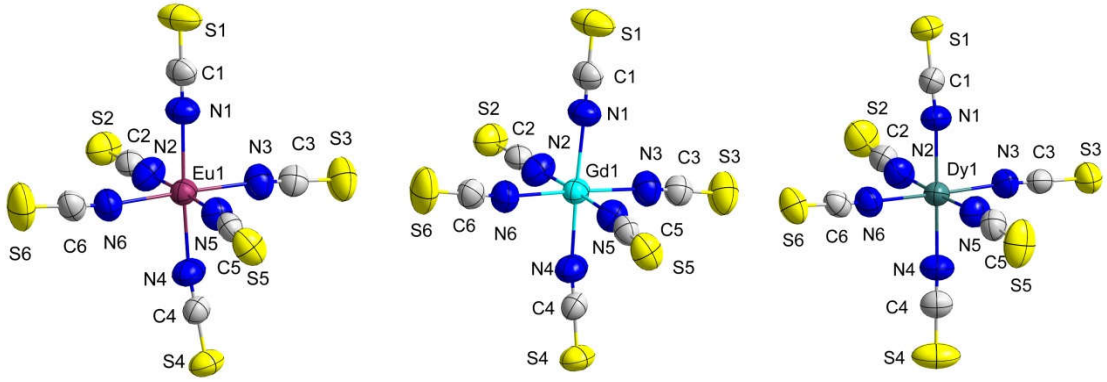

Figure 2.14 The structure of the anions of (n-$Bu_4N)_3[Eu(NCS)_6]$ (**2.17**) (left), (n-$Bu_4N)_3[Gd(NCS)_6]$ (**2.18**) (middle) and (n-$Bu_4N)_3[Dy(NCS)_6]$ (**2.19**) (right). The Bu_4N^+ ions were removed for clarity. Colour code: Purple (Eu), Light blue (Gd), Turquoise (Dy), Blue (N), Yellow (S), Gray (C).

Table 2.8 Selected bond lengths (Å) and angles (°) for (n-$Bu_4N)_3[Ln(NCS)_6]$ (Ln = Eu(III) (**2.17**), Gd(III) (**2.18**) and Dy(III) (**2.19**)).

Compounds	2.17	2.18	2.19
M-N1	2.379(3)	2.390(4)	2.341(4)
M-N2	2.395(3)	2.395(4)	2.340(4)
M-N3	2.382(3)	2.398(4)	2.350(4)
M-N4	2.387(3)	2.365(4)	2.333(4)
M-N5	2.405(3)	2.376(4)	2.340(4)
M-N6	2.381(3)	2.396(4)	2.364(4)
M-N1-C	176.2(3)	171.3(4)	172.7(4)
M-N2-C	174.8(3)	173.9(4)	172.3(4)
M-N3-C	171.8(3)	175.3(4)	174.6(4)
M-N4-C	172.5(3)	175.6(4)	176.5(4)
M-N5-C	174.4(3)	170.7(4)	172.7(4)
M-N6-C	172.0(3)	174.5(4)	174.0(4)

2.4.7. Discussion of the crystallographic data

The structures presented above illustrate some trends in the solid-state structural behaviour of first row transition-metal isothiocyanometallates. The Cr(III) salts tend to adopt structures isostructural to, or very similar to, the Fe(III) salts and some of the Co(III) salts. For example, the metallic core of $(Me_4N)_3[Cr(NCS)_6]$ (**2.3**) is isostructural to $(Me_4N)_3[Fe(NCS)_6]$ (**2.11**) and $(n\text{-}Bu_4N)_3[Cr(NCS)_6]$ (**2.7**) is isostructural to $(n\text{-}Bu_4N)_3[Fe(NCS)_6]$ (**2.13**). The unit cell of $(Et_4N)_3[Cr(NCS)_6]$ (**2.5**) is also similar to the one observed for $[Co(NH_4)_6](ClO_4)_3]$,[149] another classic Werner complex for which the counteranion is similar in size to Et_4N^+. On the other hand, the Mn(II)-containing structures can be compared to the published salts of Ni(II) for which, in both cases, electrostatic interactions between the isothiocyanate ligand and certain countercations stabilize five-coordinate complexes. Clearly, this series of isothiocyanometallates indicate that the structural behaviour of these isothiocyanate-based Werner complexes can still yield surprises and is highly dependent on the nature of the metal centres and of the countercations.

Overall, when comparing the analogous first-row transition metal complexes to each other, the complexes tend to follow trends as expected in terms of coordination distances and angles. For Cr(III) and Fe(III), the coordination distances are approximately the same (~2.01 vs. ~2.02 Å) and a trend between the metal centres cannot be clearly established. In the case of Mn(II) and Ni(II), an increase in the coordination distance by approximately 0.1-0.2 Å is observed when compared to Cr(III) and Fe(III), which is as expected due to the lower charge of the former complexes. When comparing the Me_4N^+ complexes of Mn(II) and Ni(II), a reduction of approximately 0.1 Å is observed in the coordination distances (~2.20 vs. ~2.10 Å), which is as expected when migrating from a larger Mn(II) to a smaller Ni(II) metal centre.[141-143] Similarly, the coordination distances of Eu(III) and Gd(III) are the same, but a decrease is observed for Dy(III). In all cases, the coordination angles do not present considerable variation when comparing the octahedral analogous complexes.

2.5. Light Scattering of $Q_3[Fe(NCS)_6]$ (Q = Me_4N^+ (2.11), Et_4N^+ (2.12), Bu_4N^+ (2.13)).

While performing synthetic work for the Iron(III) salts, a substantial difference between the colour of the crystals and of the powder was noted. In the case of **2.11**, the difference was small (Figure 2.16), but still noteworthy, whereas for **2.12** and **2.13** (Figure 2.18 top), the difference is considerable (very dark green to dark red). Under a direct light source, such as a microscope light, the top of the crystals tended to be dark red whereas the sides tended to be dark green. In the laboratory, under diffuse light, the crystals appeared dark green on all sides. This difference in color prompted an investigation of this phenomenon. In the literature, this phenomenon was often mentioned in the experimental sections regarding iron isothiocyanometallates complexes but was never thoroughly investigated.[119]

In solution, the complexes appeared dark red as is expected for iron(III) NCS^- salts. The solution UV-Visible spectra of **2.12** and **2.13** are identical to **2.11**, and to each other, with a single absorbance band at 496 nm (Figure 2.15), illustrating that no colour difference exists in solution.

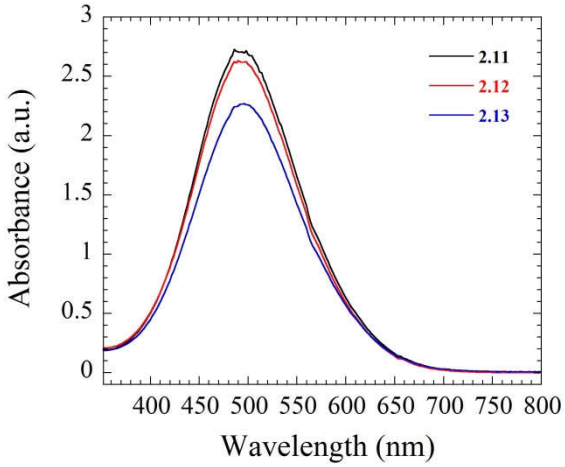

Figure 2.15 The solution UV-visible absorbance spectra of **2.11** (black), **2.12** (red) and **2.13** (blue), illustrating the identical single absorbance band at 496 nm for all three complexes.

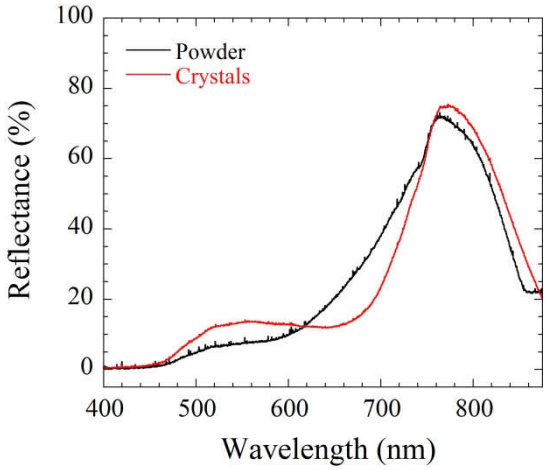

Figure 2.16 The solid-state visible reflectance spectra of $(Me_4N)_3[Fe(NCS)_6]$ (**2.11**) as powder (black) and crystals (red).

As shown in Figure 2.17 and 2.18, the solid-state reflectance spectra of **2.12** and **2.13** present differences between the crystals and powders of both complexes. As a comparison, the solid-state spectrum of **2.11** was also measured (Figure 2.16) and only small differences were noted between the crystals and the power. This set of spectra confirmed that this phenomenon occurs in the solid-state only, and is more significant in **2.12** and **2.13**. In the case of the analogous Cr(III) complex to **2.13**, $(n\text{-}Bu_4N)_3[Cr(NCS)_6]$ (**2.5**), the crystals did not present a difference in color when compared to a powder, thus suggesting that this phenomenon is specific to the iron(III) salts only (Figure 2.19).

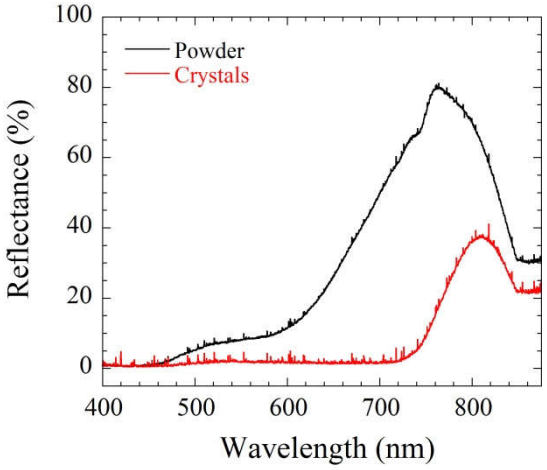

Figure 2.17 The solid-state visible reflectance spectra of **2.12** as crystals (red) and powder (black).

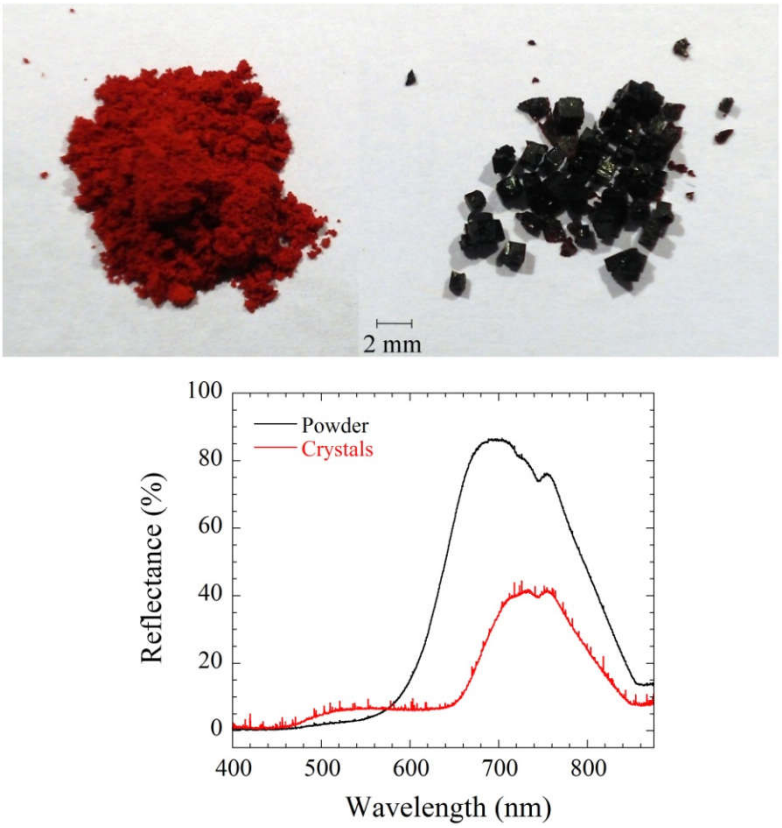

Figure 2.18 Picture of powder (top left) and crystals (top right) of **2.13** in ambient light, illustrating the significant difference in reflective colour and their respective solid-state reflectance spectra (bottom).

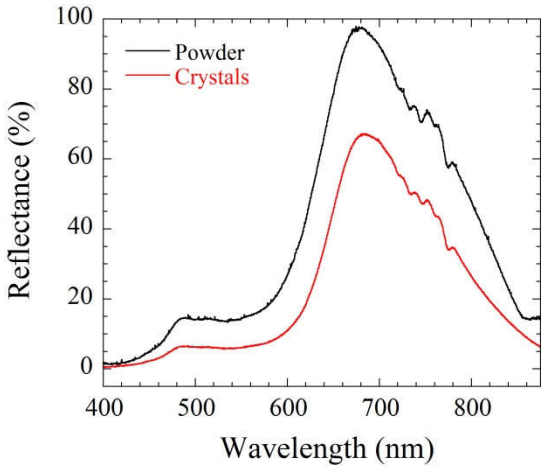

Figure 2.19 The solid-state visible reflectance spectra of (n-$Bu_4N)_3[Cr(NCS)_6]$ (**2.7**) as crystals (red) and powder (black).

During the synthetic work, it was noted that the resulting colour of the solid was dependent on the grain size of the crystalline material: the bigger the crystals, the darker they appeared to the naked eye. To quantify this effect, crystals of **2.13** were crushed carefully using a mortar and pestle and then separated by grain size using 106 and 250 μm sieves in three categories (<106 μm, 106 to 250 μm, >250 μm). Once separated, the crystals were washed thoroughly using a 90:10 mixture of H_2O:EtOH, a solution in which the crystals were sparingly soluble. This was to ensure that no impurities were present on the surface of the crystals during the measurement. The solid-state visible spectra of each sample were then measured in a dark room. Crystals of **2.13** were chosen as the subject sample for this grain size study due to their cubic morphology and space group, which favours the crystals to break as cubic pieces, when carefully crushed, that can be roughly separated by size regardless of their orientation, as opposed to the plate-shaped crystals of **2.12** which tended to break into elongated rods and plates. As shown in Figure 2.20, when the average grain size of the sample increased, the reflectance band at 753 nm did not shift significantly. However, the broad reflection peak located between 600 and 800 nm gradually increases in wavelength and decreases in intensity from 693 nm and 86% for crystals of less than 106 μm in size to 712 nm and 32% for crystals larger than 250 μm. The spectrum for a single large crystal (> 8 mm^3) was used in Figure 2.17 and presents a reflectance maximum at 732 nm. This investigation suggested that the change in colour of the crystals could be attributed to a size-dependent effect; this is a phenomenon usually associated with Brillouin light scattering.[150] Brillouin light

scattering occurs when the acoustic vibrations of a material interact with the absorption and refraction of wavelengths in a similar fashion as observed for Raman scattering, but instead involving the acoustic vibrations of said material instead of the vibrational modes of the molecules. As such, this phenomenon is dependent on both the chemical composition of the material and the geometric parameters (e.g., shape and size) of the material being sampled. In order to measure the Brillouin scattering spectra of a sample, a specialized Fabry-Perot Interferometer must be used[151] due to the technical challenges of measuring inherently low frequencies, and thus, further investigations were not performed regarding this phenomenon for **2.12** and **2.13**.

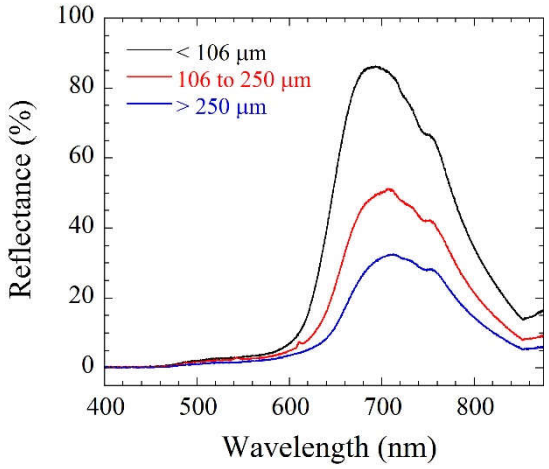

Figure 2.20 Visible reflectance spectra of **2.13** for crystals smaller than 106 µm (black), between 106 and 250 µm (purple) and larger than 250 µm (green). The maxima are located at 693, 707, and 712 nm with intensities of 86, 71 and 32 %, respectively.

2.6. Discussion

2.6.1. Challenges in crystallization and purification

As mentioned in Section 2.1, there was a definite lack of information available regarding the structural properties of these complexes in the literature. In most cases, only the Infrared and Raman spectra were available in older publications, and for a few select complexes, the formation constants were also measured. Since these complexes were going to be the basic building blocks for the synthesis of heterobimetallic CPs, further investigation of their structural properties was required, in order to assess a) their

coordination number, b) their spin-state (for Mn(II)) and c) any incongruities present in the system that would lead to interesting structural arrangements.

After the synthetic investigations, it became clear that the reason for this lack of information was because of the difficulty of syntheses, crystallization and purification of these materials. In essence, the synthesis of these materials in a somewhat pure form (~90%, established by EA) can be accomplished by mixing the precursors in acetone or H_2O, but this usually results in heavily twinned crystals or amorphous materials. Nonetheless, the purity of these materials was sufficient to establish the IR and Raman spectra and to measure their formation constants with the instruments available in the 1950s-1980s. However, a combination of the relatively low purity and lability of these substances prevented the crystallization of the materials for SC-XRD studies. For the synthesis of CPs using a building block approach, pure materials are often required since impurities can inhibit or interfere in the crystallization process, leading to crystals that are heavily twinned or polycrystalline masses.

In order to purify the complexes, our investigations were performed using different synthetic methods and crystallization techniques, as detailed in Section 2.2. First, the purity of the sample was addressed by establishing a synthetic method that would allow one to eliminate most of the side product by filtration, usually KCl or KBr, leading to liquors from which the complexes could be crystallized as pure samples. Multiple solvent combinations were attempted, and in most cases, acetone was found to be the optimal solvent for the task in most cases.

The crystallization challenges were also addressed. It was found that the most common crystallization techniques, such as slow evaporation and H-tubes at room temperature, were not adequate and led to heavily twinned crystals in most cases. Optimally, a very slow evaporation process was required, and crystallization to obtain single crystals was performed in test tubes (with a diameter of <2 cm) and/or NMR tubes by slow diffusion layering. Any wider medium for crystallization resulted in amorphous products or heavily twinned crystals. In some cases, even these narrow media were insufficient to obtain crystals, and it was found out that lowering the temperature and extended crystallization periods were the appropriate methods to obtain single-crystals and pure products.

2.7. Using first-row transition metal cations for the synthesis of coordination polymers with isothiocyanometallates

Once the structural properties of the building block precursors **2.1**-**2.19** were established and the synthetic method refined, attempts at the synthesis of CPs were made using synthetic methods well established in the Leznoff group. This procedure consists of dissolving the precursors in appropriate solvents, most often polar ones such as H_2O and MeOH, and choosing a combination of countercations, counteranions and solvents that would lead to the precipitation of a salt. The latter salt must be mostly insoluble in the solvents of choice to be filtered out easily, leaving the combination of building blocks of interest in solution which forms the targeted CP upon crystallization (See Section 1.3). For example, theoretically, one can combine $K_3[Fe(NCS)_6]$ and $[Co(2,2'\text{-bipy})_2]Br_2$ in a 2:3 ratio in ethanol in order to encourage the precipitation of KBr and the formation of the coordination polymer $[Co(2,2'\text{-bipy})_2]_3[Fe(NCS)_6]_2$ (Equation 2.1). This method was successful for a large variety of CPs, using different anions such as $[Au(CN)_2]^-$ or $[Au(CN)_4]^-$.

$$3[Co(2,2'\text{-bipy})_2]Br_2 + 2K_3[Fe(NCS)_6] \xrightarrow[\text{Solvents}]{} [Co(2,2'\text{-bipy})_2]_3[Fe(NCS)_6]_2 + 6KBr$$

Equation 2.2 Example of the combination of a Co(II) 2,2'-bipy-based precursor with a $[Fe(NCS)_6]^{3-}$ precursor to synthesize a CP.

Using these parameters, the synthesis of coordination polymers was attempted using a combination of the Cr(III), Fe(III) and Co(II) salts from this chapter, ligands such as 2,2'-bipyridine, 4,4'-bipyridine, terpy and ethylenediamine (en), and chloride salts of Fe(II), Mn(II), Co(II) and Ni(II). The chloride salts of the metals were chosen due to the resulting secondary salt of the synthesis, such as potassium or ammonium chloride, being slightly less soluble in acetone than other similar salts, such as KNO_3, and thus could be easily filtered out upon completion of the synthesis.

$$3MCl_2\cdot 6H_2O + 6L + 2(Et_4N)_3[X(NCS)_6] \xrightarrow[\text{Solvents}]{} [M(L)_2]_3[X(NCS)_6]_2 + 6(Et_4N)Cl$$

M = Fe(II), Mn(II), Co(II), Ni(II); X = Cr(III), Fe(III)
L = 2,2'-bipy, 4,4'-bipy, terpy, en, tmeda, phen

Equation 2.3 Examples of attempts at the synthesis of CPs using $(Et_4N)_3[Cr(NCS)_6]$ (**2.5**) and $(Et_4N)_3[Fe(NCS)_6]$ (**2.12**).

$$MCl_2{\cdot}6H_2O + 2L + (n\text{-}Bu_4N)_2[Co(NCS)_4] \xrightarrow[\text{Solvents}]{} [M(L)_2Co(NCS)_4] + 2(n\text{-}Bu_4N)Cl$$

M = Fe(II), Mn(II), Co(II), Ni(II)
L = 2,2'-bipy, 4,4'-bipy, terpy, en, tmeda, phen

Equation 2.4 Examples of attempts at the synthesis of CPs using (*n*-$Bu_4N)_2[Co(NCS)_4]$ (**2.14**).

Initially, the syntheses were attempted using the Fe(III) precursors, including $K_3[Fe(NCS)_6]$, **2.11**, **2.12** and **2.13** using the method described above. A series of crystalline products were obtained. After varied attempts and unit cells investigations, it was determined that these materials consisted of complexes of the type $[M(L)_x(NCS)_2]$ (where $M(L)_x$ was the metal-ligand building block initially chosen). These complexes always crystallized from the solution instead of the CPs sought after by design which indicated that the Fe(III) species were too labile in commonly used polar solvents and allowed the transfer of the NCS^- ligand to the secondary metal centre. Further attempts were then performed using less polar solvents, such as ethyl acetate, in combination with the *n*-Bu_4N^+ salt **2.13** in order to limit the lability of the Fe(III) complexes and encourage the formation of the planned CPs, but it was established that even in less polar solvents, the lability of the Fe(III) complexes was still an issue.

This lability was in agreement with the published formation constants for $Q_x[Fe(SCN)_y]$ complexes in H_2O (ranging between 10 and 10^3 for all the SCN^- ions), which are much lower than the value of 2.0×10^{38} for the typically used $[Au(CN)_2]^-$ in the Leznoff group.[47-53] Thus, based on the reported formation constants, it was established that retaining the isothiocyanate ligand on the Fe(III) metal centre would be a difficult task. In combination with the fact that the hard N-site would also be the preferred coordination site for the choice of hard secondary metal centres, such as Fe(II), Mn(II), Co(II) and Ni(II), in the initial design, it was determined that a better choice of less labile metal centres would be required to overcome this challenge.

Attempts were next performed using the Cr(III) and Co(II) salts, using the same synthetic methods, solvents, ligands, and precursor salts combinations, since Cr(III) and Co(II) salts are known to be far less labile than their Fe(III) counterparts. Unfortunately, these attempts also resulted in the crystallization of the $[M(L)_x(NCS)_2]$ species despite the fact that Cr(III) and Co(II) presented higher formation constants for all SCN^- ions

(approximately 10^4 and 10^3, respectively), and thus less lability was to be expected. No further investigations were performed using the first-row transition metals precursors, as the lability of these species represented a significant problem that was not readily overcome. Instead, it was decided to shift our interest toward the less labile late-transition metal anions, which were already proven to be adequate for the synthesis of cyanide-based coordination polymers. This decision to migrate our efforts to 2nd and 3rd row late-transition metals such as Pd(II), Pt(II), Rh(III), Ir(III), etc., was further supported by the much higher reported formation constants (most varying between 10 and 30, the highest $[Pt(SCN)_4]^{2-}$ being 33.6) for heavier transition metals when compared to first-row transition metals, but also by the general understanding of the theory behind the lability of complexes as established by Taube and ligand-field theory, where a metal with a greater Δ splitting of the d-orbitals for a given configuration and set of ligands will result in a more inert complex.[152]

2.8. **Conclusions and future work**

In this chapter, the synthesis, crystallization, purify ication, structural characterization, and optical properties of first-row transition metal isothiocyanometallates of the type $Q_x[M(NCS)_y]$ were presented. As established in Section 2.1, very little structural information regarding these species was available in the literature, and thus, in contrast with older literature, detailed synthetic approaches and extensive structural studies for these fundamental complexes were pursued. In most cases, the materials consist of classic Werner complexes without deviations from the expected octahedral structure and properties. However, in the case of the Mn(II) series, it was found that $(Et_4N)_3[Mn(NCS)_5]$ is indeed not an octahedral complex but instead a heavily distorted five-coordinate complex. For the Fe(III) salts, the often mentioned but never studied colour change phenomena was investigated. It was established that these salts present a change in solid-state colour that is dependent on the grain size of the crystallites, which is a phenomenon that can be attributed to a light scattering effect.

Despite the presence of a small amount of evidence for the successful synthesis of CPs using first-row transition metal bridging complexes of the type $Q_x[M(NCS)_y]$, the lability of these building blocks presented a considerable challenge to overcome and CPs were

not successfully synthesized using the traditional synthetic methods of the Leznoff group. The attempts at the synthesis of CPs using these first-row transition metal building blocks could be further improved by inducing ways to limit the lability of the building blocks in the chosen solvents, such as by using dry reagents such as $FeCl_3$, $CoCl_2$, etc. in combination with the targeted ligands and the *n*-Bu_4N^+ salts of Cr(III) and Fe(III) in non-polar solvents. Similarly, the synthesis of these first-row transition metal building blocks could be performed using other less polar cations, such as PPh_4^+ that would allow for the synthesis of CPs in non-polar solvents using these first-row transition metals. There is also the possibility of using the S-bound first-row transition metal building block, $Q_x[Zn(SCN)_4]$ for the synthesis of (iso)thiocyanate-based CPs, for which there already are a handful of publications,[153-154] that present less lability than the other first-row transition metal counterparts and a free hard nitrogen-based coordination site, an asset when combining it with other hard first-row transition metals for the preparation of heterobimetallic CPs.

Nonetheless, the availability of clear synthetic approaches for the preparation and purification of isothiocyanometallate building blocks and the additional structural and spectroscopic information presented herein should facilitate the use of these complexes in the design and synthesis of new solid-state materials with unique structural and optical properties and in future related work.

2.9. Experimental

2.9.1. General Procedures and Materials.

Unless otherwise noted, all reagents were purchased from commercial sources and were used without further purification. *n*-Bu_4NNCS was synthesized via metathesis by stirring *n*-Bu_4NBr and KSCN in acetone for 30 minutes. The resulting KBr was removed by filtration and the solvent was removed *in vacuo* to yield *n*-Bu_4NNCS as a powder. 106 μm (140 Mesh) and 250 μm (70 Mesh) sieves were purchased from Newark Wire Cloth Company and were made of stainless steel. The sieves were washed thoroughly with water and acetone before usage to prevent contamination of the samples.

Vibrational spectroscopy. Infrared spectra were measured in the 4000-700 cm^{-1} range using a Thermo Nicolet Nexus 670 FT-IR spectrophotometer equipped with a Pike MIRacle attenuated total reflection (ATR) sampling accessory or with a KBr pellet apparatus, as stated. Raman spectra were recorded on a Renishaw inVia Raman Microscope equipped with a 200 mW 785 nm laser or with a 15 mW 532 nm laser. Spectra were obtained from 100 to 4000 cm^{-1} using a 1200 l/mm grating and an exposure time of 10 seconds. Specific accumulations (a) and laser power (%lp) are stated for each experiment.

UV-Visible spectroscopy. Solid-state UV visible reflectance spectra were measured using an Ocean Optics SD2000 spectrophotometer equipped with a tungsten halogen lamp and a fibre optic cable. Solution UV visible spectra were measured using a Hewlett Packard 8452A diode array spectrophotometer.

Elemental analysis. Microanalyses (C, H, N) were obtained on a Carlo Erba EA 1110 CHN elemental analyzer by CE Instruments Ltd and were collected by Mr. Paul Mulyk or Mr. Frank Haftbaradaran.

Magnetometry. The dc susceptibility of selected compounds was measured using a Quantum Design MPMS-XL7 SQUID magnetometer at 300 K under a magnetic field of 1000 Oe. Samples were measured in low background gel caps and polyethylene straws supplied by Quantum Design. The data was corrected for TIP and the constituent atoms by use of Pascal constants.[146]

Single-crystal X-ray Diffraction. Crystals of selected samples were mounted on glass fibres or MiTeGen sample holders using paratone oil or epoxy glue. X-ray data for the compounds were collected at room temperature or 150 K (see text and crystallographic data, Appendix C) using a Bruker Smart APEX II instrument using either a Cu Kα (λ = 1.54184 nm) or a Mo Kα (λ = 0.71073 nm) source. All frames were collected using a 0.5° scan width in ω or ϕ. The frames were integrated using the Bruker SAINT software package[155] and the data were corrected for absorption effects using empirical multi-scan techniques. Final unit cell dimensions were determined on the refinement of XYZ-centroids of the reflections. In the case of twinned crystals, twin laws for the samples were determined using CELL_NOW[156] and were modelled in CRYSTALS[158] or ShelXle.

All structures were solved using either Sir92 direct methods[159] or superflip charge flipping method.[160] Subsequent refinements were performed in CRYSTALS or ShelXle. Refinement of all structures included the coordinates and anisotropic temperature factors for all non-hydrogen atoms unless otherwise noted. Hydrogen atoms were placed geometrically and refined using isotropic temperature factors using a riding model linking them to their respective atom. All compounds included a statistical weighing scheme. All relevant crystallographic data for all complexes is available in Appendix D and representations were made using Diamond 3.0.[161]

Unless otherwise stated, all structures in this work are depicted with thermal ellipsoids drawn at 50% probability with hydrogen atoms, solvent molecules and countercations removed for clarity. The crystallographic data files are available as supplementary information (see Appendix D).

Powder X-ray Diffraction. Powders of the samples were mounted on a MiTeGen sample holder using paratone oil, and the data was collected at room temperature on a Bruker Smart APEX II instrument equipped with a Cu Kα (λ = 1.54184 nm) source. Data were collected by spinning ϕ scans over the ranges of 1-23 °, 12-35 °, 24-47 °, 36-59 °, 48-79 ° and 60-83 ° with 360 s exposure times, leading to a full 2θ range of 1-83 °. The data were integrated using Pilot from 5 ° to 83 ° with a step size of 0.02 °. The refinement parameters for **2.5**, **2.7**, **2.9** and **2.10** are available in Table 2.10.

2.9.2. Synthetic procedures

$K_3[Cr(NCS)_6]\cdot H_2O$ (2.1).

To a solution of $CrCl_3\bullet 6H_2O$ (1.00 mmol, 237 mg) in H_2O (10 mL) was added a solution of KSCN (6.00 mmol, 583 mg) in H_2O (10 mL). The mixture was stirred for 15 minutes and the solvent was then removed under vacuum. The crude residue was then stirred in acetone until all the colored precipitate was dissolved, leaving a white precipitate of KCl which was then removed by filtration. Slow evaporation of the liquor resulted in large purple crystals of $K_3[Cr(NCS)_6]\cdot H_2O$ (2.1) overnight. Yield: 0.476 g (91.9 %). FT-IR (**2.1**, ATR, cm^{-1}): 2084 (s), 1071 (s), 846 (s). Raman (**2.1**, 514 nm, %Ip: 100, cm^{-1}): 2085 (s),

830 (s). Anal. Calcd. for $C_6N_6CrK_3S_6{\cdot}H_2O$: C, 13.45; H, 0.38 N, 15.68 %. Found: C, 13.41; H, 0.21; N, 16.56 %.

$(NH_4)_3[Cr(NCS)_6]\cdot x(H_2O)\cdot y[(CH_3)_2CO]$ (2.2, 2.3).

A solution of NH_4NCS (6.00 mmol, 456 mg) in acetone (10 mL) was added to $CrCl_3{\cdot}6H_2O$ (1.00 mmol, 237 mg) in acetone (10 mL). The mixture was refluxed for 2 hours and then filtered to remove the precipitate of NH_4Cl. The solvent was removed *in vacuo* and the resulting residue was washed with Et_2O, resulting in $(NH_4)_3[Cr(NCS)_6]\cdot 3(H_2O)$ (**2.2**). Yield: 0.483 g (95.0 %). FT-IR (**2.2**, ATR, cm^{-1}): 3170 (br), 2089 (s), 1603 (w), 1402 (s). Raman (**2.2**, 514 nm, %Ip: 100, cm^{-1}): 3109, 2092, 829, 473, 234. Raman (**2.2**, 785 nm, %Ip: 50, cm^{-1}): 2131, 2091, 835, 477, 240. Anal. Calcd. for $C_6H_{18}N_9CrO_3S_6$: C, 14.16; H, 3.56; N, 24.78 %. Found: C, 14.24; H, 3.32; N, 24.56 %. Purple crystals of $(NH_4)_3[Cr(NCS)_6]\cdot[(CH_3)_2CO]$ (**2.3**) were grown by slow evaporation from a dry (distilled over $CaSO_4$) acetone solution. The crystals were dried prior to measuring their optical properties due to the rapid loss of solvent occurring at room temperature. FT-IR (**2.3**, ATR, cm^{-1}): 3167 (br), 3027 (w), 2084 (s), 1604 (w), 1399 (s).

$(Me_4N)_3[Cr(NCS)_6]$ (2.4).

A solution of KSCN (6.00 mmol, 583 mg) in acetone (10 mL) was added to a solution of $CrCl_3{\cdot}6H2O$ (1.00 mmol, 237 mg) in acetone (10 mL). The mixture was stirred for 5 minutes and then solid Me_4NCl (3.00 mmol, 329 mg) was directly added to the mixture. The suspension was heated at 50 °C for 2 hours while stirring vigorously. The KCl precipitate was filtered off and the solvent was removed in vacuo to yield a fine powder of $(Me_4N)_3[Cr(NCS)_6]$ (**2.4**). Recrystallization of **2.4** was achieved from a 50:50 Acetone:Et_2O solution at -30 °C over three months, yielding purple plates. Yield: 0.391 g (62.8 %). FT-IR (ATR, cm^{-1}): 2081 (s), 1476 (m), 943 (m). Raman (785 nm, %Ip: 50, cm^{-1}): 2134, 2085, 2054, 1450, 1414, 1286, 947, 839, 753, 484, 455, 367, 242. Anal. Calcd. for $C_{18}H_{36}N_9CrS_6$: C, 34.70; H, 5.82; N, 20.23 %. Found: C, 34.83; H, 5.70; N, 19.98 %.

$(Et_4N)_3[Cr(NCS)_6]$ (2.5).

KSCN (6.00 mmol, 583 mg), $CrCl_3 \cdot 6H2O$ (1.00 mmol, 237 mg) and Et_4NBr (3.00 mmol, 630 mg) were mixed together in 40 mL of H_2O. The suspension was heated at 90 °C for 2 hours and the precipitate was filtered off. A polycrystalline sample of $(Et_4N)_3[Cr(NCS)_6]$ (**2.5**) was obtained by slow evaporation of the mother liquor over a period of two weeks. Separation of the polymorph **2.6** (see main text) as a pure polycrystalline sample was accomplished from a 50:50 Acetone:Et_2O solution at -30 °C over three days. Yield: 0.274 g (34.6 %). FT-IR (KBr, cm^{-1}): 3439 (br), 2983 (w), 2919 (w), 2080 (s), 1487 (m), 1391 (w), 1218 (w), 1171 (w), 1000 (w), 782 (w). Raman (785 nm, %Ip: 50, cm^{-1}): 2134, 2093, 830, 248. Anal. Calcd. for $C_{30}H_{60}N_9CrS_6$: C, 45.53; H, 7.64; N, 15.93 %. Found: C, 45.21; H, 7.68; N, 15.75 %.

$(n\text{-}Bu_4N)_3[Cr(NCS)_6]$ (2.7).

To a 20 mL solution of KSCN (6.00 mmol, 583 mg) and $CrCl_3 \cdot 6H_2O$ (1.00 mmol, 237 mg) in acetone was added a 20 mL solution of *n*-Bu_4NBr (3.00 mmol, 966 mg) in acetone. The mixture was refluxed for 2 hours at 60 °C and the precipitate was filtered off. The solvent was removed *in vacuo* and the crude product was dissolved in ethanol. A polycrystalline sample of (*n*-$Bu_4N)_3[Cr(NCS)_6]$ (**2.7**) was obtained by slow evaporation of this ethanolic solution over a period of four days. Yield: 1.05 g (92.3 %). FT-IR (KBr, cm^{-1}): 3434 (br), 2959 (m), 2933 (w), 2874 (w), 2137 (s), 2085 (s), 1486 (w), 1465 (w), 1378 (w), 1150 (w), 1106 (w), 1054 (w), 1022 (w), 880 (w), 733 (w), 478 (w). Raman (514 nm, %Ip: 100, cm^{-1}): 2932, 2872, 2128, 2079, 1456, 1052, 833, 232. The crystals were dried *in vacuo*. Anal. Calcd. for $C_{54}H_{108}N_9CrS_6$: C, 57.51; H, 9.66; N, 11.18 %. Found: C, 57.29; H, 9.62; N, 11.05 %.

$K_4[Mn(NCS)_6]$ (2.8).

Complex **2.8** was synthesized using the same method as for **2.1**, but by instead using $MnCl_2 \cdot 4H_2O$ (1 mmol, 197 mg) as the metal precursor. Large colorless crystals of $K_4[Mn(NCS)_6]$ (**2.8**) were obtained by slowly evaporating the acetone solution over two days. Yield: 0.482 g (86 %). FT-IR (**2.8**, ATR, cm^{-1}): 2312 (br), 2074 (s), 770 (m). Raman (**2.8**, 785 nm, %Ip: 50, cm^{-1}): 2096 (s), 2071 (s), 782 (s). Anal. Calcd. for $C_6N_6MnK_4S_6$: C,

12.87; H, 0.00 N, 15.01 %. Anal. Calcd. for $C_6N_6MnK_4S_6 \cdot H_2O$: C, 12.47; H, 0.35 N, 14.54 %. Found: C, 12.47; H, 0.31; N, 14.62 %.

$(Me_4N)_4[Mn(NCS)_6]$ (2.9).

$MnCl_2 \cdot 4H_2O$ (1 mmol, 197 mg), Me_4NCl (4.00 mmol, 438 mg) and KSCN (6.00 mmol, 583 mg) were suspended in acetone (20 mL). The mixture was then refluxed for 2 hours, followed by filtration. The solvent was removed *in vacuo* and the crude mixture was redissolved in ethanol, yielding colourless crystals of $(Me_4N)_4[Mn(NCS)_6]$ (**2.9**) over a period of one day by slow evaporation. Yield: 0.321 g (45.9 %). FT-IR (KBr, cm^{-1}): 3023 (m), 2849 (m), 2073 (s), 1614 (w), 1482 (s), 1414 (m), 1282 (w), 947 (s), 779 (m). Raman (785 nm, %Ip: 50, cm^{-1}): 3022, 2978, 2953, 2920, 2095, 2073, 1452, 1415, 1170, 950, 786, 754, 458, 370, 175. Anal. Calcd. for $C_6H_{16}N_{10}CrS_6$: C, 37.75; H, 6.91; N, 20.02 %. Found: C, 37.45; H, 7.14; N, 19.63 %. $\chi_M T$ (300 K) = 4.37 cm^3 K / mol.

$(Et_4N)_3[Mn(NCS)_5]$ (2.10).

Compound $(Et_4N)_3[Mn(NCS)_5]$ (**2.10**) was prepared using the same procedure as for **2.9** but using Et_4NBr (4.00 mmol, 840 mg) instead of Me_4NCl. Yield: 0.376 g (51.2 %). FT-IR (KBr, cm^{-1}): 2981 (m), 2949 (m), 2067 (s), 2050 (s), 1485 (s), 1440 (s), 1392 (m), 1173 (m), 1068 (m), 1052 (m), 999 (m), 960 (s), 785 (s). Raman (785 nm, %Ip: 50, cm^{-1}): 2988, 2941, 2115, 2070, 2059, 1462, 1304, 1175, 1119, 1069, 1000, 906, 795, 672, 427, 266, 208, 199. Anal. Calcd. For $C_{22}H_{48}N_{10}MnS_6$: C, 47.32; H, 8.22; N, 15.23 %. Found: C, 47.29; H, 8.57; N, 15.11 %. $\chi_M T$ (300 K) = 4.08 cm^3 K / mol.

$(Me_4N)_3[Fe(NCS)_6]$ (2.11).

Compound $(Me_4N)_3[Fe(NCS)_6]$ (**2.11**) was prepared by modification of a reported procedure.[119] An ethanolic solution (5 mL) of KSCN (6.00 mmol, 583 mg) was added to an ethanolic solution (5 mL) of $FeCl_3$ (1.00 mmol, 162 mg). The mixture was stirred for 5 minutes and solid Me_4NCl (3.00 mmol, 329 mg) was added directly to the mixture. The precipitated KCl was filtered out and the mixture was evaporated to dryness. The crude residue was dissolved in water and green crystals of $(Me_4N)_3[Fe(NCS)_6]$ (**2.11**) were obtained by slow evaporation of the solution over one week. Yield: 0.353 g (56.4 %). FT-IR (ATR, cm^{-1}): 2073 (s), 2058 (s), 2023 (s), 1480 (m), 946 (m). Raman (785 nm, %Ip: 1,

cm^{-1}): 2115, 2101, 2073, 2055, 2025, 1484, 1448, 946, 753, 494, 479, 454, 291, 253, 220, 172.

$(Et_4N)_3[Fe(NCS)_6]$ (2.12).

The synthesis of $(Et_4N)_3[Fe(NCS)_6]$ (**2.12**) was conducted according to a modified synthetic strategy.[120] An aqueous solution (5 mL) of KSCN (6.00 mmol, 583 mg) was added to an aqueous solution (5 mL) of $FeCl_3$ (1.00 mmol, 162 mg). The mixture was stirred for 5 minutes and solid Et_4NBr (3.00 mmol, 630 mg) was added directly to the mixture. The resulting suspension was stirred for 1 hour. Floating green crystals of $(Et_4N)_3[Fe(NCS)_6]$ (**2.12**) were obtained directly from the surface of the mother liquor after one week. Yield: 0.605 g (76.1 %). FT-IR (ATR, cm^{-1}): 2101 (w), 2070 (s), 2054 (s), 1480 (m), 943 (m). Raman (785 nm, %Ip: 1, cm^{-1}): 2114, 2101, 2055, 2026, 1483, 1446, 1413, 946, 752, 494, 455, 293, 253, 217, 172.

$(n\text{-}Bu_4N)_3[Fe(NCS)_6]$ (2.13).

An aqueous solution (15 mL) of KSCN (6.00 mmol, 583 mg) was added to an aqueous solution (15 mL) of $FeCl_3$ (1.00 mmol, 162 mg). The mixture was stirred for 5 minutes and was then extracted three times using a 50 mL solution of *n*-Bu_4NBr (3.00 mmol, 966 mg) in CH_2Cl_2. The organic extract was washed with a saturated aqueous solution of NaCl three times (3 x 10 mL) and was dried over Na_2SO_4. The solvent was removed in vacuo to yield a powder of $(n\text{-}Bu_4N)_3[Fe(NCS)_6]$ (**2.13**). Recrystallization was performed by slow evaporation from methanol over two days, yielding dark green cubic crystals. Yield: 1.04 g (92.4%). FT-IR (ATR, cm^{-1}): 2956 (w), 2869 (w), 2111 (w), 2064 (s), 2057 (s), 1480 (m), 1453 (w), 1379 (w), 1151 (w), 1024 (w), 883 (m), 783 (m). Raman (514 nm, %Ip: 100, cm^{-1}): 2930, 2872, 2742, 2086, 2058, 1453, 1322, 1107, 1060, 1009, 877, 431. The crystals were dried *in vacuo*. Anal. Calcd. for $C_{54}H_{108}N_9FeS_6$: C, 57.31; H, 9.62; N, 11.14 %. Found: C, 57.17; H, 9.27; N, 11.13 %.

$(n\text{-}Bu_4N)_2[Co(NCS)_4]$ (2.14).

$CoCl_2 \cdot 6H_2O$ (1.00 mmol, 237 mg) and KSCN (4.00 mmol, 388 mg) were dissolved in acetone (10 mL). To this solution was added *n*-Bu_4NBr (2.00 mmol, 644 mg) and the suspension was refluxed for 1 hour. The mixture was then filtered and the solvent was

removed over a steam bath. The crude residue was then dissolved in H_2O and extracted using $CHCl_3$, which was then removed *in vacuo*. Slow evaporation from a 50:50 Acetone/MeOH solution of this residue over three days resulted in multiply twinned blue plate-shaped crystals of $(n\text{-}Bu_4N)_2[Co(NCS)_4]$ (**2.14**). Yield: 0.662 g (85.4 %). FT-IR (KBr, cm^{-1}): 3448 (br), 2962 (m), 2933 (w), 2875 (m), 2070 (s), 1482 (m), 1380 (w), 882 (m). Raman (785 nm, %Ip: 50, cm^{-1}): 2095, 2072, 1454, 1110, 1063, 961, 907, 831, 479, 305, 153. Anal. Calcd. for $C_{36}H_{72}N_6CoS_4$: C, 55.70; H, 9.34; N, 10.82 %. Found: C, 56.08; H, 9.29; N, 10.60 %.

$(Me_4N)_4[Ni(NCS)_6]\cdot x(H_2O)$ (2.15, x = 1; 2.16, x = 0).

Complex **2.15** was synthesized using a similar method to **2.11**, but by replacing $FeCl_3$ with $NiCl_2\cdot 6H_2O$ (1 mmol, 237 mg) as the metal precursor. Green heavily twinned crystals of $(Me_4N)_4[Ni(NCS)_6]\cdot H_2O$ (**2.15**) were obtained by slowly evaporating the aqueous solution over two days. Yield: 0.582 g (84.4 %). FT-IR (**2.15**, ATR, cm^{-1}): 3012 (m), 2069 (s), 1610 (w), 1479 (s), 1412 (m), 1279 (w), 942 (s), 778 (m). Raman (**2.15**, 785 nm, %Ip: 100, cm^{-1}): 3010, 2951, 2081, 2068, 1446, 1410, 1169, 948, 784, 752, 451, 361. When leaving the crystals in a desiccator for a period of two days, they quickly changed colour from dark green to pale yellow, which indicated dehydration of the complex. Loss of crystallinity occurred upon using the latter method, thus dehydration of the complex was also achieved by recrystallizing the complex in methanol, which resulted in heavily twinned pale yellow crystals $(Me_4N)_4[Ni(NCS)_6]$ (**2.16**). FT-IR (**2.16**, ATR, cm^{-1}): 2062 (s), 1608 (w), 1471 (s), 1418 (m), 1273 (w), 949 (s), 753 (m). Raman (**2.16**, 785 nm, %Ip: 100, cm^{-1}): 2084, 2071, 1449, 1405, 1163, 943, 789, 755, 454, 363. The IR and Raman spectra for **2.15** corresponds closely to the values previously published in the literature.[125]

$(n\text{-}Bu_4N)_3[Eu(NCS)_6]$ (2.17).

Compound $(n\text{-}Bu_4N)_3[Eu(NCS)_6]$ (**2.17**) was prepared by a modification of a reported procedure.[131, 141-143] A 5 mL ethanolic solution of KSCN (3.00 mmol, 292 mg) was prepared by heating the solid in EtOH at 60 °C for 15 mins. The resulting mixture was added to an ethanolic solution (5 mL) of $EuCl_3\cdot 6H_2O$ (1.00 mmol, 366 mg), which was then stirred for 1 hour at room temperature. Then, an ethanolic solution (5 mL) of $n\text{-}Bu_4NSCN$ (3.00 mmol, 900 mg) was added to the resulting mixture, which was further

stirred for 2 hours and the precipitate of KCl was removed by filtration. The solvent was removed *in vacuo* and the crude product was dissolved in 30 mL of a 50:50 CH_2Cl_2/Et_2O solution which was then left undisturbed at -30 °C for three days, yielding pale yellow crystals of $(n\text{-}Bu_4N)_3[Eu(NCS)_6]$ (**2.17**) which were dried *in vacuo*. Yield: 0.584 g (47.6 %). FT-IR (KBr, cm^{-1}): 2960 (m), 2936 (m), 2874 (m), 2047 (s), 2037 (s), 1482 (m), 1461 (w), 1409 (w), 1378 (m), 1154 (w), 1107 (w), 1060 (w), 1026 (w), 936 (w), 881 (w), 802 (w), 739 (w). Raman (785 nm, %Ip: 50, cm^{-1}): 2935, 2873, 2083, 2054, 2042, 1939, 1459, 1447, 1323, 1151, 1132, 1055, 1033, 1003, 968, 909, 877, 821, 741, 251, 217, 143. Anal. Calcd. for $C_{54}H_{108}N_9EuS_6$: C, 52.82; H, 8.86; N, 10.26 %. Found: C, 53.12; H, 8.94; N, 10.06 %.

$(n\text{-}Bu_4N)_3[Gd(NCS)_6]$ (2.18).

Compound $(n\text{-}Bu_4N)_3[Gd(NCS)_6]$ (**2.18**) was prepared using the same method as for **2.17** but by replacing $EuCl_3 \cdot 6H_2O$ with $GdCl_3 \cdot 6H_2O$ (1.00 mmol, 371 mg). Yield: 0.580 g (47.0 %). FT-IR (KBr, cm^{-1}): 2960 (m), 2936 (m), 2874 (m), 2043 (s), 1482 (m), 1462 (w), 1415 (w), 1378 (m), 1181 (w), 1149 (w), 1106 (w), 1057 (w), 1026 (w), 964 (w), 881 (w), 802 (w), 739 (w). Raman (785 nm, %Ip: 50, cm^{-1}): 2935, 2873, 2084, 2044, 1458, 1322, 1150, 1132, 1055, 1032, 1003, 970, 909, 880, 821, 742, 253, 216, 147. Anal. Calcd. for $C_{54}H_{108}N_9GdS_6$: C, 52.59; H, 8.82; N, 10.22 %. Found: C, 52.44; H, 8.62; N, 10.29 %.

$(n\text{-}Bu_4N)_3[Dy(NCS)_6]$ (2.19).

Compound $(n\text{-}Bu_4N)_3[Dy(NCS)_6]$ (**2.19**) was prepared using the same method as for **2.17** but by replacing $EuCl_3 \cdot 6H_2O$ with $DyCl_3 \cdot 6H_2O$ (1.00 mmol, 376 mg). Yield: 0.711 g (69.8 %). FT-IR (KBr, cm^{-1}): 2960 (m), 2936 (m), 2874 (m), 2054 (s), 1483 (m), 1462 (w), 1415 (w), 1378 (m), 1149 (w), 1106 (w), 1066 (w), 1026 (w), 968 (w), 881 (w), 802 (w), 739 (w). Raman (785 nm, %Ip: 50, cm^{-1}): 2920, 2874, 2088, 2046, 1459, 1323, 1132, 1055, 965, 909, 877, 823, 257, 151. Anal. Calcd. for $C_{54}H_{108}N_9DyS_6$: C, 52.37; H, 8.79; N, 10.17 %. Found: C, 52.02; H, 8.78; N, 10.13 %.

2.9.3. **Powder X-ray Diffraction Refinement parameters**

Table 2.9 Pawley refinement parameters for $(Et_4N)_3[Cr(NCS)_6]$ (**2.5**), $(Bu_4N)_3[Cr(NCS)_6]$ (**2.7**), $(Me_4N)_4[Mn(NCS)_6]$ (**2.9**) and $(Et_4N)_3[Mn(NCS)_5]$ (**2.10**).

Compound	**2.5**	**2.7**	**2.9**	**2.10**
System	Cubic	Cubic	Monoclinic	Triclinic
Space group	Ia-3	Pa-3	$P2_1/n$	P-1
a (Å)	26.92(1)	24.44(1)	12.49(1)	9.86(1)
b (Å)	26.92(1)	24.44(1)	12.23(1)	14.53(1)
c (Å)	26.92(1)	24.44(1)	12.63(1)	15.70(1)
α (°)	90	90	90	80.34(1)
β (°)	90	90	90.30(1)	72.63(1)
γ (°)	90	90	90	81.42(1)
Rexp / Rexp ‘	0.754 / 5.964	11.398 / 23.388	0.702 / 5.574	0.501 / 1.024
Rwp / Rwp ‘	1.076 / 8.504	8.889 / 22.824	0.556 / 4.421	0.632 / 1.291
Rp / Rp ‘	0.727 / 10.738	1.2839	0.343 / 4.648	0.335 / 0.918
GoF	1.426	1.371	0.793	1.261
DW_d	0.128	1.594	0.453	0.791

Chapter 3. **Steps towards the design of homobimetallic coordination polymers using $[Pt(SCN)_4]^{2-}$ as a building block.**[2]

3.1. **Introduction**

In Chapter 2, it was established that first-row transition metal building blocks of the type $Q_x[M(NCS)_6]$ (where M is Cr(III), Fe(II), Fe(III), or Co(II)) were too labile to be used for the synthesis of coordination polymers. When mixed with compatible building blocks of the type $[M(L)_x]Cl_y$, the crystallization process resulted in crystals of species of the type $[M(L)_x(NCS)_y]$ because of ligand transfer from the thiocyanate species, $Q_x[M(NCS)_6]$, to the ligated metallate, $[M(L)_x]Cl_2$. Attempts were made at the synthesis of CPs by changing the reaction conditions, such as but not limited to using organic solvents, but the results were the same. Thus, our focus shifted towards the theoretically less labile 2nd and 3rd row late-transition metal building blocks such as $[Pt(SCN)_4]^{2-}$, $[Rh(SCN)_6]^{3-}$, and $[Pd(SCN)_4]^{2-}$.

As mentioned in Chapter 1, late-transition metal cyanometalate building blocks have been used extensively for the synthesis of coordination polymers.[162-171] In the Leznoff group, one of the building blocks of choice for the synthesis of coordination polymers has been dicyanoaurate, $[Au(CN)_2]^-$.[47-53] This building block is a linear bridging ligand that consists of two cyanides coordinated to a Au(I) metal centre. Not only does the linear geometry of this building block make it a great bridging ligand, it also has

[2] Part of the work in this chapter is reproduced with permission from M. Kobayashi, D. Savard, A. R. Geisheimer, K. Sakai and D. B. Leznoff, "Heterobimetallic Coordination Polymers Based on the $[Pt(SCN)_4]^{2-}$ and $[Pt(SeCN)_4]^{2-}$ Building Blocks", *Inorg. Chem.*, **2013**, pp. 4842-4852, Copyright **2013** The American Chemical Society. Initial synthethic work, structural analysis and optical measurements were performed by M. Kobayashi and A. R. Geisheimer as collaborative work between Prof. Sakai and Prof. Leznoff.

extremely low lability in solution. Previously, other d^8 building blocks were synthesized, such as $[Au(CN_4)]^-$ and $[AuX_2(CN)_2]^-$ (where X = Cl, Br),[54] for which vastly decreased lability was observed compared to first-row transition metal analogues, which is due to a greater Ligand Field Activation Energy for square-planar d^8 species, as established by Taube using ligand-field theory.[152]

Similarly, d^8 late-transition metal cyanometallates have also been used in the synthesis of coordination polymers.[172-192] Species such as the square-planar $[Pt(CN)_4]^{2-}$ and $[Pd(CN)_4]^{2-}$ have been demonstrated to show decreased lability and an ability to act as bridging ligands in either the *cis*- or *trans*- mode, or with all four cyanides.[162-171] Based on all these observations, it seemed rational that a d^8 thiocyanate-based analogous species could be utilized due to their decreased lability in solution and an ability to generate unique topologies based on its multiple bridging modes denoted above.

The work on the synthesis of a $[Pt(SCN)_4]^{2-}$ building block was first initiated by Masayuki Kobayashi, a student of Prof. Ken Sakai from Kyushu University in Japan. At first, the building block was synthesized using a potassium countercation, leading to the species $K_2[Pt(SCN)_4]$. This synthesis was established in the literature.[193] Crystal structure investigations revealed that this complex is also a planar d^8 species analogous to $[Pt(CN)_4]^{2-}$, and also that the thiocyanate ligand is S-bound. This was easily explained by the fact that Pt(II) is a soft metal; based on the soft/hard acid/base theory, it preferably binds to the soft end of the thiocyanate species, the sulfur atom (S), leaving the N-bound end of the thiocyanate to freely coordinate to the harder first-row transition metals. The complex also presented a coordination angle for the thiocyanate ligand which varies between complexes suggesting that more interesting geometries could be obtained when used as a bridging ligand compared to the strictly square-based coordination of the CN^- analogue due to this additional degree of freedom.

In this work, Mr. Kobayashi, under the supervision of Prof. Sakai at Kyushu University, initially synthesized several species where the bridging ligand precursor, in this case $K_2[Pt(SCN)_4]$, was mixed with first-row transition metal precursors of the type $[M(L)_x]Cl_y$ (where L = en, tmeda, 2,2'-bipy, phen, terpy, etc. and M = Fe(II), Co(II), Ni(II), Cu(II)) (see section 3.2.2). In most cases, CPs or double salts were obtained and their structure

and optical properties measured by both Mr. Kobayashi and Mr. Geisheimer, an undergraduate student in the Leznoff group. In addition, Mr. Geisheimer also did some synthetic work in order to reproduce the results obtained by Mr. Kobayashi. However, the work was only partially completed; some synthetic protocols still needed refinement in order to synthesize a pure product and to obtain crystallographic data suitable for publication. Thus, in the context of this chapter, this research set out to better explore the chemistry of the $[Pt(SCN)_4]^{2-}$ species.

In the first section of this chapter, the synthesis of CPs using a combination of $K_2[Pt(SCN)_4]$, transition metals (Mn(II), Cu(II), Ni(II) and Pb(II)) and bidentate or tridentate ligands (terpy, en, tmeda and phen) is presented which resulted in CPs of the type $[M(L)_xPt(SCN)_4]$ or in double salts and their crystal structures and their optical properties are assessed. In the second section of this chapter, the synthesis of coordination polymers using $K_2[Pt(SCN)_4]$ or KSCN as bridging ligands with the tetradentate ligands N,N'-bis(methylpyridine)ethane-1,2-diamine (bmpeda) and N,N'-bis(methylpyridine)cyclohexane-1,2-diamine (bmpchda) and the transition metals Fe(II), Pb(II) and Zn(II) is presented. This effort resulted in coordination polymers of the type $[M(L)Pt(SCN)_4]$ or $[M(L)(SCN)_2]$ and their double salt analogues. Their crystal structures and their optical properties are described.

3.2. Synthesis and structures of $[Pt(SCN)_4]^{2-}$based CPs using terpy, en, tmeda and phen ancillary ligands.

3.2.1. General approach for the synthesis of $[Pt(SCN)_4]^{2-}$ CPs.

As mentioned in Chapter 1 and 2, and in Section 3.1, the synthesis of CPs is most often performed using a standardized method. This synthetic strategy also used in Chapter 2 proved successful for the synthesis of a large number of CPs in the Leznoff group, but unfortunately, it was not the case for some of the $[Pt(SCN)_4]^{2-}$ complexes. Table 3.1 and 3.2 show the matrices used for the purpose of the work presented in this section, and it shows that this method was successful for only about half of the combinations. For the materials presented in this chapter, the syntheses had to be refined in order to produce the species of interest as a pure material and crystals suitable for SC-XRD.

3.2.2. **Previous work done by Kobayashi & synthetic matrix.**

Synthesis of $K_2[Pt(SCN)_4]$. The synthesis of $K_2[Pt(SCN)_4]$ was previously published and improved upon by Mr. Kobayashi and Dr. Sakai.[193] The synthesis consisted of preparing the sample by mixing $K_2[PtCl_4]$ with KSCN in a concentrated solution, which precipitated $K_2[Pt(SCN)_4]$ as dark red crystals in a low yield and questionable purity. Pt(II) is an expensive metal; currently, in 2017, a sample of 99% $K_2[Pt(SCN)_4]$ can cost upwards of 60$ / g. To minimize this cost, one needs to minimize the loss of product during the synthesis of the precursor metals. In order to synthesize pure product and in higher yield, the synthesis of this complex was examined using the knowledge accumulated during the work performed in Chapter 2. The used synthesis consists of first preparing the product in H_2O by mixing $K_2[PtCl_4]$ with KSCN then removing the excess H_2O by heating the solution and forcing the precipitation of the KCl by adding an excess of acetone. The product is purified by washing the precipitate with copious amounts of ethanol, dissolving it in ethyl acetate and precipitating it again using dichloromethane. This overall reworked synthesis resulted in a pure product of this simple salt in a 98% yield.

Table 3.1 Synthetic matrix for the synthesis of CPs using $[Pt(SCN)_4]^{2-}$ and the ligands terpy, en and 2,2'-bipy.

	terpy	**En**
Mn(II)	$[Mn(terpy)Pt(SCN)_4]$ (**3.1**) $[Mn(terpy)_2][Pt(SCN)_4]$ (**3.2**)	--
Co(II)	$[Co(terpy)Pt(SCN)_4]$ (**3.3**) $[Co(terpy)_2][Pt(SCN)_4]$ (**3.4**)	--
Ni(II)	--	*cis*-$[Ni(en)_2Pt(SCN)_4]$ (**3.7**)
Cu(II)	$[Cu(terpy)][Pt(SCN)_4]$	*cis*-$[Cu(en)_2Pt(SCN)_4]$ (**3.5**) *trans*-$[Cu(en)_2Pt(SCN)_4]$ (**3.6**)
	tmeda	**phen**
Ni(II)	$[Ni(tmeda)][Pt(SCN)_4]$ (**3.8**)	$[Ni(phen)_2][Pt(SCN)_4]$
Cu(II)	$[Cu(tmeda)Pt(SCN)_4]$	$[Cu(phen)_2][Pt(SCN)_4]$
Pb(II)	--	$[Pb(phen)_2Pt(SCN)_4]$ (**3.9**)

Synthesis of CPs. Initially, Mr. Kobayashi tried to synthesize CPs using $K_2[Pt(SCN)_4]$ following our standard procedure, described below. By mixing $K_2[Pt(SCN)_4]$ with an ancillary ligand-capped first-row transition metal cation, one can synthesize

heterobimetallic CPs in a systematic way using first-row transition metals ranging from Cr(III) to Zn(II). Usually, the choice of solvent consists of polar solvents, such as water, methanol, ethanol, acetone, DMF, etc. and any combination thereof allows the dissolution of the metal chloride salt and of the other precursors. Depending on the ligand, non-polar organic solvents are sometimes necessary, but we try to limit our choice to solvents such as ethyl acetate and dichloromethane, which are better suited for mixing with alcohols.

Initial work by Mr. Kobayashi consisted of using the ligands en, 2,2'-bipy, terpy, phen and tmeda and his results (along with those presented in this section) are shown in Table 3.1. With the 2,2'-bipy ligands, the double salts and tetranuclear complexes were obtained instead of the expected CPs of the type $[M(bipy)Pt(SCN)_4]$. Changing the ligand ratios in the common procedure described in Chapter 2, the choice of solvents and/or the crystallization method did not change the result of the reaction, which indicated that the ligand played a definitive role in directing the final crystal structure of the complex.

In the case of the CPs *cis*-$[Cu(en)_2Pt(SCN)_4]$ (**3.5**), *trans*-$[Cu(en)_2Pt(SCN)_4]$ (**3.6**) and *cis*-$[Ni(en)_2Pt(SCN)_4]$ (**3.7**), the synthesis was not refined and presented issues with co-crystallization of the complexes and/or the presence of unknown species in the bulk material. For the purpose of this work, the synthetic procedure had to result in crystals suitable for SC-XRD and optical analyses, so the synthesis of these complexes had to be further improved.

3.2.3. Synthesis and structure of $[Mn(terpy)Pt(SCN)_4]$ (3.1), $[Mn(terpy)_2][Pt(SCN)_4]$ (3.2), $[Co(terpy)Pt(SCN)_4]$ (3.3) and $[Co(terpy)_2][Pt(SCN)_4]$ (3.4).

As stated above, the regular method used for the synthesis of CPs did not result in suitable materials for SC-XRD and other measurements. This was especially the case for **3.1-3.4**, where the regular methodology resulted in a mixture of CPs, namely $[Mn(terpy)Pt(SCN)_4]$ (**3.1**) and $[Co(terpy)Pt(SCN)_4]$ (**3.3**), and double salts, $[Mn(terpy)_2][Pt(SCN)_4]$ (**3.2**) and $[Co(terpy)_2][Pt(SCN)_4]$ (**3.4**), in an approximate ratio of 40:60. The two sets of crystals were very similar in appearance with only a slight

difference in color and prompted an investigation to create separate synthetic methods for either of these species.

By mixing two equivalents of terpy with $MnCl_2 \cdot 4H_2O$ in H_2O, the metal precursor $[Mn(terpy)_2]Cl_2$ was synthesized *in situ*. This species was then treated by slow diffusion with $K_2[Pt(SCN)_4]$ in methanol by layering the latter over the former solution which resulted in crystals of the CP $[Mn(terpy)Pt(SCN)_4]$ (**3.1**). If the precursors were mixed quickly together, for example by adding the $K_2[Pt(SCN)_4]$ directly to the $[Mn(terpy)_2]Cl_2$ solution, $[Mn(terpy)_2][Pt(SCN)_4]$ (**3.2**) was obtained as a precipitate. In order to recrystallize **3.2**, the species were dissolved in an appropriate alcoholic solvent and stored for several days at 5-8 °C. For **3.1**, changes in the solvent mixtures or crystallization technique, such as using an H-tube or slow addition, all resulted in a precipitate of **3.2** instead. To assess the identity of the precipitate, PXRD was performed and the resulting pattern was compared to the measured structure of **3.2** (see below).

In the case of the Co(II) analogues, a similar method was established for the synthesis of the CP. However, in this case, the metal precursor ($Co(NO_3)_2 \cdot 6H_2O$) and the ligand (terpy) were mixed in MeOH and layered over an aqueous solution of $K_2[Pt(SCN)_4]$, which resulted in crystals of $[Co(terpy)Pt(SCN)_4]$ (**3.3**) and $[Co(terpy)_2][Pt(SCN)_4]$ (**3.4**) at the interface, as red plates and red blocks, respectively. The crystals were manually separated for the purpose of SC-XRD and other measurements. Attempts at changing the solvents and their ratios or the synthetic method resulted in a precipitate of **3.4** only. The structure of **3.3** was determined by SC-XRD whereas the structure of **3.4** was proposed to be analogous to **3.2** using FT-IR and Raman spectroscopies. When the precursors were directly mixed, an unknown species was produced. Due to the difficulty of separation of the crystals manually and the lack of a viable synthetic method for either complex as a pure material, elemental analyses were not performed. The structure of **3.4** could not be measured due to the fact that the red blocks were heavily twinned and no method was found to produce crystals of higher quality.

Complex **3.1** crystallizes as yellow plates from its mother liquor when stored at low temperature for several days. Structural analyses revealed that the complex crystallizes in the monoclinic space group $P2_1/n$. It consists of a single Mn(II) metal centre

coordinated to one terpy ligand and three N-bound NCS^- bridging ligands to the $[Pt(SCN)_4]^{2-}$ bridging unit (Figure 3.1). The coordination distances to the terpy ligand range between 2.221(3) and 2.248(3) Å, and the distances to the NCS- units are 2.208(3), 2.271(3) and 2.180(3) Å (Table 3.2). These values are within the expected range for N-bound ligands to a Mn(II) metal centre. For the $[Pt(SCN)_4]^{2-}$ bridging unit, three of the ligands are coordinated to adjacent Mn(II) metal centre and one ligand is dangling between the 2D sheets of the CP. In this case, none of the four SCN^- moieties are coplanar with the PtS4 plane; they present out-of-plane torsion angles ranging between 20 and 72°. This absence of coplanarity is an important steric detriment towards the formation of Pt-Pt interactions in this system (and the other systems throughout this chapter). By looking at the coordination profile of the ligand and of the Pt(II) bridging unit, one can establish a nomenclature for the purpose of comparing the supramolecular arrangement of the complexes. In this case, the ligand is tridentate and occupies three coordination sites on the metal centre, and three Pt(II) bridging units coordinate to the metal cation. Hence, we will refer to this system as a 3+3 nodal system.

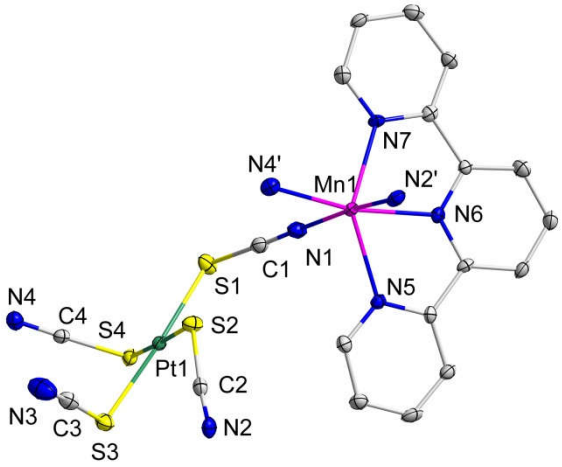

Figure 3.1 The molecular structure of $[Mn(terpy)Pt(SCN)_4]$ (**3.1**). The hydrogen atoms were removed for clarity. Color code: Purple (Mn), Green (Pt), Blue (N), Gray (C), Yellow (S).

The supramolecular structure consists of 2D sheets where three of the Mn(II) are bridged with one Pt(II) unit, and three distinct Pt(II) units are bridged to one Mn(II) metal centre (Figure 3.2). This arrangement is known for this type of system using the terpy ligand, and is called a (6,3)-type grid array.[194-195] Compared to the previously studied

structures of Mr. Kobayashi, the $[Mn(terpy)]^{2+}$ ligand and metal centre unit shows more open coordination sites and is the likely source of this preferred 2D arrangement. For example, a 4+2 nodal system (with four coordination sites occupied by the ligands and two coordination sites occupied by the bridging units), such as for *trans*-$[Cu(en)_2Pt(SCN)_4]$ (**3.6**) shown below, led to a 1D CP in the crystal structure. It is important to note that the 2D sheets of **3.1** further stack with each other through π-π interactions between the terpy ligand, leading to an overall 3D supramolecular structure.

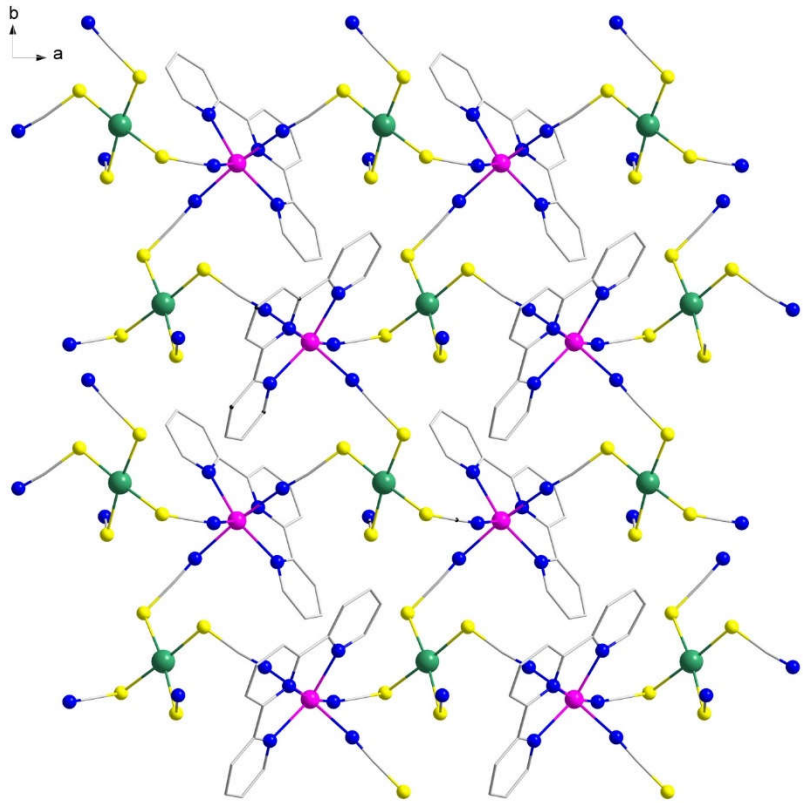

Figure 3.2 The 2-D sheet arrangement of $[Mn(terpy)Pt(SCN)_4]$ (**3.1**). The hydrogen atoms were removed for clarity. Colour code: Purple (Mn), Green (Pt), Blue (N), Gray (C), Yellow (S)

Table 3.2 Selected bond lengths (Å) and angles (°) for [Mn(terpy)Pt(SCN)$_4$] (**3.1**), [Mn(terpy)$_2$][Pt(SCN)$_4$] (**3.2**) and [Co(terpy)Pt(SCN)$_4$] (**3.3**).

3.1		**3.2**		**3.3**	
Pt1-S1	2.325(1)	Pt1-S1	2.296(2)	Pt1-S1	2.339(1)
Pt1-S2	2.311(1)	Pt1-S2	2.322(2)	Pt1-S2	2.322(1)
Pt1-S3	2.320(1)	Mn1-N3	2.239(6)	Pt1-S3	2.326(1)
Pt1-S4	2.356(1)	Mn1-N4	2.198(5)	Pt1-S4	2.317(1)
Mn1-N1	2.208(3)	Mn1-N5	2.262(5)	Co1-N1	2.330(4)
Mn1-N4’	2.180(3)	Mn1-N6	2.234(5)	Co1-N4’’	1.956(4)
Mn1-N6	2.221(3)	Mn1-N7	2.195(5)	Co1-N6	1.939(4)
Mn1-N2’	2.271(3)	Mn1-N8	2.246(5)	Co1-N3’	2.793(4)
Mn1-N5	2.247(3)	N3-Mn1-N4	73.2(2)	Co1-N5	2.037(4)
Mn1-N7	2.248(3)	N3-Mn1-N5	145.3(2)	Co1-N7	2.043(4)
S1-Pt1-S2	91.81(4)	N3-Mn1-N6	101.1(2)	S1-Pt1-S2	87.52(5)
S1-Pt1-S4	84.05(3)	N3-Mn1-N7	112.1(2)	S1-Pt1-S4	91.64(5)
S2-Pt1-S4	175.85(3)	N3-Mn1-N8	89.9(2)	S2-Pt1-S4	177.01(5)
S1-Pt1-S3	172.46(3)	N4-Mn1-N5	72.1(2)	S1-Pt1-S3	176.22(4)
S2-Pt1-S3	95.45(4)	N4-Mn1-N6	113.3(2)	S2-Pt1-S3	90.06(5)
S3-Pt1-S4	88.69(3)	N4-Mn1-N7	172.0(2)	S3-Pt1-S4	90.63(5)
N1-Mn1-N2’	169.7(1)	N4-Mn1-N8	102.6(2)	N1-Co1-N3’	173.2(1)
N1-Mn1-N5	88.3(1)	N5-Mn1-N6	91.8(2)	N1-Co1-N5	88.0(1)
N1-Mn1-N7	96.6(1)	N5-Mn1-N7	102.5(2)	N1-Co1-N7	97.4(1)
N2’-Mn1-N5	87.3(1)	N5-Mn1-N8	98.3(2)	N3’-Co1-N5	91.7(1)
N2’-Mn1-N7	92.2(1)	N6-Mn1-N7	72.5(2)	N3’-Co1-N7	85.0(1)
N4’’-Mn1-N6	169.2(1)	N6-Mn1-N8	144.5(2)	N4’’-Co1-N6	164.2(1)
N5-Mn1-N6	72.4(1)	N7-Mn1-N8	72.0(2)	N5-Co1-N6	80.2(1)
N6-Mn1-N7	72.10(1)	S1-Pt1-S2	89.07(9)	N6-Co1-N7	79.9(1)
N1-Mn1-N4’’	84.5(1)	S1-Pt1-S1’	179.995(1)	N1-Co1-N4’’	92.0(1)
N1-Mn1-N6	100.5(1)	Pt1-S1-C1	110.3(4)	N1-Co1-N6	103.6(1)
N2’-Mn1-N4’’	89.2(1)	Pt1-S2-C2	106.6(2)	N3’-Co1-N4’’	81.2(1)
N2’-Mn1-N6	87.0(1)			N3’-Co1-N6	82.9(1)
N4’’-Mn1-N5	117.4(1)			N4’’-Co1-N5	100.2(2)
N4’’-Mn1-N7	97.9(1)			N4’’-Co1-N7	98.6(2)
N5-Mn1-N7	144.5(1)			N5-Co1-N7	160.2(2)

Complex **3.2** is a double salt crystallizing in the monoclinic space group P2$_1$/c comprised of one unit of [Pt(SCN)$_4$]$^{2-}$ that is a counteranion to [Mn(terpy)$_2$]$^{2+}$ (Figure 3.3). The

coordination distances of the terpy ligands to the Mn(II) varies between 2.198(2) and 2.262(5) Å, which is within the expected range for a Mn(II) metal centre. For the $[Pt(SCN)_4]^{2-}$, the coordination distances range between 2.313(2) and 2.318(2) Å and the coordination angles are between 69.8(1) and 70.8(1)°. Despite the fact that the $[Pt(SCN)_4]^{2-}$ is not coordinated to any other metal centre, the system is not fully planar. In fact, all four of the NCS^- present out-of-plane angles, with two of them showing angles of 1.5(1)° and the other two showing angles of 24.5(1)°. The steric interactions between the ligand and the $[Pt(SCN)_4]^{2-}$ might be the source of this disparity.

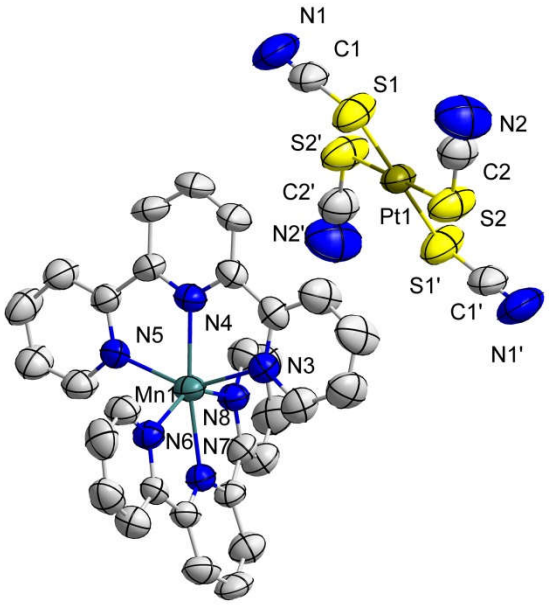

Figure 3.3 The molecular structure of $[Mn(terpy)_2][Pt(SCN)_4]$ (**3.2**). The hydrogen atoms were removed for clarity. Colour code: Purple (Mn), Green (Pt), Blue (N), Gray (C), Yellow (S).

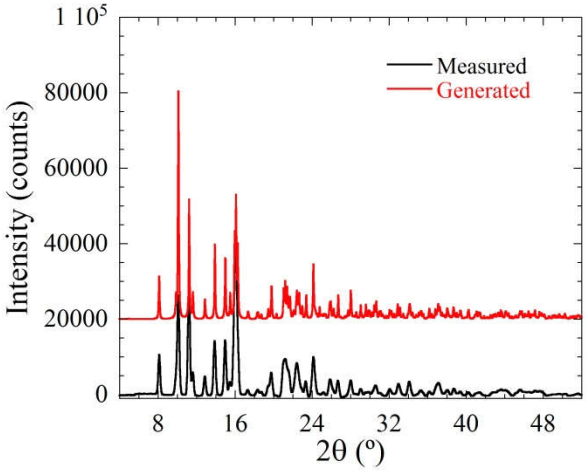

Figure 3.4 Comparison of the measured powder pattern of the precipitate of $[Mn(terpy)_2][Pt(SCN)_4]$ (**3.2**, black) and the powder pattern generated from its crystal structure (red). The differences in intensity are attributed to preferred orientation.

Complex **3.3** is very similar to **3.1**; it crystallizes as red plates using a similar synthetic method. However, the system crystallizes in the different orthorhombic space group P n a 2_1. As for **3.1**, the system consists of a single Co(II) coordinated to one terpy ligand and three NCS^- N-bound bridging ligands from the adjacent $[Pt(SCN)_4]^{2-}$ units (Figure

3.5). On their end, the $[Pt(SCN)_4]^{2-}$ units are coordinated to three distinct Co(II) metal centres, leading to a 3+3 nodal system. The coordination distances of the Co(II) metal centre to the terpy ligand are between 1.939(4) and 2.043(4) Å and the distances to the N-bound bridging ligands range between 1.956(4) and 2.793(4) Å. The elongated coordinated distance of N3 to the Co(II) metal centre (N3-Co1 = 2.793(4) Å) could be due to the trans effect (SCN^- *vs.* terpy). For the $[Pt(SCN)_4]^{2-}$, the coordination distances are varying between 2.317(1) and 2.339(1) Å and the angles are between 71.6 and 82.5 °.

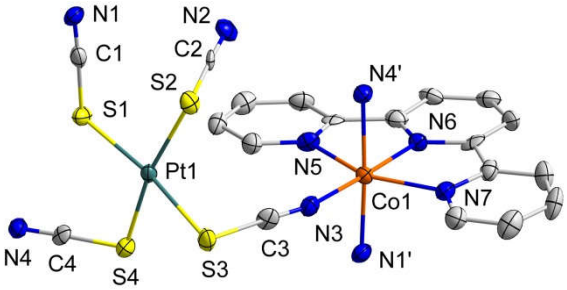

Figure 3.5 The molecular structure of $[Co(terpy)Pt(SCN)_4]$ (**3.3**). The hydrogen atoms were removed for clarity. Colour code: Orange (Co), Green (Pt), Blue (N), Gray (C), Yellow (S).

The supramolecular structure of **3.3** consists of 2D sheets of the 3+3 nodal system CP and π-π interactions between the terpy ligands which makes it an overall 3D supramolecular structure (Figure 3.6). One notable difference for **3.3** is that, in the packing arrangement, the type of (6, 3) grid observed is different to that of **3.1**. The only difference between the overall structure of **3.1** and **3.3** is the orientation of the dangling NCS^- ligand on the $[Pt(SCN)_4]^{2-}$ unit. In **3.1**, the dangling unit is between the terpy ligands, whereas in **3.3**, it is located on the opposite side of the terpy ligands (or one could say on the opposite sides of the 2D sheet formed by the planar arrangement of Pt(II) and M(II) metal centres).

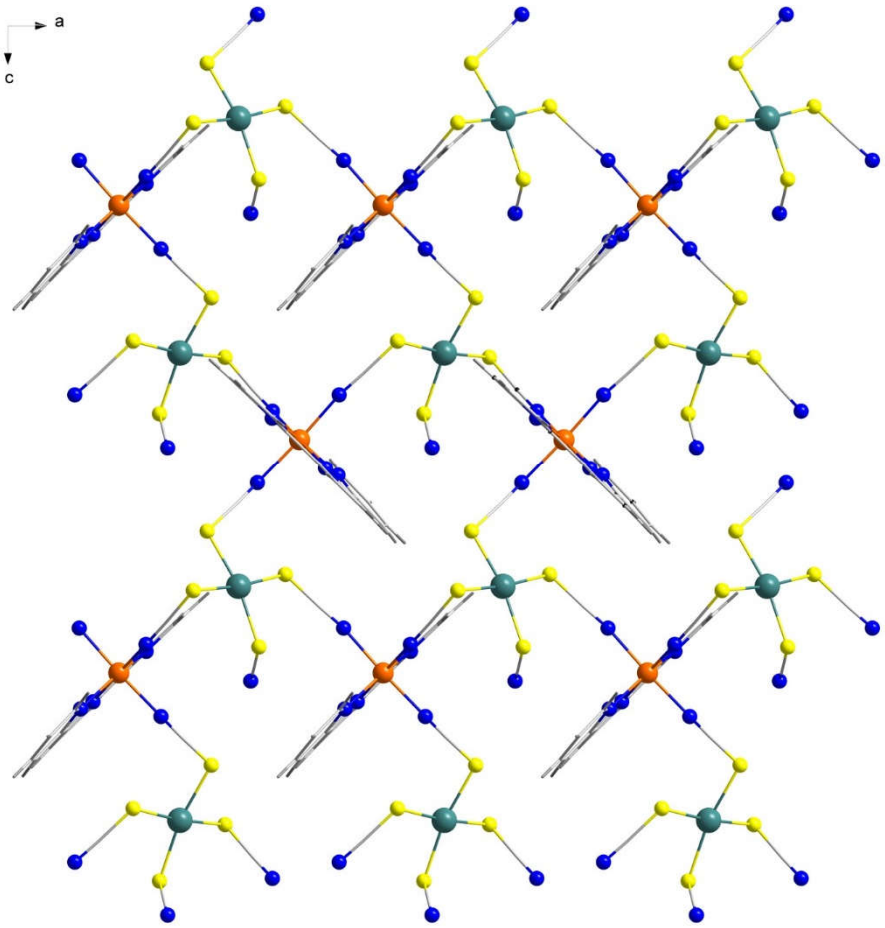

Figure 3.6 The 2-D sheet arrangement of $[Co(terpy)Pt(SCN)_4]$ (**3.3**). Colour code: Orange (Co), Green (Pt), Blue (N), Gray (C), Yellow (S)

For **3.4**, the system was suggested to be isostructural to **3.2** using Raman and FT-IR spectroscopies, but the crystal structure was not collected because **3.4** could not be properly isolated manually and showed heavy twinning of the crystals. In the case of PXRD measurements, the complex presented a very weak diffraction pattern that could not be confidently compared to that of **3.2**.

3.2.4. Synthesis and structure of $[Cu(en)_2Pt(SCN)_4]$ (cis: 3.5; trans: 3.6) and $Ni(en)_2Pt(SCN)_4]$ (3.7).

Using the protocol described above, the mixing of $Cu(ClO_4)_2 \cdot 6H_2O$ or $NiCl_2 \cdot 6H_2O$, en, and $K_2[Pt(SCN)_4]$ in appropriate solvents led to an unknown species that could not be identified. To synthesize **3.5**, to a solution of $[Cu(en)_2](ClO_4)_2$, which was prepared *in situ*

resulting in a dark purple colour, was added dropwise $K_2[Pt(SCN)_4]$ in MeOH:H_2O, resulting in precipitation of *cis*-$[Cu(en)_2Pt(SCN)_4]$ (**3.5**). Initially, to crystallize **3.5**, the two precursor solutions were slowly diffused through a filter paper set in a petri dish, where the two solutions are added on either side of the filter paper. This resulted in a mixture of **3.5** and *trans*-$[Cu(en)_2Pt(SCN)_4]$ (**3.6**) as brown plates and purple plates, respectively. There were identified as being two polymorphs of the complex $[Cu(en)_2Pt(SCN)_4]$ by structural analyses (see below). Layering of the two solutions also resulted in a mixture of **3.5** and **3.6**. Using either method, the crystals of **3.6** were manually separated in order to evaluate their structure and optical properties. The complex *cis*-$[Ni(en)_2Pt(SCN)_4]$ (**3.7**) was synthesized using the same layering method and solvents, which resulted exclusively in crystals of the *cis*- complex **3.7** instead of a mixture of the *cis*- and *trans*-analogues. For **3.7**, using alternative solvents and crystallization methods resulted in unknown complexes which could not be identified. For **3.5** and **3.6**, it resulted in a polycrystalline mixture of the two species.

For the brown plates of the complex *cis*-$[Cu(en)_2Pt(SCN)_4]$ (**3.5**), structural analysis revealed that the system crystallizes in the monoclinic space group P $2_1/n$. It consists of one Cu(II) metal coordinated to two en ligands and two N-bound NCS^- bridging units from adjacent $[Pt(SCN)_4]^{2-}$ in an octahedral geometry. The two NCS^- coordinate on the Cu axial positions (Figure 3.7). For the $[Pt(SCN)_4]^{2-}$ unit, the bridging ligands to adjacent Cu(II) metal centres are in the *cis*- position, hence the *cis*- prefix for **3.5**, whereas for **3.6**, they are in the *trans*- position (see below). The coordination distances of the Cu(II) to the en ligands are of 2.007(3) and 2.022(3) Å and the distances to the N-bound NCS^- are of 2.444(3) and 2.448(3) Å. These values are within the expected range for Cu(II) with N-bound ligands. The elongated coordination of the NCS^- ligands at the axial positions on the Cu(II) metal centres suggest the presence of a Jahn-Teller effect.[68] For the $[Pt(SCN)_4]^{2-}$, the unit is coordinated to two adjacent Cu(II) metal centres in a *cis* fashion, where the two adjacent NCS^- ligands are coordinated and the two other are dangling ligands which results in a 1D CP. The coordination distances of the NCS^- to the Pt(II) metal centre are ranging between 2.299(1) and 2.338(1) Å, and the angles are between 70.2(1) and 76.8(1)°. In this case, using the aforementioned nomenclature, the 1D CP consists of a 4+2 nodal system coordinated in a zig-zag fashion. As for the terpy systems, the $[Pt(SCN)_4]^{2-}$ units are not planar, with out-of-plane angles varying greatly

between 31.9(1) and 80.1(1)°; the two dangling ligands present the largest out-of-plane angles. In the supramolecular structure, **3.5** does not present any interactions other than the steric interactions between the dangling ligands of the $[Pt(SCN)_4]^{2-}$ units (Figure 3.8).

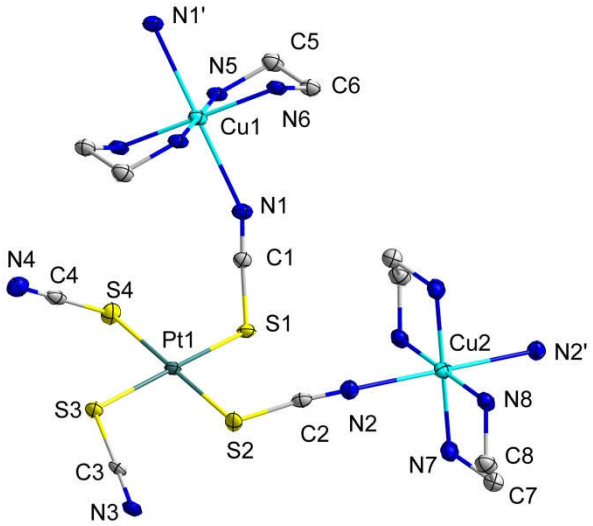

Figure 3.7 The molecular structure of *cis*-$[Cu(en)_2Pt(SCN)_4]$ (**3.5**). The hydrogen atoms were removed for clarity. Colour code: Light blue (Cu), Green (Pt), Blue (N), Gray (C), Yellow (S).

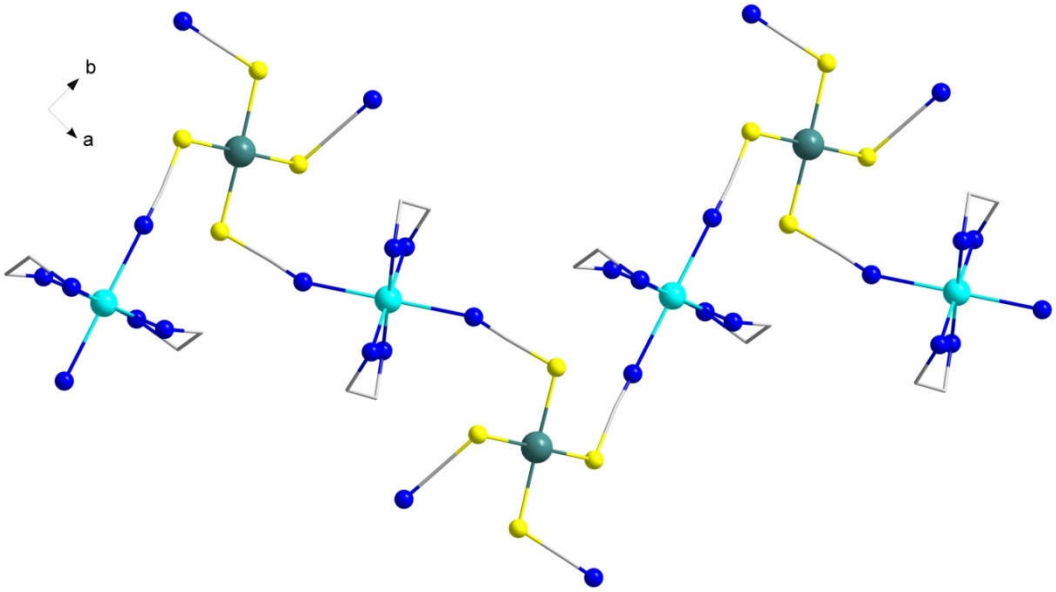

Figure 3.8 The 1-D zig-zag chain arrangement of *cis*-$[Cu(en)_2Pt(SCN)_4]$ (**3.5**). The hydrogen atoms were removed for clarity. Colour code: Light blue (Cu), Green (Pt), Blue (N), Gray (C), Yellow (S)

As mentioned above, **3.6** is a polymorph of **3.5**. It crystallizes as purple plates in the triclinic space group P-1 and consists of a Cu(II) metal centre coordinated to two en ligands and two NCS^- N-bound bridging ligands (Figure 3.9). However, in this case, the $[Pt(SCN)_4]^{2-}$ bridges two Cu(II) units in a *trans-* fashion instead *cis-*, meaning that the two

opposite NCS^- ligands are bound to the adjacent Cu(II) metal centre. The coordination distances and angles for both the Cu(II) and Pt(II) metal centre are similar to **3.5** (see Table 3.3). Due to this trans- coordination, instead of a zig-zag chain, a linear 1D CP is obtained and its nodal arrangement is 4+2, like for **3.5**. In the packing arrangement, the dangling ligands on the $[Pt(SCN)_4]^{2-}$ units are located on either side of the 1D chain, and just like for **3.5**, they dictate the supramolecular arrangement of the structure via steric interactions (Figure 3.10).

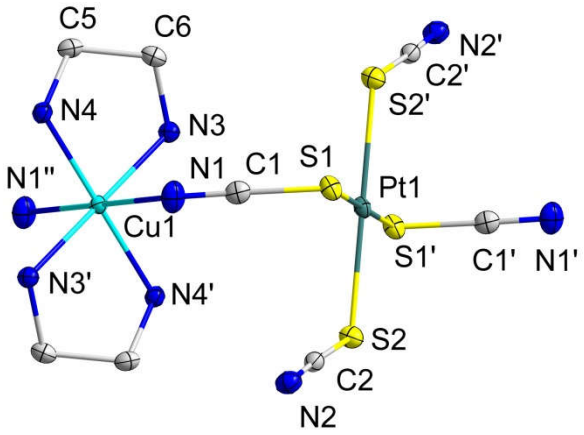

Figure 3.9 The molecular structure of trans-$[Cu(en)_2Pt(SCN)_4]$ (**3.6**). The hydrogen atoms were removed for clarity. Colour code: Light blue (Cu), Green (Pt), Blue (N), Gray (C), Yellow (S).

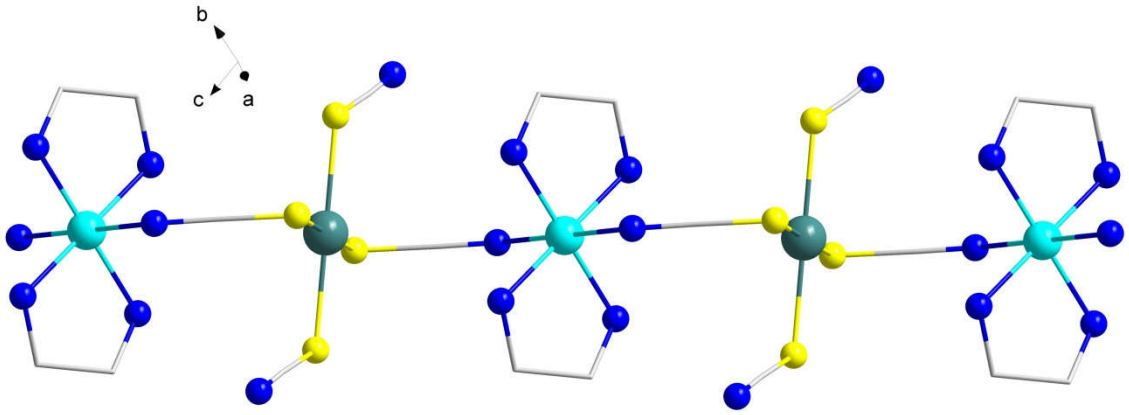

Figure 3.10 The 1-D linear chain arrangement of *trans*-$[Cu(en)_2Pt(SCN)_4]$ (**3.6**). The hydrogen atoms were removed for clarity. Colour code: Light blue (Cu), Green (Pt), Blue (N), Gray (C), Yellow (S).

Complex **3.7** is isostructural to **3.5**, with slightly longer coordination distances due to the presence of a Ni(II) atom instead of Cu(II) (Figure 3.11). Overall, the 1D CP presents the same features as for **3.5**, both in the CP itself and in the supramolecular arrangement.

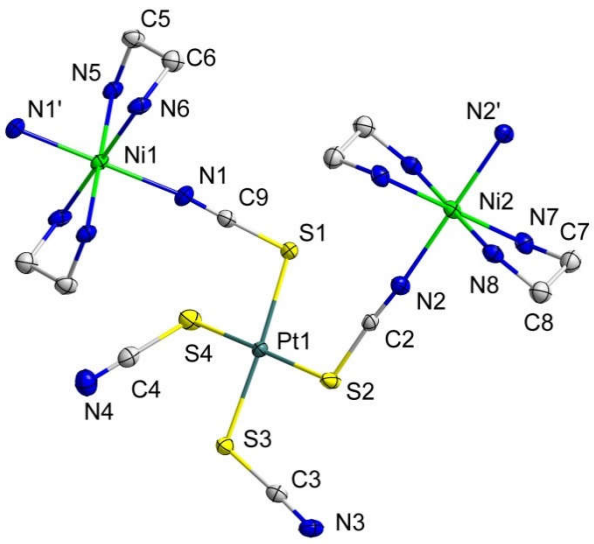

Figure 3.11 The molecular structure of *cis*-[Ni(en)$_2$Pt(SCN)$_4$] (**3.7**). The hydrogen atoms were removed for clarity. Colour code: Light green (Ni), Green (Pt), Blue (N), Gray (C), Yellow (S)

Table 3.3 Selected bond lengths (Å) and angles (°) for *cis*-[Cu(en)$_2$Pt(SCN)$_4$] (**3.5**), *trans*-[Cu(en)$_2$Pt(SCN)$_4$] (**3.6**) and *cis*-[Ni(en)$_2$Pt(SCN)$_4$] (**3.7**).

	3.5	**3.6**	**3.7**	
Pt1-S1	2.322(1)	2.321(1)	Pt1-S1	2.3374(5)
Pt1-S2	2.300(1)	2.313(1)	Pt1-S2	2.3275(5)
Pt1-S3	2.331(1)	2.328(1)	Ni1-N1	2.504(2)
Pt1-S4	2.338(1)	2.336(1)	Ni1-N4	2.019(2)
M1-N1	2.444(3)	2.109(3)	Ni1-N3	2.014(2)
M1-N5	2.007(3)	2.084(3)	S1-Pt1-S2	95.73(2)
M1-N6	2.022(3)	2.091(3)	N3-Ni1-N4	84.94(6)
M2-N2	2.448(3)	2.125(3)	C1-S1-Pt1	98.13(6)
M2-N7	2.028(3)	2.101(3)	C2-S2-Pt1	108.45(6)
M2-N8	2.028(3)	2.125(3)	Ni1' -N1-C1	124.9(1)
S1-Pt1-S2	93.68(4)	94.64(3)	C3-N3-Ni1	108.4(1)
S1-Pt1-S4	86.38(4)	86.19(4)	C4-N4-Ni1	108.1(1)
S2-Pt1-S4	179.61(4)	177.95(4)		
S1-Pt1-S3	173.04(3)	174.27(3)		
S2-Pt1-S3	90.28(3)	90.88(3)		
S3-Pt1-S4	89.70(4)	88.24(4)		
N1-M1-N5	88.0(1)	90.6(1)		
N5-M1-N6	95.2(1)	91.2(1)		
N2-M2-N8	87.7(1)	91.2(1)		
N1-M1-N6	87.0(1)	96.9(1)		
N2-M2-N7	87.6(1)	88.2(1)		
N7-M2-N8	84.1(1)	97.1(1)		

3.2.5. Structure of [Ni(tmeda)Pt(SCN)$_4$] (3.8)

Complex **3.8** is similar to [Cu(tmeda)Pt(SCN)$_4$] (**Cu-3.8**) based on PXRD measurements. **Cu-3.8**, synthesized by Mr. Masayuki Kobayashi, consists of one Cu(II) metal centre coordinated to one tmeda ligand and three N-bound NCS^- units (Figure 3.12). The Cu(II) metal centre presents a distorted trigonal bipyramidal geometry, and the resulting structure is a 2D "wavy sheet" type of CP with a 2+3 nodal system. The nickel analogue of the complex could not be crystallized using standard methods, and as such, the similarity between the complexes was established by PXRD (Figure 3.13). The unit cell of **3.8** could not be refined to satisfactory values using standard refinement methods.

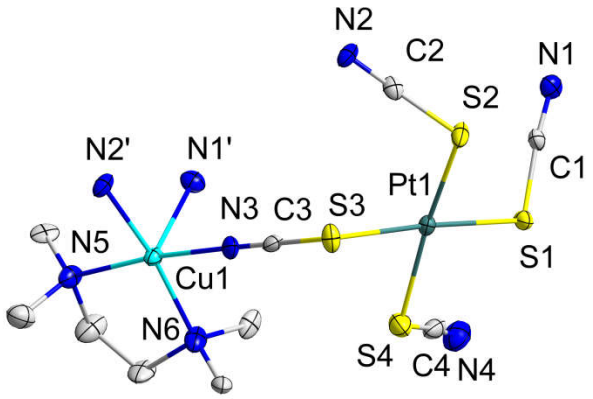

Figure 3.12 The molecular structure of [Cu(tmeda)Pt(SCN)$_4$] (**Cu-3.8**) as synthesized by Masayuki Kobayashi. The hydrogen atoms were removed for clarity. Color code: Light blue (Cu), Green (Pt), Blue (N), Gray (C), Yellow (S).

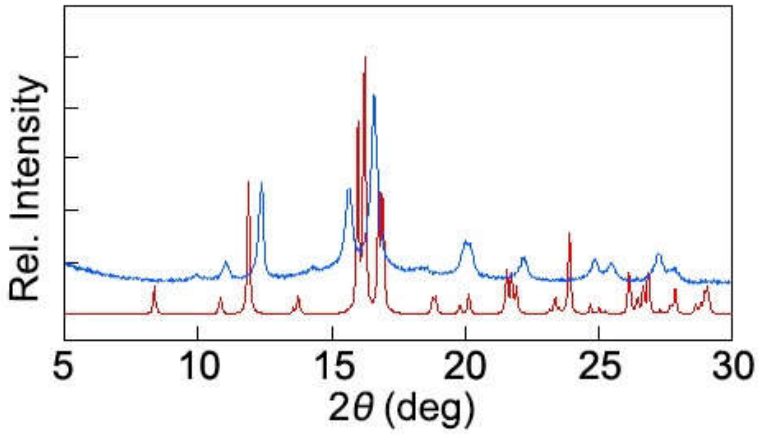

Figure 3.13 The PXRD spectrum of [Ni(tmeda)Pt(SCN)$_4$] (**3.8**, blue) compared to the spectrum of [Cu(tmeda)Pt(SCN)$_4$] (Cu-**3.8**, red) generated from its crystal structure.

3.2.6. Structure of [Pb(phen)$_2$Pt(SCN)$_4$] (3.9)

Complex **3.9** crystallized as orange plates in the monoclinic space group C2/c. Structural analyses revealed that the complex is an eight coordinate square antiprismatic lead(II) metal centre coordinated to two phen ligands and four thiocyanate ligands from [Pt(SCN)$_4$]$^{2-}$ units (Figure 3.14). Each of the thiocyanate ligands coordinated to the Pt(II) metal centre in turn coordinate to four different Pb(II) metal centres. The coordination distances of the terpy ligands to the Pb(II) metal centre range between 2.577(6) Å and 2.605(7) Å and the coordination distances to the axial thiocyanate ligands are 2.811(6) Å (Table 3.4). These coordination distances are close to the expected values for the

coordination of N-based ligands to a Pb(II) metal centre. The coordination distances of the thiocyanate ligands to the Pt(II) metal centre range between of 2.324(2) and 2.326(2) Å and the coordination angles range between 83.37(8) and 96.63(8)°. The coordination of the Pt(II) bridging unit to four other Pb(II) metal centre results in a 3D CP. This structure consists of a 4+4 nodal system (Figure 3.15). Furthermore, the ligands units in the polymer further interact with adjacent units via a π-π interaction (3.08(1) Å).

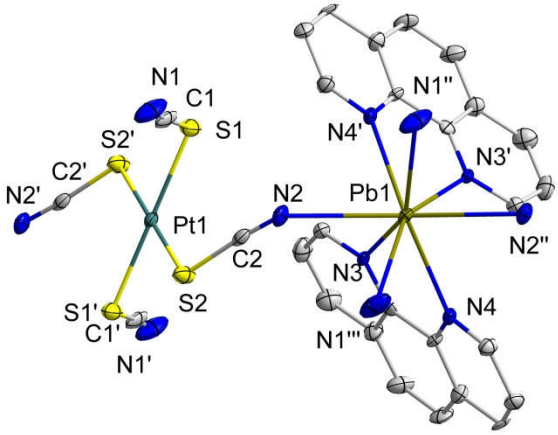

Figure 3.14 The molecular structure of $[Pb(phen)_2Pt(SCN)_4]$ (**3.9**). The hydrogen atoms were removed for clarity. Color code: Dark yellow (Pb), Green (Pt), Blue (N), Gray (C), Yellow (S).

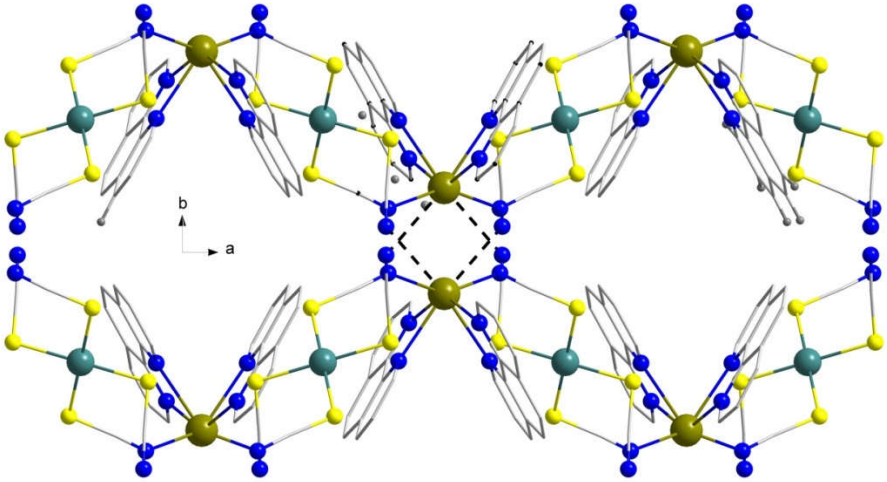

Figure 3.15 The 3-D supramolecular arrangement of $[Pb(phen)_2Pt(SCN)_4]$ (**3.9**) viewed down the α-axis (top) and down the c-axis (bottom). The hydrogen atoms have been omitted for clarity. Interchain coordination is depicted as black dashed lines. Color code: Dark yellow (Pb), Green (Pt), Blue (N), Gray (C), Yellow (S)

Table 3.4 Selected bond lengths (Å) and angles (°) for $[Pb(phen)_2Pt(SCN)_4]$ (**3.9**).

Pb1-N1'	2.996(8)	N1'-Pb1-N2	89.1(2)
Pb1-N3	2.608(6)	N1'-Pb1-N4	142.8(2)
Pb1-N2	2.811(6)	N2-Pb1-N4	114.5(2)
Pb1-N4	2.575(6)	N1'-Pb1-N3	153.4(2)
Pt1-S1	2.326(2)	N2-Pb1-N3	75.7(2)
Pt1-S2	2.325(2)	N3-Pb1-N4	63.6(2)
		S1-Pt1-S2	96.63(8)

3.2.7. Discussion

By analyzing the series of $[Pt(SCN)_4]^{2-}$ complexes presented herein, one can establish trends regarding the effects of the various elements on the supramolecular arrangement favored in these types of CPs, specifically (a) the choice of transition metal, (b) the choice of ligand and (c) the bridging unit $[Pt(SCN)_4]^{2-}$.

Influence of the transition metal ion/ancillary ligand combination. First-row transition metals usually present between four and six coordination sites. In most of the work, bidentate or tridentate ligands were chosen and allowed to react in a 1:1 ratio with

the first-row transition metal centre in order to promote the coordination of the ligands to some of the coordination sites, but not all of them. In the case of the 2,2'-bipy and phen ligands, the hardness of the ligand promoted the formation of double salts when combined with the first-row transition metals. Only when phen was combined with Pb(II) was a CP obtained, which was most likely due to the increased number of coordination sites on the metal centre. Increasing the number of coordination sites available on the metal centre played a definitive role in the formation of that CP. When softer ligands were used (i.e., en and tmeda), CPs were synthesized successfully, which was likely due to the fact that these ligands present hardness similar to that of N-bound thiocyanates, which would promote a mixed coordination between the ligands (isothiocyanate and the ancillary ligand) at a single metal centre.

We can theorize that the capping ligand plays a definitive role in directing the resulting supramolecular arrangement of the system. In the literature, and in the work presented, the capping ligand is usually the determining factor that directs the resulting CP architecture. It controls not only the number of available coordination sites on the transition metal centre, but also the availability of intermolecular interaction sites. In this work, the en ligand capped four of the six coordination sites, which led to the synthesis of 1D coordination polymers as a 4+2 nodal system, whereas the terpy ligand capped three of the coordination sites and resulted in the 2D 3+3 nodal system. For the tmeda ligand, the combination resulted in a 2D CP with a 2+3 nodal system. By comparing those structures, one can say that the highest amount of remaining open coordination sites (second number) favours an increased dimensionality in the supramolecular arrangement of the polymers.

Influence of the coordination of $[Pt(SCN)_4]^{2-}$. The $[Pt(SCN)_4]^{2-}$ building block can coordinate up to four different metal cations via the SCN- bridging moieties. By analyzing the structures, clearly, a larger number of metal centres bridged by the $[Pt(SCN)_4]^{2-}$ unit resulted in a greater dimensionality of the CP overall. However, control over the number and geometry of the bridging SCN^- units was not achievable by changing the synthetic conditions. It is important to note that, as opposed to the $[Pt(CN)_4]^{2-}$analogue, this bridging unit is not strictly planar. Further degrees of freedom in the structure were observed, which did not result in strictly planar structures, as opposed to those usually

observed with cyanide analogues. In the systems presented herein, the Pt-S-C-N torsion varied greatly depending on multiple factors: 1) the number of metal cations to which the $[Pt(SCN)_4]^{2-}$ building block is connected, 2) the steric hindrance, and 3) the presence of hydrogen-bonding interactions between the ancillary capping ligands on the metal cation and the dangling SCN^- species (as seen for complex **4.5**). With judicious choice of ancillary ligand (such as one with a pseudohalide group), one could control the presence of strong intermolecular interaction and thus further increase the dimensionality since the SCN^- unit is prone to hydrogen bonding. It is noteworthy to mention that despite the initial hypothesis, no metal-metal bonding or axial interactions were observed in the structures, as opposed to what is often observed in $[Au(CN)_2]^-$ and $[Pt(CN)_4]^{2-}$. This is most likely due to the presence of the torsion angle on the $[Pt(SCN)_4]^{2-}$ unit, which causes steric blockage around the Pt(II) metal centre.

Overall, the work presented in this section indicated that a systematic study using a range of ligands and metal precursors in combination with $[Pt(SCN)_4]^{2-}$ can be used to establish a trend between the choice of ligands and metals and the resulting dimensionality when synthesizing CPs. This was already observed in the Leznoff group when synthesizing CPs using $[Au(CN)_2]^-$, but in this case the work was performed using a tetradentate thiocyanometallate that can form hydrogen bonds, instead of a strictly linear one like previously, thus adding two degrees of freedom in the overall synthesis of CPs (*cis*- vs. *trans*- coordination, and supramolecular hydrogen bonds).

3.3. Synthesis and properties of CPs prepared using a combination of the bmpeda and bmpchda ligands, and of the $[Pt(SCN)_4]^{2-}$ and SCN^- building blocks.

In addition to the traditionally used capping ligands, the synthesis of CPs using $[Pt(SCN)_4]^{2-}$ in combination with tetradentate ligands was also targeted. There are few coordination polymers synthesized in the Leznoff group using an ancillary tetradentate ligand because most of the work has been focused towards the synthesis of CPs using readily available bi- and tridentate ligands (such as en, tmeda, phen, 2,2'-bipy, terpy, etc.).[47-53] There are many hypothetical advantages to using a planar tetradentate ligand such as a planar geometry with a strong π system which limits their degrees of freedom

when it comes to coordinating to a first-row transition metal species. It not only does limit how many ligands can be coordinated to the metal centre, but also makes the species more inclined towards the coordination of species at the axial positions in an octahedral geometry.

An example of a candidate tetradentate ligand is salen (*N*,*N*′-ethylenebis(salicylimine)) and its derivatives.[196] Unfortunately, the salen ligand is often not suitable for the synthesis of coordination polymers due to the presence of the two alcohol functional groups, which leads most often to the dianionic species salen^{2-} in solution resulting in the neutral [M(salen)] when coordinated to first-row transition metals with an oxidation state of 2. The fact that this resulting species is neutral is limiting in the synthesis of coordination polymers and thus is often overlooked in the context of CP synthesis.

However, if the tetradentate ligand is neutral, it could be used for the synthesis of coordination polymers in a similar fashion to bidentate and tridentate ligands previously used in the Leznoff group, generating species of the type ML^{2+}. Thus, the species N,N'-bis(methylpyridine)ethane-1,2-diamine (bmpeda) and N,N'-bis(methylpyridine)cyclohexane-1,2-diamine (bmpchda) were prepared and their chemistry in combination with SCN^- and $[Pt(SCN)_4]^{2-}$ assessed.

3.3.1. **Synthesis of bmpeda and bmpchda**

As mentioned in the introduction, bmpeda and bmpchda are known ligands which have been published before. The synthesis of these products was conducted by modifying the previously published synthesis by Q. T. Nguyen and J. H. Jeong.[198] To synthesize the material, ethylene diamine is first added to a dry solution of dichloromethane with an excess amount of anhydrous solid magnesium sulfate. Then, 2-pyridinecarboxylaldehyde is added dropwise to the solution and it is stirred for 2 hours. The magnesium sulfate is then filtered off, the dichloromethane removed *in vacuo* and the resulting brown oil of bmpeda or bmpchda is dissolved in a small amount of ethyl acetate and layered with petroleum ether, then left at -30 °C for a few days which results in needles of bmpeda or bmpchda. It is noteworthy to mention that this synthesis is highly water sensitive. As such, one must take precautions during the work to avoid the

hydrolysis of the resulting product and to maximize its yield. From our observations, when another drying agent is used instead of magnesium sulfate, such as molecular sieves or calcium sulfate, there is a greater presence of impurities in the final product and crystallization is much more difficult. Changing the reaction solvent to another non-polar organic solvent did not change the overall outcome significantly. Dichloromethane was thus simply chosen for its availability and ease of drying. Recrystallization of the final product can also be performed by simply dissolving the product in a minimal amount of ethyl acetate and storing at low temperature. However, this resulted in a crystalline mass that was much harder to wash after the product was isolated. The petroleum ether was mostly used to allow the crystal growth to result in well-defined crystals instead of a single crystalline mass.

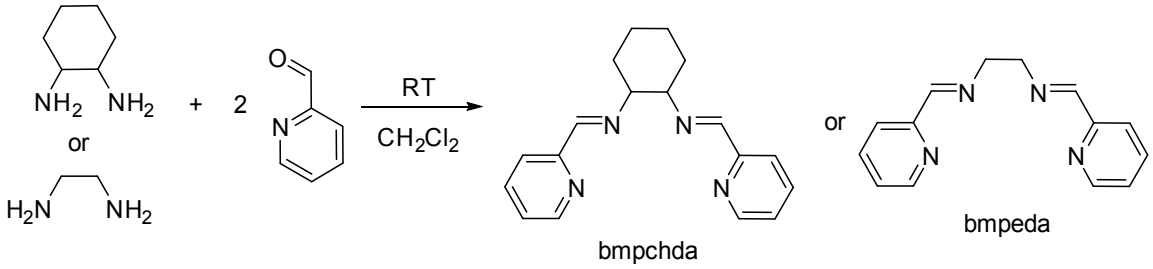

Equation 3.1 The preparation of N,N'-bis(methylpyridine)cyclohexane-1,2-diamine (bmpchda) and N,N'-bis(methylpyridine)ethane-1,2-diamine (bmpeda).

3.3.2. Synthesis of novel complexes using bmpeda and bmpchda

The general synthetic work for the preparation of the complexes shown below consisted mostly of using the well-established techniques mentioned in Chapter 2 and in Section 3.2. Minimal changes were made to the protocol for the synthesis of the compounds presented below besides changes in the choice of solvents and ratios of the precursors. In most cases, a combination of alcohols, in which the ligand is soluble, and water, in which the precursor metals are soluble, were used. It is noteworthy to mention that as opposed to the ligands regularly used for the synthesis of CPs, such as 2,2'-bipy, en, tmeda, etc., bmpeda and bmpchda are less polar, and thus require a different combination of solvents in order for the synthesis and crystallization to be successful. Since the ligand is also prone to hydrolysis in the presence of water when coordinated to a metal centre, the solutions could not be heated above room temperature under the presence of an alcohol or water in the mother liquor.

Most of the work to target CPs with these ligands was done by Ian Johnston, an undergraduate student in the Leznoff group, for his summer research project (supervised by D. Savard). In the case where the ligands (bmpeda or bmpchda) were combined with first-row transition metals, such as Fe(II), Fe(III), Mn(II), Co(II), Ni(II), etc., CPs could not be crystallized and analyzed. In most cases, the resulting products precipitated quickly as a polycrystalline material. Changing the method of mixing and crystallization (direct mixing, layering, H-tube, slow diffusion through a media), the solvents and their ratios (H_2O, MeOH, EtOH, DMF and EtOAc), or the reaction conditions did not have an effect on the outcome. Some of these reactions, when increasing the amount of H_2O in the reaction mixture, led to decomposition of the ligand via hydrolysis, thus limiting the choice of solvents that could be used at the time. However, as seen below, using Pb(II) as a metal of choice resulted in the crystallization of many complexes when combined with either SCN^- or with $[Pt(SCN)_4]^{2-}$.

3.3.3. **[Pb(bmpeda)(SCN)$_2$] (3.10) and [Pb(bmpchda)(SCN)$_2$] (3.11)**

Complexes [Pb(bmpeda)$(SCN)_2$] (**3.10**) and [Pb(bmpchda)$(SCN)_2$] (**3.11**) were synthesized as yellow plates that crystallize in the triclinic space group P-1. The structures were isostructural with only a small difference in the unit cell size, which can be attributed to the presence of the extra cyclohexane in bmpchda (Figure 3.16 and 3.17). The complex consists of an eight coordinate distorted square antiprismatic Pb(II) metal centre coordinated to one tetradentate ligand, two N-bound isothiocyanate ligands and two S-bound thiocyanates from adjacent units. Overall, the structure is very similar to those set out in Chapter 5. The coordination distances of the ligands are depicted in Table 3.5 and are within the expected ranges for N-bound and S-bound ligands to a Pb(II) metal centre. The supramolecular structure consists of a 1D coordination polymer for which the thiocyanate units are bound in a 1,3 pattern (Figure 3.18). However, for both **3.10** and **3.11**, there is no evidence of interactions between the ligands as the ligands are aligned side by side in the supramolecular structure (where the closest point between the ligands is the ethylene or cyclohexane moieties), instead of one over the other, nor is there evidence of significant birefringence in the system after analysis of the crystals under a polarized light microscope.

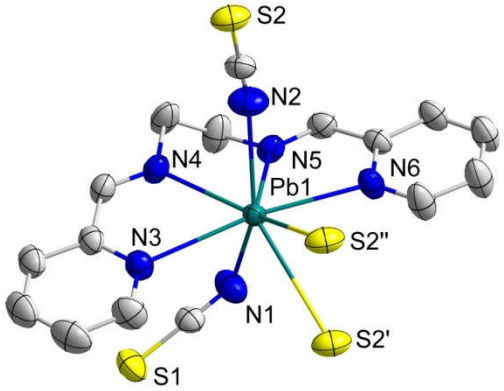

Figure 3.16 The structure of [Pb(bmpeda)$(SCN)_2$] (**3.10**). The hydrogen atoms were removed for clarity. Colour code: Green (Pb), Blue (N), Gray (C), Yellow (S).

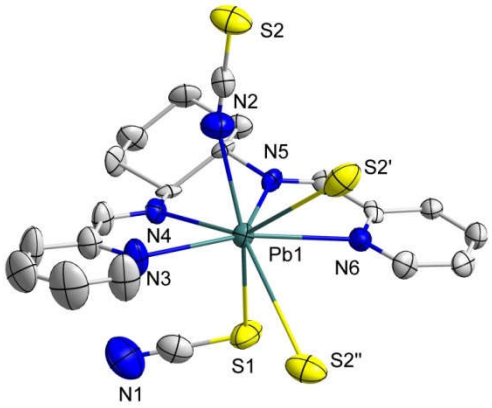

Figure 3.17 The structure of [Pb(bmpchda)$(SCN)_2$] (**3.11**). The hydrogen atoms were removed for clarity. Colour code: Green (Pb), Blue (N), Gray (C), Yellow (S).

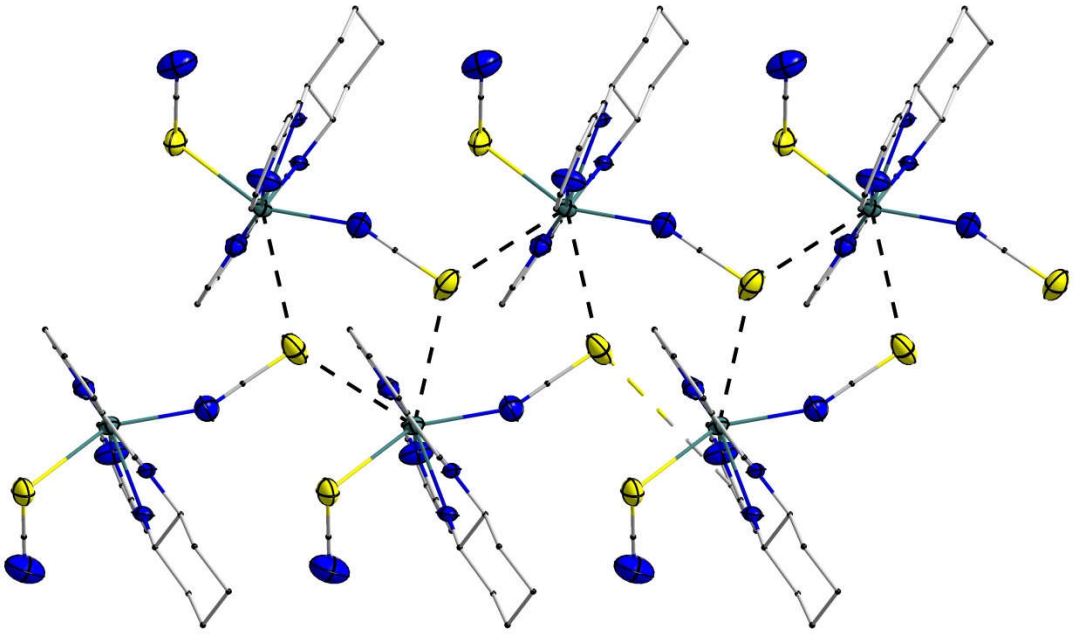

Figure 3.18 The 1-D linear chain arrangement of [Pb(bmpchda)$(SCN)_2$] (**3.11**). The hydrogen atoms were removed for clarity. Colour code: Green (Pb), Blue (N), Gray (C), Yellow (S).

Table 3.5 Selected bond lengths (Å) and angles (°) for [Pb(bmpeda)$(SCN)_2$] (**3.10**) and [Pb(bmpchda)$(SCN)_2$] (**3.11**).

	3.10	**3.11**
Pb1-N2	2.525(3)	--
Pb1-S2	--	2.971(3)
Pb1-S2'	3.728(2)	--
Pb1-N1	2.659(3)	2.633(1)
Pb1-S1'	--	3.783(1)
Pb1-N3	2.845(2)	2.648(8)
Pb1-N4	2.569(2)	2.531(8)
Pb1-N5	2.534(2)	2.554(7)
Pb1-N6	2.734(2)	2.736(7)
S1-C1	1.625(3)	1.64(1)
C1-N1	1.160(4)	1.14(1)
S2-C2	1.627(3)	1.64(1)
C2-N2	1.159(4)	1.15(2)
Pb1-N1-C1	127.5(2)	155.6(9)
Pb1-N2-C2	152.1(3)	152.1(1)
Pb1-S1-C1	127.5(1)	--
Pb1-S2-C2	121.2(1)	102.1(1)
S1-C1-N1	178.6(3)	178.7(8)
S2-C2-N2	178.7(3)	178.9(1)

3.3.4. **[Pb(bmpchda)Pt$(SCN)_4$] (3.12)**

Complex [Pb(bmpchda)Pt$(SCN)_4$] (**3.12**) crystallizes as yellow plates in the monoclinic space group P 2_1/n. Structural analysis indicated that the complex consists of a seven coordinate Pb(II) metal centre coordinated to one bmpchda ligand, two N-bound thiocyanates from adjacent $[Pt(SCN)_4]^{2-}$ units and one S-bound thiocyanate (Figure 3.19). The coordination distances of the ligand to the Pb(II) metal centre range between 2.481(5) and 2.705(5) Å and are within the expected values for a Pb(II) metal centre.[172-192] In the case of the thiocyanate ligands, the coordination distances for the N-bound ligands are 2.426(5) and 2.896(6) Å, indicating that they are in fact coordinated. The coordination distance for the S-bound ligand is 3.48(1) Å, which is longer than expected

suggesting that is it in fact a weak intermolecular interaction (sum of van der waals radius = 3.82 Å).[141] For the $[Pt(SCN)_4]^{2-}$ unit, two of the ligands (in a *trans*- fashion) are bound to adjacent Pb(II) metal centres and one interacts with an adjacent Pb(II) metal centre as aforementioned. The fourth SCN^- ligand is dangling between the planes of the bmpchda ligands. The coordination distances of the SCN^- ligands to the Pt(II) metal centre range between 2.306(2) and 2.332(2) Å and the coordination angles are between 99.4(2) and 108.8(3)° (Table 3.6). The cyclohexane section of the ligand was found to be disordered in a 50/50 ratio over two positions.

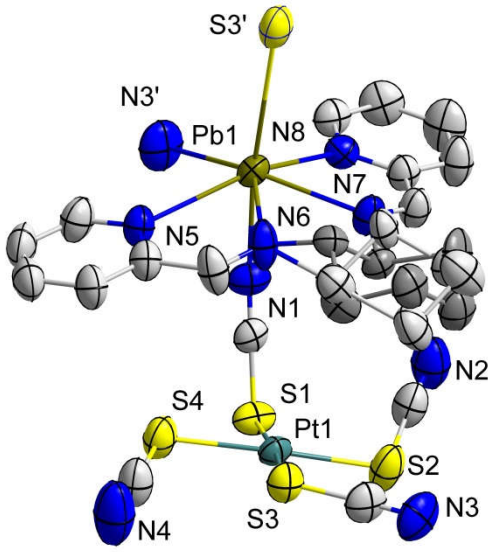

Figure 3.19 The structure of $[Pt(bmpchda)Pt(SCN)_4]$ (**3.12**). The hydrogen atoms were removed for clarity. Colour code: Dark Yellow (Pb), Green (Pt), Blue (N), Gray or Dark Gray (C), Yellow (S).

The supramolecular structure includes of a 1D CP through the 1-3 coordination of the SCN^- units from $[Pt(SCN)_4]^{2-}$ (Figure 3.20). The dimensionality of the structure is further increased from the interaction of the S atom from the $[Pt(SCN)_4]^{2-}$ units with the next chain over, making it an overall 2D structure. Using the aforementioned classification system (see section 3.2.3), this is a 4+3 nodal system. In the packing arrangement, there is no evidence of interactions between the ligands or the presence of hydrogen bonds.

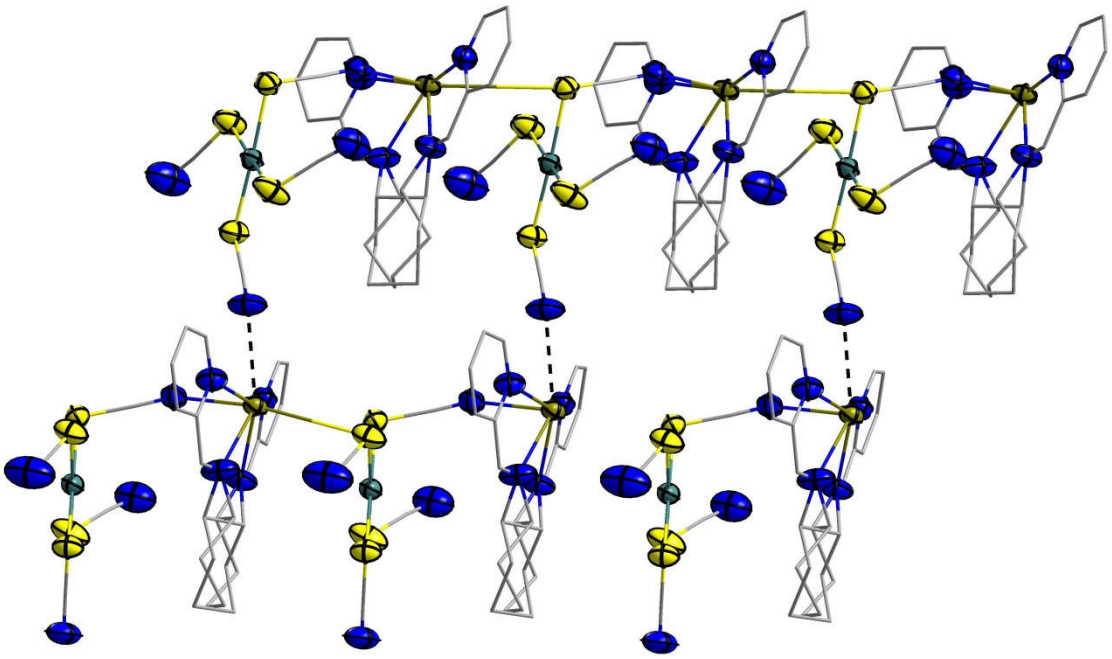

Figure 3.20 The 1D linear chain arrangement of [Pt(bmpchda)Pt(SCN)$_4$] (**3.12**). The hydrogen atoms were removed for clarity. Interchain coordination are shown as black fragmented lines. Colour code: Dark Yellow (Pb), Green (Pt), Blue (N), Gray (C), Yellow (S).

Table 3.6 Selected bond lengths (Å) and angles (°) for [Pt(bmpchda)Pt(SCN)$_4$] (**3.12**).

Pb1-N5	2.691(5)	S2-C2	1.672(8
Pb1-N6	2.481(5)	C2-N2	1.146(9)
Pb1-N7	2.508(5)	S3-C3	1.682(7)
Pb1-N8	2.705(5)	C3-N3	1.129(9)
Pb1-N1	2.426(5)	S4-C4	1.666(8)
Pb1-N3’	2.896(6)	C4-N4	1.116(10)
Pb1-S3’	3.482(1)	Pb1-N1-C1	156.2(5)
Pt1-S1	2.3263(15)	Pb1-N3’-C3’	147.8(6)
Pt1-S2	2.3060(18)	Pb1-S3’-C3’	87.03(1)
Pt1-S3	2.3144(15)	S1-C1-N1	176.0(5)
Pt1-S4	2.3324(18)	S2-C2-N2	174.8(7)
S1-C1	1.671(6)	S3-C3-N3	173.6(7)
C1-N1	1.136(7)	S4-C4-N4	174.2(8)

3.3.5. $[Pb(bmpeda)(SCN)]_2[Pt(SCN)_4]$ (3.13)

Complex $[Pb(bmpeda)(SCN)]_2[Pt(SCN)_4]$ (**3.13**) crystallizes in the triclinic space group P-1 as orange plates. It consists of a distorted face capped seven coordinate Pb(II) metal centre coordinated to one tetradentate bmpeda ligand, one NCS^- ligand, and one S and one N atoms from the adjacent $[Pt(SCN)_4]^{2-}$ building block (Figure 3.21). Overall, the structure results in a 1D coordination polymer where the SCN^- on the adjacent Pt(II) unit act as S-Pt-S bridge (using the 1,1 coordination mode of the SCN^- species) where the dangling NCS^- ligand on the Pb(II) unit is coordinated to another Pb(II) metal centre as a symmetrical Pb-N-Pb bridge that uses the N 1,1 coordination mode of SCN^- (Figure 1.3). The coordination distances of the ligand and N-bound NCS^- ligand to the Pb(II) metal centre are ranging between 2.451(8) and 2.965(1) Å and are unexceptional.[141-143] The coordination distance of the S-bound ligand from the adjacent $[Pt(SCN)_4]^{2-}$ unit is 3.776(1) Å, indicating weak intermolecular coordination.

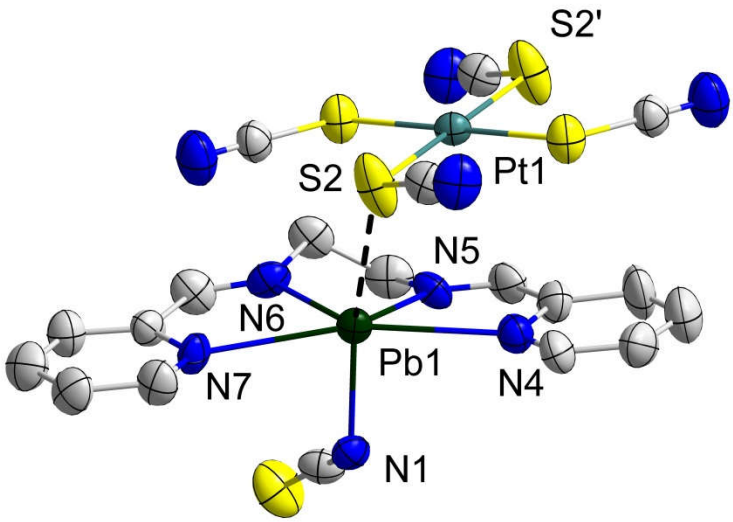

Figure 3.21 The structure of $[Pt(bmpeda)(SCN)]_2[Pt(SCN)_4]$ (**3.13**). The hydrogen atoms were removed for clarity. Colour code: Dark Green (Pb), Green (Pt), Blue (N), Gray (C), Yellow (S).

As mentioned above, in the packing arrangement, the 1D CP aspect of this structure propagates via two intermolecular coordinations. The first consists of a 1,1 coordination of the SCN- ligands on the Pt(II) unit in a *trans*- fashion and the second is the 1,1 bridging coordination of the NCS- ligand on the Pb(II) unit (Figure 3.22). Overall, this results in a 1D coordination polymer where the two metal centres are sterically hindered

by the presence of those coordinating units. There is no further evidence of other intermolecular interactions in the structure.

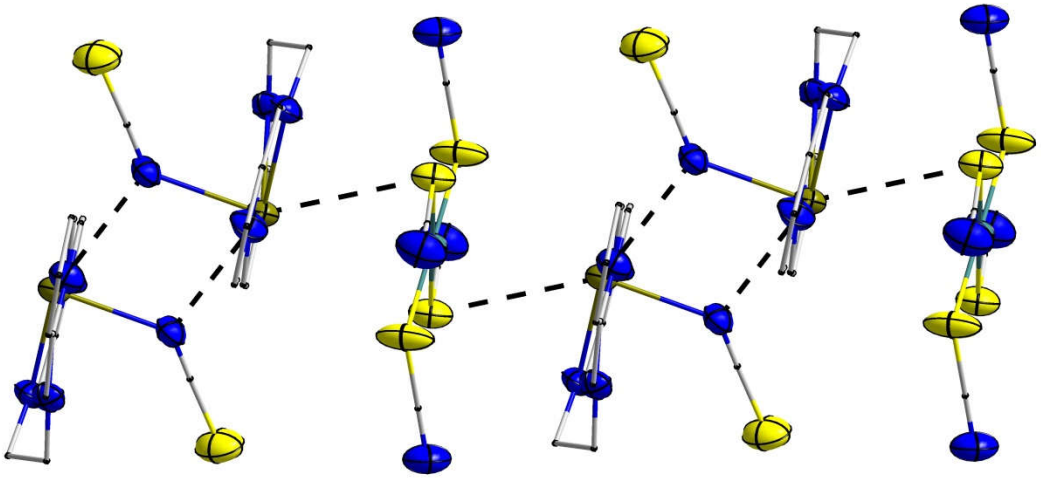

Figure 3.22 The 1-D linear chain arrangement of $[Pt(bmpeda)(SCN)]_2[Pt(SCN)_4]$ (**3.13**). The hydrogen atoms were removed for clarity. Color code: Dark Yellow (Pb), Green (Pt), Blue (N), Gray (C), Yellow (S).

Table 3.7 Selected bond lengths (Å) and angles (°) for $[Pt(bmpeda)(SCN)]_2[Pt(SCN)_4]$ (**3.13**).

Pb1-N4	2.701(9)	S1-C1	1.709(13)
Pb1-N5	2.508(9)	C1-N1	1.104(17)
Pb1-N6	2.531(9)	S2-C2	1.657(13)
Pb1-N7	2.721(9)	C2-N2	1.148(17)
Pb1-N1	2.451(8)	Pb1-N1-C1	129.1(1)
Pb1-S2	3.776(1)	Pb1-S2-C2	137.0(1)
Pb1-N1’	2.965(1)	Pb1-N1’-C1’	114.1(1)
Pt1-S1	2.317(3)	S1-C1-N1	174.9(13)
Pt1-S2	2.316(3)	S2-C2-N2	176.2(13)

3.3.6. **Discussion**

In this section, it was established that the ligands N,N’-bis(methylpyridine)ethane-1,2-diamine (**bmpeda**) and N,N’-bis(methylpyridine)cyclohexane-1,2-diamine (**bmpchda**) can be used to synthesize CP and be used strategically for controlling the dimensionality of the CP. As for the work shown in Section 3.2, selection of the ligand plays an

important role in controlling the number of coordination sites available on the metal centre and for the overall supramolecular arrangement of the system. By choosing a tetradentate ligand which causes steric hindrance near the metal centre, it was demonstrated that only a limited number of sites are available on the Pb(II) metal centre. This limits the overall number of coordination sites to seven or eight, four of which are from the ligand itself. Using the same nomenclature established in section 3.2.7, complexes **3.10** and **3.11** would be 2D CPs with a 4+4 nodal system, complex **3.12** a 2D CP with a 4+3 node, and complex **3.13** a 1D CP with a 4+3 node. In order to establish a definitive trend using bmpeda and bmpchda, further work is needed using $[Au(CN)_2]^-$ or $[Au(CN)_4]^-$ as bridges and to crystallize the first-row transition metal complexes, which, like for the work in Section 3.2, would be definitive in establishing the trend regarding the choice of metal centre coordinated to the ancillary ligand. Unfortunately, despite the ligands themselves being highly fluorescent, quenching occurred when they were coordinated to a metal centre, and no further investigation in the optical properties of these systems were made.

3.4. **Alternate late-transition metals thiocyanometallates.**

As mentioned in Section 3.1, our interest in 2nd and 3rd row late-transition metal $[M(SCN)_x]^{y-}$ building blocks rose from the fact that these might present decreased lability in solution. These metals are also softer, allowing the coordination of the sulfur end of the SCN^- ligand to the central metal instead of the hard nitrogen end. That property can be used to facilitate the synthesis of CPs by using first-row transition metals capped with ancillary ligands with the 2nd and 3rd row building blocks. As demonstrated in this chapter, Pt(II) was an excellent candidate for the synthesis of CPs due to its low lability and square planar geometry, resulting in multiple structures with unique topologies. To our knowledge, no clearly established synthesis of these building blocks had been published, but the formation constants were reported without synthetic details.[95] In order to further assess the possibility of using related 2nd and 3rd row late-transition thiocyanate metal building blocks, attempts at synthesizing the Pd(II), Rh(III), Ir(III), and Ir(IV) analogues were made, as shown below.

3.4.1. $K_2[Pd(SCN)_4]$

In order to synthesize the known Pd(II) analogue, $K_2[Pd(SCN)_4]$,[198] the metallic precursor K_2PdCl_4 was mixed with four equivalents of KSCN in H_2O which yielded a bright orange precipitate of $K_2[Pd(SCN)_4]$. The complex was identified to be analogous to $K_2[Pt(SCN)_4]$ by IR, with peaks at 2131, 2101 and 2057 cm^{-1}, and by elemental analyses. The complex could not be crystallized for further structural characterization using SC-XRD.

Attempts at the synthesis of CPs using this building block were made with the same selection of metals, ligands and methodology depicted in section 3.2. Unfortunately, these syntheses were unsuccessful and resulted in the crystallization of complexes of the type $[M(L)_x(SCN)_2]$, which were the same as described in section 2.7. These complexes were identified using a combination of IR and Raman spectroscopies and no further investigations were made. These results suggests that the building block $K_2[Pd(SCN)_4]$ presents surprisingly high lability in solution, similar to that observed for first-row transition metals, and is not a suitable candidate for the synthesis of heterobimetallic CPs.

3.4.2. $K_3[Rh(SCN)_6]$

The complex $[Rh(SCN)_6]^{3-}$ was targeted in order to assess the lability of an octahedral 2nd row d^6 building block, as compared to the square planar d^8 $[Pt(SCN)_4]^{2-}$, and to access unique topologies in targeted CPs. To our knowledge, no synthetic details have been provided regarding the synthesis of $K_3[Rh(SCN)_6]$ and only its formation constants and infrared data were reported.[95] The complex was synthesized by mixing $RhCl_3 \cdot 3H_2O$ with a small excess of KSCN (slightly over six equivalents) in H_2O. The reaction between the salts was slow, and heating of the solution to 50 °C for 30 minutes was required in order to drive the reaction to completion. During the reaction, the color of the solution changed from a bright red color to a deep crimson, similar to that observed for Fe(III). As opposed to Pd(II) and Pt(II), the complex could not be precipitated by dissolving it in ethyl acetate and adding dichloromethane. In most attempts, a red oil was obtained instead of a precipitate. After investigation by IR spectroscopy and a handful of unsuccessful attempts at precipitation, it was determined that the resulting complex, $K_3[Rh(SCN)_6]$, is highly hygroscopic. When left under atmospheric conditions or when

exposed to a minimal amount of water vapor, the precipitate of $K_3[Rh(SCN)_6]$ quickly absorbs the H_2O and turns into an oil. Attempts were made at the synthesis of the complex using dry solvents and a dry inert atmosphere, but the reaction proved to be very difficult and highly inconvenient, as even the smallest amount of H_2O was quickly absorbed.

Obviously, this hygroscopic effect made it very difficult to measure the correct amount this complex for the synthesis of CPs in a practical fashion. Nonetheless, syntheses of CPs were attempted. The results were similar as for Pd(II); the complex proved to be surprisingly labile in solution or subject to ligand-transfer with the ancillary ligand capped metal centre, which resulted in the crystallization of complexes of the type $[M(L)_x(SCN)_2]$ as observed in Chapter 2.

3.4.3. $K_3[Ir(SCN)_6]$ and $K_2[Ir(SCN)_6]$

In a similar way to the Rh(III) analogue, complexes of Ir(III) and Ir(IV) were targeted to assess their lability. In the case of Ir(IV), the low spin d^5 ion could be used for multifunctional CPs presenting magnetic properties. In an attempt to synthesize $K_3[Ir(SCN)_6]$, $IrCl_3$ was mixed with six equivalents of KSCN in H_2O. The solution was heated slightly in order to fully dissolve the precursor salt. When the KSCN was added, the solution quickly turned to a dark brown colour before an oily black substance settled at the bottom of the reaction vessel. This oily substance could not be identified, but FTIR analysis indicated the absence of SCN^- in the product. Such behaviour was previously observed for Ir(III) when exposed to a source of sulfur, and most likely consists of the oxidation of Ir(III) to Ir(IV) by reduction of the SCN^- unit present in the reaction mixture.[199] Attempts at controlling this side reaction were unsuccessful using conventional methods such as changing the solvent to organic solvents or less polar solvents, using dry solvents, lowering the temperature, and/or using schlenk line techniques. Attempts at synthesizing the product with a sterically hindering countercation, such as $AsPh_4^+$ were also unsuccessful as similar results were observed.

In the case of Ir(IV), using $IrCl_4$ and a similar synthetic method also resulted in a black oil settling at the bottom of the reaction vessel which could not be identified. Like for Ir(III),

this black oil did not present a signal near 2100 cm^{-1} in the FTIR spectra as would be expected for a thiocyanate salt. Similarly, attempts at preventing this side reaction from occurring were unsuccessful.

3.5. Attempts at the synthesis of capping ligand-free $[MPt(SCN)_4]$ complexes

Previously, in the Leznoff group, it was established that capping ligand-free complexes can present unique properties when compared to CPs with ancillary capping ligands.[200-204] Such properties include negative thermal expansion, magnetic properties and metal-metal bond fluorescence.[47-53] In an attempt to synthesize ligand-free complexes of the type $[MPt(SCN)_4]$ or $[M_2(Pt(SCN)_4)_3]$, reactions were first performed by mixing metal chloride precursors such as $FeCl_3$, $CoCl_2 \cdot 6H_2O$ or $NiCl_2 \cdot 6H_2O$ in H_2O with $K_2[Pt(SCN)_4]$ in an appropriate ratio, precipitating KCl using acetone, and then slowly evaporating the resulting liquor to recrystallize the complex. Unfortunately, this method was proved to be unsuccessful. The liquor evaporated over a period of a few days and resulted in oily substances that could not be identified. Subsequently, attempts were made using other common crystallization methods, such as H-tubes and low temperature, but all were proven to be inadequate. In most cases, no product crystallized even after a few months of slow diffusion or low temperature.

In order to synthesize these complexes, attempts were made using a mechanochemical method which consists of grinding the reagents in the solid state with a minimal amount of solvent. When mixing $CoCl_2$ and $K_2[Pt(SCN)_4]$ in the solid state and after a few minutes of grinding using a mortar and pestle and one drop of methanol, the salts, which were initially red and orange, respectively, quickly changed to a dark purple color, suggesting the presence of a solid state reaction between the complexes to give potentially $[CoPt(SCN)_4]$ and KCl. Analysis by infrared spectroscopy showed a single peak at 2156 cm^{-1}, which is at a different value than the three peaks observed for $[Pt(SCN)_4]^{2-}$, which suggests that the reaction was successful. However, the product would still be impure due to the presence of KCl. Unfortunately, attempts at recrystallizing the product were unsuccessful. When dissolved in a minimal amount of solvent, the colour of the salt quickly reverted back to the orange color of $[Pt(SCN)_4]^{2-}$,

suggesting that the product decomposes when dissolved in any solvent. When using a solvent in which KCl is insoluble, an oily orange substance was obtained after slow evaporation of the solvent or attempts at precipitation. Infrared spectroscopy of the oily orange substance indicated the lack of coordination to the $[Pt(SCN)_4]^{2-}$ building block, as its three common peaks around 2100 cm^{-1} were observed. PXRD analysis indicated that the ground product consists of a combination of two salts, KCl and another for which the unit cell could not be identified. This behavior was observed for all first-row transition metals, from Cr(III) to Zn(II), and due to these limitations, no further attempts at synthesizing ancillary ligand-free $[MPt(SCN)_4]$ complexes were made.

3.6. **Conclusions and future work**

In the first section of this chapter, it was shown that heterobimetallic $[Pt(SCN)_4]^{2-}$ CPs can be successfully synthesized using simple synthetic methods, and that a variety of ligands and metal centers can be chosen in order to control the structural parameters of the CPs. Unlike for first-row transition metals, $[Pt(SCN)_4]^{2-}$ does not present extreme lability in solution which makes it viable for the rational synthesis of the targeted systems. On the other hand, CPs synthesized using simple bidentate and tridentate ancillary ligands, such as 2,2'-bipy, en, tmeda, terpy, etc., did not present any physical properties of interest, as opposed to the $[Au(CN)_2]^-$ analogues. Hence, further exploration in the choice of ligand was required in order to fine tune the properties of the CPs. In the second section, the ligands bmpeda and bmpchda were successfully synthesized and utilized in the synthesis of CPs in combination with $[Pt(SCN)_4]^{2-}$. Synthetic work and analysis of the crystal structures of these complexes revealed that these ligands are indeed planar tetradentate and ancillary, but also are prone to hydrolysis if the reaction conditions are not properly controlled.

Overall, a great deal of work remains to be done regarding the synthesis, crystallization, and analysis of these complexes to establish a clear trend in the role of the bmpeda and bmpchda ligands for controlling the dimensionality of CPs. When using first row transition metals as metal centres capped with the latter ligands as the node units, initial work showed that the ligand tends to either hydrolyze over time, leading to a metal centre fully coordinated to two half ligands as the crystallization product, or that the

system does not react at all with bridging units such as $[Pt(SCN)_4]^{2-}$ under the typical reaction conditions. Future work regarding these systems should involve preventing the hydrolysis reaction by using an inert atmosphere and dry solvents and/or to use more aggressive reaction conditions, such as high temperatures or higher concentrations, in order to promote the synthesis of CPs with first row transition metals as nodal metal centres. Successfully completing this work would allow a more thorough comparison of the systems using the bmpeda and bmpchda ligands with, for example, the systems presented in section 3.2 of this chapter, and thus further explore the chemistry of $[Pt(SCN)_4]^{2-}$-based CPs and of their structural features and topology.

Overall, it was shown that other building blocks could be chosen in combination with $[Pt(SCN)_4]^{2-}$ to synthesize CPs with high dimensionality, due to the four coordination sites available and the flexibility in the coordination angles of the unit, unique topologies and targeted physical properties. Hence, in Chapter 4, we will explore the possibility of using building blocks of the type $[Cu_2(\mu\text{-}OH)_2(L)_2]^{2+}$ in combination with different bridging ligands, including $[Pt(SCN)_4]^{2-}$, in order to target magnetism as a property of interest.

3.7. **Experimental**

3.7.1. **General Procedures and Materials.**

All manipulations were performed in air using purified solvents. K_2PtCl_4 was purchased from Tanaka Kikinzoku Kogyo or Precious Metals Online and was used as received. Microanalyses (C, H, N) were performed at Simon Fraser University using a computer-controlled Carlo Erba (Model 1106) CHN analyzer. Powder X-ray diffractograms were obtained using a Bruker D8 ADVANCE equipped with a Cu Kα source (λ = 1.54056 Å) at Kyushu University or using the method described in Chapter 2 at Simon Fraser University. Unless otherwise noted, all other experimental procedures were as described in Chapter 2.

3.7.2. Synthetic procedures

$K_2[Pt(SCN)_4]$

$K_2[Pt(SCN)_4]$ was synthesized by modification of a literature procedure.[193] To a 10 mL aqueous solution of $K_2[PtCl_4]$ (1.03 g, 2.50 mmol) was added a 10 mL aqueous solution of KSCN (0.972 g, 10.0 mmol). The solution was heated at 60°C for 15 mins and the volume of the solution reduced to approximately 5 mL by heating over a steam bath. Then 20 mL of acetone was added to the mixture and the white precipitate of KCl was isolated by filtration. The solvent was removed using a rotary evaporator and the crude residue was dissolved in a minimum amount of ethyl acetate. The white precipitate of KSCN was removed by filtration and the solvent was removed using a rotary evaporator. The resulting crude residue of $K_2[Pt(SCN)_4]$ was recrystallized from acetone by slow evaporation. Yield: 1.24 g (97.8%). FT-IR (ATR, cm^{-1}): 3433, 2795, 2124 (ν_{CN}), 2097 (ν_{CN}), 2047 (ν_{CN}), 1624, 1111, 967, 957, 749, 484. Raman (785 nm, a: 1, %Ip: 50, cm^{-1}): 2128 (ν_{CN}), 2102 (ν_{CN}), 700, 464, 309, 293, 174, 142, 122. The spectroscopic data was consistent with reported literature values.[193]

$[Mn(terpy)Pt(SCN)_4]$ (3.1) and $[Mn(terpy)_2][Pt(SCN)_4]$ (3.2).

To a 5 mL aqueous solution of $MnCl_2 \cdot 4H_2O$ (0.020 g, 0.10 mmol) was added a 5 mL methanolic solution of terpyridine (terpy; 0.022 g, 0.094 mmol). Then, a 10 mL methanolic solution of $K_2[Pt(SCN)_4]$ (0.050 g, 0.10 mmol) was diffused slowly into this solution by layering or slow diffusion through a filter paper. Yellow plate-like crystals of $[Mn(terpy)Pt(SCN)_4]$ (**3.1**) were obtained in low yield after several days at 5 °C. Yield: 0.019 g (26 %). Anal. Calcd. for $C_{19}H_{11}N_7MnPtS_4$: C, 31.85; H, 1.55; N, 13.70. Found: C, 31.91; H, 1.70; N, 13.44. FT-IR (ATR, cm^{-1}): 2119 (ν_{CN}), 1592, 1571, 1474, 1459, 1448, 1438, 1402, 1312, 1247, 1186, 1168, 1159, 1094, 1014, 768, 658, 651, 639, 512, 425. Attempts to make **3.1** in powder form by mixing the reagents in a range of solvents (water, methanol, ethanol etc.) resulted in a yellow powder. Crystals of $[Mn(terpy)_2][Pt(SCN)_4]$ (**3.2**) were grown from the filtered mixtures after several days at 5-8 °C or from the reaction mixture of **3.1** after disturbance of the layers. The PXRD patterns measured for the powders resulting from direct mixing of the reagents were the same as the PXRD pattern generated from the crystals of **3.2**. Yield: 0.085 g (89 %).

Anal. Calcd. for $C_{34}H_{22}N_{10}MnPtS_4$: C, 43.03; H, 2.33; N, 14.76. Found: C, 42.74; H, 2.28; N, 14.91. FT-IR (ATR, cm^{-1}): 2107 (ν_{CN}), 1594, 1572, 1476, 1459, 1451, 1438, 1312, 1290, 1245, 1191, 1166, 1159, 1013, 769. 0

[Co(terpy)Pt(SCN)$_4$] (3.3) and [Co(terpy)$_2$][Pt(SCN)$_4$] (3.4).

To a 5 mL aqueous solution of $Co(NO_3)_2 \cdot 6H_2O$ (0.030 g, 0.10 mmol) was added a 5 mL methanolic solution of terpyridine (0.023 g, 0.099 mmol). Then, the resulting mixture was layered over a 10 mL aqueous solution of $K_2[Pt(SCN)_4]$ (0.050 g, 0.10 mmol). After 24 hours, a co-crystallized 60:40 mixture of red plates (**3.3**) and red blocks (**3.4**) was obtained. Direct mixing of the reagents resulted in an orange powder that consists of **3.3** and **3.4** in a similar ratio. Yield (mixture): 0.045 g (62 %). Anal. Calcd. for 60:40 mixture $C_{25}H_{15.4}CoN_{8.2}PtS_4$: C, 36.93; H, 1.90; N, 14.12. Found: C, 36.78; H, 1.73; N, 13.64. FT-IR (**3.4**, ATR, cm^{-1}): 2315 (ν_{CN}), 2112 (ν_{CN}), 1598, 1571, 1467, 1444, 1396, 1249, 1160, 1016, 770, 769. FT-IR (**13**, ATR, cm^{-1}): 2135 (ν_{CN}), 1597, 1570, 1465, 1444, 1396, 1283, 1242, 1186, 1155, 1013, 769, 648, 515, 456, 426, 417. FT-IR (**3.4**, KBr, cm^{-1}): 2113 (ν_{CN}), 1597, 1570, 1465, 1444, 1396, 1286, 1242, 1186, 1153, 1054, 1013, 770.

[Cu(en)$_2$Pt(SCN)$_4$] (cis: 3.5; trans: 3.6).

To a 4 mL aqueous solution of $Cu(NO_3)_2 \cdot 3H_2O$ (0.025 g, 0.10 mmol) was added a 2 mL stock methanolic solution (0.1 M) of ethylenediamine (en). Then, a 6 mL methanol/water (1:2) solution of $K_2[Pt(SCN)_4]$ (0.051 g, 0.10 mmol) was added dropwise to this purple solution. An immediate brown precipitate of *cis*-$[Cu(en)_2Pt(SCN)_4]$ (**3.5**) formed, which was collected by filtration and dried *in vacuo*. Yield: 0.037 g (59 %). Anal. Calcd. for $C_8H_{16}N_8CuPtS_4$: C, 15.72; H, 2.64; N, 18.33. Found: C, 15.59; H, 2.48; N, 18.17. FT-IR (ATR, cm^{-1}) : 3305, 3253, 3156, 2942, 2883, 2126 (ν_{CN}), 2108 (ν_{CN}), 1581, 1456, 1394, 1369, 1321, 1276, 1157, 1090, 1026, 968, 878, 698, 529, 459, 432, 420. $\chi_M T$ (300 K, 1000 Oe) = 0.39 cm^3 K mol^{-1}. To obtain X-ray quality crystals the "Petri dish diffusion method" was used, in which a Petri dish containing an aqueous solution of $Cu(ClO_4)_2 \cdot 6H_2O$ and two equivalents of en on one side and an aqueous solution of $K_2[Pt(SCN)_4]$ on the other side was prepared. Slow diffusion of the two reagents yielded brown crystals of **3.5** over several days. The simulated powder X-ray diffraction (PXRD)

pattern from this crystal after structure solution was comparable to the PXRD pattern of the initial powder.

By layering a solution of $Cu(ClO_4)_2 \cdot 6H_2O$ and two equivalents of en in methanol onto a solution of $K_2[Pt(SCN)_4]$ in methanol and storing this in a sealed vial at 5 °C for several days, a mixture of brown crystals of **3.5** and purple crystals of *trans*-$[Cu(en)_2Pt(SCN)_4]$ (**3.6**) were obtained, which were separated by hand. For **3.6**: Anal. Calcd. for $C_8H_{16}N_8CuPtS_4$: C, 15.72; H, 2.64; N, 18.33. Found: C, 15.89; H, 2.57; N, 18.33. FT-IR (ATR, cm^{-1}) : 3318, 3264, 2978, 2941, 2883, 2811, 2122 (ν_{CN}), 2103 (ν_{CN}), 1606, 1572, 1457, 1364, 1312, 1276, 1252, 1142, 1078, 1028, 1012, 961, 876, 860, 692, 603, 530, 469, 428, 421, 407.

$[Ni(en)_2Pt(SCN)_4]$ (3.7).

$Ni(NO_3)_2 \cdot 6H_2O$ (0.029 g, 0.10 mmol) was added to a 5 mL aqueous stock solution (0.04 M) of ethylenediamine. Then, a 5 mL aqueous solution of $K_2[Pt(SCN)_4]$ (0.051 g, 0.10 mmol) was added dropwise to this pale purple solution. An immediate orange precipitate of $[Ni(en)_2Pt(SCN)_4]$ (**3.7**) formed, was collected by filtration and dried *in vacuo*. Yield: 0.058 g (96 %). Anal. Calcd. for $C_8H_{16}N_8NiPtS_4$: C, 15.85; H, 2.66; N, 18.48. Found: C, 15.75; H, 2.59; N, 18.38. FT-IR (ATR, cm^{-1}) : 3331, 3278, 2944, 2878, 2140 (ν_{CN}), 2110 (ν_{CN}), 1581, 1456, 1324, 1275, 1146, 1087, 1024, 1004, 960, 872, 667, 515, 427. $\chi_M T$ (300 K, 1000 Oe) = 1.19 cm^3 K mol^{-1}. To obtain the X-ray quality crystals of **3.7**, a Petri dish was divided with a filter paper. One mL of a 20 mM aqueous solution of $[Ni(en)_2](NO_3)_2$ was prepared on one side and 1 mL of a 20 mM aqueous solution of $K_2[Pt(SCN)_4]$ was inserted on the other side.[77] The two solutions diffused slowly into each other. Several days later, yellow plate-like crystals of X-ray quality were obtained. The IR and PXRD data of the crystals matched that of powdered **3.7**.

$[Ni(tmeda)Pt(SCN)_4]$ (3.8)

To a 15 mL solution of $NiCl_2 \cdot 6H_2O$ (0.10 mmol, 0.013 g) in H_2O was added a 15 mL solution of $K_2[Pt(SCN)_4]$ (0.10 mmol, 0.051 g) in H_2O. This solution was left stirring for 15 minutes, and then a 15 mL methanolic solution of tmeda (0.20 mmol, 0.30 mL) was added dropwise. Immediately, a precipitate of $[Ni(tmeda)Pt(SCN)_4]$ (**3.8**) formed which could not be crystallized. PXRD, IR and elemental analyses indicated that the precipitate

was isostructural to [Cu(tmeda)Pt(SCN)$_4$]. Yield: 0.058 g (96 %). Anal. Calcd. for $C_{10}H_{16}N_6NiPtS_4$: C, 19.94; H, 2.68; N, 13.95. Found: C, 19.61; H, 2.51; N, 13.89. FT-IR (ATR, cm^{-1}) : 2157 (ν_{CN}), 2136 (ν_{CN}), 2118 (ν_{CN}), 2096 (ν_{CN}), 1460, 1395, 1282, 1122, 1047, 1023, 1005, 958, 816, 772, 591, 518, 461, 441.

[Pb(phen)$_2$Pt(SCN)$_4$] (3.9)

$Pb(NO_3)_2$ (0.10 mmol, 0.033 g) was first dissolved in 15 mL of H_2O. Then, a solution of phen (0.20 mmol, 0.036 g) in 15 mL of methanol was added slowly to the former solution. This resulted in a cloudy solution, which was stirred for 15 minutes. A 15 mL solution of $K_2[Pt(SCN)_4]$ (0.10 mmol, 0.051 g) in H_2O:MeOH 1:1 was then added dropwise, and the resulting solution was stirred for another 15 minutes. The solution was then filtered and set out for slow evaporation which yielded crystals of [Pb(phen)$_2$Pt(SCN)$_4$] (**3.9**) over a period of two weeks. Yield: 0.086 g (85%). Anal. Calcd. for $C_{28}H_{16}N_8PbPtS_4$: C, 33.80; H, 1.62; N, 11.26. Found: C, 33.54; H, 1.62; N, 11.30. FT-IR (ATR, cm^{-1}): 2103 (ν_{CN}), 1622, 1589, 1572, 1513, 1495, 1423, 1342, 1300, 1219, 1204, 1141, 1099, 1034, 969, 956, 860, 843, 767, 725, 719, 635, 469, 427, 414.

N,N'-bis(methylpyridine)ethane-1,2-diamine (bmpeda)

The ligand was synthesized according to a modified synthetic procedure.[204] To a solution of ethylene diamine (10 mmol, 0.67 mL) in 40 mL of dichloromethane was added a significant excess (approx. 6 g) of magnesium sulfate. With vigorous stirring, 2-pyridinecarboxylaldehyde (20 mmol, 1.9 mL) was added dropwise which results in a yellow-orange color. After 2 hours of stirring, the solution was then filtered and the solvent removed, which resulted in a viscous brown oil of bmpeda. To purify the sample, the brown oil was dissolved in a minimum amount of ethyl acetate, layered with excess petroleum ether and allowed to crystallize overnight at -40 °C which resulted in large brown crystals of N,N'-bis(methylpyridine)ethane-1,2-diamine (bmpeda). Yield: 2.14 g (90%). ^{1}H-NMR ($CDCl_3$, 400MHz): 8.59 (2H, dd, H), 8.39 (2.05H, s, N=CH), 7.95 (2H, dd, H), 7.69 (2.16H, ddd, H), 7.27 (2.02H, ddd, H), 4.03 (4.15H, s, CH_2). The spectral data match the data found in the literature.

N,N'-bis(methylpyridine)cyclohexane-1,2-diamine (bmpchda)

N,N'-bis(methylpyridine)cyclohexane-1,2-diamine (bmpchda) was synthesized using the same method as for bmpeda, but by using 1,2-diaminocyclohexane (10 mmol, 0.83 mL, 1:1 mixture of *cis*- and *trans*-) instead of ethylene diamine. Crystallization resulted in pale yellow needles of bmpchda. Yield: 2.48 g (85%). ^{1}H-NMR($CDCl_3$, 400MHz): 8.52 (2H, ddd, H), 8.31 (1.93H, s, N=CH), 7.85 (ddd, 2.11H, H), 7.61 (2.03H, ddd, H), 7.19 (2.06H, ddd, H), 3.51 (m, 2.19H, N-CH), 1.87 (6.61H, m, CyH).

[Pb(bmpeda)(SCN)$_2$] (3.10)

$Pb(NO_3)_2$ (0.10 mmol, 0.033 g) and KSCN (0.20 mmol, 0.018 g) was first dissolved in a 20 mL solution of H_2O. Then, a 20 mL methanolic solution of bmpeda (0.10 mmol, 0.023 g) was added dropwise and the solution stirred for 15 minutes. The mother liquor was then filtered and set out for slow evaporation which yielded pale-yellow plates of [Pb(bmpeda)$(SCN)_2$] (**3.10**) over a period of two weeks. Yield: 0.050 g (89 %). Anal. Calcd. for $C_{16}H_{14}N_6PbS_2$: C, 34.22; H, 2.51; N, 14.96. Found: C, 34.01; H, 2.48; N, 15.14. FT-IR (ATR, cm^{-1}) : 2052 (ν_{CN}), 2024 (ν_{CN}), 1775, 1657, 1587, 1435, 1386, 1309, 1265, 1211, 1151, 1101, 1041, 1002, 981, 943. Raman (785 nm, %Ip: 100, cm^{-1}): 1952 (ν_{CN}), 1672, 1604, 1548, 1219, 1182, 993.

[Pb(bmpchda)(SCN)$_2$] (3.11)

[Pb(bmpchda)$(SCN)_2$] (**3.11**) was synthesized using the same method as for **3.10** but by using bmpchda (0.10 mmol, 0.030 g) instead of bmpeda. Yield: 0.055 g (90 %). Anal. Calcd. for $C_{20}H_{20}N_6PbS_2$: C, 39.01; H, 3.27; N, 13.65. Found: C, 39.12; H, 3.40; N, 13.49. FT-IR (ATR, cm^{-1}) : 2988, 2900, 2094 (ν_{CN}), 2045 (ν_{CN}), 1644, 1586, 1407, 1312, 1228, 1066, 1008, 884. Raman (785 nm, %Ip: 100, cm^{-1}): 2096 (ν_{CN}), 2043 (ν_{CN}), 1647, 1588, 1568, 1345, 1227, 1049, 1008, 695.

[Pb(bmpchda)Pt(SCN)$_4$] (3.12)

[Pb(bmpchda)$Pt(SCN)_4$] (**3.13**) was synthesized using the same method as for **3.10** but by using $K_2[Pt(SCN)_4]$ (0.10 mmol, 0.051 g) instead of KSCN and bmpchda (0.10 mmol, 0.030 g) instead of bmpeda. Yield: 0.071 g (77 %). Anal. Calcd. for $C_{22}H_{20}N_8PbPtS_4$: C, 28.51; H, 2.17; N, 12.09. Found: C, 28.75; H, 2.40; N, 11.89. FT-IR (ATR, cm^{-1}) : 2126

(ν_{CN}), 2110 (ν_{CN}), 1648, 1589, 1476, 1440, 1387, 1350, 1315, 1300, 1242, 1228, 1155, 1104, 1047, 1006, 975, 914, 893, 852, 789, 779. Raman (785 nm, %lp: 100, cm^{-1}): 2090 (ν_{CN}), 2071 (ν_{CN}), 2041 (ν_{CN}), 1642, 1581, 1561, 1343, 1227, 1048, 1002, 691.

[Pb(bmpeda)(SCN)]$_2$[Pt(SCN)$_4$] (3.13)

[Pb(bmpeda)(SCN)]$_2$[Pt(SCN)$_4$] (**3.14**) was synthesized using the same method as for **3.10** but by using $K_2[Pt(SCN)_4]$ (0.10 mmol, 0.051 g) instead of KSCN. Yield: 0.058 g (96 %). Anal. Calcd. for $C_{34}H_{28}N_{14}Pb_2PtS_6$: C, 28.47; H, 1.97; N, 13.67. Found: C, 28.59; H, 2.30; N, 13.49. FT-IR (ATR, cm^{-1}) : 2096 (ν_{CN}), 2011 (ν_{CN}), 1935 (ν_{CN}), 1610, 1592, 1541, 1536, 1502, 1415, 1371, 1203, 1132, 1023, 990. Raman (785 nm, %lp: 100, cm^{-1}): 2015 (ν_{CN}), 1952 (ν_{CN}), 1671, 1608, 1542, 1212, 1181, 991.

$K_2[Pd(SCN)_4]$

$K_2[Pd(SCN)_4]$ was prepared using the same method as for $K_2[Pt(SCN)_4]$ but by using K_2PdCl_4 (0.816 g, 2.50 mmol) instead along with KSCN (0.972 g, 10.0 mmol). Yield: 1.00 g (96 %). Anal. Calcd. for $C_4N_4K_2PdS_4$: C, 11.52; H, 0.00; N, 13.44. Found: C, 11.40; H, 0.21; N, 13.20. FT-IR (ATR, cm^{-1}): 2105 (sh), 1109 (m).

$K_3[Rh(SCN)_6]$

To a mixture of $RhCl_3 \cdot 3H_2O$ (1.00 g, 3.79 mmol) was added a small excess of KSCN (2.23 g, 23.0 mmol) in 20 mL of H_2O. The solution was stirred and heated to 50 °C for 30 minutes. Then, the solvent was reduced to 5 mL and an excess amount of Acetone was added. The solution was filtered and the solvent was removed. To purify the product, the resulting oil was dissolved in a minimal amount of dry ethyl acetate and an excess amount of dry dichloromethane was added, which resulted in a dark crimson power of $K_3[Rh(SCN)_6]$. Due to the highly hygroscopic nature of the powder, elemental analyses were not performed successfully on the product. The powder was kept in a desiccator for subsequent usage. Yield: 1.96 g (91 %). FT-IR (ATR, cm^{-1}): 2101 (sh), 2095 (sh), 1103 (m).

Chapter 4. **Magnetostructural characterization of copper(II) hydroxide dimers and coordination polymers coordinated to apical isothiocyanate and cyanide-based counteranions.**[3]

4.1. **Introduction**

In Chapter 3, it was demonstrated that the $[Pt(SCN)_4]^{2-}$ anion was an effective building blocks for directing the supramolecular structure of coordination polymers and double salts. With that in mind, this chapter focuses on using this concept for directing the inter- and intramolecular interactions in the well-studied d^9-d^9 magnetic system $[Cu(\mu\text{-}OH)(L)]_2^{2+}$ and thus their overall magnetic properties, as explained below.

The $[Cu(\mu\text{-}OH)(L)]_2^{2+}$ system has been of strong interest to the magnetochemistry community since the 1950s because its electronic configuration allows for the magnetic properties of the system to be systematically explored and for magnetostructural correlations to be extracted without the presence of other complicating contributions to the magnetic properties arising from the complexes.[205-212] The magnetostructural correlations for the most basic iterations of this dinuclear system, first established by Hatfield and Hodgson, indicated that the sign and the amplitude of the magnetic interaction (J-coupling) between the two Cu(II) metal centres is strongly influenced by the Cu-O-Cu angle of the complex.[205]

[3] Part of the work in this chapter is reproduced with permission from D. Savard, T. Storr, and D. B. Leznoff, "Magnetostructural characterization of copper(II) hydroxide dimers and coordination polymers coordinated to apical isothiocyanate and cyanide-based counteranions", *Canadian Journal of Chemistry*, vol. 92, pp. 1021-1030, 2014, Copyright 2014 Canadian Science Publishing. The DFT calculations were partially done by Prof. Tim Storr.

To date, most of the synthesized and magnetically characterized Cu(II) hydroxide dimers that have been reported follow this magnetostructural correlation closely and consist of complexes of the type $[Cu(\mu\text{-}OH)(L)]_2(Q)_x$ where L is a bidentate nitrogen donor and Q is a non- or weakly coordinating ligand to the Cu(II) metal centre.[206-212] The focus of these previous reports has been on altering the bidentate nitrogen donor ligand L and characterizing the resulting optical properties,[213] magnetic properties,[214-217] and their potential industrial applications.[218] In addition, there has also been some work toward preparing multifunctional materials using the dinuclear complex cation as a scaffold for biological applications.[219-220]

In the field of molecular magnetism, controlling the structural parameters of the structure is a key element in determining the magnetic properties of a material. More specifically, in the case of the Cu(II) dimer core, the geometry of the core and the interconnectivity of the units are the key aspects.[221-223] Thus, controlling the dimensionality of the material containing the $[Cu(\mu\text{-}OH)(L)]_2^{2+}$ dimers by using them as building blocks has been of interest as of late.[224-230] For example, in the Leznoff group, $[Cu(\mu\text{-}OH)(tmeda)]_2^{2+}$ and the cyanometallate anion $[Au(CN)_4]^-$ were combined in order to synthesize novel materials. The resulting complexes consisted of a series of molecular polymorphs with bound apical ligands, $[Cu(\mu\text{-}OH)(tmeda)Au(CN)_4]_2$ and $[\{Cu(\mu\text{-}OH)(tmeda)\}_2Au(CN)_4][ClO_4]\cdot MeOH$, and one coordination polymer, $[\{Cu(\mu\text{-}OH)(tmeda)\}_2Au(CN)_4][Au(CN)_4]$.
It is noteworthy to mention that these materials presented magnetic properties different from those normally observed for Cu(II) hydroxide dimers.[214-217]

With this in mind, it was of interest to further explore the coordination behaviour of these Cu(II) hydroxide dimers when attempting to synthesize CPs using the bridging ligands NCS^- and $[Pt(SCN)_4]^{2-}$, along with, $[Au(CN)_4]^-$. This guides the dimensionality of the resulting coordination polymers and allow their magnetic properties to be probed. It also enables us to characterize the effect of appending (iso)thiocyanate and cyanide-based apical ligands to the dimers, an aspect that remained relatively unexplored in the literature to date. Furthermore, this work would also allow us to assess the coordination potential of NCS^- and $[Pt(SCN)_4]^{2-}$ to systems other than the more common mononuclear $[M(L)_x]^{y+}$, an aspect which remains relatively unexplored in (iso)thiocyanate coordination

chemistry to date. Thus, in this work, the synthesis and characterization of complexes from a series of $[Cu(\mu\text{-}OH)(L)]_2^{2+}$ cations (L = 1,10-phenanthroline, 2,2'-bipyridine, N,N,N',N'-tetramethylethylenediamine) with NCS^-, $[Au(CN)_4]^-$ and $[Pt(SCN)_4]^{2-}$ salts (Figure 4.1) was targeted and the structural factors influencing the magnetic interactions between the Cu(II) centres in the resulting materials was examined.

4.2. **Syntheses**

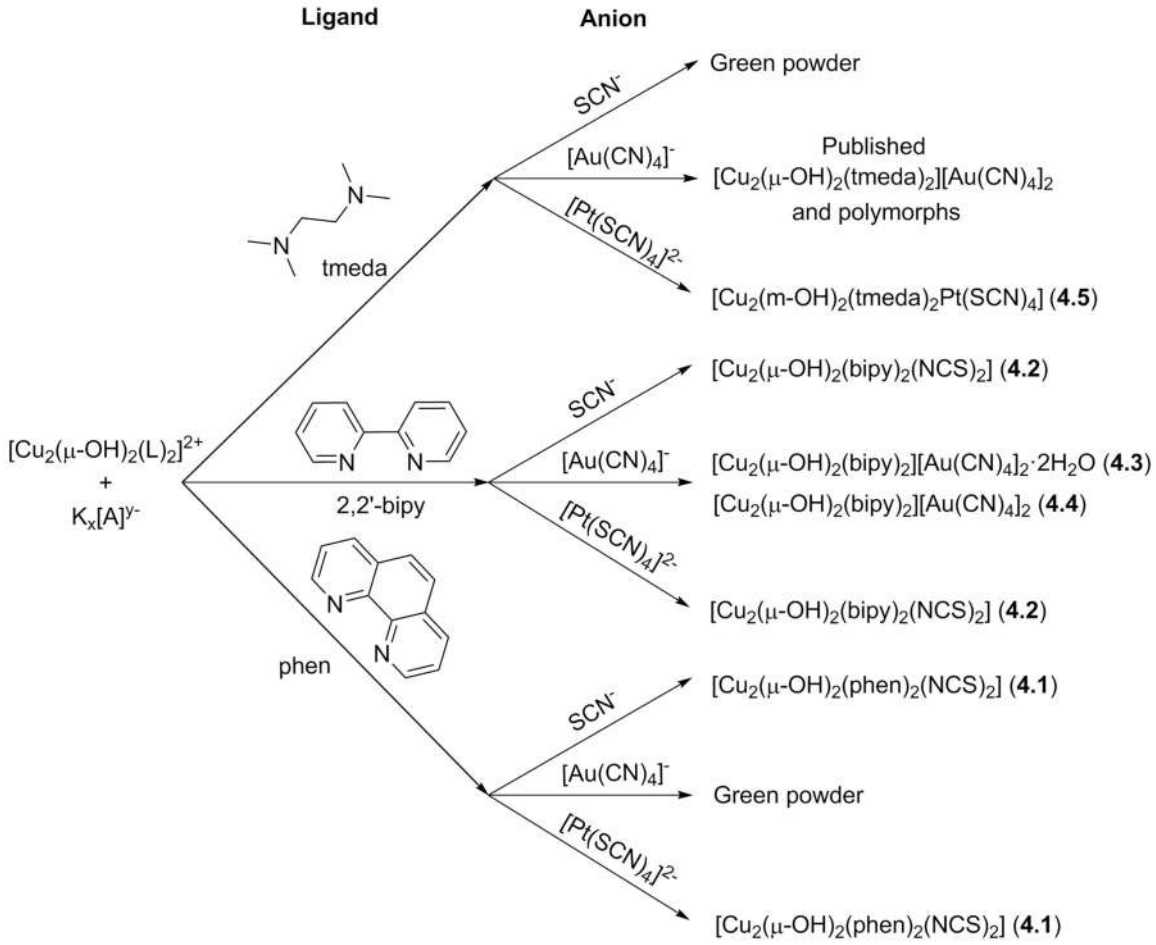

Figure 4.1 Synthetic matrix of Cu(II)-hydroxo dimers with various ancillary ligands and NCS^-, $[Au(CN)_4]^-$ and $[Pt(SCN)_4]^{2-}$.

To synthesize a $[Pt(SCN)_4]^{2-}$-based CP, the first attempt consisted of mixing $K_2[Pt(SCN)_4]$ and $[Cu(\mu\text{-}OH)(phen)]_2(BF_4)_2$ in water. This resulted in a microcrystalline material that was the result of a ligand transfer between $[Pt(SCN)_4]^{2-}$ and [Cu(μ-

OH)(phen)]$_2^{2+}$, as established by identifying the material as a precipitate of [Cu(μ-OH)(phen)(NCS)]$_2$ (**4.1**) and an unidentified Pt-containing byproduct. To synthesize pure **4.1**, [Cu(μ-OH)(phen)]$_2$(BF$_4$)$_2$ and KSCN were mixed slowly in a 1:1 EtOH:H$_2$O solution. After a few minutes, a blue-green powder of **4.1** was separated, isolated by filtration and washed with EtOH. Changing the ratios or solvents resulted in lower yields of **4.1** and other unidentified impure products. Crystals of **4.1** were obtained by layering the reagents in EtOH and H$_2$O.

When using 2,2'-bipy as a ligand instead of phen, the reaction resulted in a ligand transfer between the reagents to yield an impure powder of [Cu(μ-OH)(bipy)(NCS)]$_2$ (**4.2**) and an unknown Pt-containing product. The rational synthesis of **4.2** was completed by mixing [Cu(μ-OH)(bipy)]$_2$(BF$_4$)$_2$ and KSCN in a 1:2 ratio in a 1:1 EtOH:H$_2$O solution, as for **4.1**. Layering the reagents in EtOH and H$_2$O gave crystals of **4.2**; changing the ratios also resulted in lower yields and lower purity.

On the other hand, in previously reported work, [Au(CN)$_4$]$^-$ was treated with [Cu(μ-OH)(tmeda)]$_2$(BF$_4$)$_2$, resulting in multiple polymorphs of the product [Cu(μ-OH)(tmeda)]$_2$[Au(CN)$_4$]$_2$.[231] In order to characterize the full range of products when [Au(CN)$_4$]$^-$ reacts with various Cu(II) hydroxide dimers (where L = 2,2'-bipy and phen), K[Au(CN)$_4$] was mixed with [Cu(μ-OH)(phen)]$_2$(BF$_4$)$_2$ or [Cu(μ-OH)(2,2'-bipy)]$_2$(BF$_4$)$_2$. During the attempts to prepare the phen-containing species, a green powder of unknown composition immediately precipitated no matter what solvent and ratio combinations were used. The species could not be identified properly using standard methods. When mixing K[Au(CN)$_4$] with the bipy-based precursor in a 1:1 MeOH:H$_2$O solution, crystals of Cu(μ-OH)(bipy)]$_2$[Au(CN)$_4$]$_2$·2H$_2$O (**4.3**) were obtained after a few hours of slow evaporation of the mother liquor. Initial attempts at recrystallization of that material in MeOH resulted in crystals of a new product, [Cu(μ-OH)(bipy)]$_2$[Au(CN)$_4$]$_2$ (**4.4**). Subsequent attempts at recrystallization of **4.3** in any solvent other than H$_2$O always resulted in a polycrystalline sample of **4.4**, a pseudopolymorph of **4.3** without interstitial water molecules. Large enough crystals of **4.4** for XRD analysis were obtained from recrystallizing in MeOH. Finally, [Cu$_2$(μ-OH)$_2$(tmeda)$_2$Pt(SCN)$_4$] (**4.5**) was prepared by layering an aqueous solution of [Cu(μ-OH)(tmeda)]$_2$(BF$_4$)$_2$ with an alcoholic (MeOH or

EtOH) solution of $K_2[Pt(SCN)_4]$ in a test tube, which resulted in large orange crystals of the species.

4.3. **Vibrational spectroscopy**

The infrared and Raman spectra for all five complexes were measured between 4000-600 cm^{-1} and 4000-300 cm^{-1}, respectively. The ν_{CN} bands for each of the complexes are presented in Table 4.1 shown below.

Table 4.1 Infrared and Raman ν_{CN} shifts for **4.1**-**4.5**.

Compound	Infrared (cm^{-1})	Raman (cm^{-1})
$[Cu(\mu\text{-}OH)(phen)(NCS)]_2$ (**4.1**)	2091	2085
$[Cu(\mu\text{-}OH)(bipy)]_2[Au(CN)_4]_2 \cdot 2H_2O$ (**4.2**)	2077	2077
$[Cu(\mu\text{-}OH)(bipy)]_2[Au(CN)_4]_2 \cdot 2H_2O$ (**4.3**)	--	2207
	--	2183
$[Cu(\mu\text{-}OH)(bipy)]_2[Au(CN)_4]_2$ (**4.4**)	--	2234
	--	2249
$[Cu_2(\mu\text{-}OH)_2(tmeda)_2Pt(SCN)_4]$ (**4.5**)	2111	2114

For **4.1** and **4.2**, the ν_{CN} peaks are slightly higher in energy than that of an uncoordinated SCN^- unit (2050 cm^{-1} for KSCN) which is in agreement with the general observation that IR and Raman bands of coordinated (iso)thiocyanate ligands shift to higher energy values, as explained in section 2.3.[109] For **4.3**, the ν_{CN} bands in the Raman spectra are close to the expected value for an uncoordinated and/or weakly interacting $[Au(CN)_4]^-$ anion (approx. 2190 cm^{-1}).[232] For **4.4**, the higher values observed for the ν_{CN} bands may be due to the presence of hydrogen bonds between the one $[Au(CN)_4]^-$ counteranion and the Cu(II) core or due to the presence of weak Au-NC interactions (Au1-N4 = 3.27(1) Å, sum of Van der Waals radii = 3.21 Å[141-143]) between the two $[Au(CN)_4]^-$ anions. It is well established that $[Au(CN)_4]^-$ ν_{CN} bands shift to higher energy values when hydrogen bonded or when coordinated to metal centres.[232] For **4.3** and **4.4**, the infrared data did not show any $\mathbf{\nu_{CN}}$ peaks as is expected for $[Au(CN)_4]^-$ due to its D_{4h} point group symmetry and its non IR active symmetrical stretches. For **4.5**, the ν_{CN} bands are observed in the expected range (see Chapter 3) for a $[Pt(SCN)_4]^{2-}$ anion weakly coordinated to a metal centre.

4.4. **Structural Analyses**

4.4.1. **$[Cu(\mu\text{-}OH)(L)(NCS)]_2$ (4.1, L = phen; 4.2, L = bipy).**

The crystal structure of **4.1** is shown in Figure 4.2 and the crystallographic data is shown in Table 4.8. Structural analysis revealed that the asymmetric unit consists of a Cu(II) hydroxo-bridged dimer coordinated to two apical NCS^- anions, one on each metal centre. The dimer is formed by the presence of a crystallographic inversion centre between the two units. The coordination of the anions to the metal centres generate two five-coordinate Cu(II) ions rather than the typically observed square planar Cu(II) units in hydroxide dimers. The tau (τ) value for a five-coordinate geometry indicates the level of distortion of the structure compared to an ideal geometry (square-based pyramidal = 0, trigonal bipyramidal = 1).[147] In this case, τ equals 0.024, indicating a nearly ideal square-based pyramidal geometry for the Cu(II) centres. The coordination distances shown in Table 4.2 are all within the expected range for a Cu(II) metal centre (Cu1-N2 = 2.043(1) Å, Cu1-N3 = 2.026(1) Å and Cu1-O1 = 1.958(1) Å). However, the apical ligand shows a slightly elongated coordination length (Cu1-N1 = 2.199(2) Å) which is expected in five coordinated geometries. There's also the presence of two interstitial water molecules that do not show hydrogen bonding or other interactions with the Cu(II) units. As discussed below in section **4.5**, the magnetic properties of the dimeric unit are influenced by the Cu-O-Cu angle (θ), the co-planarity of the two Cu(II)(OH) units (γ) and the out-of-plane hydrogen angle on the OH- bridge (τ) (Figure 4.3). For **4.1**, the angles θ, γ and τ angles are 97.02(1), 0.0(1) and 37.7(1)°, respectively.

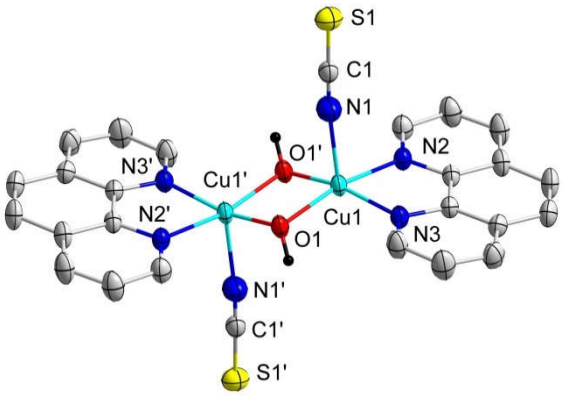

Figure 4.2 The structure of $[Cu(\mu\text{-}OH)(phen)(NCS)]_2 \cdot 2H_2O$ (**4.1**). The phen ligand hydrogen atoms were removed for clarity. Colour code: Turquoise (Cu), Blue (N), Yellow (S), Red (O), Gray (C), Black (H).

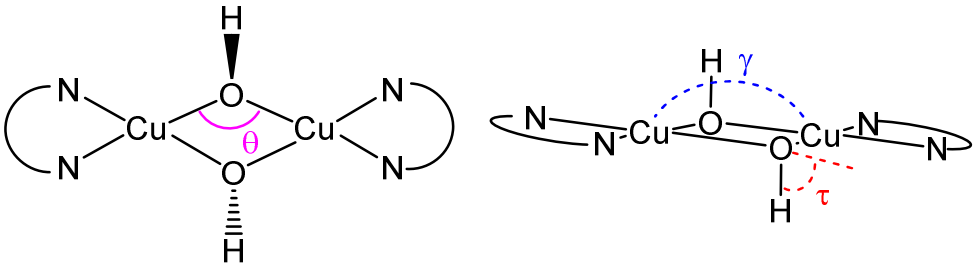

Figure 4.3 Representation of the Cu-O-Cu angle (θ), the co-planarity of the two Cu(II)(OH) units (γ) and the out-of-plane hydrogen angle on the OH-bridge (τ) in a Cu-OH-Cu dimer.

Table 4.2 Selected bond lengths (Å) and angles (°) for $[Cu(\mu\text{-}OH)(phen)(NCS)]_2 \cdot 2H_2O$ (**4.1**).

Cu1-N1	2.199(2)	N2-Cu1-N3	81.26(5)
Cu1-N2	2.043(1)	O1-Cu1-O1'	82.98(5)
Cu1-N3	2.026(1)	N1-Cu1-N2	95.67(6)
Cu1-O1	1.958(1)	N1-Cu1-N3	97.28(7)
Cu1-O1'	1.956(1)	O1-Cu1-N1	98.20(6)
Cu1-Cu1'	2.9315(4)	O1'-Cu1-N1	98.00(7)
Cu1-N1-C1	172.2(2)	N2-Cu1-O1'	95.50(5)
N2-Cu1-O1	166.12(5)	N3-Cu1-O1	96.54(5)
N3-Cu1-O1'	164.63(6)	Cu1-O1-Cu1'	97.02(5)

The structure of $[Cu(\mu\text{-}OH)(bipy)(NCS)]_2$ (**4.2**) shown in Figure 4.4 is similar to **4.1**, but is composed of two crystallographically unique dimers in the unit cell. In this case, one dimer shows hydrogen bonds between the hydroxide bridges and the interstitial water

(O1-O3 = 2.87(1) Å) molecules, whereas the other dimer shows hydrogen bonds between the hydroxide bridges and the coordinated isothiocyanate anions from the adjacent units (O2-S2 = 3.49(1) Å sum of the van der Waals radii = 3.32 Å). In a similar way to **4.1**, the basal coordination distances (Table 4.3) are within the expected ranges for a square-based pyramidal coordination geometry and the apical coordination distances are slightly elongated. τ equals 0.06 and 0.02 for the two crystallographically unique dimers, respectively, indicating a near perfect square-based pyramid coordination geometry in both cases. The apical coordination distances for Cu1-N1 and Cu2-N2 are of 2.267(4) and 2.187(4) Å, respectively. The key θ, γ and τ angles are 97.28(1), 0.0(1), and 52.0(1)° and 97.37(1), 0.0(1), and 51.0(1)° for the first and second crystallographically unique units, respectively.

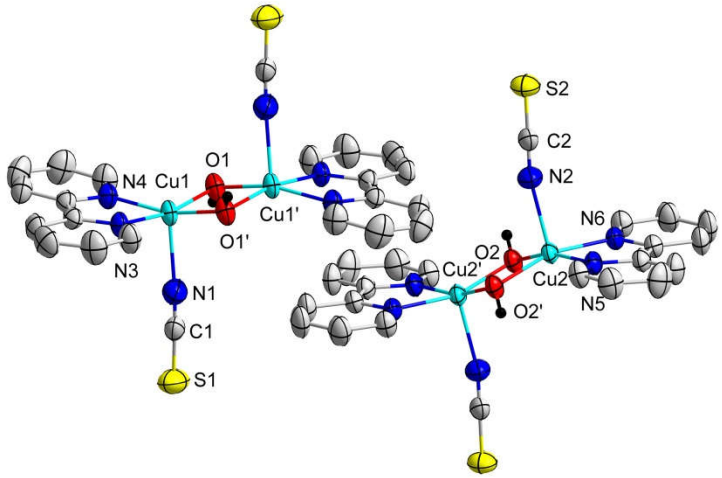

Figure 4.4 The structure of $[Cu(\mu\text{-}OH)(bipy)(NCS)]_2 \cdot H_2O$ (**4.2**). The bipy ligand hydrogen atoms were removed for clarity. Colour code: Turquoise (Cu), Blue (N), Yellow (S), Red (O), Gray (C), Black (H).

Table 4.3 Selected bond lengths (Å) and angles (°) for $[Cu(\mu\text{-}OH)(bipy)(NCS)]_2 \cdot H_2O$ (**4.2**).

Cu1-N1	2.267(4)	N3-Cu1-N4	80.1(1)
Cu1-N3	2.015(3)	O1-Cu1-O1'	82.5(5)
Cu1-N4	2.030(4)	N1-Cu1-N3	95.6(2)
Cu2-N2	2.187(4)	N1-Cu1-N4	98.1(2)
Cu2-N5	1.993(3)	N1-Cu1-O1	96.8(2)
Cu2-N6	2.035(3)	N1-Cu1-O1'	98.1(2)
Cu1-O1	1.937(3)	Cu2-N2-C2	163.2(3)
Cu1-O1'	1.951(3)	N5-Cu2-O2	163.7(2)
Cu2-O2	1.925(3)	N6-Cu2-O2'	162.8(2)
Cu2-O2'	1.949(3)	N5-Cu2-O2'	95.7(1)
Cu1-Cu1'	2.924(1)	N6-Cu2-O2	97.1(1)
Cu2-Cu2'	2.919(1)	N5-Cu2-N6	80.1(1)
Cu1-N1-C1	168.1(3)	O2-Cu2-O2'	82.2(2)
N3-Cu1-O1	167.6(2)	N2-Cu2-N5	97.2(2)
N4-Cu1-O1'	163.7(2)	N2-Cu2-N6	97.1(2)
N4-Cu1-O1	98.0(1)	N2-Cu2-O2	99.1(2)
N3-Cu1-O1'	96.0(1)	N2-Cu2-O2'	100.0(2)

To our knowledge, **4.1** and **4.2** are the first structurally characterized Cu(II) hydroxide dimers with coordinated pseudohalide apical ligands. The reported combinations of dimer cores with potentially coordinating apical ligands (such as NO_3^- or ClO_4^-) resulted in either non- or weakly interacting counteranions with the Cu(II) units,[206-212] whereas for halides, the counteranions are located between the dimers and form hydrogen bonds with the hydroxide bridges instead of being located near the apical positions. In $[Cu(\mu\text{-}OH)(bipy)(CF_3SO_3)]_2$,[233] the coordination distance of the apical $CF_3SO_3^-$ unit is 2.45(1) Å, which is much longer than the 2.199(2), 2.267(4) and 2.187(4) Å distances observed for **4.1** and **4.2**. For +the anions Cl^-[234] and Br^-,[235] the distance between the hydroxo- bridge and the anion is approximately 3.4 Å, suggesting the presence of a weak hydrogen bond interacting with the core unit and the distance to the nearest Cu(II) ion is approximately 4.9 Å, indicating the lack of any coordination to the apical position.

4.4.2. $[Cu(\mu\text{-}OH)(bipy)]_2[Au(CN)_4]_2 \cdot x(H_2O)$ (4.3: x = 2; 4.4: x = 0).

Complexes **4.3** and **4.4** consist of pseudo-polymorphs[237-238] made of two Cu(II) hydroxide-bridged dimers with two $[Au(CN)_4]^-$ counter anions (Figure 4.5). The coordination distances of interest for these two complexes are shown in Table 4.4. As explained in Section 4.2, the formation of these two complexes is controlled *via* the crystallization conditions and the structural differences between the complexes are attributed to the presence or absence of two H_2O molecules in the interstitial lattice for **4.3** and **4.4**, respectively. In the former complex, the two water molecules form hydrogen bonds with both the hydroxide bridges of the Cu(II) units and the $[Au(CN)_4]^-$ unit (O1-O2 = 3.042(1) Å, O2-N3 = 2.92(1) Å). In **4.4**, the absence of these interstitial water molecules causes the hydroxide bridges to hydrogen bond directly with the $[Au(CN)_4]^-$ counter anions (N3-O1' = 2.931(6) Å). For both complexes, the coordination geometry for the Cu(II) metal centre is square planar with minimal distortion and minimal interactions with the counter anions in the axial positions (Cu1-N1 = 3.08(1) Å and Cu1'-N2 = 3.13(1) Å for **4.3**, and Cu1-N3 = 2.95(1) Å for **4.4**, sum of the van der Waals radii = 2.95 Å).[141-143] No Au-Au interactions were observed in either system, consistent with the d^8 Au(III) metal centre. For **4.3** and **4.4**, the θ, γ and τ angles are 102.1(1), 0.0(1), and 4.44(1)° and 98.4(1), 0.0(1), and 38.5(1)°, respectively.

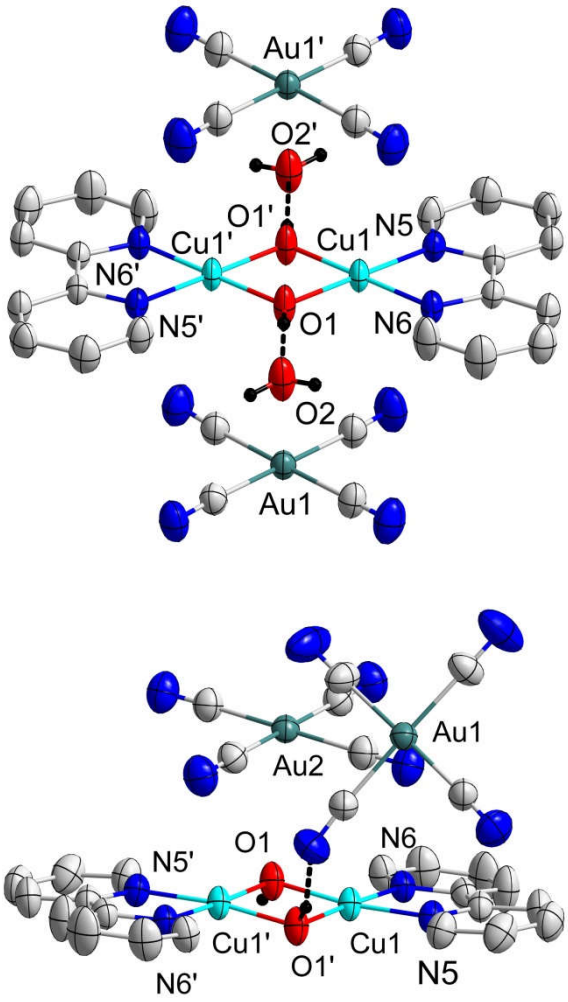

Figure 4.5 The structure of $[Cu(\mu\text{-}OH)(bipy)]_2[Au(CN)_4]_2 \cdot 2H_2O$ (**4.3**, top) and the structure of $[Cu(\mu\text{-}OH)(bipy)]_2[Au(CN)_4]_2$ (**4.4**, bottom). Hydrogen bonds are depicted as black fragmented lines. The bipy ligand hydrogen atoms were removed for clarity. Colour code: Green (Au), Turquoise (Cu), Blue (N), Yellow (S), Red (O), Gray (C), Black (H).

4.4.3. $[Cu_2(\mu\text{-}OH)_2(tmeda)_2Pt(SCN)_4]$ (4.5).

Complex **4.5** consists of a 1D coordination polymer in which the Cu(II) hydroxide dimers are bridged via two *trans*-NCS units from a $[Pt(SCN)_4]^{2-}$ anion (Figure 4.6). A general depiction of structure of **4.5** is shown in Figure 4.6 whereas its supramolecular structure is shown in Figure 4.7. The coordination distances (Table 4.5) of these two NCS^- units is strongly elongated (Cu1-N2 = 2.521(4) Å) suggesting weak coordination for the two apical units, more so than for complexes **4.1** and **4.2**. Similarly to these two complexes,

the weak coordination of the apical units results in a non-distorted square-based pyramidal geometry for the Cu(II) units with τ = 0.03. In this case however, the two non-coordinating SCN^- ligands of the $[Pt(SCN)_4]^{2-}$ unit form a hydrogen bond (Figure 4.7) with the hydroxide bridges of the Cu(II) dimer (N1-O1 = 3.015(1) Å) of the adjacent chains as opposed to interstitial water molecules. The hydrogen bonds further increase the dimensionality of the system to a 2D sheet instead of a linear 1D coordination polymer. For **4.5**, the θ, γ and τ angles are 100.39(1), 0.0(1), and 24.9(1)°, respectively.

Table 4.4. Selected bond lengths (Å) and angles (°) for $[Cu(\mu\text{-}OH)(bipy)]_2[Au(CN)_4]_2 \cdot 2H_2O$ (**4.3**) and $[Cu(\mu\text{-}OH)(bipy)]_2[Au(CN)_4]_2$ (**4.4**).

	4.3	**4.4**
Cu1-N5	1.987(3)	1.996(3)
Cu1-N6	1.983(3)	1.978(3)
Cu1-O1	1.921(2)	1.919(3)
Cu1-O1’	1.922(2)	1.930(3)
Cu1-N1	3.08(1)	--
Cu1’-N2	3.13(1)	--
Cu1-N3	--	2.95(1)
N5-Cu1-O1	177.4(1)	172.9(1)
N6-Cu1-O1’	177.7(1)	176.1(1)
N5-Cu1-N6	81.7(1)	81.6(1)
N5-Cu1-O1’	100.3(1)	99.8(1)
N6-Cu1-O1	100.2(1)	97.5(1)
O1-Cu1-O1’	77.9(1)	81.6(1)

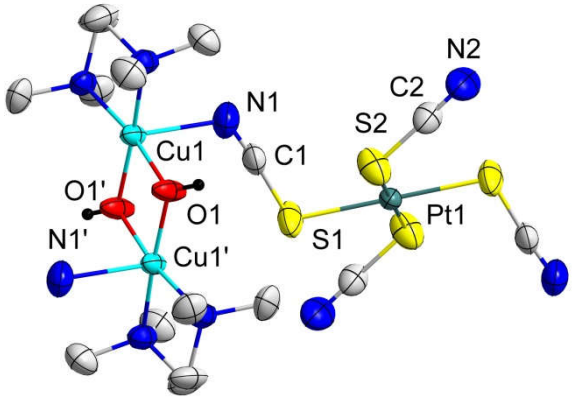

Figure 4.6 The structure of $[Cu_2(\mu\text{-}OH)_2(tmeda)_2Pt(SCN)_4]$ (**4.5**). The tmeda ligand hydrogen atoms were removed for clarity. Colour code: Turquoise (Cu), Green (Pt), Blue (N), Yellow (S), Red (O), Gray (C), Black (H).

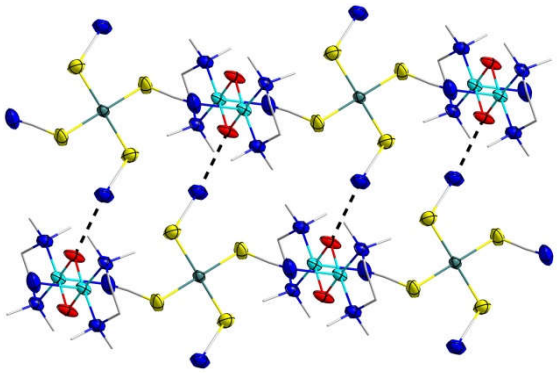

Figure 4.7 The supramolecular structure of $[Cu_2(\mu\text{-}OH)_2(tmeda)_2Pt(SCN)_4]$ (**4.5**) showing the presence of the hydrogen bonds between the hydroxo-bridges and the SCN^- ligands as black dashed lines. The tmeda ligand hydrogen atoms were removed for clarity. Colour code: Turquoise (Cu), Green (Pt), Blue (N), Yellow (S), Red (O), Gray (C), Black (H).

Table 4.5. Selected bond lengths (Å) and angles (°) for $[Cu_2(\mu\text{-}OH)_2(tmeda)_2Pt(SCN)_4]$ (**4.5**).

Cu1-N2	2.521(4)	N3-Cu1-O1	171.1(1)
Cu1-N3	2.040(3)	N4-Cu1-O1'	172.7(1)
Cu1-N4	2.066(3)	N3-Cu1-O1'	96.0(1)
Cu1-O1	1.911(2)	N4-Cu1-O1	96.7(1)
Cu1-O1'	1.927(2)	N3-Cu1-N4	87.0(1)
Cu1-Cu1'	2.9506(7)	O1-Cu1-O1'	79.5(1)
Pt1-S1	2.320(1)	N1-Cu1-N3	93.5(1)
Pt1-S2	2.316(1)	N1-Cu1-N4	95.9(1)
S1-Pt1-S2'	91.42(4)	N1-Cu1-O1	94.3(1)
S1-Pt1-S1'	179.995(1)	N1-Cu1-O1'	90.6(1)
Cu1-N2-C2	120.4(3)		

4.5. **Magnetic properties.**

The dc susceptibility data for **4.1** to **4.5** were obtained between 1.8 and 300 K under a dc applied field of 1000 Oe. The $\chi_M T$ *vs T* plots are presented in Figure 4.8 for **4.1** to **4.5**, respectively. The χ_M *vs T* and $1/\chi_M$ *vs T* are shown in Figure 4.9. For all complexes, at room temperature, the $\chi_M T$ values (Table 4.5) correspond closely to the predicted value of 0.82. cm^3 K mol^{-1} for two non-interacting Cu(II) metal centres (with g = 2.10). Upon cooling, **4.1**, **4.2**, **4.3** and **4.4** exhibit ferromagnetic interactions between the Cu(II) metal centres while **4.5** shows antiferromagnetic interactions. For **4.1**-**4.4**, the $\chi_M T$ *vs T* data reaches maximum values of 1.03, 1.08, 1.39 and 1.11 cm^3 K mol^{-1} at 12.0, 13.7, 8.0 and 12.1 K, respectively, before quickly decreasing below that temperature. For **4.5**, the $\chi_M T$ *vs T* product decreases slowly as the temperature decreases, reaching a minimum of 0.63 cm^3 K mol^{-1} at 1.8 K, suggesting the presence of only antiferromagnetic interactions between the metal centres. In all cases, the rapid decrease at low temperature can be attributed to either a thermal depopulation of the low lying excited states, intermolecular antiferromagnetic interactions between the complexes or saturation. In the case of **4.5**, magnetic anisotropy could also be the cause of this rapid decrease at low temperature.

The field dependence of the magnetization data of all complexes are shown in Figure 4.10. For **4.1**-**4.4**, the curve reaches saturation at 7 T and approximately 2 μ_β as

expected for dinuclear Cu(II) complexes (counted as 1 μ_β per unpaired electron). For **4.5**, the lack of saturation at 7 T suggests the presence of magnetic anisotropy in the complex.

For **4.1**-**4.4**, the χ_M *vs T* data was fit to the Bleaney-Bowers equation with an intermolecular interaction component (*zJ'*), as shown in equations 1 and 2.[239] For **4.5**, the data was modeled to the Bleaney-Bowers equation without the intermolecular interaction component, which generated a better fit of the data overall. The resulting fitting parameters for all five complexes are shown in Table 4.6.

$$H = -2J[\hat{S}_1\hat{S}_2] \qquad \textbf{Equation 4.1}$$

$$\chi = \frac{2Ng^2\beta^2}{\left[kT - \frac{2zJ'}{3+\exp\left(-\frac{2J}{kT}\right)}\right][3+\exp\left(-\frac{2J}{kT}\right)]} \qquad \textbf{Equation 4.2}$$

Table 4.4 Magnetic susceptibility data and fitting parameters for **4.1**-**4.5**.

Complex	χT *vs T* product at 300 K (cm^3 K / mol)	Fitting parameters with Bleaney-Bowers for χ_M vs *T*		
		g	*J* (cm^{-1})	*zJ'* (cm^{-1})
4.1	0.909(1)	2.167(1)	11.7(3)	-0.48(2)
4.2	0.942(1)	2.197(2)	15.4(4)	-0.55(1)
4.3	0.889(1)	2.141(1)	17.8(3)	-0.113(6)
4.4	0.974(1)	2.248(2)	8.1(3)	-0.29(1)
4.5	0.795(1)	2.071(2)	-0.37(1)	--

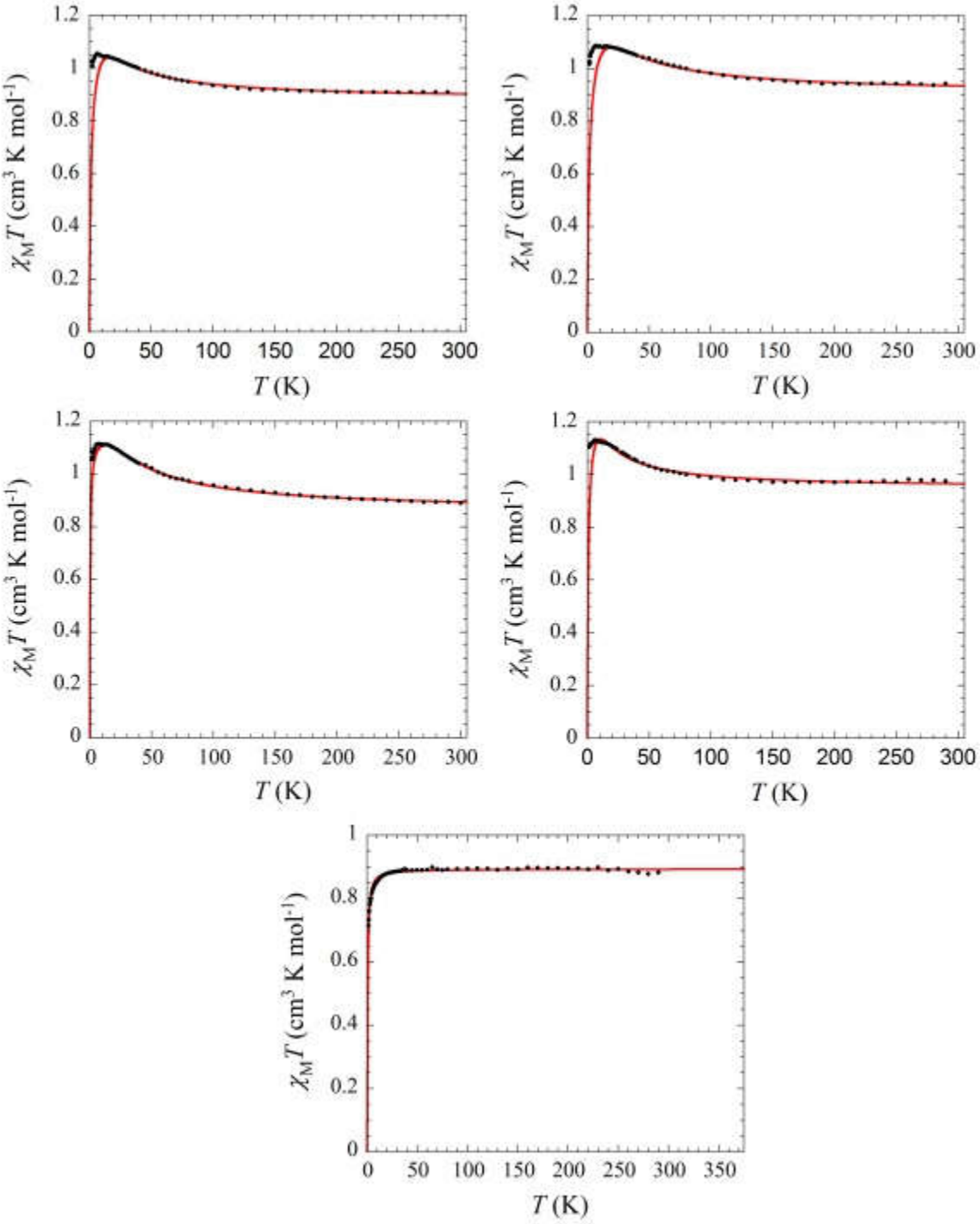

Figure 4.8 $\chi_M T$ *vs* T data for **4.1** (top left), **4.2** (top right), **4.3** (middle left), **4.4** (middle right) and **4.5** (bottom) at 1000 Oe between 1.8 and 300 K. The solid lines represent the fits to the data (see text).

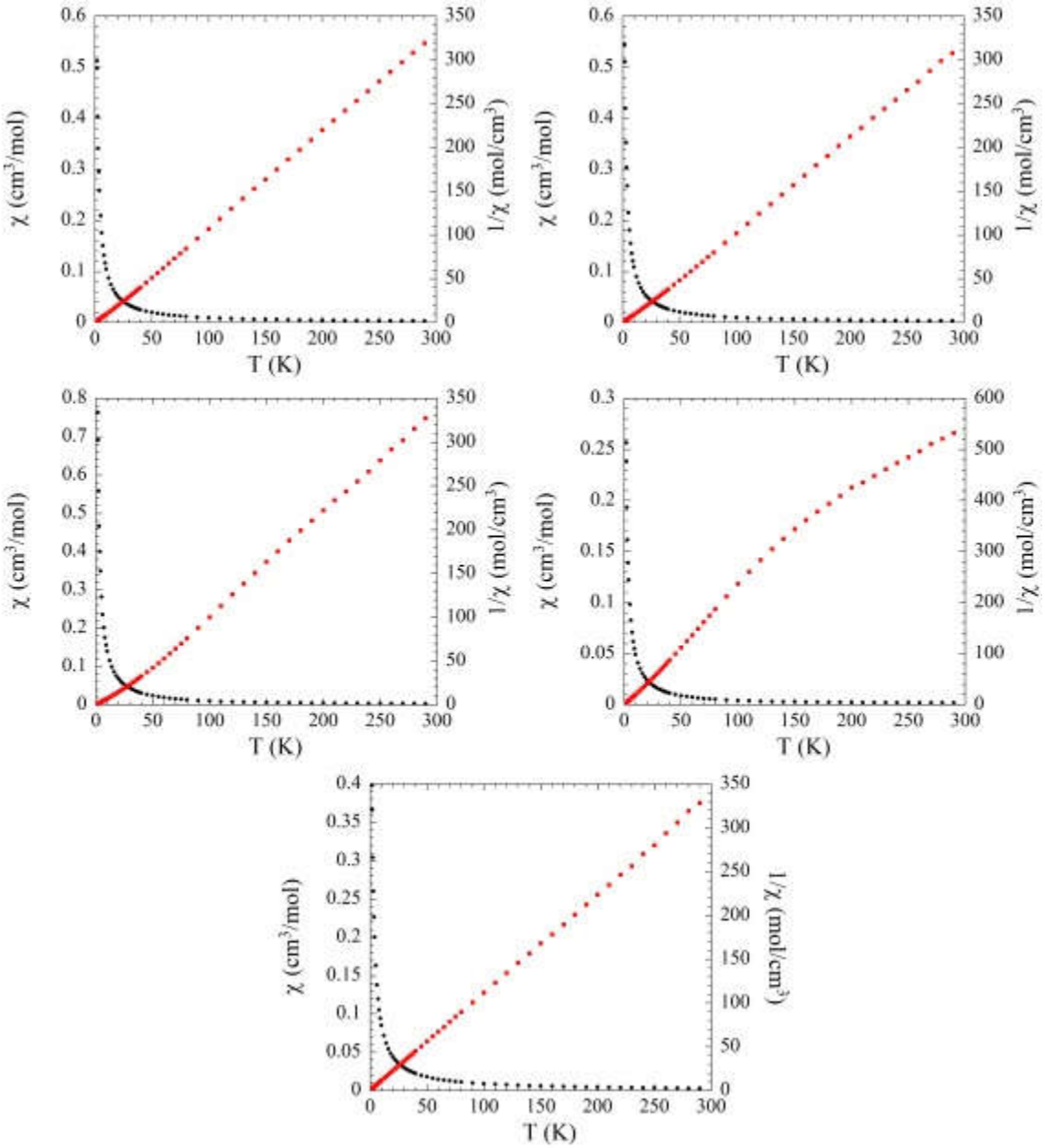

Figure 4.9 χ_M *vs T* and $1/\chi_M$ *vs T* data for **4.1** (top left), **4.2** (top right), **4.3** (middle left), **4.4** (middle right) and **4.5** (bottom) at 1000 Oe between 1.8 and 300 K.

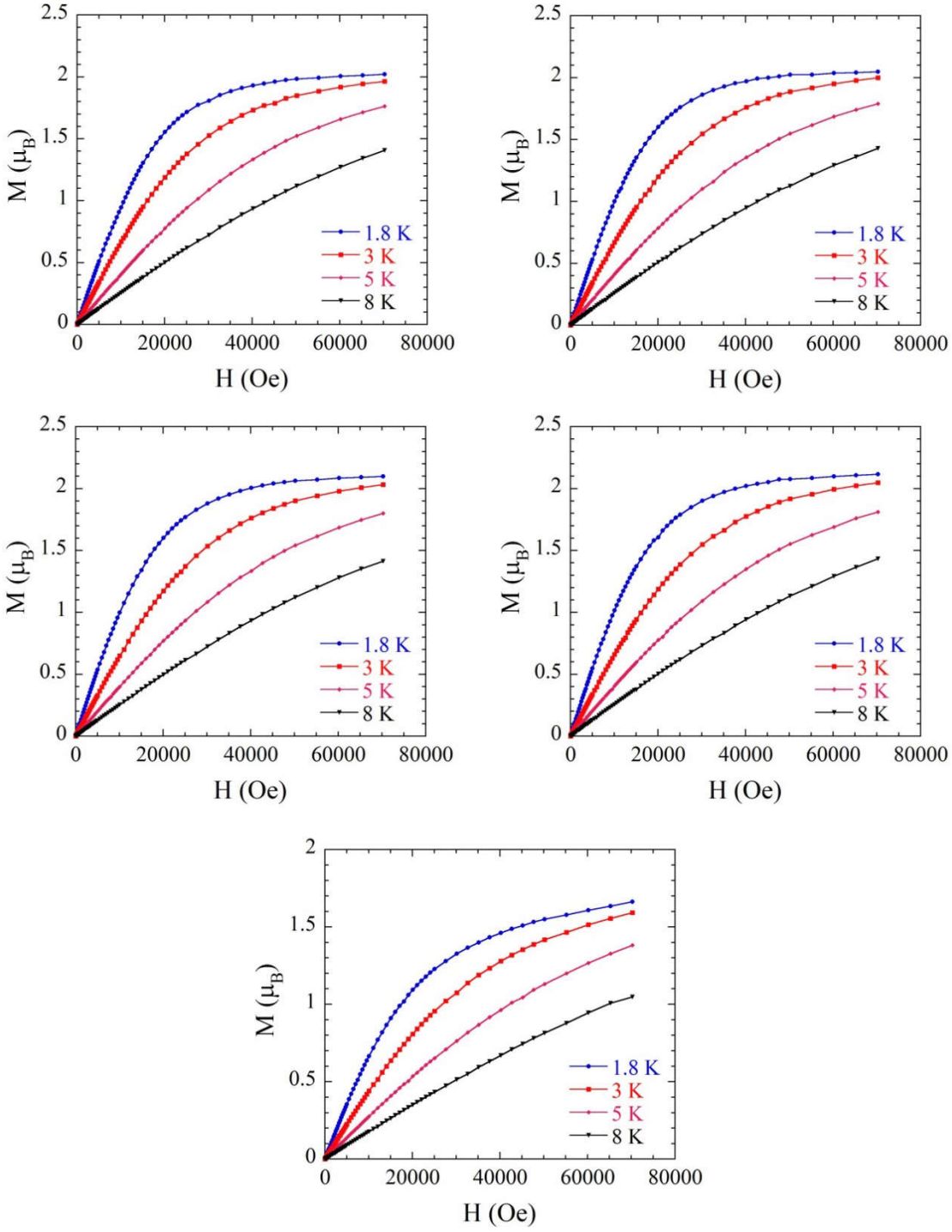

Figure 4.10 Field dependence of the magnetization data for **4.1** (top left), **4.2** (top right), **4.3** (middle left), **4.4** (middle right) and **4.5** (bottom) at 1.8, 3, 5 and 8 K between 0 and 70 000 Oe. The solid lines are guides to the eye only.

The landmark magnetostructural correlation for Cu(II) hydroxide-bridged dimers reported by Hatfield and Hodgson in 1974 states that the J-coupling in a Cu(II) dimer is dependent on the Cu-O-Cu angle (θ), where a Cu-O-Cu angle of > 97.5˚ generates antiferromagnetic coupling while an angle of < 97.5˚ yields ferromagnetic coupling.[240-242] To date, most reported dimers, which contain non- or weakly- interacting counteranions, follow this trend fairly well.[206-212, 214-217] As established by these numerous experimental observations, the J-couplings also depend on the nature of the ligand because of the binding properties of the ligand impacts the Cu_2O_2 core geometry. For example, as a general trend, tmeda-based complexes show Cu-O-Cu angles varying between 100 and 102° and antiferromagnetic interactions, whereas bipy-based complexes show angles between 95 and 97° and ferromagnetic interactions. These observations are in agreement with the structural correlation first established by Hatfield and Hodgson. On the other hand, to our knowledge, phen-based Cu(II) hydroxo-bridged dimers have not been properly magnetically characterized to date.

More recently, E. Ruiz and co-workers demonstrated that the magnetic properties of the dimers are also dependent on several other structural factors.[242-243] These factors consist of the out-of-plane hydroxide hydrogen angle (τ) and the planarity of the Cu_2O_2 dimer core (γ) (Figure 4.3). Using DFT calculations,[245-254] they demonstrated that gradually increasing τ from 0° to 60° increased the value of interaction (J) ferromagnetically up to 150 cm^{-1}. Similarly, increasing γ angle also caused a substantial change in the value of the interaction in the model dimer. They concluded that even a small distortion of the structure caused by forces, such as intermolecular interactions and/or an apical ligand, could have considerable effect on the resulting interaction for the dimer.

With this in mind, a summary of the key geometric angles, namely θ, γ and τ, for **4.1**-**4.5** is shown in Table 4.5. In addition, the empirically predicted J-value J_{emp} based on the Hatfield model (i.e., only considering the Cu-O-Cu angle, with g = 2) is shown, along with the experimentally determined J_{exp}. In the case of **4.1** and **4.2**, deviations were observed between J_{emp} and the fit to the experimental data (**4.1**: J_{emp} = 42 cm^{-1}, J_{exp} = 11.7(3) cm^{-1}; **4.2**: J_{emp} = 13 cm^{-1}, J_{exp} = 15.4(4) cm^{-1}). On the other hand, for **4.3**, **4.4** and **4.5**, larger deviations were observed by as much as 176 cm^{-1} for **4.3**.

When comparing **4.3** to **4.1** and **4.2**, one might suggest that the presence of an apical ligand has little effect on the J-coupling itself, but instead has an indirect effect by influencing the geometry of the core, which in turn affects the magnetic coupling between the Cu(II) metal centres. Indeed, **4.3** shows little apical influence from the counteranions yet demonstrates a different coupling value when compared to the empirical value established by Hatfield and Hodgson.

In order to explain this deviation, a closer look at the geometry of the core was necessary. For **4.3**, **4.4** and **4.5**, the complexes are perfect co-planar systems since the γ angle is 0.0(1)°. This suggests that the discrepancy in the magnetic interaction cannot be attributed to a distortion of the planarity of the Cu(II) system. However, in all three cases, the τ angle varies significantly when compared to the typical angles in similar Cu(II) dimers with the same or similar bidentate nitrogen ligands. According to published data,[206-217] when the hydrogen out-of-plane angle τ varies between 40 and 60°, the coupling value is close to the Hatfield and Hodgson empirical value. This is dependent on the ligand itself, with aliphatic ligands leading to smaller τ angles and aromatic ligands resulting in greater τ angles.[242-243] For **4.5**, the τ angle is 24.9 ° which is much smaller than the typical angle observed for aliphatic ligands. This difference should generate a more antiferromagnetic interaction between the Cu(II) metal centres due to a smaller oxygen 2p orbital contribution to the superexchange pathway.[242-243] For **4.5** however, the experimental value of -0.37(1) cm^{-1} is more ferromagnetic than the calculated empirical value of -102 cm^{-1}. On the other hand, as mentioned in the structural section, the dangling SCN^- ligands on the $[Pt(SCN)_4]^{2-}$ bridging units form a hydrogen bond with the hydroxo-bridge of the adjacent 1D chain. Structural contributions that affect the orbital contributions in the hydroxo- bridges can be significant factors in the overall magnetic properties of the systems and that they need to be carefully considered.[214-217]

For **4.3** and **4.4**, the τ angles are 4.44(1) and 38.5(1)°, respectively, which are also smaller than the typical τ angle for bipy-based systems, and the experimental values of 17.8(3) and 8.1(3) cm^{-1}, respectively, are also more ferromagnetic than the calculated empirical values. Complex **4.3** has a particularly large discrepancy in both the τ angle and the coupling value. In both cases, hydrogen bonds are also observed between the

core unit and either the interstitial water molecules (for **4.3**) or the counteranions (for **4.4**). Overall, the sum of these two factors, namely the discrepancy in the τ angle and the presence of hydrogen bonds likely can alter the orbital contributions of the hydroxo-bridges, and thus the resulting magnetic interaction between the Cu(II) metal centres.

Table 4.5 Summary of the magnetostructural parameters for **4.1**-**4.5**.

		θ (°)	γ (°)	τ (°)	J_{emp} (cm^{-1})	J_{exp} (cm^{-1})
2	**1**	97.02(1)	0.0(1)	37.7(1)	42	11.7(3)
	molecule 1	97.28(1)	0.0(1)	52.0(1)	13	15.4(4)
	molecule 2	97.37(1)	0.0(1)	51.0(1)	13	
	3	102.1(1)	0.0(1)	4.44(1)	-158	17.8(3)
	4	98.4(1)	0.0(1)	38.5(1)	-31	8.1(3)
	5	100.39(1)	0.0(1)	24.9(1)	-102	-0.37(1)

In previous work, the $[Cu_2(\mu\text{-}OH)_2(tmeda)_2]$ / $[Au(CN)_4]$ systems presented experimental values that were in good agreement with the calculated empirical values.[50] For $[Cu(\mu\text{-}OH)(tmeda)Au(CN)_4]_2$ and $[\{Cu(\mu\text{-}OH)(tmeda)\}_2Au(CN)_4]\text{-}[ClO_4]\cdot MeOH$, the experimental values were -143.6 and -64.8 cm^{-1}, respectively, and the empirical values were -102.5 and -63.75 cm^{-1}. In these two cases, the τ angles were found to be within the range of the usually observed angles (47.8 and 57.5°) and no significant hydrogen bonds were observed between the units. However, in the case of $[Cu(\mu\text{-}OH)(tmeda)Au(CN)_4]_2$, the experimental value was 57.5 cm^{-1} and the empirical value was 70.4 cm^{-1}. Despite the fact that hydrogen bonding was observed between the chains, it appears that in this case, it had little to no effect on the magnetic coupling between the metal centres.

In the literature, there are multiple examples where hydrogen bonding has a significant effect on the coupling between the metal centres. For example, the system $[Cu(\mu\text{-}OH)(tmeda)]_2Cl_2$ presents hydrogen bonding between the counteranion and the hydroxo-bridges, has no apical coordination of the counteranions and has very little distortion in the geometry of the core, and has experimental and empirical values of -463 and -301 cm^{-1}, respectively. Overall, this suggests that, in this case, the hydrogen bond has a significant effect on the magnetic interactions and reinforces our hypothesis that the hydrogen bonding plays an important role in determining the magnetic properties of these Cu(II) hydroxo-bridged dimers.

4.6. **DFT Calculations**

In an attempt to understand the effect of hydrogen bonding and geometrical distortion of the core on our systems, DFT calculations were performed using the B3LYP functional and a variety of basis sets. When geometry optimizations were performed on **4.1**-**4.5** using the XRD structural data as a source, the resulting structures were highly distorted and did not correspond to the observed experimental structures. Thus, it was necessary to do single point calculations in order to assess the energy levels and be able to use the Yamaguchi formula[255-256] to get the theoretical value of the magnetic coupling between the units. This method was the same as used by E. Ruiz and co-workers in their theoretical investigation of the effect of the geometry of the core on the magnetic coupling.[242-243]

For **4.1** and **4.2**, the calculations resulted in magnetic couplings that were close to the experimental and empirical values observed in our work, indicating that the method used was valid. Unfortunately, for **4.3**-**4.5**, the single point calculations resulted in magnetic interactions that were either much more antiferromagnetic or ferromagnetic than the experimental and empirical data (by as much as 400 cm^{-1} in **4.3**) or were failed calculations that could not converge. In light of the fact that these results did not correspond to the observed and empirical data, we did not complete the full study and could not determine the effect of the hydrogen bonding on the structure accurately from a theoretical approach.

Nonetheless, these preliminary calculations on the triplet (**4.4**) and broken symmetry singlet (**4.3** and **4.5**) electronic states show minimal spin density (less than approximately 0.001) on the counteranion units, suggesting that the deviation from the empirical magnetostructural correlation model is likely due to a distortion of the core.

4.7. **Conclusions and future work**

In this chapter, new hydroxide-bridged Cu(II) coordination dimers and one 1D polymer were synthesized in an effort to control their inter- and intra-molecular interactions and in turn to tune their magnetic properties using the building blocks of interest, namely NCS^-

, $[Pt(SCN)_4]^{2-}$ and $[Au(CN)_4]^-$. As a result, a new family of Cu(II) hydroxo-bridged dimers were prepared, one that contains late-transition metal counteranions (**4.3**, **4.4** and **4.5**), along with two new Cu(II) hydroxo-bridged dimers with coordinated NCS^- apical ligands (**4.1** and **4.2**). Structural analyses revealed that **4.3** and **4.4** are double salts of the Cu(II) dimers with $[Au(CN)_4]^-$ counter anions whereas **4.5** consists of a 1D coordination polymer composed of the dimer core bridged by trans-bridging $[Pt(SCN)_4]^{2-}$ units.

In an attempt to establish a magnetostructural correlation for this new family of Cu(II) hydroxide-bridged dimers, the magnetic properties of all five complexes were measured using SQUID magnetometry. For **4.1** and **4.2**, the magnetic interaction between the Cu(II) metal centres corresponded closely to the empirical correlation first established by Hatfield and Hodgson.[205] However, in the case of **4.3**, **4.4** and **4.5**, a large difference was observed between the experimental data and the empirical trend.

In all cases, after further investigations, it was established that the presence of an apical ligand does not appear to directly impact the magnetic properties of the Cu(II) hydroxide-bridged units. On the other hand, these apical coordinations can cause a distortion in the geometry of the core that leads indirectly to an alteration of the magnetic interactions between the metal centres. In fact, as established theoretically by E. Ruiz and co-workers, any structural distortion that affects the 2p orbital contribution of the hydroxide bridges will have a significant effect on the magnetic interaction between the Cu(II) metal centres and will force a deviation from the simple magnetostructural correlation established by Hatfield and Hodgson.

In this work, it was suggested that the presence of a hydrogen bond to the OH^- bridge could also have a significant effect on the magnetic properties of the system. Further work is necessary in order to establish the exact effect of the presence of that hydrogen bond on the interaction between the metal centres *via* either successful DFT calculations or by synthesizing a series of new complexes containing the hydrogen bond in question and to establish a magnetostructural trend between the complexes. In theory, this could be achieved by coupling a variety of building blocks other than $[Au(CN)_4]^-$ and $[Pt(SCN)_4]^{2-}$ prone to hydrogen bonding, such as $[AuX_2(CN)_2]^-$ and $[Pt(CN)_4]^{2-}$, with the series of Cu_2O_2 cores used in this work, using the ligands tmeda, 2,2'-bipy and phen.

Overall, this work demonstrated that CPs of interest with unique physical properties, such as magnetism, can be synthesized using select building blocks in combination with $[Pt(SCN)_4]^{2-}$ or SCN^-, and cyanide-based analogues. This was first shown in Chapter 3 by simply changing the ligand of choice in our regular synthetic strategy, but in this case, the building blocks consisted of molecules showing unique magnetic properties which were observed in the resulting CPs, showing that $[Pt(SCN)_4]^{2-}$ can be used as a bridging unit of choice in the synthesis of CPs and that the latter presents enough kinetic stability in solution to avoid decomposition in most cases. The work in this Chapter could be further refined by attempting to synthesize the $[Pt(SCN)_4]^{2-}$ CPs using the phen and 2,2'-bipy ligand-based building blocks using alcoholic solvents and water to lessen the lability of $[Pt(SCN)_4]^{2-}$ in solution, and thus hopefully synthesize the targeted CPs.

4.8. **Experimental**

4.8.1. **General Procedures and Materials.**

The complex $[Cu(\mu\text{-}OH)(tmeda)]_2(BF_4)_2$ was prepared according to previously published syntheses.[50] $[Cu(\mu\text{-}OH)(bipy)]_2(BF_4)_2$ and $[Cu(\mu\text{-}OH)(phen)]_2(BF_4)_2$ were prepared using the same synthetic strategy as for $[Cu(\mu\text{-}OH)(tmeda)]_2(BF_4)_2$ but by replacing tmeda with the appropriate ligand in the same ratio. $K_2[Pt(SCN)_4]$ was prepared as described in section 3.7.2. All other starting materials were bought directly from commercial sources and were used without further purification. All other procedures and materials are as described in section 2.8.1.

4.8.2. **Synthetic procedures**

$[Cu(\mu\text{-}OH)(phen)(NCS)]_2 \cdot 2H_2O$ (4.1).

To a 10 mL aqueous solution of $[Cu(\mu\text{-}OH)(phen)]_2(BF_4)_2$ (69 mg, 0.10 mmol) was added a 5 mL aqueous solution of KSCN (19 mg, 0.2 mmol). A precipitate of $[Cu(\mu\text{-}OH)(phen)(NCS)]_2 \cdot 2H_2O$ (**4.1**) was immediately obtained and was isolated by filtration and dried *in vacuo*. Green plate-shaped crystals of **4.1** were obtained from the filtrate after 24 hours. Yield: 92.0 % (0.062 g). IR (ATR, cm-1): 3537, 3497, 3060, 2091 (ν_{CN}),

1625, 1585, 1519, 1494, 1470, 1456, 1431, 1220, 1149, 1104, 848, 771, 735, 719. Anal. Calcd. for $C_{26}H_{18}N_6Cu_2O_2S_2 \cdot 2H_2O$: C, 46.43; H, 3.29; N, 12.50 %. Found: C, 46.68; H, 3.17; N, 12.36 %. Raman (514 nm, %Ip: 1, cm^{-1}): 3072, 2085 (ν_{CN}), 1645, 1603, 1582, 1506, 1451, 1425, 1307, 1050, 763, 732, 553, 427, 368, 255, 126. Mixing a stoichiometric amount of $K_2[Pt(SCN)_4]$ and $[Cu(OH)(phen)]_2(BF_4)_2$ in water also results in a green precipitate of **4.1** (but of lower purity), along with an orange solution.

[Cu(μ-OH)(bipy)(NCS)]$_2$·H$_2$O (4.2).

To a 10 mL solution of $[Cu(\mu\text{-}OH)(bipy)]_2(BF_4)_2$ (64 mg, 0.10 mmol) in EtOH:H_2O 1:1 was slowly added a 10 mL solution of KSCN (19 mg, 0.2 mmol) in EtOH:H_2O 1:1. The mixture was stirred for 15 minutes, yielding a blue-green powder of $[Cu(\mu\text{-}OH)(bipy)(NCS)]_2 \cdot H_2O$ (**4.2**) which was isolated by filtration and dried *in vacuo*. Yield: 67 % (0.040 g). IR (ATR, cm-1): 3518, 2077 (ν_{CN}), 1606, 1599, 1574, 1492, 1470, 1444, 1313, 1249, 1171, 1160, 1096, 1071, 1059, 1029, 1016, 872, 763, 731. Anal. Calcd. for $C_{22}H_{18}N_6Cu_2O_2S_2$: C, 44.90; H, 3.08; N, 14.29%. Found: C, 44.28; H, 2.92; N, 13.94%. Raman (785 nm, %Ip: 0.5, cm-1): 2077 (ν_{CN}), 1598, 1567, 1491, 1319, 1265, 1158, 1058, 1029, 770, 477, 366, 247, 227, 215, 183, 124. Crystals of **4.2** were obtained after 3 days by layering a 5 mL ethanolic solution of KSCN (19 mg, 0.2 mmol) over a 5 mL aqueous solution of $[Cu(\mu\text{-}OH)(bipy)]_2(BF_4)_2$ (64 mg, 0.10 mmol). The spectroscopic data of the crystals corresponded to the spectroscopic data of the powder. As for **4.1**, **4.2** can also be prepared (in lower purity) by mixing a stoichiometric amount of $K_2[Pt(SCN)_4]$ and $[Cu(\mu\text{-}OH)(bipy)]_2(BF_4)_2$ in water.

[Cu(μ-OH)(bipy)]$_2$[Au(CN)$_4$]$_2$·2H$_2$O (4.3).

To a 20 mL aqueous solution of $[Cu(\mu\text{-}OH)(bipy)]_2(BF_4)_2$ (64 mg, 0.10 mmol) was slowly added a 20 mL aqueous solution of $K[Au(CN)_4]$ (66 mg, 0.20 mmol). A resulting blue precipitate of $[Cu(\mu\text{-}OH)(bipy)]_2[Au(CN)_4]_2 \cdot 2H_2O$ (**4.3**) appeared immediately. The solution was stirred for 15 minutes and then filtered. Recrystallization of **4.3** was performed by slow evaporation in 10 mL of 1:1 MeOH:H_2O. In order to fully dissolve **4.3**, the solution was heated at 60 °C for 15 minutes. Crystals of **4.3** were obtained after approximately 48 hours. Yield: 56 % (0.062 g). IR (ATR, cm^{-1}): 3457, 3345, 1687, 1612, 1577, 1501, 1477, 1457, 1444, 1419, 1318, 1251, 1170, 1156, 1109, 1035, 1023, 975, 902, 772, 73. Anal. Calcd. for $C_{28}H_{18}N_{12}Au_2Cu_2O_2 \cdot 2H_2O$: C, 30.27; H, 1.99; N, 15.13 %.

Found: C, 30.11; H, 1.56; N, 15.23%. Raman (785 nm, %Ip: 1, cm-1): 2207 (ν_{CN}), 2183 (ν_{CN}), 1605, 1571, 1502, 1323, 1273, 1166, 1154, 1109, 1063, 1035, 769, 467, 456, 373, 310, 290, 248, 223, 193, 137.

[Cu(μ-OH)(bipy)]$_2$[Au(CN)$_4$]$_2$ (4.4).

A powder of **4.3** was washed thoroughly with MeOH multiple times and was then heated in 10 mL of boiling MeOH until most of the material was dissolved. The resulting mixture was filtered to remove undissolved **4.3** and the filtrate left undisturbed for 24 hours, during which purple plate-shaped crystals of [Cu(μ-OH)(bipy)]$_2$[Au(CN)$_4$]$_2$ (**4.4**) were deposited. Yield: 72 % (0.077 g). IR (ATR, cm^{-1}): 3459, 1612, 1603, 1572, 1489, 1477, 1450, 1321, 1252, 1176, 1164, 1106, 1075, 1034, 1019, 981, 939, 809, 771, 731, 667. Anal. Calcd. for $C_{28}H_{18}N_{12}Au_2Cu_2O_2$: C, 31.28; H, 1.68; N, 15.64 %. Found: C, 31.24; H, 1.81; N, 15.72 %. Raman (514 nm, %Ip: 50, cm-1): 3117, 2249 (ν_{CN}), 2234 (ν_{CN}), 1648, 1545, 1371, 1316, 1085, 820, 512, 245, 172.

[Cu$_2$(μ-OH)$_2$(tmeda)$_2$Pt(SCN)$_4$] (4.5).

A 5 mL aqueous solution of [Cu(μ-OH)(tmeda)]$_2$(BF$_4$)$_2$ (56 mg, 0.10 mmol) was layered with a 5 mL methanolic solution of K_2[Pt(SCN)$_4$] (50 mg, 0.10 mmol). The layered mixture was left undisturbed for 24 hours, during which iridescent blue-green crystals of [Cu$_2$(μ-OH)$_2$(tmeda)$_2$Pt(SCN)$_4$] (**4.5**) were deposited. Yield: 27 % (0.022 g). IR (ATR, cm-1): 2111 (ν_{CN}), 1462, 1281, 1120, 1049, 1020, 1001, 950, 805, 768, 701. Anal. Calcd. for $C_{16}H_{34}N_8Cu_2O_2PtS_4$: C, 23.44; H, 4.18; N, 13.67 %. Found: C, 23.12; H, 4.38; N, 13.51 %. Raman (785 nm, %Ip: 1, cm-1): 2114 (ν_{CN}), 1440, 1170, 807, 792, 767, 511, 468, 303, 218, 167, 131.

4.8.3. **DFT Calculations.**

DFT calculations were performed using the Gaussian 09 program (Revision D.01),[244] the B3LYP functional,[245] the 6-21G, 6-31G, 6-31G* basis sets for light atoms (C, H, N, S, O, Cu) and the SDDAll or LanL2DZ basis sets and related Effective Core Potential[247-250] for heavy atoms (Pt, Au). Broken symmetry (BS) density functional theory (DFT) calculations were performed with the same functional and basis set.[251-253]

Chapter 5. **Synthesis and optical properties of [Pb(terpy)(SCN)$_2$] and its derivatives.**

5.1. **Introduction**

In the previous chapters, notably Chapter 3, it was established that using isothiocyanate-based species for the synthesis of coordination polymers can be used for controlling the supramolecular arrangement of the units due to the possibility of intermolecular interactions and of hydrogen bonding between the thiocyanate units and the ligands. Consequently, using thiocyanates could allow one to control the properties of a material that are related to its supramolecular arrangement, such as porosity,[10-15] birefringence,[28-29] and magnetism.[7-9]

As mentioned in Chapter 1, another interest in the design of coordination polymers is the generation of multifunctional materials. By carefully choosing the building blocks, one can synthesize coordination polymers that possess two or more properties of interest. In this chapter, SCN–based complexes that show both birefringence and fluorescence were targeted. 2,2';6',2"-terpyridine (terpy) is a well-known ligand in regard to its luminescent properties. There are many examples of luminescence studies of the terpy ligand and its derivatives when coordinated to a metal centre.[257-260]

Initial work to study the birefringence property of terpy-based CPs was first performed by Dr. Michael J. Katz. In his work, Dr. Katz synthesized [Pb(terpy)(Au(CN)$_2$)$_2$]$_\infty$ which presented uniquely high birefringence of $\Delta n = 0.38$.[259] In this work, it was established that the parallel arrangement of the terpy ligand of the crystal structure, which is partially due to the coordination of the [Au(CN)$_2$]$^-$ units, was the main cause of the high birefringence value. Since the birefringence of a species depends on the difference between the density and the bond polarization along the axes of a structure (see Appendix A), one can theorize that by choosing a building block that is more polarizable

than $[Au(CN)_2]^-$, the resulting CP could cause the birefringence value to be higher than that of the $[Au(CN)_2]^-$ based species due to the higher polarizability of the system. As established in previous chapters, the SCN^- species present similarities to $[Au(CN)_2]^-$ in terms of coordination, but also is more polarizable than the latter species, and thus analogous CPs using the SCN- unit instead of $[Au(CN)_2]^-$ were targeted as a comparison to examine the effect of changing polarizability and possibly density.

The addition of a polarizable bond on the terpy species and its effect on the birefringence value when compared to $[Pb(terpy)(Au(CN)_2)_2]_\infty$ was also explored by Dr. Katz. As explained in Appendix A, the refractive index of a system along an axis is also dependent on the overall polarizability of the system along that axis. By adding more polarizable bonds along said axis, such as highly polarizable cation-halide bonds, one can potentially increase the overall birefringence of the system by increasing the refractive index along one of the two axis involved in the phenomenon. Thus, the possibility of using 4'-HO-terpy, 4'-Cl-terpy and 4'-Br-terpy instead of terpy was explored. In the case of Cl-terpy, it was found that by adding this X-group on the ligand, a similar birefringence value was retained despite the fact that the ligands were significantly angled to each other, instead of being parallel like in the original species. For Br-terpy, a significant loss of birefringence was noted due to the misalignment of the species in the packing arrangement.

Furthermore, these structures were made using $[Au(CN)_2]^-$, which does not tend to form hydrogen bonds with the ligands. As seen in Chapter 3, the thiocyanate species is prone to forming hydrogen bonds, and thus increases the overall density of the resulting supramolecular structure. Thus, it was postulated that using thiocyanate in combination with Cl-terpy/Br-terpy would lead to an increase in the birefringence value, due to the presence of 1) the polarizable bond on the ligand, 2) the hydrogen bond leading to a highly organized structure and 3) the thiocyanate ligand coordinated to the metal centre, leading to an increased polarizability. This chapter presents the synthesis of [Pb(4'-R-terpy)$(SCN)_2$] (where R = H, OH, Cl and Br), the study of their optical properties and the measurement of their birefringence values.

5.2. **Syntheses**

The synthesis of [Pb(terpy)$(SCN)_2$] (**5.1**) was performed using the same methodology described in chapters 2 and 3 where the building blocks were mixed in water or alcohols and crystallization was performed by slow evaporation. To synthesize **5.1**, $Pb(NO_3)_2$ and KSCN were mixed in a 1:2 ratio in water and an ethanolic solution of the terpy ligand was slowly added dropwise. Slow evaporation resulted in large pale-yellow plates of **5.1** over a few days which were suitable for birefringence measurements. When the order of addition is changed, an unknown pale-yellow species was obtained as a precipitate after a few minutes. This species could not be recrystallized, but its IR spectra suggested the presence of SCN^- in the final product with a single band at 2078 cm^{-1}. If the solvents are changed or their final ratio altered, very twinned crystals of **5.1** were instead obtained which were not suitable for birefringence measurements. [Pb(HO-terpy)$(SCN)_2$] (**5.2**), [Pb(Cl-terpy)$(SCN)_2$] (**5.3**) and [Pb(Br-terpy)$(SCN)_2$] (**5.4**) were synthesized using the same methodology as for **5.1**, which resulted in large pale-yellow (or dark-brown in the case of **5.3**) crystals. For measuring birefringence, large crystals that preferably are transparent or lightly colored are necessary, and the crystallization methods used for the systems in Chapter 3 worked well for SCN-based systems.

In order to assess the effect of SCN^- on the birefringence of the systems, attempts at the synthesis of SCN^--free analogous systems were also made by complexing the ligand to $Pb(NO_3)_2$. [Pb(terpy)$(NO_3)_2$] was prepared according to the published methodology.[261] For Cl-terpy and Br-terpy, the systems were not synthesized successfully as the reaction resulted in the quick precipitation of an unknown powder. $[Pb_3(HO\text{-}terpy)_3(H_2O)_3](NO_3)_3$ (**5.5**) was synthesized by slowly mixing $Pb(NO_3)_2$ and HO-terpy and slow evaporation resulted in colorless blocks. In this case, altering the solvent ratio resulted in either in the unknown complex (if H_2O was in a higher ratio) or in very twinned crystals (if ethanol was in a higher ratio). For **5.5**, the synthetic procedure required significant optimization of solvent, temperature, and method of addition to generate the desired material.

For **5.1**, **5.2**, **5.3** and **5.4**, a ν_{CN} absorption peak was found in both the IR and Raman spectra between 2020 and 2098 cm^{-1}. These values correspond closely to the expected values for thiocyanate-based species, but overall the signals were broader than

expected for SCN^- ν_{CN} signals. This was most likely due to the asymmetrical coordination of the SCN^- species in the overall structure (which led to supramolecular packing arrangement of the systems) and resulted in multiple SCN^- species with unique coordination environments, and thus an assortment of unique SCN^- peaks closely located to each other which could not be resolved at the resolution at which the spectra were measured (1 cm^{-1}).

5.3. **Structural Analyses**

Crystals of $[Pb(terpy)(SCN)_2]$ (**5.1**) crystallize in the monoclinic space group C2/c (Figure 5.1). The structure consists of a seven-coordinated pentagonal bipyramidal Pb(II) metal centre coordinated to one terpy ligand, two SCN- ligands and two NCS- ligands from adjacent metal centres. The coordination distances of the terpy ligand range between 2.575(3) and 2.631(3) Å which is close to the expected values for the coordination of this ligand to a Pb(II) metal centre. The Pb-SCN distance is 2.986(2) Å and the Pb-NCS distance is 2.631(3) Å. These values are within the expected range for the coordination of NCS^- and SCN^- ligands to a Pb(II) metal centre. The Pb-SCN and Pb-NCS angles are 94.0(2)° and 150.6(1)°, respectively, which are higher than the average coordination angle of thiocyanates and isothiocyanates ligands most likely due to the presence of steric interactions with the terpy-ligands and the overall packing arrangement of the structure.

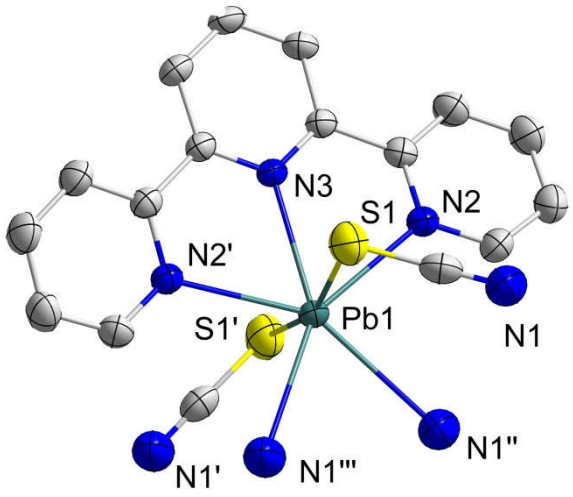

Figure 5.1 Crystal structure of [Pb(terpy)$(SCN)_2$] (**5.1**). The hydrogen atoms were removed for clarity. Colour code: Green (Pb), Blue (N), Yellow (S), Gray (C).

The coordination of the adjacent NCS^- units leads to the formation of a 1D coordination polymer along the c-axis of the crystal. The polymer propagates in a zig-zag fashion with two intermolecular bonds forming between each unit. For these intermolecular interactions, the thiocyanate ligands coordinate in a 1,3 pattern. As seen in Chapter 1, this type of structure is common for thiocyanate-based structures. However, the difference in this case is the coordination angle of almost 90°, which is quite unusual for thiocyanometallates. In the supramolecular structure, there is evidence of π-π interactions between the terpy ligands of each chain based on the short distance between them (distance between ligand planes = 2.95(1) Å). This further adds to the dimensionality of the coordination polymers, making it a 2D sheet instead of a 1D polymer (Figure 5.2).

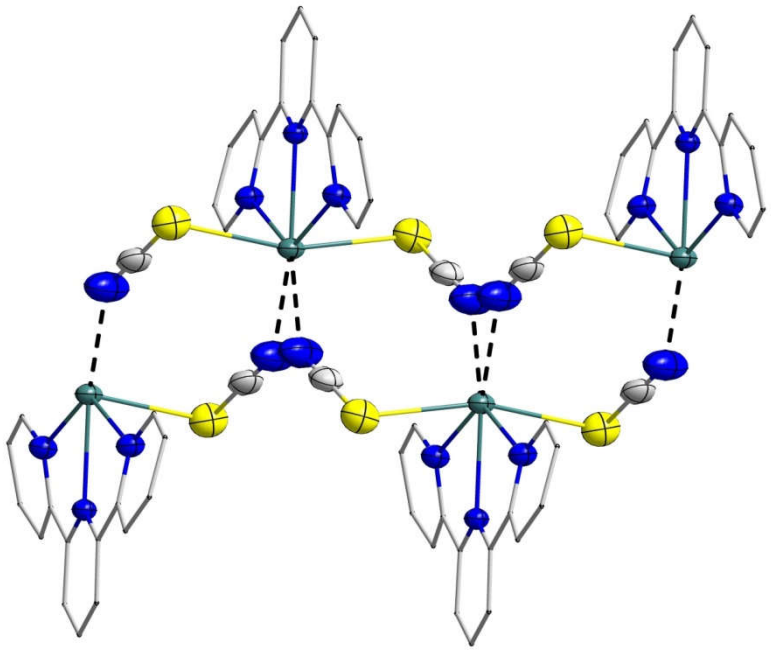

Figure 5.2 The 1D chain of [Pb(terpy)$(SCN)_2$] (**5.1**). The equatorial coordinations to the Pb(II) metal centre are depicted as black fragmented lines. The hydrogen atoms were removed for clarity. Colour code: Green (Pb), Blue (N), Yellow (S), Gray (C).

The structure of [Pb(HO-terpy)$(SCN)_2$] (**5.2**) is similar to that of **5.1**. It consists of a seven-coordinate pentagonal bipyramidal Pb(II) metal centre coordinated to one terpy ligand and four thiocyanates (Figure 5.3). However, in this case, the Pb(II) metal centre is coordinated to three sulfur atoms and one nitrogen atom from the thiocyanate ligands instead of two sulfur atoms and two nitrogen atoms for **5.1**, making it a PbN_4S_3 core instead of a PbN_5S_2 core for **5.1**. Just like for **5.1**, two of the thiocyanate ligands belong to the molecular unit and two come from adjacent units, thus forming a coordination polymer. The Pb-NCS distance is 2.407(3) Å and the Pb-SCN distance is 3.206(1) Å. The latter is longer than a typical Pb-SCN coordination distance suggesting only a weak interaction exists between the two (sum of Van der Waals radius for S and Pb = 3.82 Å).[141-143] The coordination distances of the ligands from adjacent species are of 3.36(1) Å and 3.67(1) Å, which again suggests weak interactions. The coordination angles of the ligands are 90.6(2)° for Pb1-S2-C2 and 168.0(2)° for Pb1-N1-C1. As for **5.1**, the coordination angle of almost 90 ° is unusual for thiocyanate ligands, as angle of 12-15 ° is usually expected for N-bound species.

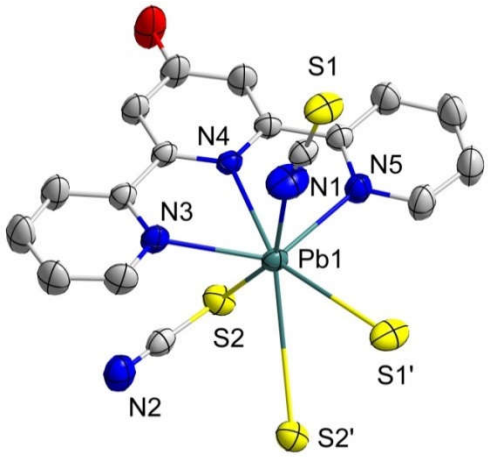

Figure 5.3 Crystal structure of [Pb(HO-terpy)$(SCN)_2$] (**5.2**). The hydrogen atoms were removed for clarity. Colour code: Red (O), Green (Pb), Blue (N), Yellow (S), Gray (C).

As for **5.1**, the coordination of the thiocyanate species in **5.2** from adjacent units form a 1D zig-zag coordination polymer. However, in this case, the coordination of the thiocyanate species alternates between 1,3 and 1,1 patterns (Figure 5.4). In a similar fashion to **5.1**, in the supramolecular structure, evidence of π-π interactions are found in the short distance between the π systems of the ligands (π-π = 3.67(1) Å) and from the general arrangement of the structure. One noticeable difference however is the presence of a hydrogen bond between the OH group of the ligand with the nitrogen atom of the 1,1 coordinated thiocyanate species (O-N = 2.72(1) Å). The presence of this hydrogen bond could be the cause of the weak coordination of that NCS^- unit to the Pb(II) metal centre.

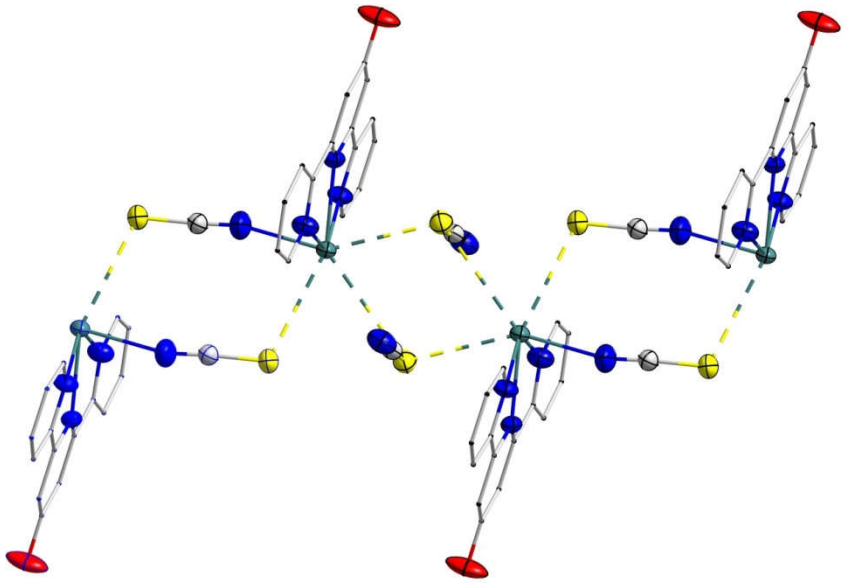

Figure 5.4 The 1D structure of [Pb(HO-terpy)$(SCN)_2$] (**5.2**). The weak Pb-S coordinations are depicted as fragmented lines. The hydrogen atoms were removed for clarity. Colour code: Red (O), Green (Pb), Blue (N), Yellow (S), Gray (C).

For **5.3**, the structure is very similar to **5.2**. It consists of a seven-coordinate pentagonal bipyramidal Pb(II) metal centre coordinated to one terpy ligand, one NCS^- species, one SCN^- unit, and two (iso)thiocyanate ligands from an adjacent species (Figure 5.5). This results in a PbN_5S_2 core with two nitrogen and two sulfur coordinations from the thiocyanate ligands just like for **5.1**. The coordination distances of the two S-bound thiocyanates are 3.049(2) and 3.50(1) Å, where one is directly coordinated to the Pb(II) metal centre and the other is coordinated to the adjacent species and interact weakly with the Pb(II) metal centre. The coordination distances (Table 5.1) are within the expected range (approx. 2.5 to 3.5 Å) for an S-coordinated thiocyanate species to a Pb(II) metal centre. In the case of the N-bound species, the Pb-N distance is a typical 2.462(5) Å. The angles for the four thiocyanate species are 167.4(1), 87.6(1), 113.0(1), and 62.1(1)°. The third and fourth angles (which are the two S-bound (iso)thiocyanates from adjacent species) are higher than the expected value for S-bound thiocyanates most likely due to the presence of steric interactions arising from the adjacent units and the terpy-ligands.

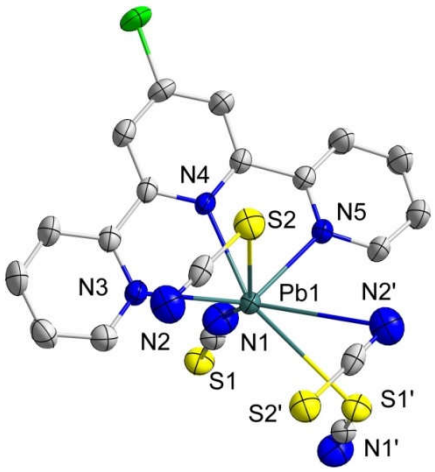

Figure 5.5 Crystal structure of [Pb(Cl-terpy)$(SCN)_2$] (**5.3**). The hydrogen atoms were removed for clarity. Colour code: Pale green (Cl), Green (Pb), Blue (N), Yellow (S), Gray (C).

As for the supramolecular structure of **5.3**, in a similar way to **5.1** and **5.2**, a 1D coordination polymer is formed from the coordination of the adjacent thiocyanates (Figure 5.6). In this case, the coordination polymer is formed following an alternating 1,1 and 1,3 pattern. The close distance of 3.68(1) Å between the planes of the Cl-terpy ligands of adjacent chains suggest the presence of π-π interactions between them, leading to a 2D supramolecular arrangement.

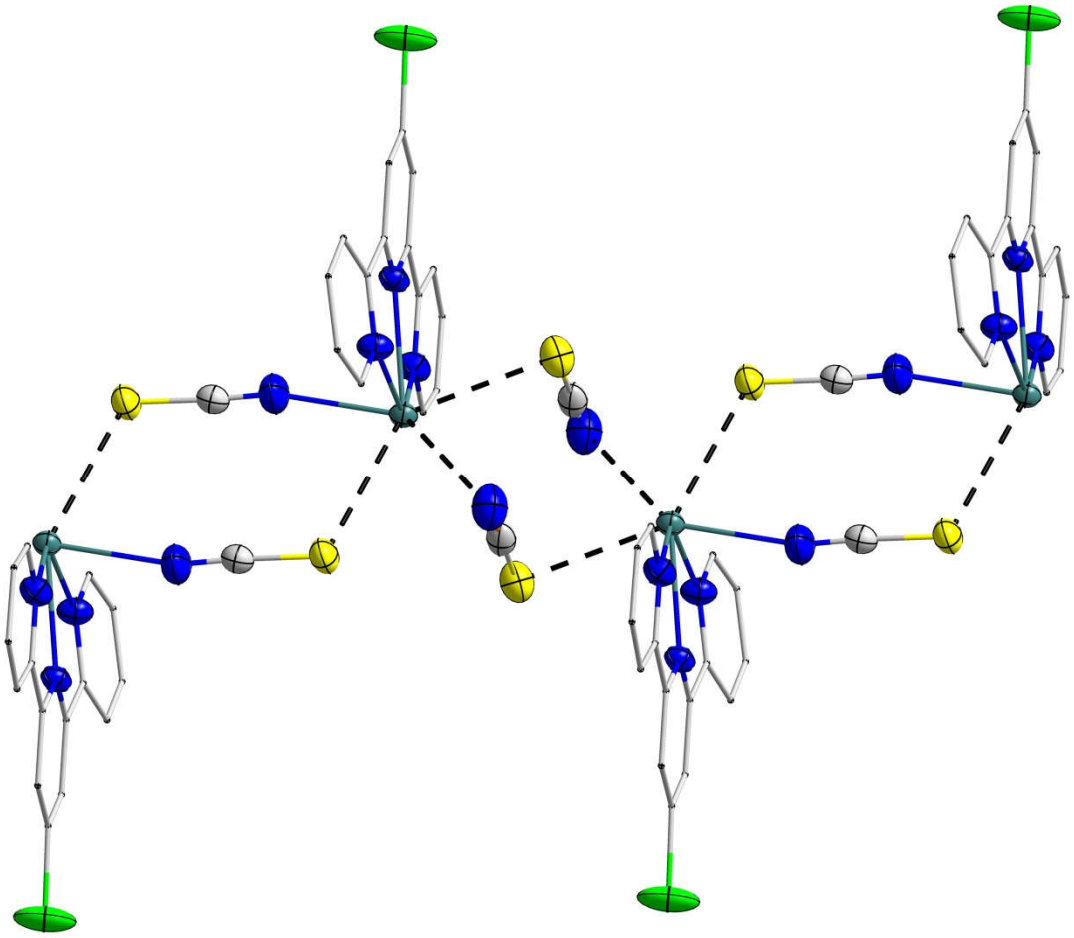

Figure 5.6 The 1D chain of [Pb(Cl-terpy)$(SCN)_2$] (**5.3**). The weak Pb-S and Pb-N coordinations are depicted as black fragmented lines. The hydrogen atoms were removed for clarity. Colour code: Pale green (Cl), Green (Pb), Blue (N), Yellow (S), Gray (C).

For complex **5.4**, the crystal structure consists also of a seven coordinate Pb(II) metal centre coordinated to one terpy ligand and four thiocyanate units. In this case, the core is composed of two N-bound isothiocyanates and two S-bound thiocyanates that are from adjacent species (Figure 5.7). The coordination distances of the NCS^- ligands are 2.55(1) Å and 2.59(2) Å, which are within the expected range for N-bound thiocyanates to a Pb(II) metal centre. The latter value corresponds to the coordination distance of the dangling NCS^- species (see below). The distances for the S-bound units are 3.53(1) Å and 3.59(1) Å, which indicates that they are weak intermolecular interactions, just like for **5.1**-**5.3**. The coordination angles of the thiocyanates are 173.0(1), 127.7(1), 101.0(1), and 116.2(1)°. The second angle is unusually high for an N-coordinated isothiocyanate,

and may be due to the fact that it is a dangling species between the ligands in the packing arrangement and is subject to steric interactions (see below).

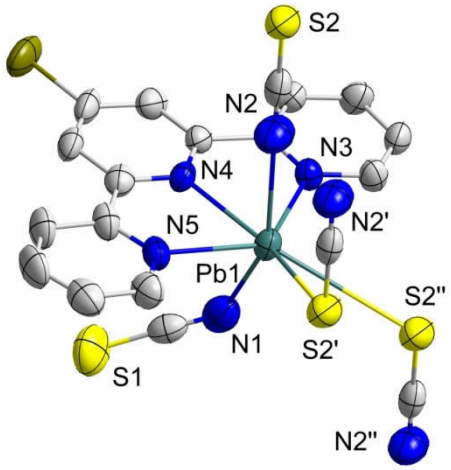

Figure 5.7 Crystal structure of [Pb(Br-terpy)$(SCN)_2$] (**5.4**). The hydrogen atoms were removed for clarity. Colour code: Green (Pb), Blue (N), Yellow (S), Gray (C).

The units in the crystal structure of **5.4** form a 1D coordination polymer similar to **5.1**, **5.2** and **5.3** via the coordination of two thiocyanates from adjacent species. However, in this case, only one of the two thiocyanates form the 1D coordination polymer, the other one being a coordinated only to one Pb(II) metal centre and dangling between the 1D chains (Figure 5.8). In this case, the bridging thiocyanate is bound in a 1,3 pattern and forms an alternating chain where two species are coordinated to the adjacent Pb(II) metal centres followed by a single one. As opposed to **5.1**-**5.3** however, there is no evidence of π-π interaction between the Br-terpy ligands, as they do not align their π systems with each other and are further spread apart.

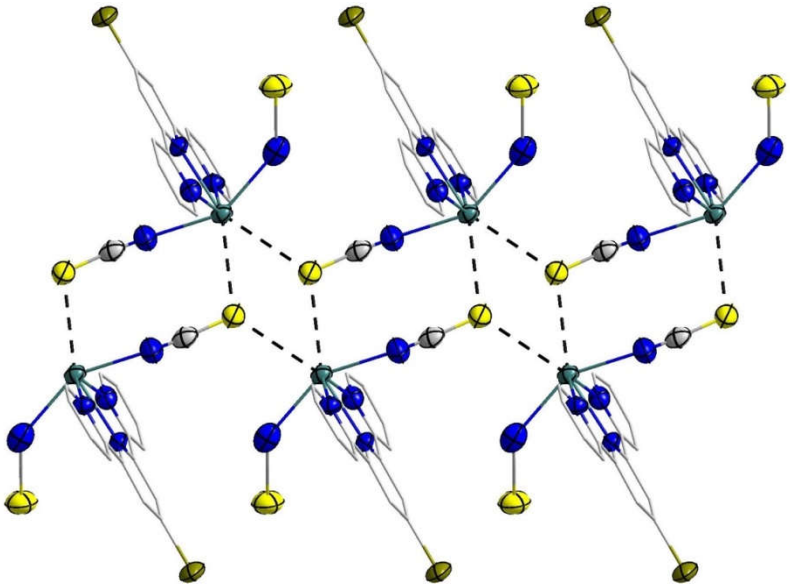

Figure 5.8 The 1D chain of [Pb(Br-terpy)$(SCN)_2$] (**5.4**). The equatorial coordinations to the Pb(II) metal centre are depicted as black fragmented lines. The hydrogen atoms were removed for clarity. Colour code: Green (Pb), Blue (N), Yellow (S), Gray (C).

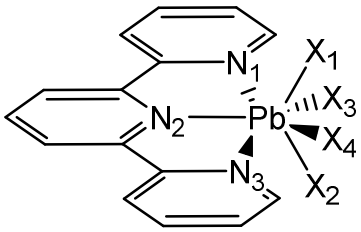

Figure 5.9 Naming convention for the selected bonds and angles of **5.1**-**5.4**.

Table 5.1 Selected bond lengths (Å) and angles (°) for [Pb(R-terpy)$(SCN)_2$] (**5.1**, R = H; **5.2**, R = OH; **5.3**, R = Cl; **5.4**, R = Br) where X consists of the coordinated thiocyanate species (either N-coordinated or S-coordinated, see Figure 5.9).

Compounds	5.1		5.2		5.3		5.4	
Pb-X1	S	2.986(2)	N	2.407(3)	N	2.462(5)	N	2.55(1)
Pb-X2	S	2.986(2)	S	3.206(1)	S	3.049(2)	N	2.59(2)
Pb–X3	N	2.631(3)	S	3.36(1)	S	3.50(1)	S	3.53(1)
Pb-X4	N	2.631(3)	S	3.67(1)	N	3.48(1)	S	3.59(1)
Pb-N1		2.631(3)		2.522(2)		2.571(4)		2.514(9)
Pb-N2		2.575(3)		2.480(2)		2.532(4)		2.471(9)
Pb-N3		2.631(3)		2.499(2)		2.510(4)		2.489(9)
Pb-X1-C1	S	94.0(2)	N	168.0(2)	N	167.4(1)	N	173.0(1)
Pb-X2-C2	S	94.0(2)	S	90.6(2)	S	87.6(1)	N	127.7(1)
Pb-X3-C3	N	150.6(1)	S	112.2(2)	S	113.0(1)	S	101.0(1)
Pb-X4-C4	N	150.6(1)	S	66.6(1)	N	62.1(1)	S	116.2(1)
X1-Pb-X2	S, S	163.3(1)	N, S	151.0(1)	N, S	149.4(1)	N, N	148.3(1)
X1-Pb-X3	S, N	105.5(1)	N, S	79.6(1)	N, S	78.3(1)	N, S	86.0(1)
X1-Pb-X4	S, N	87.9(1)	N, S	131.6(1)	N, N	130.5(1)	N, S	124.0(1)
X2-Pb-X3	S, N	87.9(1)	S, S	128.9(2)	S, S	129.5(1)	N, S	117.6(1)
X2-Pb-X4	S, N	105.6(1)	S, S	70.1(1)	S, N	73.4(1)	N, S	85.7(1)
X3-Pb-X4	N, N	74.3(1)	S, S	62.2(1)	S, N	56.3(1)	S, S	69.1(1)

Structural analysis of $[Pb_3(HO\text{-terpy})_3(H_2O)_3](NO_3)_3$ (**5.5**) revealed that the complex crystallizes in the hexagonal space group P 63/m. It consists of a ring of three five-coordinate Pb(II) centres surrounded by three nitrate counteranions located between the rings in the packing arrangement (Figure 5.10). The Pb(II) metal centres are coordinated to one HO-terpy ligand, one OH species from the adjacent HO-terpy ligand and one hydroxide anion. The nitrate ions are located close to the Pb(II) metal ligands, but the sum of the van der Waals radii indicate that they do not strongly interact with the

$[Pb_3(HO\text{-}terpy)_3(H_2O)_3]^{3+}$ units. The coordination distance of the hydroxide ion is 2.359(6) Å and for the OH unit from the adjacent ligand, this distance is 2.752(6) Å (Table 5.2). The former is within range of the expected value for the coordination of OH^- to Pb(II). The locations of the hydrogen atoms for both OH species were geometrically determined.

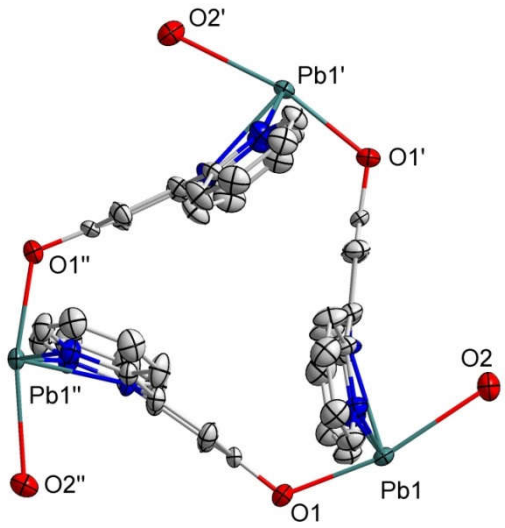

Figure 5.10 Crystal structure of $[Pb_3(HO\text{-}terpy)_3(HO)_3](NO_3)_3$ (**5.5**). The hydrogen atoms and NO_3^- counteranions were removed for clarity. Colour code: Red (O), Green (Pb), Blue (N), Yellow (S), Gray (C).

Table 5.2 Selected bond lengths (Å) and angles (°) for $[Pb_3(HO\text{-}terpy)_3(HO)_3](NO_3)_3$ (**5.5**).

Pb-N1	2.589(3)	N1-Pb-N2	64.35(7)
Pb-N2	2.506(4)	N1-Pb-N1'	126.7(2)
Pb–O1	2.359(4)	O1-Pb-O2	167.7(2)
Pb-O3	2.754(5)	O1-Pb-N1	84.60(9)
		O1-Pb-N2	93.2(2)

Complex **5.1** shows a contraction of the coordination distances of the equatorial ligands compared to the axial ligands whereas complexes **5.2**-**5.4** present elongation of the coordination distances of the equatorial ligands (with a coordination distance spread of 1.26, 1.038 and 1.119 Å, respectively). Generally, for Pb(II) terpy-based complexes, longer equatorial coordination distances and/or shorter axial coordination distances suggest the presence of a stereochemically active lone pair in the equatorial plane and opposed to the terpy-ligand.

In the case of **5.5**, structurally, there is strong evidence of a stereochemically active lone pair on the Pb(II) metal centre oriented towards the outside of the Pb_3 rings in the equatorial plane opposed to the terpy ligand (coordination distance spread = 0.395 Å). There is also evidence that the lone pair is interacting sterically with the terpy ligands, which are not perfectly planar as would be expected for terpy ligands (plane angle = 24.1°). Overall, the Pb(II) metal centre adopts a distorted trigonal prismatic geometry, where one of the coordination sites is occupied by the stereochemically active lone pair.

5.4. **Fluorescence**

When observed using a UV light (λ = 345 nm), it was readily apparent that crystals of **5.1**-**5.4** presented orange to red fluorescence (Figure 5.11). Since the terpy ligand is well known for its luminescent properties, but usually emits a yellow or green luminescence, an investigation into the luminescent properties of these materials and of the cause of this difference in fluorescent emission was initiated. For each material, the excitation and emission spectra were measured between 325 nm and 800 nm. The spectra were measured by spreading crushed crystals on a quartz substrate angled at 45 ° to the excitation beam.

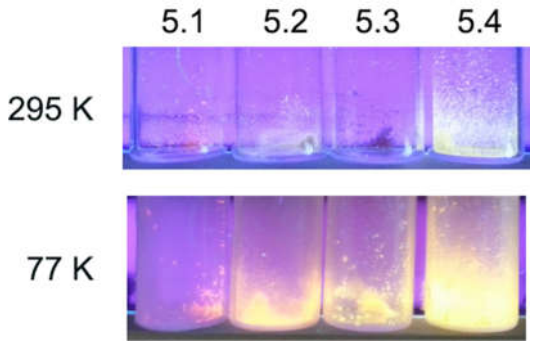

Figure 5.11 The fluorescence of crystals of **5.1-5.4** over a UV light (λ = 385 nm).

In the case of **5.1**, in the solid state, two wide excitation bands, at 390 and 450 nm (Figure 5.12) were observed. In the case of emission, **5.1** presented two broad bands with maxima located at 550 nm and 622 nm. It was established that excitation at 390 generates emission only at 550 nm, whereas excitation at 450 nm generates emission at both 550 nm and 622 nm. The excitation and emission of 390 nm and 550 nm,

respectively, are close to the typical values found for luminescence and is attributed solely to the terpy ligand,[263-264] suggesting that the additional excitation and emission pair at 450 nm and 550/622 nm is one that is affected by the presence of the metal centre and/or the thiocyanate ligand. In solution, the system did not show any luminescence, most likely due to a quenching effect by the solvent.

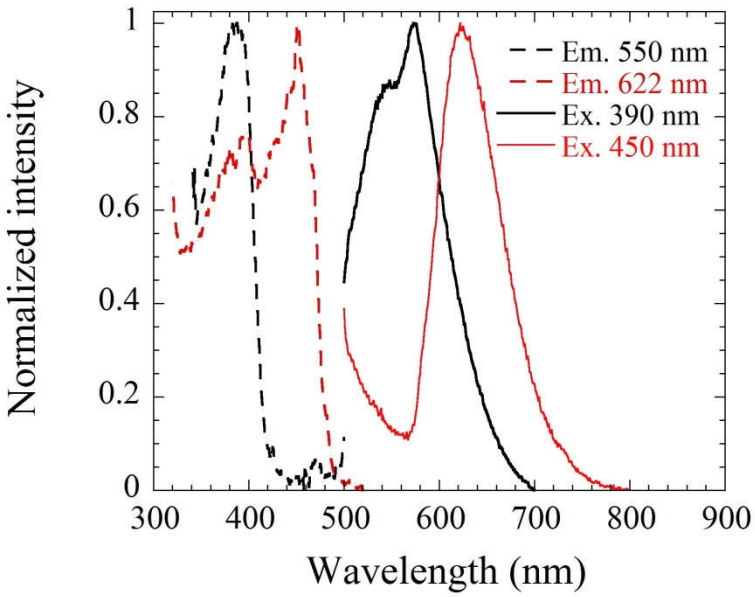

Figure 5.12 The excitation and emission spectra of [Pb(terpy)$(SCN)_2$] (**5.1**) at 150 K.

In the case of **5.2**, the fluorescence spectrum also consists of two excitation/emission pairs (Figure 5.13). The first one is located at maxima of 370 nm and 495 nm, and the second pair is located at maxima of 386 nm and 618 nm. Both pairs consist of wide bands similar to that of **5.1**.

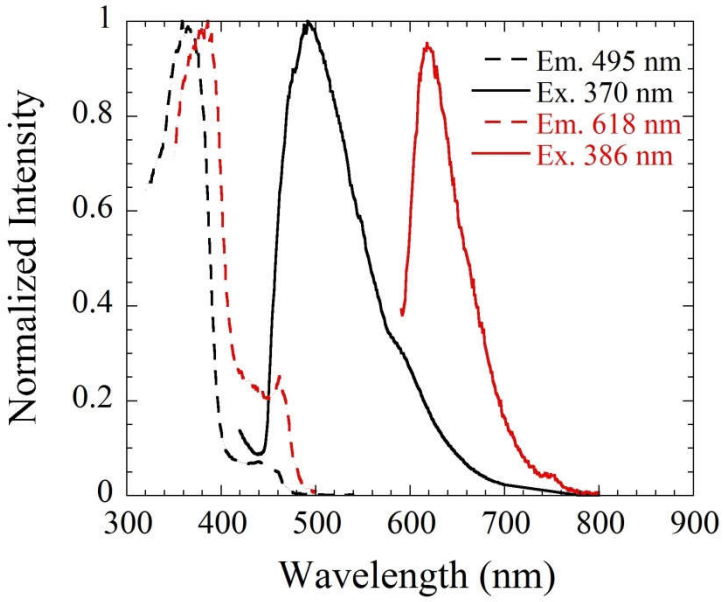

Figure 5.13 The excitation and emission spectra of [Pb(HO-terpy)$(SCN)_2$] (**5.2**).

For **5.3**, the spectra consists of a single excitation/emission pair located at maxima of 470 nm and 595 nm. The bands are wide, just like for the previous species (Figure 5.14).

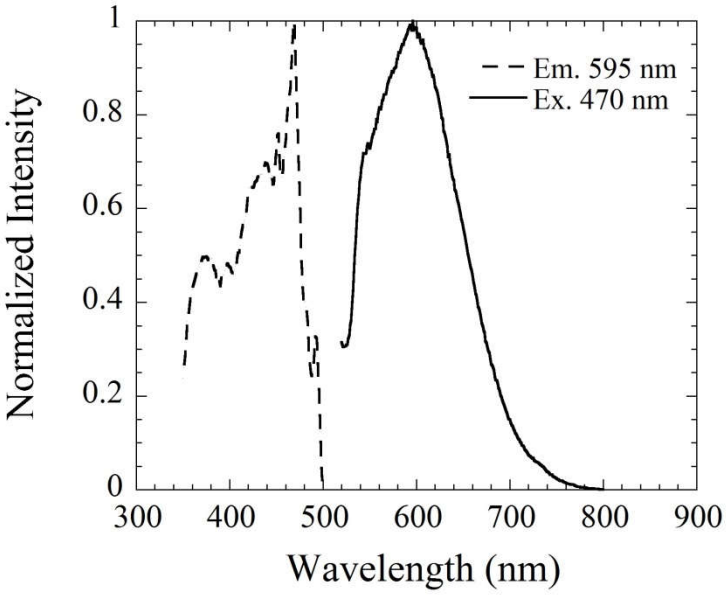

Figure 5.14 The excitation and emission spectra of [Pb(Cl-terpy)$(SCN)_2$] (**5.3**).

For **5.4**, only a single emission and excitation pair is found at 400 nm and 600 nm, respectively (Figure 5.15). These wavelengths are higher than the average wavelengths found for terpy-based excitation and emission, which again suggests that the presence

of the metal centre and ligand has an important effect on the luminescent properties of these species.

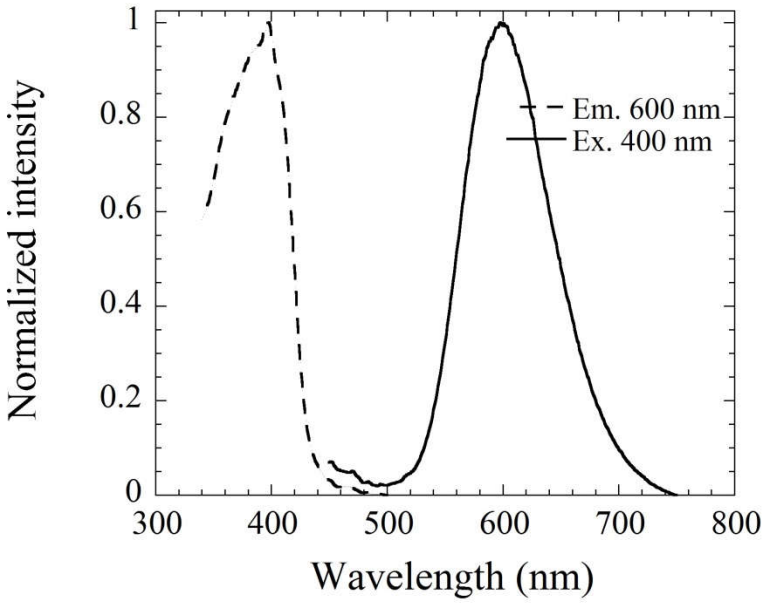

Figure 5.15 The excitation and emission spectra of [Pb(Br-terpy)$(SCN)_2$] (**5.4**).

For **5.1**-**5.4** (Table 5.3 and Figure 5.16), the emission bands located at approximately 500-550 nm are similar to each other. For **5.1** and **5.2**, these emission bands are close to that of a non-coordinated terpy ligand with a broad excitation of 350 nm and a broad emission at 540 nm.[263-264] In all four species, the bands located at approximately 600 nm resemble each other with variation only in the intensity of the band in the original spectra. The overall broadness of the bands are similar to each other, suggesting that the source of the emission in all of these species must be the same. The only common species in these four complexes are the Pb(II) metal centre and the thiocyanate ligands. This could indicate that the fluorescence emission band originates from a molecular orbital including the thiocyanate species, instead of the terpy species as usually observed for terpy-based luminescent coordination polymers. In the case of the excitation bands, the profile of the bands and the maxima vary widely, suggesting that the excitations are terpy-based. Consequently, we hypothesize that the luminescence profile for these species consist of an excitation at the terpy ligand, followed by an internal conversion to the thiocyanate ligands coordinated to the Pb(II) metal centres.

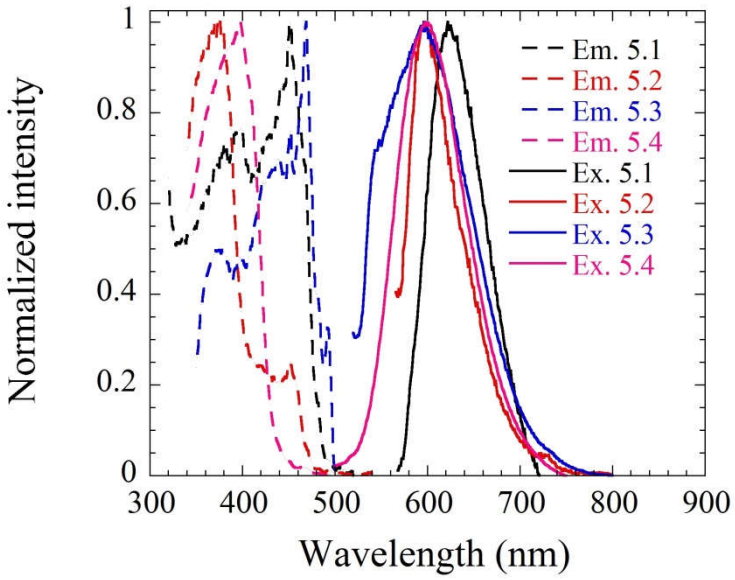

Figure 5.16 Comparison of the fluorescence of [Pb(terpy)$(SCN)_2$] (**5.1**), [Pb(HO-terpy)$(SCN)_2$] (**5.2**), [Pb(Cl-terpy)$(SCN)_2$] (**5.3**), [Pb(Br-terpy)$(SCN)_2$] (**5.4**).

In order to better establish the definitive effect of the thiocyanate species in the luminescent spectra of the species, the complex [Pb(terpy)$(NO_3)_2$] was synthesized according to a known synthetic procedure and its luminescence measured using the same instrumental procedure as for the other species (Figure 5.17). For this nitrate species, the band pair at 390 nm and 550 nm is still present, but the excitation band at 450 nm is noticeably absent; it instead shows an excitation band at 410 nm and a shoulder in the emission band at 600 nm. When compared to the thiocyanate species, it is clear that the presence of the thiocyanate ligand changes the absorption and emission profiles by a significant margin. It is noteworthy to mention that $Pb(SCN)_2$ does not present significant fluorescence, even at low temperature. For **5.5**, the species did not present any significant fluorescence both at room temperature and at 150 K.

Overall, a better assignment of the luminescence spectra could be performed by using a combination of DFT calculations and solid state quantum yield fluorescence measurements, which would allow the determination of the exact source of the signals observed at approximately 600 nm for **5.1**-**5.4**, but overcoming the technical challenges associated with such measurements and calculations were beyond the scope of this work.

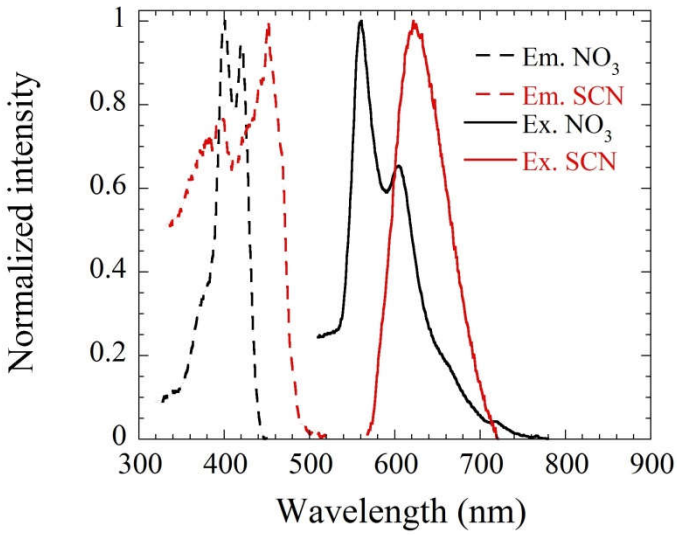

Figure 5.17 Comparison of the fluorescence of [Pb(terpy)$(SCN)_2$] (**5.1**) and [Pb(terpy)$(NO_3)_2$].

Table 5.3 Peak absorption and emission values for [Pb(R-terpy)$(SCN)_2$] (**5.1**, R = H; **5.2**, R = OH; **5.3**, R = Cl; **5.4**, R = Br), [Pb_3(HO-terpy)$_3$(HO)$_3$]$(NO_3)_3$ (**5.5**) and [Pb(terpy)$(NO_3)_2$].

Compounds	Excitation maximum (nm)	Emission maximum (nm)
5.1	390	550
	450	622
5.2	370	495
	386	618
5.3	470	595
5.4	400	600
Pb(terpy)$(NO_3)_2$	390	550
	410	600

When comparing the luminescence of **5.1** to that of [Pb(terpy)]$(NO_3)_2$, it is clear that the presence of the thiocyanate species induces a significant change, giving rise to new excitation and emission bands at 450 nm and 622 nm, respectively. In the literature, for most SCN-based structures with fluorescent ligands, the luminescence of the complexes was often dismissed as being secondary to the targeted property (usually the structural

topology) of the work.[86-101] As such, there is a significant lack of data on the effect of the thiocyanates species on the luminescence of inorganic complexes. Despite the evidence mentioned above, it is thus difficult to determine if the thiocyanate species is the cause of these new excitation and emission bands in the spectra, as there is no evidence in the literature of such effect. In order to correctly assess the source of these signals, DFT calculations and further luminescence measurements would be required, which is beyond the scope of this work.

5.5. **Birefringence**

In order to obtain the birefringence value of a crystal for the largest surface, one needs to measure both the retardation along that surface and the thickness of the crystal (see Appendix A). In all cases, the retardation values for the largest surface for the crystal were measured using the method described in Appendix A.

In the case of **5.1** and **5.4**, the crystals obtained were very thin which made it impossible to measure the thickness using our standard methodology involving a SC-XRD instrument and a microscope with a large zoom factor (see Appendix A). In order to measure the thickness of these crystals more accurately, the crystals dimensions were determined using a FEI DualBeam 235 Scanning Electron Microscope.

To measure the thickness, the crystal was placed on a sticky surface on a holder with a 90° elevation. Afterward, the crystals were thoroughly dried *in vacuo* to ensure that the surface was free of moisture, but also to insure that the crystals would survive the high vacuum established by the instrument. Once ready, the crystals were then introduced in the instrument and their picture at an angle measured, followed by a picture at a 0° angle compared to the imaging detector, which allowed us to measure their thickness accurately using the imaging software and the resulting pictures.

The viewing axis for the largest surface of the crystal were determined by measuring the unit cell of the crystal beforehand using our SC-XRD (with a mitogen holder and a limited amount of paraffin oil) and then using the Apex Software suite to attribute the orientation axes to each of the surface for the crystal.

5.5.1. **Crystal Thickness and Retardation**

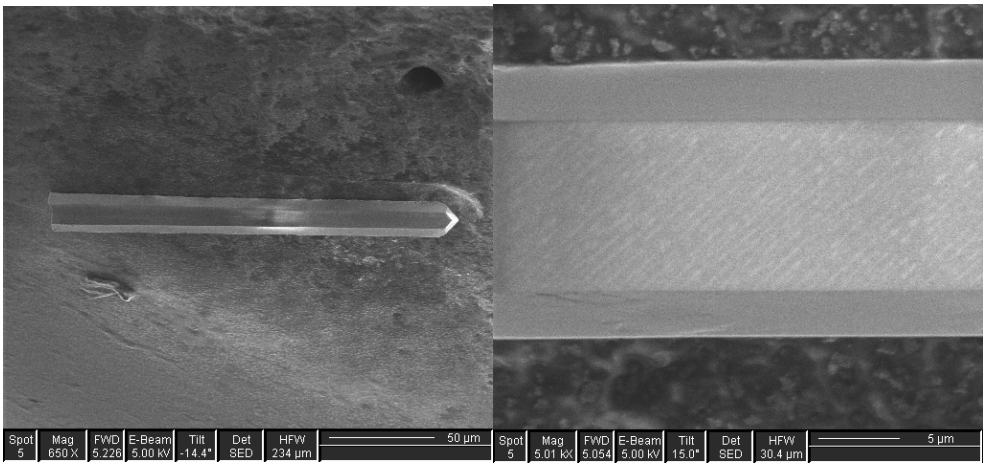

Figure 5.18 SEM pictograph of [Pb(terpy)$(SCN)_2$] (**5.1**).

In the case of **5.1**, the crystals consisted of small pale-yellow plates averaging a thickness of 23 µm (Figure 5.18). The retardation measured at the largest surface of the crystal was on average 10200 nm. On average, the birefringence values for the crystals of **5.1** was measured to be 0.34(3). In this case, the viewing axis of the crystal for the largest surface was determined to be (1,0,0), which means that the retardation value can be attributed to the difference between the refractive indexes of the (0,1,0) and the (0,0,1) axes. The packing diagram for that viewing direction is shown in Figure 5.19. In terms of birefringence, one can expect the thiocyanate species to contribute to the refractive index of both axis, to which the ligands are angled at approximately 45° and to offer the similar polarizability to both axes. The terpy ligands are expected to mostly contribute to the (0,0,1) axis, which is parallel to the orientation of their longer side. Thus, in this case, the incorporation of the SCN^- units likely only has a minor effect on the Δn value, which is moderate compared to other Pb(terpy)-based species.[259-260]

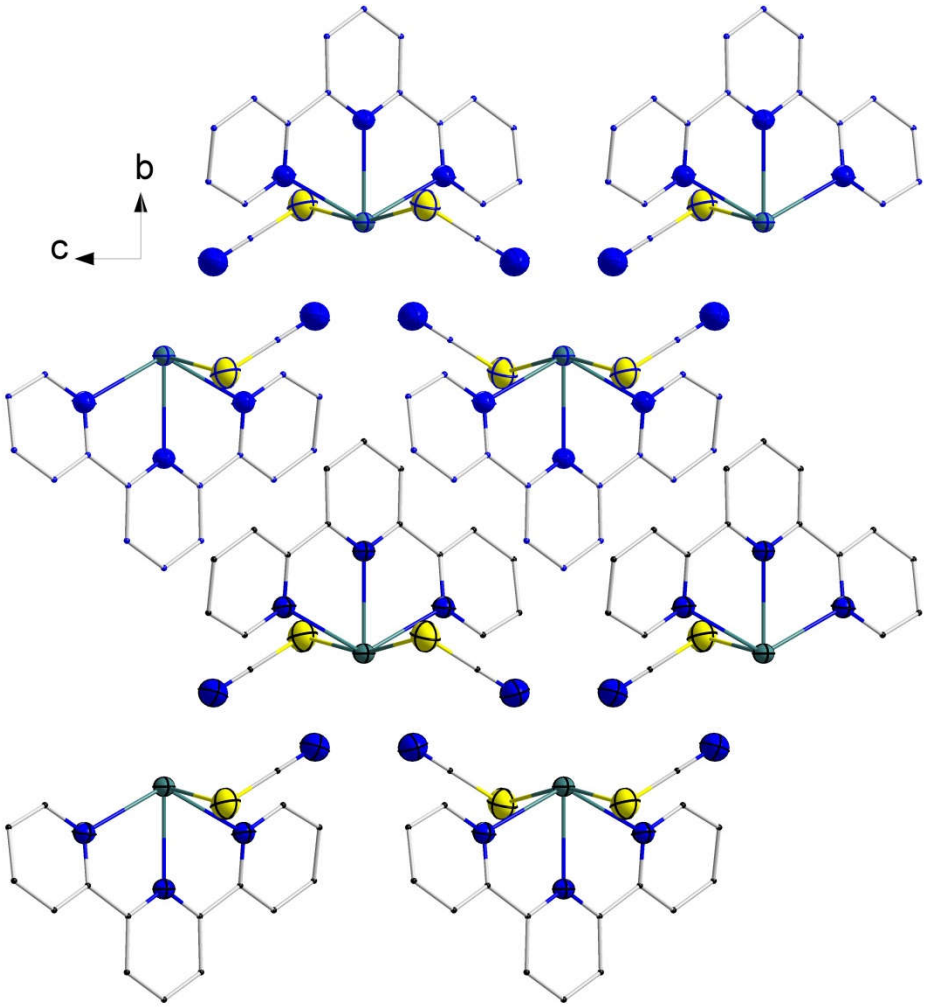

Figure 5.19 Packing diagram viewed down the (1,0,0) crystal axis of [Pb(terpy)(SCN)$_2$] (**5.1**).

For **5.2**, the crystals consisted of small colorless to pale-yellow plates with an average thickness of 32 μm (Figure 5.20). The retardation for the largest surface of the crystal was on average 12000 nm, which led to a birefringence average of 0.36(1). For this species, the largest surface corresponded to (0,1,0) which is shown in Figure 5.21. In this case, for the birefringence, the ligands are approximately angled at 30° to the (1,0,0) axis and are expected to contribute mostly to that refractive index by increased polarizability, whereas the thiocyanate species is fully parallel to the (0, 0, 1) axis and are expected to contribute exclusively to that refractive index by polarizability. As a result, the two polarizable species are independently well aligned, but they are nearly

perpendicular with respect to each other resulting in a reduction of the polarization anisotropy and a moderate Δn value again.

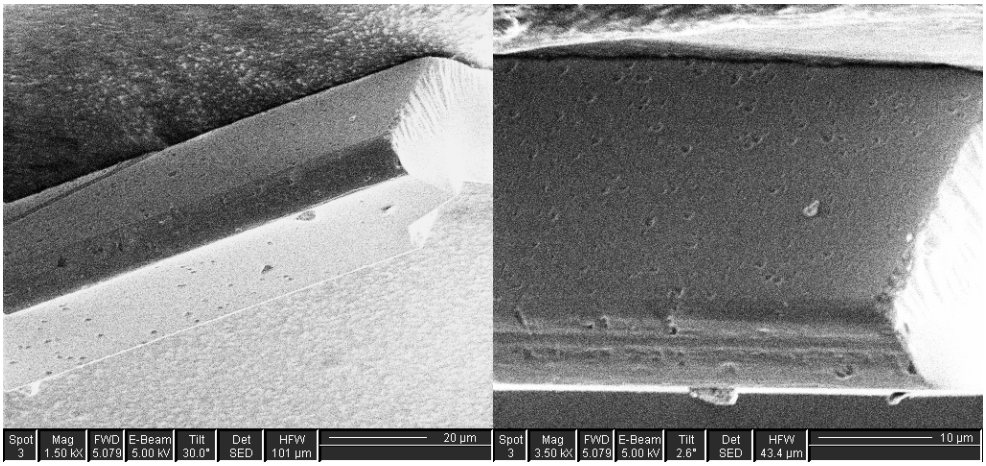

Figure 5.20 SEM pictograph of [Pb(HO-terpy)$(SCN)_2$] (**5.2**).

Crystals of **5.3** proved to be the most difficult to measure, not only because of their block-like shape, but also because of their dark brown (Figure 5.22). These crystals were also very brittle and prone to breaking when manipulated. On average, the thickness of the blocks was 50 µm and the retardation at the surface was close to 18000 nm, which is the near the upper limit of our instrument.

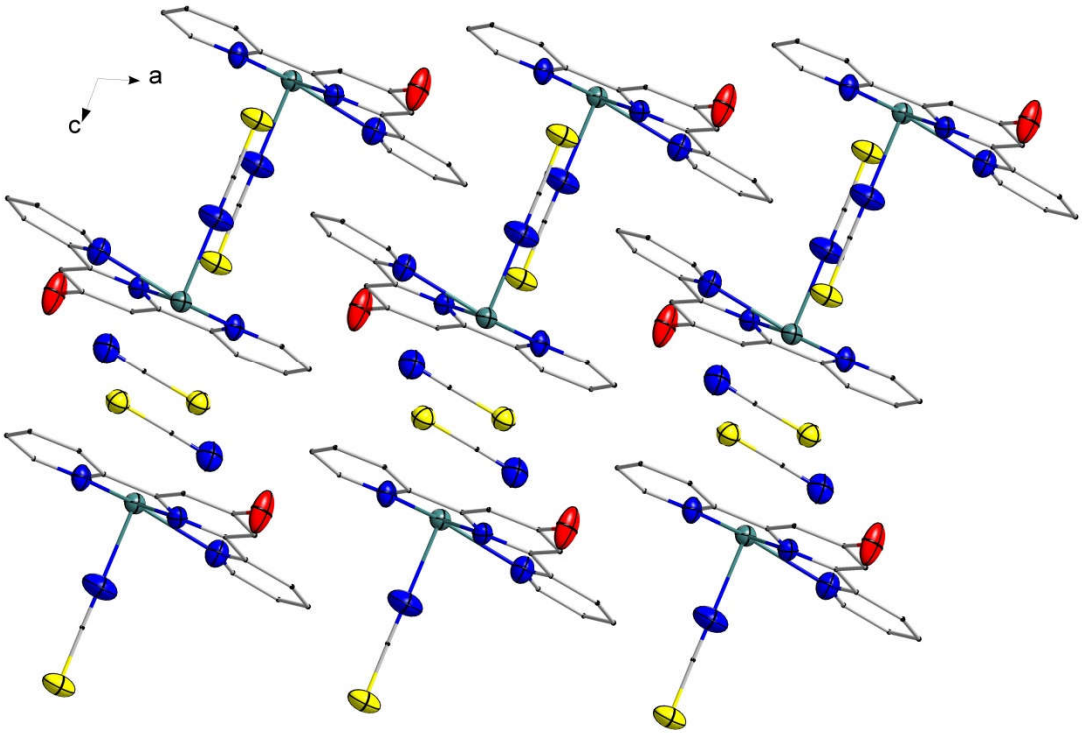

Figure 5.21 Packing diagram viewed down the (0,1,0) crystal axis of [Pb(HO-terpy)$(SCN)_2$] (**5.2**).

For complex **5.3**, the average birefringence was 0.33(1). The viewing direction for the largest surface was determined to be (0, 1, 0) and is shown in Figure 5.23. Similarly to **5.2**, the ligands in **5.3** are angled at approximately 30° to the (1, 0, 0) axis and the thiocyanate species is parallel to the (0, 0, 1) axis. Thus, similar contributions of the ligands and thiocyanate species to the two refractive indices forming Δn in this field of view are expected, and a similar Δn value to **5.2** was observed accordingly.

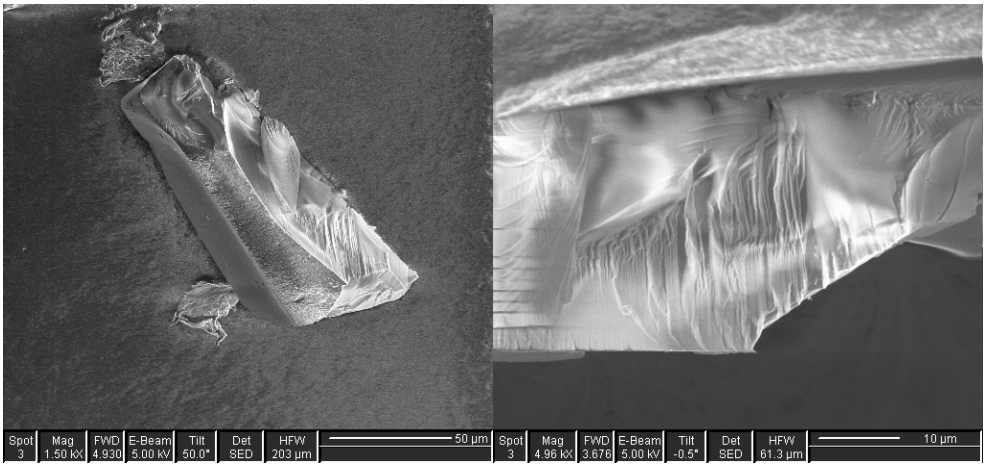

Figure 5.22 SEM pictograph of [Pb(Cl-terpy)$(SCN)_2$] (**5.3**).

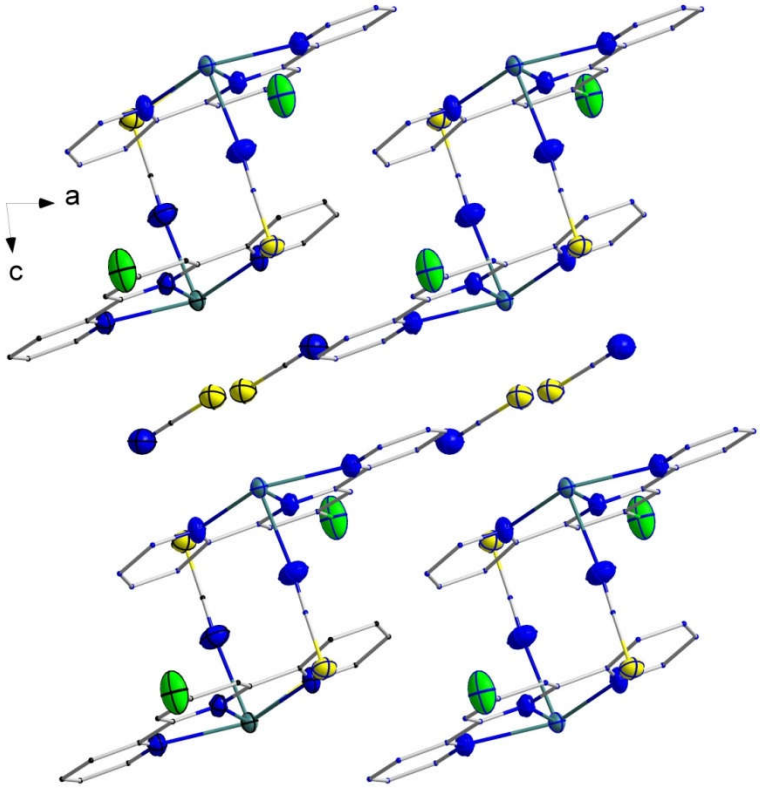

Figure 5.23 Packing diagram viewed down the (0,1,0) crystal axis of [Pb(Cl-terpy)$(SCN)_2$] (**5.3**).

Finally, in the case of **5.4**, the crystals consisted of hexagonal-shaped pale-yellow to colorless plates with an average thickness of 20 µm, which proved to be very challenging to measure using other methods (Figure 5.24). The retardation at the largest surface of the crystal was measured to be approximately 5500 nm, which led to an

average birefringence value of 0.26(1). The largest surface was determined to be (0, 1, 0) and the packing diagram for this axis is shown in Figure 5.25. In this case, regarding the birefringence, the ligands are oriented towards the (0, 0, 1) axis and the thiocyanates are slightly angled towards the (1, 0, 0) axis, and thus, like for **5.2** and **5.3**, the contribution of each species to the refractive indices is expected to be mostly related to different axes, again altering the overall possible polarizability anisotropy.

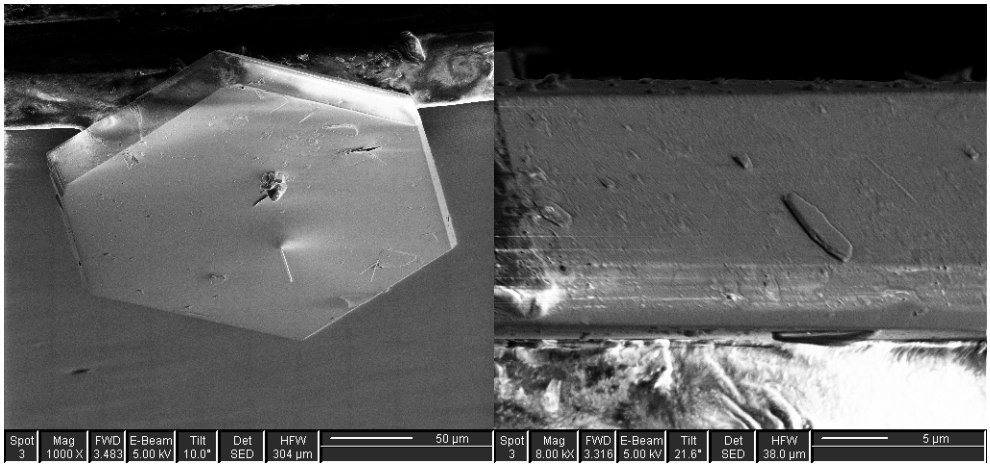

Figure 5.24 SEM pictograph of [Pb(Br-terpy)$(SCN)_2$] (**5.4**).

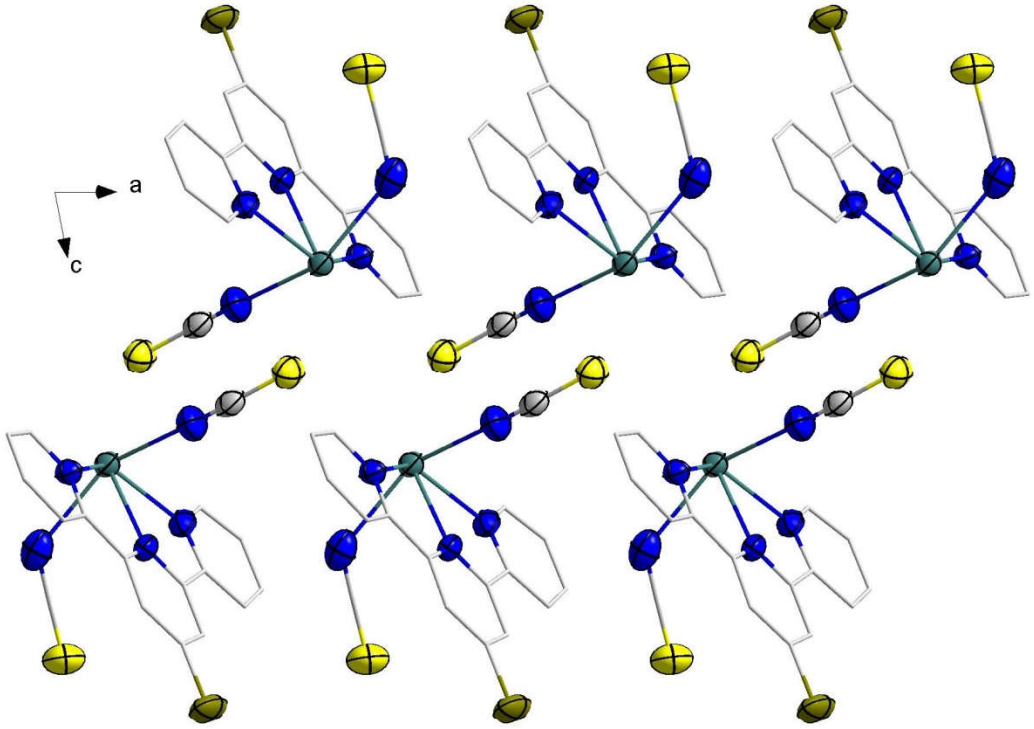

Figure 5.25 Packing diagram viewed down the (0,1,0) crystal axis of [Pb(Br-terpy)$(SCN)_2$] (**5.4**).

5.5.2. **Packing Density**

As mentioned in Section 5.1, part of the reason behind using thiocyanate instead of $[Au(CN)_2]^-$ was an attempt at increasing the packing density of the final product,

thiocyanate being a shorter linear bridging ligand with coordination angles at both end and the possibility of 1,1 coordination instead of the typical end-to-end linear coordination. Combining all these properties together could lead to an increased anisotropic packing density in the resulting product along the bridging axis of the crystal structure. Since the bridging ligands are different in each compound, we needed an even basis to compare the anisotropic packing density in a meaningful fashion between the analogues. We opted to compare the number of ligands per unit of distance (linear packing density) and volume (volumetric packing density) using arbitrary axes since all structures present a similar topology. In all cases, the three arbitrary axes were set as the following: γ consists of the axis along which the 1D chain of the CP propagates, α is the axis along which the ligands interact either via π-π stacking, Au-Au metal bonding or steric interaction from the R-group leading to the 2D supramolecular arrangement, and β is the axis representing the distance between the 2-D sheets. Table 5.4 below shows the packing density for each complex along each of those arbitrary axes, and by unit of volume for an overall comparison between the structures.

Table 5.4 Packing densities and birefringence values of **5.1**-**5.4** compared to calcite and $[(Au(CN)_2)]^-$ analogues.

Complex	Δn	Linear packing density (ligands/nm)			Volumetric packing density (ligands/nm^3)
		α	β	γ	
Calcite	0.17	-	-	-	-
$[Pb(terpy)(Au(CN)_2)_2]$[259]	0.396(8)	2.5(1)	1.7(1)	1.8(1)	7.7(1)
$[Pb(terpy)(SCN)_2]$ (**5.1**)	0.34(3)	2.5(1)	1.9(1)	2.1(1)	10.0(1)
$[Pb(HO\text{-}terpy)(SCN)_2]$ (**5.2**)	0.36(1)	2.3(1)	1.9(1)	1.7(1)	7.4(1)
$[Pb(Cl\text{-}terpy)][Au(CN)_2]_2$[260]	0.38(2)	1.3(1)	1.0(1)	0.9(1)	1.2(1)
$[Pb(Cl\text{-}terpy)(SCN)_2]$ (**5.3**)	0.33(1)	2.3(1)	2.0(1)	1.7(1)	7.8(1)
$[Pb(Br\text{-}terpy)(\mu\text{-}OH_2)_{0.5}][Au(CN)_2]_2$[260]	0.26(3)	2.5(1)	1.5(1)	1.84(1)	6.9(1)
$[Pb(Br\text{-}terpy)(SCN)_2]$ (**5.4**)	0.263(7)	2.6(1)	2.4(1)	2.4(1)	15.0(1)

When comparing complexes **5.1**-**5.4**, noticeable trends emerge for the β and the γ axes. In the case of the γ axis, the packing density decreases when the binding mode of the thiocyanate bridging ligands shifts from a unique 1,3 (in **5.1**) to an alternating 1,1 to 1,3 bridging scheme (in **5.2** and **5.3**). There is also a significant increase in packing density

when the chain propagates along a single thiocyanate bridge as opposed to two of them (when comparing **5.1** and **5.4**). In the case of the α axis, all values are comparable, which is expected as, as aforementioned, since it consists of the axis along which the π-π interactions propagates, and thus similar values would be expected for four analogous ligands with little differences in the π system. This leaves the β, which corresponds to the space between the 2D sheets. In this case, an increase in the packing density is observed between **5.1**-**5.3**, which have comparable values, and **5.4**, which could indicate that the major factor in determining the packing arrangement in the Br-terpy structure is in fact the Br atom and its interactions instead of the interactions between the π systems of the ligands, leading to a more dense packing in the final structure.

The thiocyanate-based species all show a higher ligand packing density along the γ axis. This can be explained by the fact that the thiocyanate species presents both a shorter linear coordination distance compared to $[Au(CN)_2]^-$ and coordination angles at both end, which would result in shorter distances between the bridged species in a 1D chain. For the β axis, the value for **5.1** is similar to that of its analogue but there is a noticeable difference between **5.3** and **5.4** and their $[Au(CN)_2]^-$ counterparts. This is explained by the fact that in the structure, in the case of **5.3** and **5.4**, the 2D sheets are interlaced together in a zig-zag fashion with the alternating ends of the ligands coming from the adjacent sheets, whereas in the $[Au(CN)_2]^-$ species, the 2D sheets are not interlaced, leading to a lower packing density along this axis. For the α axis, the values for **5.1** and **5.4** are similar to the values of their $[Au(CN)_2]^-$ analogues, but there is a major difference for **5.3**. In the [Pb(Cl-terpy)][$Au(CN)_2]_2$ analogue, the propagation along the α axis is due to Au-Au metal bonding instead of π-π stacking. In both cases, the intermolecular distance is approximately 3.0 to 3.6 Å, but for Au-Au metal bonding, the Au units forming the chains are oriented perpendicular to the γ axis of the crystal (the 1D chain). Thus, the distance is measured along the β axis, whereas in the case of π-π stacking, the distance is measured between the planes of the ligands, and thus along the γ axis. This difference of orientation of the intermolecular link causes the distance between the 1D-chains to be much shorter in the case of **5.3**. For the **5.1** analogue, this Au-Au metal bonding occurs perpendicular to the γ-axis and is measured along the α axis, which is comparable to the π-π stacking α axis of **5.1**. In general, all the thiocyanate species present a significant increase in volumetric packing density compared to their $[Au(CN)_2]^-$

analogues, which confirms our hypothesis that thiocyanate-based CPs can lead to higher volumetric packing densities overall.

Although larger packing densities are valuable for increasing refractive indices, one should aim to increase the anisotropic packing density, as ultimately, the birefringence value is a difference between the refractive indices of the two measured axes. If the packing density increases along one of the axes and decreases along the other, the birefringence will increase in value. When compared to the $[Au(CN)_2]^-$ analogues, all of the SCN^- complexes present a higher linear packing density along the γ axis (except when compared to **5.3**), similar packing densities for the α axis and much higher packing density for the β axis. Overall, however, the birefringence value is lower for all four complexes; this anisotropic packing density in the $[Au(CN)_2]^-$ complexes could be the cause of the increased birefringence values for those systems.

One noticeable difference between the structures was that in most cases, the Δn values for the $[Au(CN)_2]^-$ structures were measured along different crystal axis compared to the thiocyanate species. For example, the birefringence of $[Pb(terpy)(Au(CN)_2)_2]$ was measured for the (1,1,0) surface as opposed to the (1,0,0) surface for **5.1**. This means that in the case of the former species, there is a contribution from both crystal axes to the birefringence instead of just one, and thus any species contributing to the difference between either the packing density or the bond polarization along these axis will increase the overall birefringence value.

This shows that in order to assess the actual effect of polarizability and density on the birefringence of specific complexes and to establish trends in a series of complexes (such as the one presentment in this chapter), one must choose a CP system (ligands, bridges, metal centres) for which the structures are isostructural throughout the series, which would result in having crystals of similar shape and size for which the largest surfaces are the same and are comparable through birefringence measurements. This is a significant limitation to birefringence measurements since and still remains a challenge to overcome.

Despite these limitations for birefringence, complexes **5.1**-**5.4** were shown to be multifunctional materials presenting both a unique fluorescence profile and an elevated

birefringence when compared to the industry standard (i.e., calcite). What remains to be seen with these materials is how the fluorescence and the birefringence properties may interact with each other. When measuring the birefringence, as explained in Appendix A, the light is polarized, which allows for the measurement of the retardation of the crystal. In this case, since the materials show significant fluorescence, one could test if the emitted light from the fluorescence profile is polarized due to the presence of birefringence. Initial measurements of this theory by adding a polarizing filter to the fluorescence apparatus and measuring the fluorescence profile at different polarizing angles showed only a small decrease in the fluorescence emission, which could not be clearly attributed to a polarization effect.

5.6. **Conclusions**

In this chapter, the structural and optical properties of five new species, of which four are analogues of each other, were presented. These species were also analogues of published complexes using the $[Au(CN)_2]^-$ building block instead of the NCS^- building block. Structural analyses revealed that the species of the type $[Pb(R\text{-terpy})(SCN)_2]$ are 1D coordination polymers for which the supramolecular structure is further extended by interchain π-π stacking of the R-terpy ligands, leading to 2D supramolecular sheets. Analysis of the luminescent properties of the $[Pb(R\text{-terpy})(SCN)_2]$ species indicated that the fluorescence profile is unique to the species. The birefringence measurements resulted in values that are slightly lower than those obtained for the published $[Au(CN)_2]^-$ analogues. Despite the use of the thiocyanate ligand, which increased the volumetric packing density of the overall structures, there was a significant difference in the birefringence values compared to the $[Au(CN)_2]^-$ analogues possibly due to the lower anisotropic packing density of the system along the γ axis. Further investigations using SCN^--based species targeting specifically high refractive index building blocks could establish a trend between complexes and determine the exact role of the SCN^- species in the birefringence of CPs.

5.7. Experimental

5.7.1. General Procedures and Materials

Unless otherwise noted, all reagents were purchased from commercial sources and were used without further purification. The optical retardation and crystal thickness measurements were obtained by means of polarized-light microscopy using an Olympus BX60 microscope, with a tilted U-CTB thick Berek compensator at λ = 546(10) nm at room temperature. Retardation measurements were also conducted at λ = 650(20) nm, resulting in a <1% difference, which is far less than the error associated with thickness measurements. The birefringence was calculated by dividing the measured retardation by the crystal thickness. The crystal thickness was measured using a FEI DualBeam 235 Scanning Electron Microscope. In the case of all crystals reported herein, face assignment of the crystals was determined using the crystal faces application in APEX II. All other procedures and materials are as described in section 2.8.1.

Solid-state luminescence spectra were collected at 293 K or 77 K on a Photon Technology International (PTI) fluorometer using a xenon arc lamp and photomultiplier detector in conjunction with the PTI Cold Finger Dewar (CFD) Accessory. Polycrystaline samples were loaded into a standard NMR tube which was in turn loaded into the CFD. For 77 K spectra, liquid nitrogen was used as the cryogen.

5.7.2. Synthetic procedures

[Pb(terpy)(SCN)$_2$] (5.1)

$Pb(NO_3)_2$ (0.1 mmol, 0.0331 g) and KSCN (0.2 mmol, 0.0194 g) were first mixed in 15 mL of H_2O and stirred for 15 minutes. A 15 mL solution of 2,2';6',2"-terpyridine (0.1 mmol, 0.0233 g) in ethanol was then added dropwise to the previous solution. The liquor was then lightly stirred for a few seconds and transferred to a tall beaker, allowing for slow evaporation of the solution over several days, which yielded colorless plates of [Pb(terpy)$(SCN)_2$] (**5.1**). Better crystals suitable for birefringence studies were obtained by transferring the mother liquor to a test tube, allowing for a longer evaporation time of the solution. Yield: 0.050 g (90 %). FT-IR (KBr, cm^{-1}): 2069 (ν_{CN}), 2030 (ν_{CN}), 2014 (ν_{CN}),

1742, 1590, 1478, 1446, 1431, 1304, 1245, 1204, 1174, 1159, 1003, 836, 790, 773, 731. Raman (785 nm, %lp: 50, cm^{-1}): 2075, 2015, 1591, 1569, 1495, 1478, 1454, 1328, 1293, 1272, 1176, 1123, 1040, 1007, 791, 735, 651, 457, 298, 209, 161, 137. Anal. Calcd. for $C_{17}H_{11}N_5PbS_2$: C, 36.68; H, 1.99; N, 12.58 %. Found: C, 36.69; H, 1.96; N, 12.54 %.

[Pb(HO-terpy)(SCN)$_2$] (5.2)

[Pb(HO-terpy)$(SCN)_2$] (**5.2**) was synthesized using the same method as for **5.1**, but by instead using 4'-hydroxy-2,2':6',2''-terpyridine (0.1 mmol, 0.0249 g). Yield: 0.042 g (75 %). FT-IR (KBr, cm^{-1}): 2092 (ν_{CN}), 2026 (ν_{CN}), 1773, 1613, 1593, 1571, 1517, 1482, 1468, 1453, 1424, 1359, 1294, 1239, 1157, 1096, 1055, 1008, 962, 891, 871, 830, 793, 740. Raman (785 nm, %lp: 50, cm^{-1}): 2097, 1597, 1506, 1380, 1275, 1240, 1146, 1058, 1015, 566, 435, 167. Anal. Calcd. for $C_{17}H_{11}N_5PbOS_2$: C, 35.66; H, 1.94; N, 12.23 %. Found: C, 35.79; H, 2.27; N, 11.80 %.

[Pb(Cl-terpy)(SCN)$_2$] (5.3)

[Pb(Cl-terpy)$(SCN)_2$] (**5.3**) was synthesized using the same method as for **5.1**, but by instead using 4'-chloro-2,2':6',2''-terpyridine (0.1 mmol, 0.0267 g). Yield: 0.048 g (82 %). FT-IR (KBr, cm^{-1}): 2063 (ν_{CN}), 1587, 1572, 1479, 1456, 1436, 1413, 1395, 1337, 1303, 1242, 1158, 1129, 1109, 1048, 1009, 969, 896, 875, 789, 759, 739, 724. Raman (785 nm, %lp: 50, cm^{-1}): 2067, 2055, 1587, 1573, 1552, 1481, 1457, 1337, 1305, 1293, 1267, 1259, 1049, 1012, 840, 290, 215, 140, 121. Anal. Calcd. for $C_{17}H_{10}N_5PbClS_2$: C, 34.55; H, 1.71; N, 11.85 %. Found: C, 34.50; H, 1.65; N, 11.78 %.

[Pb(Br-terpy)(SCN)$_2$] (5.4)

[Pb(Br-terpy)$(SCN)_2$] (**5.4**) was synthesized using the same method as for **5.1**, but by instead using 4'-bromo-2,2':6',2''-terpyridine (0.1 mmol, 0.0312 g). Yield: 0.058 g (92 %). FT-IR (KBr, cm^{-1}): 2097 (ν_{CN}), 2072 (ν_{CN}), 2042 (ν_{CN}), 1592, 1581, 1568, 1546, 1520, 1506, 1479, 1454, 1409, 1329, 1302, 1238, 1157, 1137, 1046, 1008, 895, 872, 788, 725. Raman (785 nm, %lp: 50, cm^{-1}): 2098, 2071, 2043, 1583, 1331, 1298, 1046, 1009, 995, 904, 795, 740, 711, 680, 632, 559, 475, 453, 402, 314, 252, 227, 122. Anal. Calcd. for $C_{17}H_{10}N_5PbBrS_2$: C, 32.13; H, 1.59; N, 11.02 %. Found: C, 32.01; H, 1.57; N, 10.93 %.

[Pb_3(HO-terpy)$_3$(H_2O)$_3$](NO_3)$_3$ (5.5)

$Pb(NO_3)_2$ (0.1 mmol, 0.0331 g) and 4'-hydroxy-2,2';6',2"-terpyridine (0.1 mmol, 0.0249 g) were mixed in a 50:50 solution of H_2O:EtOH which was heated to 40 °C and stirred for 30 minutes until all the lead nitrate was dissolved. The mother liquor was then allowed to slowly evaporate over a period of three weeks which resulted in large colorless crystals of $[Pb_3(HO\text{-}terpy)_3(H_2O)_3](NO_3)_3$ (**5.5**). Yield: 0.048 g (91%). FT-IR (KBr, cm^{-1}): 3347 (w), 1588 (br), 1564 (m), 1516 (m), 1477 (w), 1429 (m), 1352 (m), 1293 (m), 1240 (m), 1158 (m), 1062 (m), 1003 (m), 960 (m), 873 (w), 820 (s), 802 (m).. Raman (785 nm, %lp: 50, cm^{-1}): 1582, 1492, 1353, 1270, 1235, 1052, 561, 430. Anal. Calcd. for $C_{45}H_{36}N_{13}Pb_3O_{15}$: C, 33.65; H, 2.26; N, 10.46 %. Found: C, 33.45; H, 2.20; N, 10.57 %.

Chapter 6. **Global conclusions and future work**

6.1. **Future work: Thallium-based systems**

As seen in Chapter 3 and 5, a lot of work has been done using lead(II) due to its properties of interest, such as the presence of the stereo active lone-pair on the metal centre, and the ability to control the activity of said lone-pair by choosing appropriate capping ligands. Similarly to lead(II), thallium(I) also presents such behavior, and the lone-pair is sometimes more stereoactive when compared to Pb(II).[270-272] As such, the possibility to use Tl(I) as a nodal metal centre for the synthesis of CPs of interest with unique topologies was explored.

Previously in the Leznoff group, a preliminary survey using thallium(I) was done by Dr. Michael J. Katz and consisted of combining $Tl(NO_3)$, $K[Au(CN)_2]$ and phen-based ligands (phen, 2,9-dimethyl-1,10-phenanthroline (Me_2phen), 3,4,7,8-Tetramethyl-1,10-phenanthroline (Me_4phen)), which resulted in the CPs $[Tl(phen)Au(CN)_2]$, $[Tl(Me_2phen)Au(CN)_2]$ and $[Tl(Me_4phen)Au(CN)_2]$. Part of my work in this project consisted of refining the purification process and to obtain some of the crystal structures of these systems (which are beyond the scope of this thesis). Nonetheless, during this work, the possibility of using Tl(I) in combination with thiocyanate-based building blocks in order to synthesize a new range of CPs was also explored.

The first attempts at synthesizing Tl(I) and SCN^--based CPs consisted of using $Tl(NO_3)$ with the classic ancillary capping ligands used in the Leznoff group, such as en, phen, 2,2'-bipy, tmeda, and terpy, in combination with KSCN to synthesize CPs of the type [Tl(L)(SCN)] where SCN^- would be the bridging ligand (Equation 6.1). In all cases, the synthesis work was attempted in both H_2O, and a H_2O:MeOH mixture, as per the methodology that was used by Dr. Katz. When using the former solvent, a white power quickly precipitated from the solution at room temperature. Heating the solution did not

help with the solubility of the product, and crystals could not be obtained from the mother liquor by slow evaporation after filtration of the powder. When using MeOH as a co-solvent, the resulting product was slightly more soluble, but crystallization again proved difficult. Multiple attempts at slow crystallization techniques, such as H-tube, cold temperatures and narrow vessels, were performed, but crystals could not be obtained. FTIR indicated the presence of SCN^- in the final products with a band at approximately 2100 cm^{-1}, but EA indicated that the product was impure, as no definite ratios could be calculated from the data obtained.

$$Tl(NO_3) + xL + KSCN \xrightarrow[Solvents]{} [Tl(L)_x(SCN)] + KNO_3$$

Equation 6.1 The combination of Tl(I) metal precursor with a ligand and SCN^- for the synthesis of CPs.

Further attempts at the synthesis of CPs using capped Tl(I) building blocks were then performed using $[Pt(SCN)_4]^{2-}$ as a building block instead of SCN^-. $K_2[Pt(SCN)_4]$ was mixed with the same building blocks stated above using similar conditions and crystallization techniques, and in most cases, an amorphous oily material was obtained as a result. When stored at low temperature, most materials separated from the mother liquor at the bottom of the reaction vessel as oil. When mixed using an H-tube, the amorphous material did not separate, but no crystals were obtained either. Slow evaporation also resulted in an oil after the solvent was completely evaporated. Heating of the solutions did not result in different products, and FTIR still indicated the presence of SCN^- in the resulting product with bands at approximately 2100 cm^{-1}. However, in the case where 2,2'-bipy was used as a capping ligand and slow evaporation was used, small plate-like orange crystals were obtained, but these crystals were shown to be heavily twinned and unsuitable for SC-XRD. Attempts at slower evaporation or using different solvents were performed, but no suitable crystals for SC-XRD were obtained. EA indicated that the material consists of a material with the approximate ratio of 1:1:1 Tl:2,2'-bipy:$[Pt(SCN)_4]^{2-}$ with the presence of at least 5% impurities.

Subsequent attempts at the synthesis of CPs were then performed using $K_3[Fe(SCN)_6]$ and $K_2[Co(SCN)_4]$, and in the case of $K_3[Fe(SCN)_6]$, dark red crystals containing $[Tl(2,2'\text{-bipy})]^+$ and SCN^- were obtained (as shown by IR, vCN =2064 cm^{-1}), but the same issues

as above were encountered (heavily twinned crystals, impure product, difficulty of recrystallization).

For Tl(I), the difficulty of recrystallization is the main issue that needs to be addressed before further work can be attempted since the regular reaction conditions used in the Leznoff group do not seem to be appropriate for Tl(I) nodal units. In order to fix those issues, one might try using less polar solvents in combination with the use of a different, slower crystallization method instead of slow evaporation or H-tubes. Nonetheless, the difficulty of using Tl(I) as a metal precursor remains and greatly limits the possibilities. Due to its toxicity, Tl(I) is not readily available, and if available at all, is only commercialized as simple inorganic salts, such as $TlNO_3$, Tl_2SO_4 and TlOAc, which are generally only soluble in H_2O, alcohols, and other polar solvents. Since Tl(I) is generally extremely toxic to humans (LD50 = 0.1 mg / m^2 by skin contact for $TlNO_3$), the synthesis of different precursors also presents a challenge as one cannot synthesize those precursors in large quantities. Nonetheless, if a synthetic procedure suitable for Tl(I) nodal units could be established for the synthesis of CPs using better bridging building blocks then work regarding the reactivity, structural trends, and physical properties of Tl(I)-based CPs could be established much more easily using SCN^--based building blocks.

6.2. **Future work: Selenocyanate-based systems**

Initial work on selenocyanate-based systems was performed by Masayuki Kobayashi and Prof. Ken Sakai as work parallel to the one depicted in Chapter 3, but by instead using $[Pt(SeCN)_4]^{2-}$ instead of $[Pt(SCN)_4]^{2-}$. In his work, Mr. Kobayashi successfully synthesized $K_2[Pt(SeCN)_4]$ and used it to synthesize $[Cu(en)_2Pt(SeCN)_4]$, which consists of a 1D CP with Se-Se bonds between the chains, effectively increasing the dimensionality to a 2D sheet. For the purpose of this thesis, attempts at recreating this work were performed but were unsuccessful, which prompted further investigations into the issues (presented below) regarding the synthesis of CPs using $[Pt(SeCN)_4]^{2-}$.

The synthesis of $K_2[Pt(SeCN)_4]$ had to be refined to obtain a pure product. In the first attempt at synthesizing $K_2[Pt(SeCN)_4]$ using the method provided by Mr. Kobayashi, it

was observed that the infrared spectra presented multiple unidentified peaks located in the 2200-2000 cm^{-1} region in a similar fashion to what was observed for $K_2[Pt(SCN)_4]$. Thus, using the same approach and synthetic strategy as for $K_2[Pt(SCN)_4]$ (see Chapter 3), $K_2[Pt(SeCN)_4]$ was synthesized as a pure dark red powder. However, when the product was left undisturbed in atmospheric conditions for a few days, it was observed that the product was very hygroscopic. In fact, after multiple attempts at the synthesis and preservation of the samples, such as storage in a desiccator and storage under N_2, the hygroscopicity of the samples still remained a major problem to be addressed. After only a few days, the samples were presenting signs of definite hygroscopicity as observed by FT-IR or qualitatively (e.g., an increase of the H_2O peak in the 3500 cm^{-1} IR region, or just becoming a liquid after a few days due to the excessive absorption of H_2O). Since using a highly hygroscopic substance is not very convenient and does not adhere to the guidelines established in Chapter 1 for which precursors are chosen for the synthesis of CPs, work using $K_2[Pt(SeCN)_4]$ as a building block for the synthesis of CPs was abandoned.

Instead, the focus of this work shifted towards addressing the hygroscopicity issue and synthesizing a viable $[Pt(SeCN)_4]^{2-}$ building block to be used in the synthesis of CPs. Initially, attempts were made at synthesizing the Na^+ and Cs^+ salts of the complex, but were unsuccessful. With Na^+, a greater hygrosopic behavior was observed whereas with Cs^+, the metathesis reaction did not occur, most likely due to the high solubility of CsCl in H_2O. Attempts at synthesizing the alkyl ammonium salts were also performed using similar methods as depicted in Chapter 2, but in the few cases where the synthesis of the salt was successful (Et_4N^+ and Bu_4N^+), the products were also highly hygroscopic. Other various cations were also used in the hopes of stabilizing the hygroscopicity of the salt, and in the cases of Ph_4P^+ and $AsPh_4^+$, it was revealed to be somewhat successful. When synthesized using these two cations, the salt is stable for a period of a few days with minimal water absorption when kept in a desiccator. In the case of Ph_4P^+, the salt is synthesized as a red powder whereas with $AsPh_4^+$, crystals of the product were obtained, but the crystals proved to be twinned and the data could not be refined.

With the issue of hygroscopicity addressed, a handful of attempts at the synthesis of CPs were made using complex $(AsPh_4)_2[Pt(SeCN)_4]$ (**6.1**) and appropriate metal

precursors and ligands (using a similar synthetic matrix to that described in Section 3.2). It is noteworthy to mention that complex **6.1** is not soluble in polar solvents, and thus metal precursors and ligands that are soluble in non-polar solvents had to be used for the synthesis of CPs. Initial work involved metal triflates and simple ligands such as en and tmeda in ethyl acetate, but crystallization of the resulting products using the H-tube method, low temperature or slow diffusion were unsuccessful. Upon further investigations, the synthesis of a wider array of CPs using $[Pt(SeCN)_4]^{2-}$ could be successful, by either further progressing down the route taken using complex **6.1,** non-polar solvents and appropriate metal precursors, or by attempting the synthesis of these CPs in polar solvent using freshly prepared $K_2[Pt(SeCN)_4]$ or by synthesizing the complex *in situ*.

6.2.1. **Experimental: $(AsPh_4)_2[Pt(SeCN)_4]$ (6.1)**

$(AsPh_4)_2[Pt(SeCN)_4]$ (**6.1**) was synthesized by modification of a published procedure.[273] To a 10 mL aqueous solution of $K_2[PtCl_4]$ (0.52 g, 1.25 mmol) was added a 10 mL aqueous solution of KSCN (0.486 g, 5.0 mmol). The solution was stirred at 60°C for 15 mins until the metathesis reaction is completed, as identified by the orange to dark red color change. Then, the solution was cooled to room temperature and a 20 mL solution of $(AsPh_4)Br$ (2.31 g, 5 mmol) in ethyl acetate was mixed in. The mixture of both solutions were thoroughly mixed using a separatory funnel until all the dark red color indicative of the $[Pt(SeCN)_4]^{2-}$ anion was located in the organic layer. The latter was then separated and thoroughly washed with a solution of H_2O and NaCl. The solvent was then removed using a rotary evaporator until a dark red powder of $(AsPh_4)_2[Pt(SeCN)_4]$ (**6.1**) was obtained. Recrystallization was performed by slow evaporation from a minimal amount of ethyl acetate. Anal. Calcd. for $C_{28}H_{20}AsN_4PtSe4$: C, 33.69; H, 2.02; N, 5.61 %. Found: C, 33.79; H, 2.15; N, 5.34 %. Yield: FT-IR (ATR, cm^{-1}): 3350 br, 2915 br, 2150 sh, 1617 s, 1578 s, 1450 s, 1392 s, 1310 s, 1102 sh, 958 sh. Raman (785 nm, a: 1, %lp: 50, cm^{-1}): 3353 br, 2911 br, 2143 sh, 1612 s, 1568 s, 1443 s, 1398 s, 1302 s, 1103 sh, 956 sh.

6.3. **Global conclusions**

The goal of this thesis was to examine the behavior of SCN^--based building blocks with respect to the synthesis of CPs. A thorough assessment of the synthetic potential of 1st, 2nd and 3rd row transition metal SCN^- building blocks was performed by attempting the synthesis of CPs using a wide variety of metal centres and ligands as nodal units in combination with said SCN^- complexes. Overall, many structural trends, physical properties of interest and potential applications were observed in the resulting CPs.

First row transition metal building blocks of the type $Q_x[M(NCS)_y]$. In the case of first-row transition metal building blocks, it was demonstrated that the building blocks were too labile in protic solvents to be reliable building blocks for the synthesis of CPs. When mixing the building blocks with the appropriate nodal precursors, neutral mononuclear complexes of the type $[M(L)_x(NCS)_y]$ were obtained as the crystallization product, suggesting ligand transfer between the SCN^- building block and the nodal metal centre. Attempts to control the lability of these building blocks by changing the reaction conditions, such as the polarity of the solvent, were unsuccessful. Further attempts using 1st row transition metal bridges were not performed. In order to synthesize such CPs, refinement of the reaction conditions in order to further control the lability of these building blocks is necessary. For example, attempts at the synthesis of CPs could be further refined using an inert atmosphere and non-polar solvents in combination with a selection of building blocks soluble in such solvents, such as the *n*-Bu_4N^+ building blocks presented in Chapter 2, despite the fact that initial work regarding this aspect suggested that the lability of the building blocks remained an issue to be tackled. Furthermore, synthesis of building blocks with countercations specifically targeting this application could also be done, such as building blocks with the $AsPh_4^+$ or PPh_4^+ cations, which would potentially allow the building block to be soluble in solvents such as hexane or dichloromethane.

$[Pt(SCN)_4]^{2-}$ as a building block. As opposed to the first-row transition metal building blocks, attempts at the synthesis of CPs were successful when $[Pt(SCN)_4]^{2-}$ was used in combination with a wide variety of nodal units. From the early work presented in Chapter 3, it was established that $[Pt(SCN)_4]^{2-}$ was much less labile in solution than the first-row

transition metal counterparts, and thus presented much greater potential for the synthesis of CPs. In Chapter 3, a thorough examination of the reactivity of the building block was performed by reacting it with the regular combination of ligands and metal centres typically used in the Leznoff group, and its potential for controlling the dimensionality of CPs along with its structural trends and topologies were established. It was demonstrated that $[Pt(SCN)_4]^{2-}$ shows multiple coordination modes which included, but were not limited to, two-coordinate N-bound linear *trans*- bridging, two-coordinate N-bound *cis*- bridging, three-coordinate N-bound bridging and two-coordinate S-Pt-S bridging. Overall, it was demonstrated that the resulting coordination mode of the $[Pt(SCN)_4]^{2-}$ unit, and subsequently the dimensionality of the CP, was mostly dependent on the choice of ligand and metal centre for the nodal unit, and that the $[Pt(SCN)_4]^{2-}$ unit tended to coordinate to any unoccupied coordination sites of the metal centre, and if available, form H-bonds with adjacent units. Furthermore, it was also demonstrated in Chapter 3 and Chapter 4 that $[Pt(SCN)_4]^{2-}$ can also be used in combination with non-conventional nodal units, such as $[Pb(bmpeda)]^{2+}$ or the dimeric nodes of the type $[Cu(\mu\text{-}OH)(L)]_2^{2+}$, which makes it a bridging unit with even greater potential for the synthesis of CPs with unique physical properties and topologies. Further work -remains to be done however when it comes to non-conventional nodal units, as the initial attempts at the synthesis of CPs with $[M(bmpeda)]^{2+}$ and $[M(bmpchda)]^{2+}$ where M is a first-row transition metal were unsuccessful. Preliminary results regarding this work suggest that the ligands tend to either hydrolyze or not react with $[Pt(SCN)_4]^{2-}$ when using our conventional reaction conditions. Just like for any other nodal units, a wide variety of CPs must be synthesized using a range of metal centres in order to establish a clear structural trend for the chosen combination of ligand and bridging units. In Chapter 4, despite the optimistic results from Chapter 3, it was demonstrated that $[Pt(SCN)_4]^{2-}$ still presents a level of lability in solution as some of the syntheses resulted in ligand transfer between the type $[Cu(\mu\text{-}OH)(L)]_2^{2+}$ dimeric units and $[Pt(SCN)_4]^{2-}$. Hence, further work regarding the $[Pt(SCN)_4]^{2-}$ building block could include the synthesis of the system using countercations soluble in non-polar solvents, such as $n\text{-}Bu_4N^+$ and Ph_4P^+, in order to limit the lability of the system and to allow the synthesis of CPs involving nodal units soluble in non-polar solvents which present physical properties of interest, such as birefringence or fluorescence.

In the case of other 2nd and 3rd row late-transition metal building blocks, attempts at their synthesis were performed, but in all cases, either the building blocks presented synthetic challenges, or the building block presented high lability similar to that observed for first-row transition metals.

SCN^- as an analogue to $[Au(CN)_2]^-$. In Chapter 4 and 5, attempts at the synthesis of CPs using SCN^- itself as an analogue to $[Au(CN)_2]^-$ were performed, and it was demonstrated that, despite the similarity between the two building blocks, such as the similarity in size, the linear coordination and the charge, the reactivity differs greatly even when using the same reaction conditions and thus, most of the time, the resulting topologies and structural features of the systems present much difference. For example, when reacted with the dimeric node $[Cu(\mu\text{-}OH)(L)]_2^{2+}$, $[Au(CN)_2]^-$ tends to form CPs, whereas SCN^- forms molecular units, most likely due to the difference in size and steric interactions with the Cu-OH-Cu units. In Chapter 5, when combined with nodes of the type $[Pb(R\text{-}terpy)]^{2+}$, it was shown that SCN^- tends to form CPs with similar topologies, but that due to the difference in size and the presence of coordination angles in SCN^-, the systems present sufficient difference to not be considered isostructural, and thus effective comparisons of the systems could not be made. Hence, overall, SCN^- cannot be used as a viable analogue to $[Au(CN)_2]^-$ and other bridging units should be sought instead.

Throughout this work, interesting CPs containing thiocyanate-based building blocks were synthesized and their optical and structural properties determined. However, a considerable amount of work remains to heighten the viability of thiocyanate-based building blocks for the strategic preparation of CPs to the same level as cyanide-based building blocks. Overall, questions remain as to how to address the lability of first-row thiocyanometallates and on how to control the structural behavior of the thiocyanate anion or of thiocyanate-based building blocks, and in order to answer these questions, more synthetic and structural data needs to be acquired for a wider variety of thiocyanate-based CPs. However, this work also demonstrated that SCN^- and $[Pt(SCN)_4]^{2-}$ can be used as a reliable building blocks in CPs. Therefore, it is clear that using thiocyanate-based building blocks in the rational design of CPs presents the potential to be a powerful tool that could enable the synthesis of a wide range of new

materials with compelling properties to the research community and for industrial commercial applications.

References

[1] Hong, M.; Chen, L. *Design and Construction of Coordination Polymers,* Wiley, Hoboken, NJ, **2009**.

[2] Guillerm, V.; Kim, D.; Eubank, J. F.; Luebke, R.; Liu, X.; Adil, K.; Lah, M. S.; Eddaoudi, M. *Chem. Soc. Rev.* **2014**, 63, (14), 6141.

[3] Burchell, T. J.; Puddephatt, R. J. *Inorg. Chem.* **2005,** 44, (10), 3718.

[4] Janiak, C. *Dalton Trans.* **2003**, (14), 2781.

[5] Champness, N. R. *Dalton Trans.* **2006**, (7), 877.

[6] Férey, G. *Chem. Soc. Rev.* **2008**, 37, (1), 191.

[7] Beauvais, L. G.; Long, J. R. *J. Am. Chem. Soc.* **2002**, 124, (41), 12096.

[8] Ohkoshi, S.-I.; Tokoro, H. *Acc. Chem. Res.* **2012**, 45, (10), 1749.

[9] Atanasov, M.; Comba, P.; Hausberg, S.; Martin, B. *Coord. Chem. Rev.* **2009**, 253, (19-20), 2306.

[10] Furukawa, H.; Cordova, K. E.; O'Keeffe, M.; Yaghi, O. M. *Science* **2013**, 341, (6149), 1230444.

[11] Song, L.; Zhang, J.; Sun, L.; Xu, F.; Li, F.; Zhang, H.; Si, X.; Jiao, C.; Li, Z.; Liu, S.; Liu, Y.; Zhou, H.; Sun, D.; Du, Y.; Cao, Z.; Gabelica, Z. *Energy Environ. Sci.* **2012**, 5, (6), 7508.

[12] Kitagawa, S.; Uemura, K. *Chem. Soc. Rev.* **2005**, 34, (2), 109.

[13] Zhang, J.-P.; Liao, P.-Q.; Zhou, H.-L.; Lin, R.-B.; Chen, X.-M. *Chem. Soc. Rev.* **2014**, 43, (16), 5789

[14] Herm, Z. R.; Wiers, B. M.; Mason, J. A.; van Baten, J. M.; Hudson, M. R.; Zajdel, P.; Brown, C. M.; Masciocchi, N.; Krishna, R.; Long, J. R. *Science* **2013**, 340, (6135), 960.

[15] Taylor, J. M.; Dawson, K. W.; Shimizu, G. K. H. *J. Am. Chem. Soc.* **2013**, 135, (4), 1193.

[16] Cui, Y.; Yue, Y.; Qian, G.; Chen B. *Chem. Rev.* **2012**, 112, (2), 1126.

[17] Heine, J.; Müller-Buschbaum, K. *Chem. Soc. Rev.* **2013**, 42, (24), 9232.

[18] Rocha, J.; Carlos, L. D.; Paz, F. A. A.; Ananias, D. *Chem. Soc. Rev.* **2011**, 40, (2), 926.

[19] Katz, M. J.; Ramnial, T.; Yu, H.-Z.; Leznoff, D. B. *J. Am. Chem. Soc.* **2008**, 130, (32), 10662.

[20] Roberts, R. J.; Li, X.; Lacey, T. F.; Pan, Z.; Patterson, H. H.; Leznoff, D. B. *Dalton Trans.* **2012**, 41, (23), 6992.

[21] Fernández, E. J.; Laguna, A.; López-de Luzuriaga, J. M. *Dalton Trans.* **2007**, (20), 1969.

[22] Dobrawa, R. *Synthesis and Characterization of Terpyridine-Based Fluorescent Coordination Polymers. Ph.D. Thesis*, Universität Würzburg, Würzburg, Germany, **2004**.

[23] Beauvais, L. G.; Shores, M. P.; Long, J. R. *J. Am. Chem. Soc.*, **2000**, 122, (12), 2763.

[24] Kreno, L. E.; Leong, K.; Farha, O. K.; Allendorf, M.; Van Duyne, R. P.; Hupp, J. T. *Chem. Rev.* **2012**, 112, (2), 1105.

[25] Lim, S. H.; Olmstead, M. M.; Balch, A. L. *J. Am. Chem. Soc.* **2011**, 133, (26), 10229.

[26] Lefebvre, J.; Korcok, J. L.; Katz, M. J.; Leznoff, D. B. *Sensors*, **2012**, 12, (3), 3669.

[27] Lefebvre, J.; Batchelor, R. J.; Leznoff, D. B. *J. Am. Chem. Soc.* **2004**, 126, (49), 16117.

[28] Thompson, J. R.; Williams, V. E.; Leznoff, D. B. *Cryst. Growth Des.* **2017**, 17, (3), 1180.

[29] Thompson, J. R.; Katz, M. J.; Williams, V. E.; Leznoff, D. B. *Inorg. Chem.* **2015**, 54, (13), 6462.

[30] Stavila, V.; Talin, A.; Allendorf, M. *Chem. Soc. Rev.* **2014**, 43, (16), 5994.

[31] Li, B.; Wen, H.; Zhou, W.; Chen, B. *J. Phys. Chem. Lett.* **2014**, 5, (20), 3468.

[32] Bureekaew, S.; Shimomura, S.; Kitagawa, S. *Sci. Tech. Adv. Mat.* **2008**, 9, (1), 12.

[33] Fromm, K. M. *Angew. Chem. Int. Ed.* **2009**, 48, (27), 4890.

[34] Buser, H. J.; Ludi, A.; Petter, W.; Schwarzenbach, D. *J. Chem. Soc. Chem. Commun.* **1972**, (23), 1299.

[35] Robin, M. B. *Inorg. Chem.* **1962**, 1, (2), 337.

[36] Hoffman, R. S. *Toxicol Rev.* **2003**, 22, (1), 29.

[37] Herren, F.; Fischer, P.; Ludi, A.; Haelg, W. *Inorg. Chem.* **1980**, 19, (4), 956.

[38] Batten, S. R.; Champness, N. R.; Chen, X.-M.; Garcia-Martinez, J.; Kitagawa, S.; Öhrström, L.; O'Keeffe, M.; Suh, M. P.; Reedijk, *J. Pure Appl. Chem.* **2013**, 85, (8), 1715.

[39] Ravve, A. *Principles of Polymer Chemistry.* 3rd ed., Springer, New York, **2012**.

[40] West, A. R. *Solid State Chemistry and its Applications.* John Wiley & Sons, New York, **2014**.

[41] Biradha, K.; Ramanan, A.; Vittal, J. *J. Cryst. Growth Des.* **2009**, 9, (7), 2969.

[42] Seth, S.; Matzger, A. J. *Cryst. Growth Des.* **2017**, 17, (8), 4043.

[43] Zhou, H.-C.; Long, J. R.; Yaghi, O. M. *Chem. Rev.* **2012**, 112, (2), 673.

[44] Batten, S. R.; Harris, A. R.; Jensen, P.; Murray, K. S.; Ziebell, A. *J. Chem. Soc., Dalton Trans.* **2000**, (21), 3829.

[45] Eryazici, I.; Farha, O.; Compton, O.; Stern, C.; Hupp, J.; Nguyen, S. *Dalton Trans.* **2011**, 40, (36), 9189.

[46] Leznoff, D.B.; Xue, B.; Patrick, B.; Sanchez, V.; Thompson, R. C. *Chem. Comm.* **2001**, (3), 259.

[47] Roberts, R. J.; Li, X.; Lacey, T. F.; Pan, J.; Patterson, H. H.; Leznoff, D. B. *Dalton Trans.* **2012**, 6992.

[48] Leznoff, D. B.; Xue, B.-Y.; Stevens, C. L.; Storr, A.; Thompson, R. C.; Patrick, B. O. *Polyhedron* **2001**, 20, (11-14), 1247.

[49] Katz, M. J.; Aguiar, P. M.; Batchelor, R. J.; Bokov, A. A.; Ye, Z.-G.; Kroeker, S.; Leznoff, D. B. *J. Am. Chem. Soc.* **2006**, 128, (11), 3669.

[50] Katz, M. J.; Shorrock, C. J.; Batchelor, R. J.; Leznoff, D. B. *Inorg. Chem.***2006**, 45, (4), 1757.

[51] Colacio, E.; Lloret, F.; Kivekäs, R.; Ruiz, J.; Suárez-Varela, J.; Sundberg, M. R. *Chem. Commun.* **2002**, (6), 592.

[52] Shorrock, C. J.; Jong, H.; Batchelor, R. J.; Leznoff, D. B. *Inorg. Chem.* **2003**, 42, (12), 3917.

[53] Leznoff, D. B.; Shorrock, C. J.; Batchelor, R. J. *Gold Bull.* **2007**, 40, (1), 36.

[54] Ovens, J. S. *An in-depth examination of the properties and behaviour of Au(III)-based [AuX2(CN)2]- (X = Cl, Br, I) as a coordination polymer building block. Ph.D. Thesis*, Simon Fraser University, Burnaby, BC, **2014**.

[55] Bailey, R. A.; Kozak, S. L.; Michelsen, T. W.; Mills, W. N. *Coord. Chem. Rev.* **1971**, (6), 407.

[56] Burmeister, J. L. *Coord. Chem. Rev.* **1990**, 105, 77.

[57] Klumpp, T. G. *J. Biol. Chem.* **1934**, 107, 213.

[58] Vrieze, K.; van Koten, G. in *Comprehensive coordination chemistry: the synthesis, reactions, properties & applications of coordination compounds,* Wilkinson, G., Pergamon Press, New York, **1987**, pp. 189.

[59] Walker, I. M.; McCarthy, P. J. *Inorg. Chem.* **1984**, 23, (13), 1842.

[60] Sabatini, A.; Bertini, I. *Inorg. Chem.* **1965**, 4, (7), 959.

[61] Clark, R. J. H.; Goodwin, A. D. J. *Spectrochim. Acta A* **1970**, 26A, 323.

[62] Forster, D.; Goodgame, D. M. L. *Inorg. Chem.* **1965**, 4, (6), 823.

[63] Hellner, E.; Ahsbahs, H.; Dehnicke, G.; Dehnicke, K. *Naturwissenschaften*, **1974**, 61, 502.

[64] Ozutsumi, K.; Hasegawa, E.; Kurihara, M.; Kawashima, T. *Polyhedron* **1993**, 12, (18), 2185.

[65] Bailey, R. A. *J. Inorg. Nucl. Chem.* **1971**, 33, (10), 3206.

[66] Schmidtke, H. H.; Garthoff, D. *Helv. Chim. Acta* **1967**, 50, 1631.

[67] Pearson, R. G. *J. Am. Chem. Soc.* **1963**, 85, (22), 3533.

[68] Atkins, P. W.; Shriver, D. F. *Shriver & Atkins Inorganic Chemistry*, Oxford University Press, New York, 2006.

[69] Chattopadhyay, S.; Bhar, K.; Das, S.; Chantrapromma, S.; Fun, K. F.; Ghosh, B. K. *J. Mol. Struct.* **2010**, 967, 112.

[70] Cucos, A.; Avarvari, N.; Andruh, M.; Journaux, Y.; Müller, A.; Schmidtmann, M. *Eur. J. Inorg. Chem.* **2006**, 903.

[71] Nikitina, V. M.; Nesterova, O. V.; Kokozay, V. N.; Goreshnik, E. A.; Jezierska, J. *Polyhedron* **2008**, 27, 2426.

[72] Skorupa, A.; Korybut-Daszkiewicz, B.; Mrozinski, J. *Inorg. Chim. Acta* **2001**, 324, 286.

[73] Mrozinski, J.; Klak, J.; Kruszynski, R. *Polyhedron* **2008**, 27, 1401.

[74] Machura, B.; Switlicka, A.; Mrozinski, J.; Kruszynski, R.; Kusz, J. *Polyhedron* **2010**, 29, 2023.

[75] Li, C. S.; Xue, L.; Che, Y. X.; Luo, F.; Zheng, J. M.; Mak, T. C. W. *Inorg. Chim. Acta* **2007**, 360, 3569.

[76] Bienko, A.; Klak, J.; Mrozinski, J.; Domagala, S.; Korybut-Daszkiewicz, B.; Wozniak, K. *Polyhedron* **2007**, 26, 5030.

[77] Shi, J.-M.; Xu, W.; Zhao, B.; Cheng, P.; Liao, D.-Z.; Chen, X.-Y. Eur. J. *Inorg. Chem.* **2005**, 55.

[78] Kou, H. Z.; Liao, D. Z.; Cheng, P.; Jiang, Z. H.; Yan, S. P.; Wang, G. L.; Yao, X. K.; Wan, H. G. *Can. J. Chem.* **1998**, 76, 1102.

[79] White, C. A.; Yap, G. P. A.; Raju, N. P.; Greedan, J. E.; Crutchley, R. J. *Inorg. Chem.* **1999**, 38, 2548.

[80] Wang, X.-Y.; Li, B.-L.; Zhu, X.; Gao, S. *Eur. J. Inorg. Chem.* **2005**, 3277.

[81] Shi, J.-M.; Chen, J.-N.; Wu, C.-J.; Ma, J.-P. *J. Coord. Chem.* **2007**, 60, 2009.

[82] Shi, J. M.; Sun, Y. M.; Zhang, X.; Cheng, P.; Liu, L. D. *J. Phys. Chem. A* **2006**, 110, 7677.

[83] Wriedt, M.; Näther, C. *Dalton Trans.* **2009**, 10192.

[84] Li, L. L.; Yuan, R. X.; Liu, L. L.; Ren, Z. G.; Zheng, A. X.; Cheng, H. J.; Li, H. X.; Lang, J. P. *Cryst. Growth Des.* **2010**, 10, 1929.

[85] Kawaguchi, V. S., *Variety in Coordination Modes of Ligands in Metal Complexes*, Springer, Berlin, **1988**.

[86] Jeffery, J. W. *Nature* **1947**, 159, 610.

[87] Scouloudi, H.; Carlisle, C. H. *Nature* **1950**, 166, 357.

[88] Lindqvist, I. *Acta Cryst.* **1957**, 10, 29.

[89] Cavalca, L.; Nardelli, M.; Fava, G. *Acta Crystallogr.* **1960**, 13, 125.

[90] Battaglia, L.; Ferrari, M.; Corradi, A.; Fava, G.; Pelizzi, C.; Tani, M. *J. Chem. Soc., Dalton Trans.* **1976**, 21, 2197.

[91] Nardelli, M.; Fara Gaspari, G.; Musatti, A.; Manfredotti, A. *Acta Crystallogr.* **1966**, 21, 910.

[92] Dockum, B. W.; Michael., W. R. *Inorg. Chem.* **1982**, 21, (1), 391.

[93] Healy, P. C.; Pakawatchai, C.; Papasergio, R. I.; Patrick, V. A.; White, A. H. *Inorg. Chem.* **1984**, 23, 3769.

[94] Wang, X. Q.; Xu, D.; Yuan, D. R.; Tian, Y. P.; Yu, W. T.; Sun, S. Y.; Meng, F. Q. *Mater. Research Bull.* **1999**, 34, (12), 2003.

[95] Bahta, A.; Parker, G. A.; Tuck, D. G. *Pure Appl. Chem.* **1997**, 69, (7), 1489.

[96] Blake, A. J.; Brooks, N. R.; Champness, N. A.; Crew, M.; Hanton, L. R.; Hubberstey, P.; Parsons, S.; Schröder, M. *Dalton Trans.* **1999**, 2813.

[97] Barnett, S. A.; Blake, A. J.; Champness, N. A.; Wilson, C. *Cryst. Eng. Comm.* **2000**, 2, 36.

[98] Teichert, O.; Sheldrick, W. S. *Z. anorg. allg. Chem.* **1999**, 625, 1860.

[99] Teichert, O. Sheldrick, W. S. *Z. anorg. allg. Chem.* **2000**, 626, 2196.

[100] Kromp, T.; Sheldrick, W. S.; Näther, C. *Z. anorg. allg. Chem.* **2003**, 629, 45.

[101] Shen, L.; Xu, Y. *J. Chem. Soc., Dalton Trans.* **2001**, 23, 3413.

[102] Wrzeszcz, G.; Dobrzańska, L.; Wojtczak, A.; & Grodzicki, A. *J. Am. Soc, Dalton Trans.* **2002**, 14, 2862.

[103] Ladd, M. F. C.; Palmer, R. A. *Structure Determination by X-ray Crystallography* 3rd Edition, Plenum Press, New York, **1994**.

[104] Chauhan, A.; Chauhan, P. *J. Anal. Bioanal. Tech.* **2014**, 5, 212.

[105] Jenkins, R.; Snyder, R. L. *Introduction to X-ray Powder Diffractometry* John Wiley & Sons, Inc., Hoboken, NJ, USA, **1996**.

[106] Pecharsky, V. K.; Zavalij, P. *Fundamentals of Powder Diffraction and Structural Characterization of Materials* Kluwer Academic Publishers, Boston, MA, **2003**.

[107] Griffiths, P.; de Hasseth, J. A. *Fourier Transform Infrared Spectrometry*, *2nd edition*, John Wiley & Sons, Inc., Hoboken, NJ, USA, **2007**.

[108] Gardiner, D. J.; Graves, P. R.; Bowley, H. J. *Practical Raman Spectroscopy* Springer-Verlag, Berlin, Germany, **1989**.

[109] Jones, L. H. *J. Chem. Phys.* **1956**, 25, (5), 1069.

[110] Murphy, D. B.; Spring, K. R.; Fellers, T. J.; Davidson, M. W. *Principles of Birefringence.* Available online: https://www.microscopyu.com/techniques/polarized-light/principles-of-birefringence

[111] Lewis, J.; Nyholm, R. S.; Smith, P. W. *J. Chem. Soc.* **1961**, 4590.

[112] Martin, J. L.; Thompson, L. C.; Radonovich, L. J.; Glick, M. D. *J. Am. Chem. Soc.* **1968**, 90, (16), 4493.

[113] Burmeister, J. L.; Patterson, S. D.; Deardorff, E. A. *Inorg. Chim. Acta* **1969**, 3, 105.

[114] Thompson, L. C.; Radonovich, L. *J. Acta Cryst.* **1990**, C46, 1618.

[115] Mullica, D. F.; Kautz, J. A.; Farmer, J. M.; Sappenfield, E. L. *J. Mol. Struct.* **1999**, 479, 31.

[116] Larkworthy, L. F.; Roberts, A. J.; Tucker, J.; Yavari, A. *J. Chem. Soc., Dalton Trans.* **1980**, 262.

[117] Larkworthy, L. F.; Leonard, G. A.; Povey, D. C.; Tucker, T. S. S. J.; Smith, G. W. *J. Am. Chem. Soc.* **1994**, 1425.

[118] Böhland, H.; Härtung, H.; Baumeister, U.; König, G.; Matthäus, R. *Microchim. Acta* **1997**, 125, 149.

[119] Addison, A. W.; Butcher, R. J.; Homonnay, Z.; Pavlishchuk, V. V.; Prushan, M. J.; Thompson, L. K. *Eur. J. Inorg. Chem.* **2005**, 2404.

[120] Krautscheid, H.; Gerber, S. *Z. Anorg. Allg. Chem.* **1999**, 625, 2041.

[121] Wood, J. S.; McMullan, R. K. *Acta Cryst.* **1984**, C40, 1803.

[122] Drew, M. G. B.; Hamid Bin Othman, A. *Acta Cryst.* **1975**, B31, 613.

[123] Becker, S.; Lerner, H. W.; Bolte, M. *Acta Cryst.* **2003**, E59, i156.

[124] Hoffman, D. W.; Wood, J. S. *Cryst. Struct. Comm.* **1982**, 11, 685.

[125] Hoffman, D. W.; Wood, J. S. *Cryst. Struct. Comm.* **1982**, 11, 691.

[126] Brinzari, T. V.; Tian, C.; Halder, G. J.; Musfeldt, J. L.; Whangbo, M. H.; Schlueter, J. A. *Inorg. Chem.* **2009**, 48, 7650.

[127] Larue, B.; Tran, L. T.; Luneau, D.; Reber, C. *Can. J. Chem.* **2003**, 81, 1168.

[128] Wilk, A.; Massa, W.; Friebel, C.; Reinen, D. *Z. Anorg. Allg. Chem.* **1992**, 608, 88.

[129] Beheshti, A.; Clegg, W.; Hyvadi, R.; Hekmat, H. F. *Polyhedron* **2002**, 21, 1547.

[130] Ouchi, A. *Bull. Chem. Soc. Jpn.* **1989**, 62, 2431.

[131] Arai, H.; Suzuki, Y.; Matsumura, N.; Takeuchi, T.; Ouchi, A. *Bull. Chem. Soc. Jpn.* **1989**, 62, 2530.

[132] Tateyama, Y.; Kuniyasu, Y.; Suzuki, Y.; Ouchi, A. *Bull. Chem. Soc. Jpn.* **1988**, 61, 2805.

[133] Matsumoto, F.; Takeuchi, T.; Ouchi, A. *Bull. Chem. Soc. Jpn.* **1989**, 62, 2078.

[134] Kuniyasu, Y.; Suzuki, Y.; Taniguchi, M.; Ouchi, A. *Bull. Chem. Soc. Jpn.* **1987**, 60, 179.

[135] Matsumoto, F.; Matsumura, N.; Ouchi, A. *Bull. Chem. Soc. Jpn.* **1989**, 62, 1809.

[136] Matsumura, N.; Takeuchi, T.; Ouchi, A. *Bull. Chem. Soc. Jpn.*, **1990**, 63, 620.

[137] Caglioti, V.; Sartori, G.; Scrocco, M. *J. Inorg. Nucl. Chem.* **1958**, 8, 87.

[138] Nakamoto, K. *Infrared and Raman Spectra of Inorganic and Coordination Compounds, 4th edition,* Wiley, New York, NY, **1986**.

[139] Bignozzi, C. A.; Argazzi, R.; Schoonover, J. R.; Dyer, R. B.; Scandola, F. *Inorg. Chem.* **1992**, 31, 5260.

[140] Cherkasova, E. V.; Peresypkina, E. V.; Virovets, A. V.; Podberezskaya, N. V.; Cherkasova, T. G. *Acta Cryst.* **2007**, C63, m195.

[141] Wells, A. F. *Structural Inorganic Chemistry, 5th edition*, Clarendon Press, Oxford, **1984.**

[142] Shannon, R. D. *Acta Crystallogr., Sect. A: Found. Crystallogr.* **1976**, 32, 751.

[143] Huheey, J. E.; Keiter, E. A.; Keiter, R. L. *Inorganic Chemistry: Principles of Structure and Reactivity, 4th edition* Harper Collins, New York, NY. **1993**.

[144] Yu, W. T.; Wang, X. Q.; Xu, D.; Lu, M. K.; Yuan, D. R. *Acta Cryst.* **2001**, C57, 145.

[145] Chen, H. J.; Zhang, L. Z.; Cai, Z. G.; Yang, G.; Chen, X. M. *J. Chem. Soc., Dalton Trans.* **2000**, 2463.

[146] Kahn, O. *Molecular magnetism.* VCH Publishers, Inc., New York, NY, **1993**.

[147] Munoz-Hernandez, M. A.; Keizer, T. S.; Wei, P.; Parkin, S.; Atwood, D. A. *Inorg. Chem.* **2001**, 40, (26), 6782.

[148] Housecroft, C. E.; Sharpe, A. G. *Inorganic Chemistry, 2nd edition*, Prentice Hall, New York, NY, **2004**.

[149] Górska, N.; Inaba, A.; Hirao, Y.; Mikuli, E.; Holderna-Natkaniec, K.; *RSC Adv.* **2012**, 2, 4283.

[150] Damzen, M. J.; Vlad, V.; Mocofanescu, A.; Babin, V. *Stimulated Brillouin Scattering; Fundamentals and applications*, CRC Press, London, **2003**.

[151] Thorne, A.; Litzen, U.; Johanson, S. *Spectrophysics: Principles and Applications, 2nd edition* Springer, Berlin, Germany, **1999**.

[152] Griffith, J. S.; Orgel, L. E. *Q. Rev. Chem. Soc.* **1957**, 11, 381 and references cited therein.

[153] Petrusenko, S. R.; Kokozay, V. N.; Fritsky, I. O. *Polyhedron* **1997**, 16, (2), 267.

[154] Halder, A.; Bhattacharya, B.; Sen, R.; Ghoshal, D. *Chem. Select* **2017**, 2, 5783 and references cited therein.

[155] Bruker, SAINT, Bruker AXS Inc., Madison, Wisconsin, USA, **2012**.

[156] Sheldrick, G. M. *CELL_NOW* University of Göttingen, Germany, Online, **2004**. Available online: http://xray.tamu.edu/pdf/manuals/cell_now.pdf

[157] Sheldrick, G. M. *TWINABS* University of Göttingen, Göttingen, Germany, **1996**.

[158] Betteridge, P. W.; Carruthers, J. R.; Cooper, R. I.; Prout, K.; Watkin, D. J. *J. Appl. Crystallogr.* **2003**, 36, (6), 1487.

[159] Altomare, A.; Cascarano, G.; Giacovazzo, C.; Guagliardi, A.; Burla, M. C.; Polidori, G.; Camalli, M. *J. Appl. Crystallogr.* **1994**, 27, (3), 435.

[160] Palatinus, L.; Chapuis, G. *J. Appl. Crystallogr.* **2007**, 40, (4), 786.

[161] Putz, H.; Brandenburg, K. *Diamond - Crystal and Molecular Structure Visualization* GbR, *Kreuzherrenstr.*, 102, 53227, Bonn, Germany.

[162] Nishikiori, S.; Iwamoto, T. *Bull. Chem. Soc. Jpn.* **1983**, 56, 3246.

[163] Kajnakova, M.; Cernak, J.; Kavecansky, V.; Gerard, F.; Papageorgiou, T.; Orendac, M.; Orendacova, A.; Feher, A. *Solid State Sci.* **2006**, 8, 203.

[164] Shaikh, N.; Panja, A.; Goswami, S.; Banerjee, P.; Kubiak, M.; Ciunik, Z.; Puchalska, M.; Legendziewicz, J. *Indian J. Chem.* **2004**, 43, 1403.

[165] Kendi, E.; Ulku, D.; *Z. Kristallogr.* **1976**, 144, 91.

[166] Nishikiori, S.-I.; Iwamoto, T. *Inorg. Chem.* **1986**, 25, 788.

[167] Miyoshi, T.; Iwamoto, T.; Sasaki, Y. *Inorg. Chim. Acta* **1972**, 6, 59.

[168] Lu, R.; Zhou, H.; Chen, Y.; Xiao, J.; Yuan, A. *J. Coord. Chem.* **2010**, 63, 794.

[169] Ding, E.; Sturgeon, M. R.; Rath, A.; Chen, X.; Keane, M. A.; Shore, S. G. *Inorg. Chem.* **2009**, 48, 325.

[170] Geisheimer, A. R.; Huang, W.; Pacradouni, V.; Sabok-Sayr, S. A.; Sonier, J. E.; Leznoff, D.B., *Dalton Trans.* **2011**, 40, 7505.

[171] Martínez, V.; Gaspar, A. B.; Muñoz, M. C.; Bukin, G. V.; Levchenko, G.; Real, J. A. *Chem. Eur. J.* **2009**, 15, 10960.

[172] Needham, G. F.; Johnson, P. L.; Williams, J. M. *Acta Crystallogr., B.* **1977**, 33, 1581.

[173] Dillinger, R.; Gliemann, G.; Pfleger, H. P.; Krogmann, K. *Inorg. Chem.* **1983**, 22, 1366.

[174] Akhmedov, A. I.; Yanovsky, A. I.; Babkov, A. V.; Struchkov, Y. T. *Coord. Khim. (Russ.)* **1983**, 9, 1138.

[175] Brozik, J. A.; Scott, B. L.; Swanson, B. I. *Inorg. Chim. Acta* **1999**, 294, 275.

[176] Krogmann, K.; Keim, A.; Stahl, R.; Pfleger, H. P. *Mol. Cryst. Liq. Cryst.* **1985**, 120, 401.

[177] Potocnak, I.; Vavra, M.; Cizmar, E.; Tibenska, K.; Orendacova, A.; Steinborn, D.; Wagner, C.; Dusek, M.; Fejfarova, K.; Schmidt, H.; Muller, T.; Orendac, M.; Feher, A. *J. Solid State Chem.* **2006**, 179, 1965.

[178] Liu, F.; Chen, W. *J. Coord. Chem.* **2006**, 59, 1629.

[179] Schollhorn, H.; Thewalt, U.; Raudaschl-Sieber, G.; Lippert, B. *Inorg. Chim. Acta* **1986**, 124, 207.

[180] Flay, M.-L.; Vahrenkamp, H. *Eur. J. Inorg. Chem.* **2003**, 1719.

[181] Olmstead, M. M.; Lee, M. A.; Stork, J. R. *Acta Crystallogr. E* **2005**, 61, m1048.

[182] Cordiner, R. L.; Feroze, M. P.; Lledo-Fernandez, C.; Albesa-Jove, D.; Howard, J. A. K.; Low, P. J. *Inorg. Chim. Acta* **2006**, 359, 3459.

[183] Dechambenoit, P.; Ferlay, S.; Hosseini, M. W.; Kyritsakas, N. *Chem. Commun.* **2007**, 4626.

[184] Vavra, M.; Potocnak, I.; Kajnakova, M.; Cizmar, E.; Feher, A. *Inorg. Chem. Commun.* **2009**, 12, 396.

[185] Falvello, L. R.; Tomas, M.; *Chem. Commun.* **1999**, 273.

[186] Potocnak, I.; Vavra, M.; Cizmar, E.; Kajnakova, M.; Radvakova, A.; Steinborn, D.; Zvyagin, S. A.; Wosnitza, J.; Feher, A. *J. Solid State Chem.* **2009**, 182, 196.

[187] Jana, A. D.; Saha, R.; Ghosh, A. K.; Manna, S.; Ribas, J.; Chaudhuri, N. R.; Mostafa, G. *Polyhedron* **2009**, 28, 3065.

[188] Potocnak, I.; Vavra, M.; Cizmar, E.; Dusek, M.; Muller, T.; Steinborn, D. *Inorg. Chim. Acta* **2009**, 362, 4152.

[189] Stojanovic, M.; Robinson, N. J.; Chen, X.; Sykora, R. E. *Inorg. Chim. Acta* **2011**, 370, 513.

[190] Doerrer, L. H. *Comm. Inorg. Chem*. **2008**, 29*,* 93.

[191] Buss, C. E.; Anderson, C. E.; Pomije, M. K.; Lutz, C. M.; Britton, D.; Mann, K. R. *J. Am. Chem. Soc.* **1998**, 120, 7783.

[192] Katz, M. J.; Sakai, K.; Leznoff, D. B. *Chem. Soc. Rev.* **2008**, 37, 1884.

[193] *Chemistry experiments*, 4th ed., The Chemical Society of Japan, vol. 17, 162.

[194] Batten, S. R.; Robson, R. *Angew. Chem., Int. Ed.* **1998**, 37, 1460.

[195] Öhrström, L.; Larsson, K. *Molecule-Based Materials: The Structural Network Approach*, Elsevier, Amsterdam, **2005**, 324 pages.

[196] Whiteoak, C.; Salassa, G.; Kleij, A. *Chem. Soc. Rev.* **2012**, 41, (2), 622 and references cited therein.

[197] Mawby, A.; Pringle, G. *J. Chem. Soc. D: Chem. Commun.* **1970**, (6), 385.

[198] Nguyen, Q. T.; Jeong, J. H. *Polyhedron* **2006**, 25, (8), 1787-1790.

[199] Grinberg, A A. *An Introduction to the Chemistry of Complex Compounds*. Oxford: Pergamon Press, London, , **1962**.

[200] Lefebvre, J.; Callaghan, F.; Katz, M. J.; Sonier, J. E.; Leznoff, D. B. *Chem. Eur. J.* **2006**, 12, 6748.

[201] Lefebvre, J.; Tyagi, P.; Trudel, S.; Pacradouni, V.; Kaiser, C.; Sonier, J. E.; Leznoff, D. B. *Inorg. Chem.* **2009**, 55.

[202] Lefebvre, J.; Chartrand, D.; Leznoff, D. B. *Polyhedron*, **2007**, 2189.

[203] Korčok, J. L.; Katz, M. J.; Leznoff, D. B. *J. Am. Chem. Soc.* **2009**, 4866.

[204] Gupta, Y. K.; Agarwal, S. C.; Madnawat, S. P.; Narain, R. *Res. J. Chem. Sci.* **2012**, 2, (4), 68 and references cited therein.

[205] Crawford, V. H.; Richardson, H. W.; Wasson, J. R.; Hodgson, D. J.; Hatfield, W. E. *Inorg. Chem.* **1976**, 15, 2107.

[206] Hatfield, W. E.; Piper, T. S.; Klabunde, U. *Inorg. Chem.* **1963**, 2, 629.

[207] Jeter, D. Y.; Lewis, D. L.; Hempel, J. C.; Hodgson, D. J.; Hatfield, W. E. *Inorg. Chem.* **1972**, 11, 1958.

[208] Lewis, D. L.; Hatfield, W. E.; Hodgson, D. J. *Inorg. Chem.* **1972**, 11, 2216.

[209] Lewis, D. L.; Hatfield, W. E.; Hodgson, D. J. *Inorg. Chem.* **1974**, 13, 147.

[210] Lewis, D. L.; McGregor, K. T.; Hatfield, W. E.; Hodgson, D. J. *Inorg. Chem.* **1974**, 13, 1013.

[211] McGregor, K. T.; Hodgson, D. J.; Hatfield, W. E. *Inorg. Chem.* **1976**, 15, 421.

[212] Forman, L. R.; Landee, C. P.; Wikaira, J. L.; Turnbull, M. M. *Eur. Chem. Bull.* **2014**, 3, (2), 190.

[213] Golchoubian, H.; Zarabi, R. Z. *Polyhedron* **2009**, 28, 3685.

[214] Prescimone, A.; Sanchez-Benitez, J.; Kamenev, K. K.; Moggach, S. A.; Warren, J. E.; Lennie, A. R.; Murrie, M.; Parsons, S.; Brechin, E. K. *Dalton Trans.* **2010**, 39, 113.

[215] Haase, R.; Beschnitt, T.; Flörke, U.; Herres-Pawlis, S. *Inorg. Chim. Acta* **2011**, 374, 546.

[216] Arakawa-Itoh, M.; Tokuman, K.; Mori, Y.; Kajiwara, T.; Yamashita, M.; Fukuda, Y. *Bull. Chem. Soc. Jpn.* **2009**, 82, 358.

[217] Mukherjee, J.; Mukherjee, R. *Dalton Trans.* **2006**, 1611.

[218] Allen, J. J.; Hamilton, C. E.; Barron, A. R. *Dalton Trans.* **2010**, 39, 11451.

[219] Hangan, A.; Bodoki, A.; Oprean, L; Alzuet, G.; Liu-González, M.; Borrás, J. *Polyhedron* **2010**, 29, 1305.

[220] De Munno, G.; Julve, M.; Lloret, F.; Faus, J.; Verdaguer, M.; Caneschi, A. *Inorg. Chem.* **1995**, 34, 157.

[221] Chi, Y.-N.; Cui, F.-Y.; Xu, Y.-Q.; Hu, C.-W. *J. Mol. Struct.* **2008**, 875, 42.

[222] Zhang, L.; Ling, Y.; Li, J.; Gao, H. *Struct. Chem.* **2008**, 19, 911.

[223] Paraschiv, C.; Andruh, M.; Ferlay, S.; Hosseini, M. W.; Kyritsakas, N.; Planeix, J.-M.; Stanica, N. *Dalton Trans.* **2005**, 1195.

[224] Marin, G.; Tudor, V.; Kravtsov, V. C.; Schmidtmann, M.; Simonov, Y. A.; Müller, A.; Andruh, M. *Cryst. Growth Des.* **2005**, *5*, 279.

[225] Tudor, V.; Marin, G.; Kravtsov, V.; Simonov, Y. A.; Lipkowski, J.; Brezeanu, M.; Andruh, M. *Inorg. Chim. Acta* **2003**, 353, 35.

[226] Chen, F.-T.; Li, D.-F.; Gao, S.; Wang, X.-Y.; Li, Y.-Z.; Zheng, L.-M.; Tang, W.-X. *Dalton Trans.* **2003**, 3283.

[227] Mukherjee, P. S.; Maji, T. K.; Mallah, T.; Zangrando, E.; Randaccio, L.; Chaudhuri, N. R. *Inorg. Chim. Acta* **2001**, 315, 249.

[228] Yu, J.-H.; Bie, H.-Y.; Xu, J.-Q.; Lu, J.; Zhang, X. *Inorg. Chem. Commun.* **2004**, 7, 1205.

[229] Leznoff, D. B.; Draper, N. D.; Batchelor, R. J. *Polyhedron* **2003**, 22, 1735.

[230] Thompson, J. R.; Ovens, J. S.; Williams, V. E.; Leznoff, D. B. *Chem. Eur. J.* **2013**, 16572.

[231] Katz, M. J.; Kaluarachchi, H.; Batchelor, R. J.; Schatte, G.; Leznoff, D. B. *Cryst. Growth Des.* **2007**, 1946.

[232] Castro, I.; Faus, J.; Julve, M.; Bois, C.; Real, J. A.; Lloret, F. *J. Chem. Soc., Dalton Trans.* **1992**, 47.

[233] Mitchell, T. P.; Bernard, W. H. *Acta Crystallogr.* **1970**, B26, 2096.

[234] Wasson, J. R.; Mitchell, T. P.; Bernard, W. H. *J. Inorg. Nucl. Chem.* **1968**, 30, 2865.

[235] Cole, B. J.; Brumage, W. H. *J. Chem. Phys.* **1970**, 53, 4718.

[236] Howard, J. A. K.; Madhavi, N. N. L.; Nangia, A.; Desiraju, G. R.; Allen, F. H.; Wilson, C. C. *Chem Comm.***1999**, 1675.

[237] Bernstein, J. *Polymorphism in Molecular Crystals*; Oxford University Press: Oxford, U.K., **2002**.

[238] Bleaney, B.; Bowers, K. D. *Proc. R. Soc. London A* **1952**, 214, 451.

[239] Hodgson, D. J. *Prog. Inorg. Chem.* **1974**, 19, 173.

[240] Estes, E. D.; Hatfield, W. E.; Hodgson, D. J. *Inorg. Chem.* **1974**, 13, 1654.

[241] Hatfield, W. E. In *Magneto-Structural Correlations in Exchange Coupled Systems*; Willett, R. D., Gatteschi, D., Kahn, O., Eds.; Reidel: Dordrecht, The Netherlands, 1984; p. 555 and references therein.

[242] Ruiz, E.; Alemany, P.; Alvarez, S.; Cano, J. *Inorg. Chem.* **1997**, 36, 3683.

[243] Ruiz, E.; Alemany, P.; Alvarez, S.; Cano, J. *J. Am. Chem. Soc.* **1997**, 119, 1297.

[244] Frisch, M. J.; Trucks, G. W.; Schlegel, H. B.; Scuseria, G. E.; Robb, M. A.; Cheeseman, J. R.; Scalmani, G.; Barone, V.; Mennucci, B.; Petersson, G. A.; Nakatsuji, H.; Caricato, M.; Li, X.; Hratchian, H. P.; Izmaylov, A. F.; Bloino, J.; Zheng, G.; Sonnenberg, J. L.; Hada, M.; Ehara, M.; Toyota, K.; Fukuda, R.; Hasegawa, J.; Ishida, M.; Nakajima, T.; Honda, Y.; Kitao, O.; Nakai, H.; Vreven, T.; Montgomery, J. A., Jr.; Peralta, J. E.; Ogliaro, F.; Bearpark, M.; Heyd, J. J.; Brothers, E.; Kudin, K. N.; Staroverov, V. N.; Kobayashi, R.; Normand, J.; Raghavachari, K.; Rendell, A.; Burant, J. C.; Iyengar, S. S.; Tomasi, J.; Cossi, M.; Rega, N.; Millam, N. J.; Klene, M.; Knox, J. E.; Cross, J. B.; Bakken, V.; Adamo, C.; Jaramillo, J.; Gomperts, R.; Stratmann, R. E.; Yazyev, O.; Austin, A. J.; Cammi, R.; Pomelli, C.; Ochterski, J. W.; Martin, R. L.; Morokuma, K.; Zakrzewski, V. G.; Voth, G. A.; Salvador, P.; Dannenberg, J. J.; Dapprich, S.; Daniels,A.D.;Farkas, Ö.; Foresman, J. B.; Ortiz, J. V.; Cioslowski, J.; Fox, D. J. *Gaussian 09, 773 Revision D.01*, Gaussian, Inc.: Wallingford CT, **2009**.

[245] Becke, A. D. *J. Chem. Phys.*, **1993**, 98, 5648.

[246] Stephens, P. J.; Devlin, F. J.; Chabalowski, C. F.; Frisch, M. J. *J. Phys. Chem.* **1994**, 98, 11623.

[247] Dunning, T., Jr.; Hay, P. J. *Mod. Theor. Chem.* **1977**, 3, 1.

[248] Hay, P. J.; Wadt, W. R. *J. Chem. Phys.* **1985**, 82, 270.

[249] Hay, P. J.; Wadt, W. R. *J. Chem. Phys.* **1985**, 82, 299.

[250] Wadt, W. R.; Hay, P. J. *J. Chem. Phys.* **1985**, 82, 284.

[251] Noodleman, L. *J. Chem. Phys.*, **1981**, 74, 5737.

[252] Noodleman, L.; Davidson, E. R. *Chem. Phys.*, **1986**, 109, 131.

[253] Noodleman, L.; Case, D. A. *Adv. Inorg. Chem.*, **1992**, 38, 423.

[254] Yamaguchi, K.; Fukui, H.; Fueno, T. *Chem. Lett.* **1986**, 625.

[255] Yamaguchi, K.; Takahara, Y.; Fueno, T.; Houk, K. N. *Theor. Chim. Acta* **1988**, 73, 337.

[256] Yamanaka, S.; Okumura, M.; Nakano, M.; Yamaguchi, K. *Theochem.* **1994**, 310, 205.

[257] Halcrow, M. A. *Coord. Chem. Rev.* **2005**, 249, 2880.

[258] H. Hofmeier and U. S. Schubert, Chem. Soc. Rev. **2004**, 3, 373.

[259] Katz, M. J.; Kaluarachchi, H.; Batchelor, R. J.; Bokov, A. A.; Ye, Z.-G.; Leznoff, D. B. *Angew. Chem. Int. Ed.* **2007**, 8804.

[260] Katz, M. J.; Leznoff, D. B. *J. Am. Chem. Soc.* **2009**, 18435.

[261] Howe-Grant, M.; Ldppard, S. J.; Chalilpoyil, P.; Marzilli, L. G. *Inorganic Syntheses, Volume 20*, John Wiley & Sons, Inc., Hoboken, NJ, USA., **1980**.

Appendix A. Principles of birefringence

Concepts of birefringence

Birefringence refers to the difference between two orthogonal refractive indices of a crystal. The refractive index of a material is calculated by dividing the speed of light in a vacuum (c) by the speed of light in the material (v). In order to change the value of a refractive index, one must aim towards changing the component with which light interacts in the material in question, the electron cloud. When a beam of light interacts with an atom, bond or molecule, it is scattered within the crystal which in turn results in the refraction phenomenon. To slow down the speed at which the light travels through the material, and thus increase the value of the refractive index along a provided direction, one needs to increase the amount of absorption, oscillation and emission of light within the material. For the purpose of birefringence, what affects the refractive index of a material is represented by the Lorentz-Lorenz equation (Equation A.1) where M is the molecular weight, N is Avogadro's number, α is the polarizability, ρ is the density and n is the refractive index.

$$n = \sqrt{\frac{1+\frac{2\alpha N\rho}{3M}}{1+\frac{2\alpha N\rho}{3M}}} \qquad \textbf{Equation A.1}$$

In order to create a birefringent material, one must aim towards changing the density and polarizability of the material along its respective axes, and increasing the difference between them. Regarding polarizability (i.e., their anisotropy), in general, atoms with more electrons present greater polarizability, and less bound electrons are also more polarizable. In a molecule, the polarizability of a bond is greater when measured along the bond rather than perpendicular to the bond. Linear molecules present the most anisotropic polarizability whereas, for example, tetrahedral or octahedral inorganic molecules present very little anisotropy in their polarizability. As such, in order to design a highly birefringent material, one must thus aim towards using anisotropically polarizable molecules and bonds, such as electronically delocalized systems (C=C) and highly conjugated systems (benzene). Of course, in a crystal, polarizability along an axis is an additive property and as such, the alignment of the molecules in the crystal is also

of importance. If the molecules in a crystal alternate in orientation in such a way that the difference between the overall polarizability along each axis is zero (more specifically, an isotropic distribution of the polarizability in the crystal), the overall birefringence of the molecule will be zero. Regarding the density, one must simply consider how many molecules a ray of light will interact with during its passage through the material. A lower density along an axis will result in a lower refractive index and vice-versa.

Since the refractive indices are related to their respective axes, a crystal will contain three primary refractive indices, which are represented in Figure A.1 in the optical indicatrix of a crystal, and three different birefringence value (n_a, n_b and n_c). However, depending on the symmetry of a crystal, the overall availabilities of these birefringence values may vary. For example, in a cubic system, the optical indicatrix is spherical since all axes are equivalent to each other, and thus the overall birefringence will be zero. On the other hand, a tetragonal system will have two different refractive indices, and thus one birefringence value may be greater than zero. In the case of an orthorhombic system, all three refractive indices will differ from each other, and thus one or two birefringence values greater than zero may be observed. When measuring the birefringence of a crystal with symmetry other than cubic, one must also denote the axis or the crystal face for which it was measured.

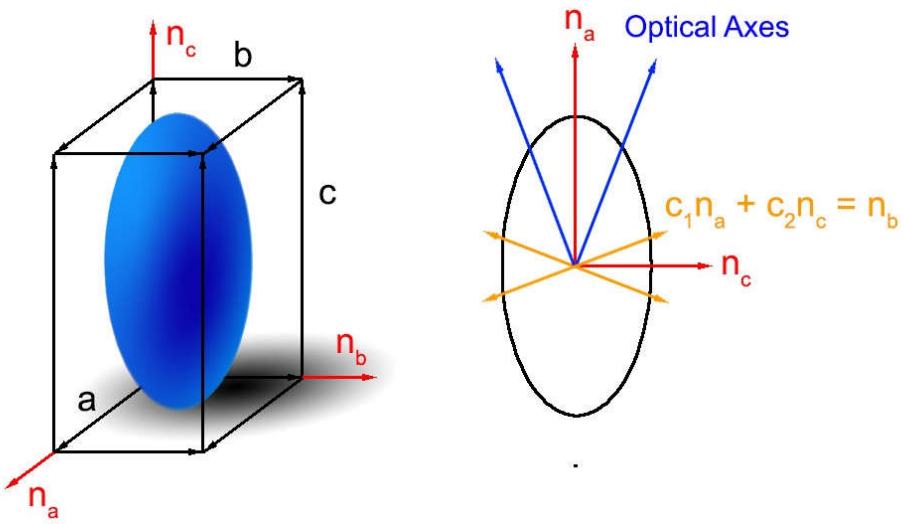

Figure A.1 Depiction of the optical indicatrix and the three primary components of the optical indicatrix (left) and the $n_a n_c$ plane of the indicatrix visualizing the four axes for which the n_a and n_c components are equivalent to n_b leading to the orthogonal optical axes (right).

In a crystal, axes that experience no birefringence are known as optical axes and occur when the perpendicular components of the indicatrix are equivalent to each other. A tetragonal system is known as uniaxial and systems with lower symmetry are known as biaxial. The term biaxial is defined by the fact that when looking at a plane, for example the $n_a n_c$ plane, there are four angles at which the contribution of n_a and n_c will be equal to n_b, and thus where the birefringence is zero, resulting in the presence of two orthogonal optical axes for the n_b refractive index.

Measuring birefringence by optical microscopy

In the Leznoff group, the birefringence values of a crystal are measured by optical microscopy. Usually, only the birefringence value for the largest surface of a crystal is measured as it is the value of interest to the scientific community, but also because of the technical limitations of measuring the birefringence of very small crystals (especially in the case of plates or needles).

In order to measure the birefringence of a crystal, the material is first observed when placed between two crossed polarizers oriented at 90° with respect to one another. The crystal is then rotated a full 360°, and one of two phenomenon can be observed: (1) the

crystal appears black independently of its orientation or (2) the intensity of light passing through the crystal varies depending on its orientation with maxima and minima oriented at 90° to one another. In the first case, the crystal is observed to not be birefringent along the measured axis. In the second case, the crystal presents birefringence along the measured axis. This is observed because when birefringence occurs, two rays of light leave the crystal (the ordinary ray and the extraordinary ray), and the two rays are polarized orthogonally to each other. When the polarized rays do not align with the polarizer axes, light is transmitted and when the axes of the rays and the polarizer align, the crystal appears as it is not transmitting light. As stated, these minima occur every 90° and are called extinction directions.

When the extinction directions are determined, the crystal is rotated such that its orientation is 45° in regards to the polarizer. At this angle, the two rays of light can be though as two orthogonally polarized rays of equal intensity travelling through the polarizer. However, due to the difference in refractive indices, and thus speed of light in the material, the extraordinary ray lags slightly behind the ordinary ray, and thus the difference between the two rays can be determined by using a tilting compensator (Figure A.3 and A.4). The compensator consists of a uniaxial birefringent material (usually calcite) which allows one to restore the lag between the two rays when the compensator is aligned with the crystal itself, thus undoing the birefringence of the crystal and is placed between the two polarizers in the optical system. The amount of lag between the two rays not only depends on the difference in the refractive indices, but also depends on the thickness of the crystal. Together, the birefringence value multiplied by the thickness of the crystal is known as retardation, which can be obtained as a direct relation to the tilting angle of the tilting compensator. The angle of the compensator is determined by slowly increasing the angle until the lag between the two rays reaches zero, and thus the birefringence of the crystal is undone and the crystal appears black. Using calibration charts, one can then determine the retardation value from the angle obtained using the compensator. It is noteworthy to mention that this method does not determine the primary birefringence of a crystal, but instead the in-plane birefringence, which coincidently is the value of interest to the scientific community, as stated above.

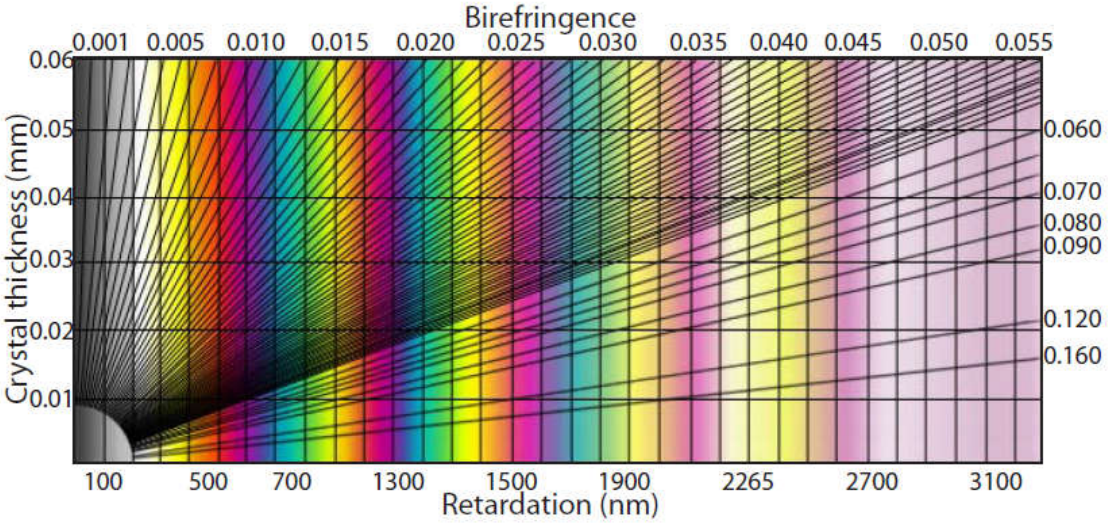

Figure A.2 **Michel-Lévy interference chart showing the relationship between birefringence, crystal thickness and apparent colour between crossed polarizers.**

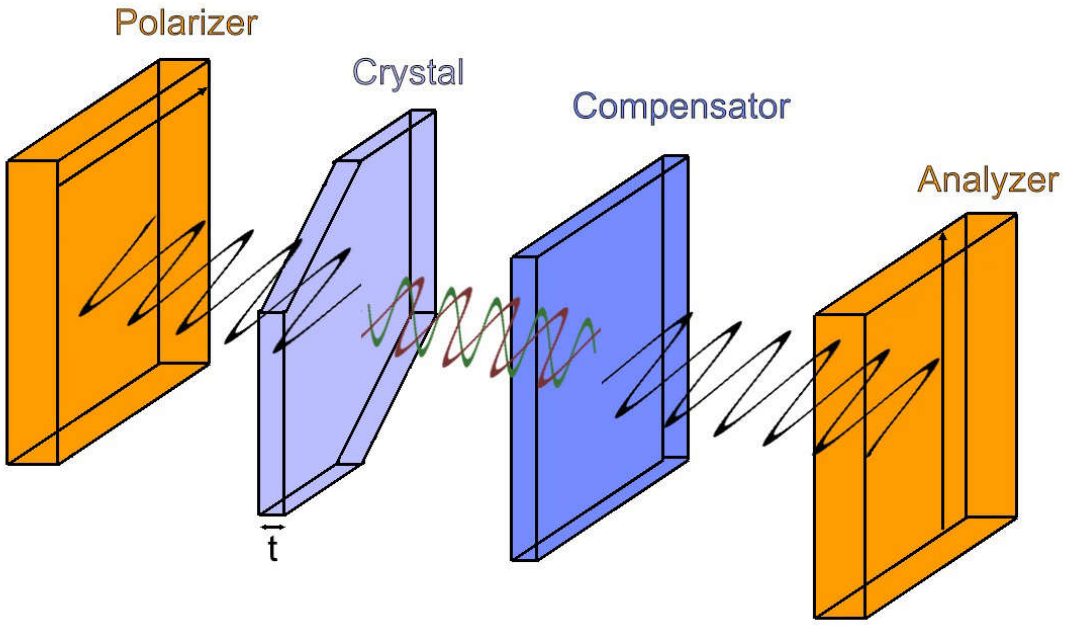

Figure A.3 Experimental setup demonstrating the effect of the compensator on the ordinary ray and the extraordinary ray when measuring birefringence. The compensator retardation is equal to the retardation between the two rays after they pass through the crystal.

In this work, determination of the thickness of the crystal was done using SEM where the crystal was placed against a sticky surface and the angle of the sample holder slowly

altered until parallel to the camera, thus allowing the accurate measurement of the thickness of the crystal using the SEM software which determines the measured distance from the amount of pixels and the zoom factor.

Appendix B. Examples of assigned infrared spectra for thiocyanate-based Werner complexes.

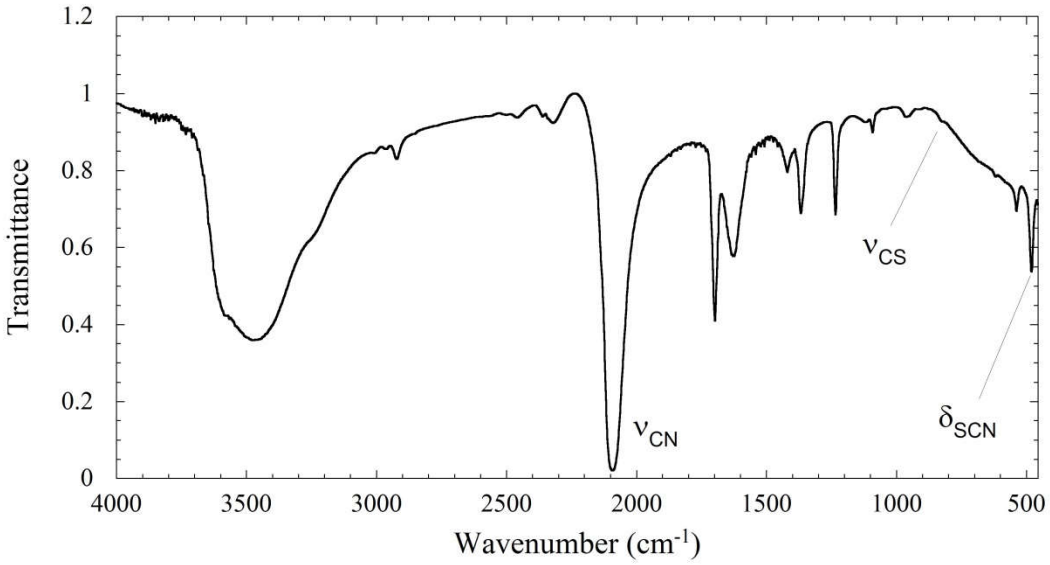

Figure B.1 The infrared spectrum of $K_3[Cr(NCS)_6]$ (**2.1**) with assigned vibrational modes.

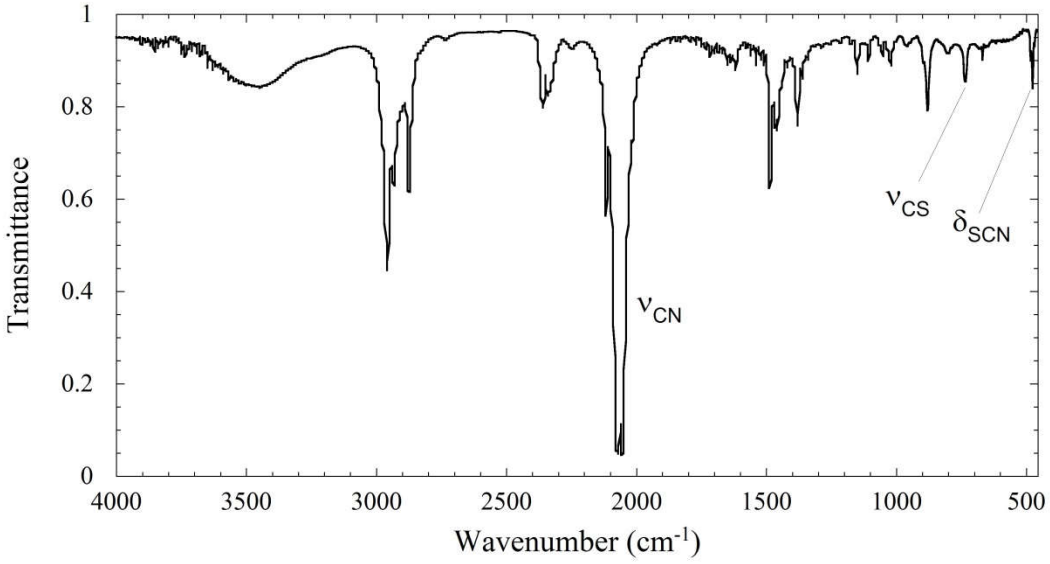

Figure B.2 The infrared spectrum of $(n\text{-Bu})_4[Fe(NCS)_6]$ (**2.13**) with assigned vibrational modes.

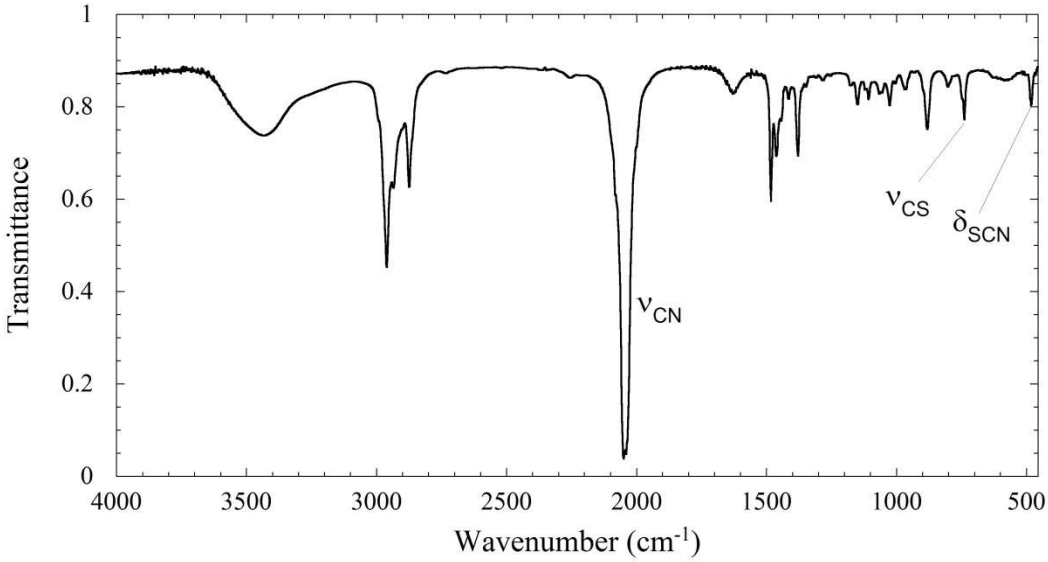

Figure B.3 The infrared spectrum of $(n\text{-}Bu)_4[Eu(NCS)_6]$ (**2.17**) with assigned vibrational modes.

Appendix C. Tables of crystallographic data

Table C.1 Crystallographic data for **2.1**, **2.2** and **2.4**.

Complex	2.1	2.2	2.4
empirical formula	$C_6CrK_3N_6OS_6$	$C_9H_{22}CrN_{10}OS_6$	$C_{18}H_{36}CrN_9S_6$
formula weight	533.79	530.73	622.94
Temperature (K)	293	293	293
crystal system	Trigonal	Orthorhombic	Monoclinic
space group	P-3m1	Pcmn	C2/c
a (Å)	14.358(3)	9.6828(16)	24.8961(10)
b (Å)	14.358(3)	14.744(2)	9.3234(4)
c (Å)	9.7042(19)	16.341(3)	28.4594(12)
α (deg)	90	90	90
β (deg)	90	90	100.021(2)
γ (deg)	120	90	90
V (Å^3)	1732.5(3)	2332.9(7)	6505.1(5)
Z	1	4	8
ρ_{calc} (g/cm^3)	1.581	1.511	1.272
μ (mm^{-1})	1.589	1.049	6.680
R [$I_o \geq 2.0\sigma(I_o)$]	0.0935	0.0564	0.0521
R_w [$I_o \geq 2.0\sigma(I_o)$]	0.1080	0.0562	0.0557

Function minimized $\Sigma w(|F_o|-|F_c|)^2$ where $w^{-1} = \sigma^2(F_o) + 0.0002\ F_o^2$, $R = \Sigma||F_o|-|F_c||/\Sigma|F_o|$, $R_w = (\Sigma w(|F_o|-|F_c|^2)/\Sigma w|F_o|^2)^{1/2}$

Table C.2 Crystallographic data for **2.8**, **2.9**, **2.10** and **2.13**.

Complex	2.8	2.9	2.10	2.13
empirical formula	$C_6Mn_1K_4N_6O_3S_6$	$C_{22}H_{48}MnN_{10}S_6$	$C_{29}H_{60}Mn_1N_8S_5$	$C_{54}H_{108}FeN_9O_{0.42}S_6$
formula weight	607.82	700.01	736.11	1138.45
Temperature (K)	293	293	293	293
crystal system	Othorhombic	Monoclinic	Triclinic	Cubic
space group	Pnma	$P2_1/n$	P-1	Pa-3
a (Å)	16.8415(11)	12.5278(6)	9.935(9)	24.1615(2)
b (Å)	15.0200(10)	12.4262(6)	14.689(14)	24.1615(2)
c (Å)	9.1098(6)	12.5900(6)	15.919(15)	24.1615(2)
α (deg)	90	90	80.442(16)	90
β (deg)	90	90.076(2)	72.682(17)	90
γ (deg)	90	90	81.387(18)	90
V (Å^3)	2304.4(3)	1959.92(16)	2175(4)	14105.0(2)
Z	4	2	2	8
ρ_{calc} (g/cm^3)	1.752	1.186	1.124	1.072
μ (mm^{-1})	1.857	0.683	0.571	0.429
R [$I_o \geq 2.0\sigma(I_o)$]	0.0632	0.0948	0.0709	0.0292
R_w [$I_o \geq 2.0\sigma(I_o)$]	0.0967	0.09	0.0787	0.0322

Function minimized $\Sigma w(|F_o|-|F_c|)^2$ where $w^{-1} = \sigma^2(F_o) + 0.0002\ F_o^2$, $R = \Sigma||F_o|-|F_c||/\Sigma|F_o|$, $R_w = (\Sigma w(|F_o|-|F_c|^2)/\Sigma w|F_o|^2)^{1/2}$

Table C.3 Crystallographic data for **2.15** and **2.16**.

Complex	2.15	2.16
empirical formula	$C_{54}H_{108}GdN_9S_6$	$C_{54}H_{108}DyN_9S_6$
formula weight	1233.16	1238.41
Temperature (K)	150	293
crystal system	Triclinic	Triclinic
space group	P-1	P-1
a (Å)	12.4039(16)	12.4126(3)
b (Å)	12.8837(16)	12.8565(3)
c (Å)	22.787(3)	22.7613(5)
α (deg)	90.877(6)	90.8850(10)
β (deg)	92.241(7)	92.3090(10)
γ (deg)	96.743(7)	96.6870(10)
V (Å^3)	3612.8(8)	3603.93(14)
Z	2	2
ρ_{calc} (g/cm^3)	1.171	1.141
μ (mm^{-1})	1.165	1.246
R [$I_o \geq 2.0\sigma(I_o)$]	0.0520	0.0353
R_w [$I_o \geq 2.0\sigma(I_o)$]	0.0504	0.0324

Function minimized $\Sigma w(|F_o|-|F_c|)^2$ where $w^{-1} = \sigma^2(F_o) + 0.0002\ F_o^2$, $R = \Sigma||F_o|-|F_c||/\Sigma|F_o|$, $R_w = (\Sigma w(|F_o|-|F_c|^2)/\Sigma w|F_o|^2)^{1/2}$

Table C.4 Crystallographic data **2.17**, **2.18** and **2.19**.

Compounds	**2.17**	**2.18**	**2.19**
empirical formula	$C_{54}H_{108}EuN_9S_6$	$C_{54}H_{108}GdN_9S_6$	$C_{54}H_{108}DyN_9S_6$
formula weight	1227.87	1233.16	1238.41
Temperature (K)	293	150	293
crystal system	Triclinic	Triclinic	Triclinic
space group	P-1	P-1	P-1
a (Å)	12.41400(10)	12.4039(16)	12.4126(3)
b (Å)	12.88360(10)	12.8837(16)	12.8565(3)
c (Å)	22.7811(2)	22.787(3)	22.7613(5)
α (deg)	90.9370(10)	90.877(6)	90.8850(10)
β (deg)	92.3400(10)	92.241(7)	92.3090(10)
γ (deg)	96.7250(10)	96.743(7)	96.6870(10)
V (Å^3)	3614.63(5)	3612.8(8)	3603.93(14)
Z	2	2	2
ρ_{calc} (g/cm^3)	1.127	1.171	1.141
μ (mm^{-1})	1.077	1.165	1.246
R [$I_o \geq 2.0\sigma(I_o)$]	0.0342	0.0520	0.0353
R_w [$I_o \geq 2.0\sigma(I_o)$]	0.0360	0.0504	0.0324

Function minimized $\Sigma w(|F_o|-|F_c|)^2$ where $w^{-1} = \sigma^2(F_o) + 0.0002\ F_o^2$, $R = \Sigma||F_o|-|F_c||/\Sigma|F_o|$, $R_w = (\Sigma w(|F_o|-|F_c|^2)/\Sigma w|F_o|^2)^{1/2}$

Table C.5 Crystallographic data for **3.1** to **3.3**.

Complex	**3.1**	**3.2**	**3.3**
empirical formula	$C_{19}H_{11}MnN_7PtS_4$	$C_{34}H_{22}N_{10}MnPtS_4$	$C_{19}H_{11}CoN_7PtS_4$
formula weight	715.62	948.89	719.61
temperature (K)	293	293	293
crystal system	Monoclinic	Monoclinic	Orthorhombic
space group	$P2_1/c$	$P2_1/c$	$P\,n\,a\,2_1$
a (Å)	9.9635(16)	19.387(4)	9.3569(17)
b (Å)	13.508(2)	8.4368(19)	14.609(3)
c (Å)	16.235(3)	23.520(5)	16.563(3)
α (deg)	90	90	90
β (deg)	90.776(2)	112.315(5)	90
γ (deg)	90	90	90
V (Å^3)	2184.8(6)	3558.8(14)	2264.1(7)
Z	4	6	4
ρ_{calc} (g/cm^3)	2.176	1.771	2.111
μ (mm^{-1})	7.380	4.558	7.296
R $[I_o \geq 2.0\sigma(I_o)]$	0.0236	0.0357	0.0461
R_w $[I_o \geq 2.0\sigma(I_o)]$	0.0563	0.0498	0.0841

Function minimized $\Sigma w(|F_o|-|F_c|)^2$ where $w^{-1} = \sigma^2(F_o) + 0.0002\,F_o^2$, $R = \Sigma||F_o|-|F_c||/\Sigma|F_o|$, $R_w = (\Sigma w(|F_o|-|F_c|)^2/\Sigma w|F_o|^2)^{1/2}$ [a] $R_w = \Sigma w(|F_o|-|F_c|)^2/\Sigma w|F_o|^2$

Table C.6 Crystallographic data for **3.5** to **3.7**.

Complex	**3.5**	**3.6**	**3.7**
empirical formula	$C_8H_{16}CuN_8PtS_4$	$C_8H_{16}CuN_8PtS_4$	$C_8H_{16}N_8NiPtS_4$
formula weight	611.16	611.16	606.33
temperature (K)	293	293	293
crystal system	Monoclinic	Triclinic	Monoclinic
space group	$P2_1/n$	P-1	$P2_1/n$
a (Å)	11.8764(18)	6.6261(10)	11.7946(18)
b (Å)	11.4014(18)	8.3050(13)	11.3401(18)
c (Å)	14.242(2)	8.7992(13)	14.312(2)
α (deg)	90	112.9030(10)	90
β (deg)	110.453(2)	98.4060(10)	111.943(2)
γ (deg)	90	94.745(2)	90
V (Å^3)	1806.9(5)	436.04(11)	1775.5(5)
Z	4	1	4
ρ_{calc} (g/cm^3)	2.247	2.327	2.268
μ (mm^{-1})	9.379	9.716	9.407
R [$I_o \geq 2.0\sigma(I_o)$]	0.0247	0.0101	0.0242
R_w [$I_o \geq 2.0\sigma(I_o)$]	0.0469	0.0278	0.0559

Function minimized $\Sigma w(|F_o|-|F_c|)^2$ where $w^{-1} = \sigma^2(F_o) + 0.0002\,F_o^2$, $R = \Sigma||F_o|-|F_c||/\Sigma|F_o|$, $R_w = (\Sigma w(|F_o|-|F_c|)^2/\Sigma w|F_o|^2)^{1/2}$ [a] $R_w = \Sigma w(|F_o|-|F_c|)^2/\Sigma w|F_o|^2$

Table C.7 Crystallographic data for **3.9** to **3.11**.

Complex	3.9	3.10	3.11
empirical formula	$C_{28}H_{16}N_8PbPtS_4$	$C_{16}H_{14}N_6Pb_1S_2$	$C_{20}H_{20}N_6PbS_2$
formula weight	995.01	561.66	615.73
temperature (K)	293	293	293
crystal system	Monoclinic	Triclinic	Orthorhombic
space group	C2/c	P-1	Pbcn
a (Å)	16.106(7)	7.7166(2)	34.1371(19)
b (Å)	15.435(7)	8.8079(2)	16.4965(9)
c (Å)	13.475(6)	104.5476(3)	8.0031(4)
α (deg)	90	101.6918(10)	90
β (deg)	106.184(6)	93.0916(10)	90
γ (deg)	90	107.2670(10)	90
V (Å^3)	3217(2)	917.70(4)	4506.9(4)
Z	4	2	8
ρ_{calc} (g/cm^3)	2.054	2.032	1.815
μ (mm^{-1})	9.862	9.431	7.690
R [$I_o \geq 2.0\sigma(I_o)$]	0.0412	0.0312	0.0375
R_w [$I_o \geq 2.0\sigma(I_o)$]	0.0791	0.0286	0.0215

Function minimized $\Sigma w(|F_o|-|F_c|)^2$ where $w^{-1} = \sigma^2(F_o) + 0.0002\,F_o^2$, $R = \Sigma||F_o|-|F_c||/\Sigma|F_o|$, $R_w = (\Sigma w(|F_o|-|F_c|)^2/\Sigma w|F_o|^2)^{1/2}$ [a] $R_w = \Sigma w(|F_o|-|F_c|)^2/\Sigma w|F_o|^2$

Table C.8 Crystallographic data for **3.12** and **3.13**.

Complex	3.12	3.13
empirical formula	$C_{22}H_{20}N_8PbPtS_4$	$C_{34}H_{28}N_{14}Pb_2PtS_6$
formula weight	926.98	1434.54
temperature (K)	293	293
crystal system	Monoclinic	Triclinic
space group	P 21/n	P-1
a (Å)	8.5760(3)	9.3859(9)
b (Å)	16.7744(7)	11.3420(12)
c (Å)	18.8088(7)	11.5733(12)
α (deg)	90	66.628(5)
β (deg)	95.3290(12)	87.508(6)
γ (deg)	90	71.190(5)
V (Å^3)	2694.09(18)	1065.48(19)
Z	4	2
ρ_{calc} (g/cm^3)	2.285	2.236
μ (mm^{-1})	24.714	11.495
R [$I_o \geq 2.0\sigma(I_o)$]	0.0383	0.0277
R_w [$I_o \geq 2.0\sigma(I_o)$]	0.0385	0.0241

Function minimized $\Sigma w(|F_o|-|F_c|)^2$ where $w^{-1} = \sigma^2(F_o) + 0.0002\,F_o^2$, $R = \Sigma||F_o|-|F_c||/\Sigma|F_o|$, $R_w = (\Sigma w(|F_o|-|F_c|)^2/\Sigma w|F_o|^2)^{1/2}$ [a] $R_w = \Sigma w(|F_o|-|F_c|)^2/\Sigma w|F_o|^2$

Table C.9 Crystallographic data for **4.1** to **4.3**.

Complex	4.1	4.2	4.3
empirical formula	$C_{26}H_{22}Cu_2N_6O_4S_2$	$C_{22}H_{20}Cu_2N_6O_3S_2$	$C_{28}H_{18}Au_2Cu_2N_{12}O_4$
formula weight	673.72	607.65	1107.55
temperature (K)	293	293	293
crystal system	Triclinic	Triclinic	Triclinic
space group	P-1	P-1	P-1
a (Å)	8.1759(2)	8.1587(8)	8.22600(10)
b (Å)	9.4443(2)	9.6864(9)	10.13900(10)
c (Å)	9.5483(2)	16.5547(15)	11.4550(2)
α (deg)	69.3570(10)	75.755(4)	105.9710(10)
β (deg)	71.4920(10)	83.684(5)	107.1760(10)
γ (deg)	79.6760(10)	73.451(5)	102.4360(10)
V (Å^3)	652.37(3)	1214.4(2)	830.53(2)
Z	1	2	1
ρ_{calc} (g/cm^3)	1.715	1.656	2.222
μ (mm^{-1})	1.837	4.086	10.121
R [$I_o \geq 2.0\sigma(I_o)$]	0.0368	0.0524	0.0197
R_w [$I_o \geq 2.0\sigma(I_o)$]	0.0340	0.1708[a]	0.0467

Function minimized $\Sigma w(|F_o|-|F_c|)^2$ where $w^{-1} = \sigma^2(F_o) + 0.0002\,F_o^2$, $R = \Sigma||F_o|-|F_c||/\Sigma|F_o|$, $R_w = (\Sigma w(|F_o|-|F_c|)^2/\Sigma w|F_o|^2)^{1/2}$ [a] $R_w = \Sigma w(|F_o|-|F_c|)^2/\Sigma w|F_o|^2$

Table C.10 Crystallographic data for **4.4** and **4.5**.

Complex	4.4	4.5
empirical formula	$C_{28}H_{18}Au_2Cu_2N_{12}O_2$	$C_{16}H_{34}Cu_2N_8O_2PtS_4$
formula weight	1075.56	820.94
temperature (K)	293	293
crystal system	Monoclinic	Triclinic
space group	C 2/c	P-1
a (Å)	22.291(2)	8.5340(3)
b (Å)	7.8710(7)	9.2598(3)
c (Å)	20.6325(18)	10.3664(3)
α (deg)	90	69.455(2)
β (deg)	118.248(4)	68.160(2)
γ (deg)	90	86.479(2)
V (Å^3)	3188.9(5)	709.77(4)
Z	4	1
ρ_{calc} (g/cm^3)	2.240	1.921
μ (mm^{-1})	10.536	6.723
R [$I_o \geq 2.0\sigma(I_o)$]	0.0318	0.0415
R_w [$I_o \geq 2.0\sigma(I_o)$]	0.0283	0.0370

Function minimized $\Sigma w(|F_o|-|F_c|)^2$ where $w^{-1} = \sigma^2(F_o) + 0.0002\ F_o^2$, $R = \Sigma||F_o|-|F_c||/\Sigma|F_o|$, $R_w = (\Sigma w(|F_o|-|F_c|)^2/\Sigma w|F_o|^2)^{1/2}$

Table C.11 Crystallographic data for **5.1** to **5.3**.

Complex	5.1	5.2	5.3
empirical formula	$C_{17}H_{11}N_5PbS_2$	$C_{17}H_{11}N_5OPbS_2$	$C_{17}H_{10}ClN_5PbS_2$
formula weight	556.64	572.64	591.08
temperature (K)	293	293	293
crystal system	Monoclinic	Triclinic	Triclinic
space group	C 2/c	P -1	P -1
a (Å)	16.122(8)	8.7387(2)	8.7523(13)
b (Å)	10.856(5)	10.3631(3)	9.9505(14)
c (Å)	10.082(5)	11.7559(3)	11.5875(17)
α (deg)	90	94.5700(10)	78.608(2)
β (deg)	94.22(3)	103.6630(10)	79.574(2)
γ (deg)	90	114.6460(10)	69.777(2)
V (Å^3)	1759.7(15)	920.91(4)	921.3(2)
Z	4	2	2
ρ_{calc} (g/cm^3)	2.101	2.065	2.131
μ (mm^{-1})	9.834	9.403	9.539
R [$I_o \geq 2.0\sigma(I_o)$]	0.0680	0.0317	0.0353
R_w [$I_o \geq 2.0\sigma(I_o)$]	0.0676	0.0307	0.0385

Function minimized $\Sigma w(|F_o|-|F_c|)^2$ where $w^{-1} = \sigma^2(F_o) + 0.0002\,F_o^2$, $R = \Sigma||F_o|-|F_c||/\Sigma|F_o|$, $R_w = (\Sigma w(|F_o|-|F_c|)^2/\Sigma w|F_o|^2)^{1/2}$ [a] $R_w = \Sigma w(|F_o|-|F_c|)^2/\Sigma w|F_o|^2$

Table C.12 Crystallographic data for **5.4** to **5.5**.

Complex	5.4	5.5
empirical formula	$C_{17}H_{10}BrN_5PbS_2$	$C_{45}H_{39}N_{12}O_{15}Pb_3$
formula weight	635.54	1609.44
temperature (K)	293	293
crystal system	Triclinic	Hexagonal
space group	P-1	P 63/m
a (Å)	7.6556(5)	13.1063(2)
b (Å)	8.1769(5)	13.1063(2)
c (Å)	16.6410(9)	15.9383(3)
α (deg)	88.064(2)	90
β (deg)	79.197(2)	90
γ (deg)	66.386(2)	120
V (Å^3)	936.58(10)	2371.01(9)
Z	2	4
ρ_{calc} (g/cm^3)	2.253	2.254
μ (mm^{-1})	22.196	10.710
R [$I_o \geq 2.0\sigma(I_o)$]	0.0638	0.0595
R_w [$I_o \geq 2.0\sigma(I_o)$]	0.0708	0.1524*

Function minimized $\Sigma w(|F_o|-|F_c|)^2$ where $w^{-1} = \sigma^2(F_o) + 0.0002\ F_o^2$, $R = \Sigma||F_o|-|F_c||/\Sigma|F_o|$, $R_w = (\Sigma w(|F_o|-|F_c|)^2/\Sigma w|F_o|^2)^{1/2}$ *$R_w = \Sigma w(|F_o|-|F_c|)^2/\Sigma w|F_o|^2$

Appendix D. Crystallographic data files

Supplementary data file

Description :

The crystallographic data files (.cif) for all reported structures in this work.

Filenames:

Composite_Chapter2.cif.txt

Composite_Chapter3.cif.txt

Composite_Chapter4.cif.txt

Composite_Chapter5.cif.txt